Accuracy and Computational Stability of Tensorally-Correct Subgrid Stress and Scalar Flux Representations in Autonomic Closure of LES

by

Eric Stallcup

A Dissertation Presented in Partial Fulfillment
of the Requirements for the Degree
Doctor of Philosophy

Approved October 2020 by the
Graduate Supervisory Committee:

Werner J.A. Dahm, Chair
Ronald Calhoun
Marcus Herrmann
Jeonglae Kim
Eric J. Kostelich

ARIZONA STATE UNIVERSITY

December 2020

ABSTRACT

Autonomic closure is a recently-proposed subgrid closure methodology for large eddy simulation (LES) that replaces the prescribed subgrid models used in traditional LES closure with highly generalized representations of subgrid terms and solution of a local system identification problem that allows the simulation itself to determine the local relation between each subgrid term and the resolved variables at every point and time. The present study demonstrates, for the first time, practical LES based on fully dynamic implementation of autonomic closure for the subgrid stress τ_{ij} and the subgrid scalar flux z_i. It leverages the inherent computational efficiency of tensorally-correct generalized representations in terms of parametric quantities, and uses the fundamental representation theory of Smith (1971) to develop complete and minimal tensorally-correct representations for τ_{ij} and z_i. It then assesses the accuracy of these representations via *a priori* tests, and compares with the corresponding accuracy from nonparametric representations and from traditional prescribed subgrid models. It then assesses the computational stability of autonomic closure with these tensorally-correct parametric representations for τ_{ij} and z_i, via forward simulations with a high-order pseudo-spectral code, including the extent to which any added stabilization is needed in τ_{ij} or z_i to ensure computational stability, and compares with the added stabilization needed in traditional closure with prescribed subgrid models. Further, it conducts *a posteriori* tests based on forward simulations of turbulent conserved scalar mixing with the same pseudo-spectral code, in which velocity and scalar statistics from autonomic closure with these representations for τ_{ij} and z_i are compared with corresponding statistics from traditional closure using prescribed models, and with corresponding statistics of filtered fields from direct numerical simulation (DNS). These comparisons show substantially greater accuracy from autonomic closure than from traditional closure. This study demonstrates that fully dynamic autonomic closure is a practical approach for LES that requires accuracy even at the smallest resolved scales.

TABLE OF CONTENTS

Page

LIST OF TABLES vii

LIST OF FIGURES viii

CHAPTER

1 INTRODUCTION 1

1.1 Governing Equations and Subgrid Terms 2

1.2 The Subgrid Stress Tensor $\tau_{ij}(\mathbf{x}, t)$ 2

1.2.1 Resolved-Scale Kinetic Energy 3

1.2.2 Subgrid Production $P(\mathbf{x}, t)$ of Resolved Kinetic Energy 4

1.3 The Subgrid Scalar Flux Vector $z_i(\mathbf{x}, t)$ 4

1.3.1 Resolved-Scale Scalar Energy 5

1.3.2 Subgrid Production $\Pi(\mathbf{x}, t)$ of Resolved Scalar Energy 6

1.4 Autonomic Closure and Subgrid Representations for τ_{ij} and z_i 6

1.5 *A Priori* Tests of Subgrid Representations 8

1.6 Forward Runs, Subgrid Energetics, and Computational Stability 9

1.7 *A Posteriori* Tests of Subgrid Representations 10

1.8 Present Study 11

1.8.1 Objectives 11

1.8.2 Organization of the Dissertation 12

2 THE AUTONOMIC CLOSURE METHODOLOGY 16

2.1 The General Autonomic Closure Methodology 16

2.1.1 Representations for the Subgrid Stress τ_{ij} 17

2.1.2 Representations for the Subgrid Scalar Flux z_i 18

2.2 Tensorally-Correct Representations for $\mathcal{F}$ and $\mathcal{J}$ 19

2.3 Solution of the Local System Identification Problem 20

2.4 Coefficient Rescaling from Test-Filter Scale to LES-Filter Scale 22

CHAPTER Page

2.5 Implementations of Autonomic Closure 23

3 COMPLETE AND MINIMAL TENSOR REPRESENTATIONS 25

3.1 Rank-Two Tensor Representations 26

3.1.1 Representation of $\boldsymbol{\tau}$ in $\mathbf{S}$ 29

3.1.2 Representations of $\boldsymbol{\tau}$ in $\mathbf{S}$ and $\mathbf{R}$ 30

3.1.3 Representations of $\boldsymbol{\tau}$ in $\mathbf{S}$, $\mathbf{R}$, $\nabla\mathbf{S}$ and $\nabla\mathbf{R}$ 32

3.1.3.1 Rank-2 contractions involving only $\nabla\mathbf{S}^{\alpha}$ 33

3.1.3.2 Rank-2 contractions involving only $\nabla\mathbf{R}^{\beta}$ 34

3.1.3.3 Rank-2 contractions involving $\nabla\mathbf{S}^{\gamma}\nabla\mathbf{R}^{\delta}$ 35

3.1.3.4 Symmetric and antisymmetric tensors $\mathbf{M}_k$ and $\mathbf{W}_p$ ... 36

3.1.3.5 Symmetric rank-2 tensor polynomial basis $\mathbf{m}_S^{(k)}$ 38

3.1.3.6 Truncation to second-order tensor products 40

3.2 Vector Representations 41

3.2.1 Representation of $\mathbf{z}$ in $\nabla\varphi$, $\mathbf{S}$, and $\mathbf{R}$ 43

3.2.2 Representations of $\mathbf{z}$ in $\nabla\varphi$ and $\mathbf{u}$ 44

3.2.3 Representations of $\mathbf{z}$ in φ and $\mathbf{u}$ 46

3.2.4 Representations of $\mathbf{z}$ in φ, $\nabla\varphi$, and $\mathbf{u}$ 46

4 COEFFICIENT RESCALING FROM TEST- TO LES-FILTER SCALE 47

4.1 General Methodology 48

4.2 Rescaling for Subgrid Stress Representations 49

4.3 Inertial-Range Scaling for $\widetilde{U}/\widehat{U}$ 51

4.4 Rescaling for Subgrid Scalar Flux Representations 52

4.5 Inertial-Range Scaling for $\widetilde{Y}/\widehat{Y}$ 54

5 *A PRIORI* TESTS: SUBGRID STRESS REPRESENTATIONS 56

5.1 Subgrid Stress Representations 56

5.1.1 Traditional Prescribed Models for τ_{ij} 57

CHAPTER Page

5.1.1.1 Basic Smagorinsky model 57

5.1.1.2 Dynamic Smagorinsky model 58

5.1.1.3 Bardina scale similarity model 59

5.1.2 Nonparametric Representations for Autonomic Closure 60

5.1.2.1 CL24 representation 60

5.1.2.2 TF27 representation 60

5.1.3 Parametric Representations for Autonomic Closure 61

5.1.3.1 TF19 representation 61

5.1.3.2 TF11 representation 62

5.1.3.3 TF8 representation 62

5.1.3.4 TF5 representation 63

5.2 *A Priori* Tests: Comparisons of τ_{ij} Representations 63

6 STABILITY OF SUBGRID STRESS REPRESENTATIONS 77

6.1 The Pseudo-Spectral LES Code 77

6.2 Computational Stability of Subgrid Stress Representations 80

6.2.1 Traditional Closure with Prescribed Models 83

6.2.1.1 Dynamic Smagorinsky model 83

6.2.1.2 Bardina scale similarity model 83

6.2.2 Autonomic Closure with Nonparametric Representations ... 84

6.2.2.1 CL24 representation 84

6.2.2.2 TF27 representation 84

6.2.3 Autonomic Closure with Parametric Representations 85

6.2.3.1 TF19 representation 85

6.2.3.2 TF11 representation 85

6.2.3.3 TF8 representation 86

6.2.3.4 TF5 representation 87

CHAPTER Page

7 *A PRIORI* TESTS: SUBGRID SCALAR FLUX REPRESENTATIONS 104

7.1 Prescribed Models for Traditional Closure 104

7.1.1 Basic Smagorinsky Model 105

7.1.2 Dynamic Smagorinsky Model 106

7.1.3 Bardina Scale Similarity Model 107

7.2 Nonparametric Representations for Autonomic Closure 107

7.2.1 VF27a Representation 107

7.2.2 VF27b Representation 107

7.2.3 VF54 Representation 108

7.3 Parametric Representations for Autonomic Closure 108

7.3.1 VF6 Representation 108

7.4 Metrics for Assessing Accuracy in *A Priori* Tests 108

7.5 Comparisons of *A Priori* Test Results 110

8 STABILITY OF SUBGRID SCALAR FLUX REPRESENTATIONS . . . 167

8.1 Scalar Mixing Simulations with the Pseudo-Spectral LES Code . . . 167

8.1.1 Asymptotic Scalar Energy Decay Scaling 168

8.1.2 Comparison with Simulation Results 169

8.2 Computational Stability of Turbulent Conserved Scalar Mixing . . . 170

8.2.1 Traditional Closure with Prescribed Models 171

8.2.2 Autonomic Closure with Parametric Representations 172

9 *A POSTERIORI* TEST: SCALAR MIXING IN TURBULENT FLOW 190

9.1 Description of the *A Posteriori* Tests 191

9.2 Statistical Quantities in the Governing Equations 191

9.3 Inner-Scale and Outer-Scale Statistical Quantities 192

9.4 Results from *A Posteriori* Tests 193

9.4.1 Velocity-Based Statistics 193

CHAPTER Page

9.4.1.1 Inner-scale quantities 194

9.4.1.2 Outer-scale quantities 194

9.4.2 Scalar-Based Statistics 195

9.4.2.1 Inner-scale quantities 195

9.4.2.2 Outer-scale quantities 196

10 CONCLUSIONS 209

REFERENCES 212

LIST OF TABLES

Table Page

1 Stabilization Requirements for Each Subgrid Stress Representation 89

2 Run-time per Time Step 90

3 Computational Stability of TF27 Representation 91

4 Computational Stability of TF19 Representation 91

5 Computational Stability of TF11 Representation 92

6 Computational Stability of TF8 Representation 92

7 Computational Stability of TF5 Representation 93

8 Spectral Ranges in the Kinetic Energy Spectrum $E(k)$ and Scalar Energy Spectrum $E_\varphi(k)$ Where Wavenumbers Corresponding to Test-Scale ($\widehat{\Delta}$) and LES-Scale ($\widetilde{\Delta}$) Filters are Located for the High-Re DNS Dataset. 114

9 Spectral Ranges in the Kinetic Energy Spectrum $E(k)$ and Scalar Energy Spectrum $E_\varphi(k)$ Where Wavenumbers Corresponding to Test-Scale ($\widehat{\Delta}$) and LES-Scale ($\widetilde{\Delta}$) Filters are Located for the High-Re DNS Dataset. 114

10 Average and 95% Uncertainty Interval for Decay Rate C_χ in Asymptotic Scalar Energy Decay Scaling from the Five Cases Shown in Figure 76. 176

11 Combinations of Subgrid Stress Representation for $\boldsymbol{\tau}$ and Subgrid Scalar Flux Representation for $\mathbf{z}$, with Corresponding Minimum $c_{BS,\tau}$ and $c_{BS,z}$ Values Needed in (8.11) for Stable Forward Simulations, for Each Case in Figures 74-85. 176

LIST OF FIGURES

Figure Page

1 Inertial-Range Kinetic Energy Spectrum $E(k)$ From the Johns Hopkins DNS Data Used in the Present *A Priori* Tests, Showing LES-Filter Wavenumber $k_{\widetilde{\Delta}} = 40$ and Test-Filter Wavenumber $k_{\widehat{\Delta}} = 20$. 67

2 Typical Results From *A Priori* Tests of Traditional *Prescribed* Models for τ_{ij}, Showing a *Normal* Stress Component τ_{11} in a Typical Plane. 68

3 Similar to Fig. 2 but Showing Results From Traditional *Prescribed* Models for a *Shear* Stress Component τ_{12} in the Same Plane. 69

4 Similar to Figs. 2 and 3 but Showing Results From Traditional *Prescribed* Models for the *Subgrid Production* P in the Same Plane. 70

5 Typical Results From *A Priori* Tests of *Nonparametric* Representations for τ_{ij} in Autonomic Closure, Showing a *Normal* Stress Component τ_{11} in a Typical Plane. Note CL24 is Not Tensorally Correct, Whereas TF27 is Tensorally Correct. 71

6 Similar to Fig. 5 but Showing Results From *Nonparametric* Representations of a *Shear* Stress Component τ_{12} in Autonomic Closuree. Note CL24 is Not Tensorally Correct, Whereas TF27 is Tensorally Correct. 72

7 Similar to Figs. 5 and 6 but Showing Results From *Nonparametric* Representations for the *Subgrid Production* P in Autonomic Closure. Note CL24 is Not Tensorally Correct, Whereas TF27 is Tensorally Correct. 73

8 Typical Results from *A Priori* Tests of *Parametric* Representations of τ_{ij} in Autonomic Closure, Showing a *Normal* Stress Component τ_{11} in a Typical Plane. TF19, TF11, TF8, and TF5 are All Tensorally-Correct Representations. 74

Figure Page

9 Similar to Fig. 8 but Showing Results From *Parametric* Representations of a *Shear* Stress Component τ_{12} in Autonomic Closure. TF19, TF11, TF8, and TF5 are All Tensorally-Correct Representations. 75

10 Similar to Figs. 8 and 9 but Showing Results From *Parametric* Representations for the *Subgrid Production* P in Autonomic Closure. TF19, TF11, TF8, and TF5 are All Tensorally-Correct Representations. 76

11 Results From Forward Simulations With No Subgrid Stress Model, Including (a) Time Evolution of Turbulence Kinetic Energy at a Single Point in the Domain, (b) Time Evolution of Volume-Averaged Turbulence Kinetic Energy, and (c) Energy Spectrum. 94

12 Results From Forward Simulations With the Basic Smagorinsky Model, Including (a) Time Evolution of Turbulence Kinetic Energy at a Single Point in the Domain, (b) Time Evolution of Volume-Averaged Turbulence Kinetic Energy, and (c) Energy Spectrum. 95

13 Results From Forward Simulations With the Dynamic Smagorinsky Model, Including (a) Time Evolution of Turbulence Kinetic Energy at a Single Point in the Domain, (b) Time Evolution of Volume-Averaged Turbulence Kinetic Energy, and (c) Energy Spectrum. 96

14 Results From Forward Simulations With the Bardina Scale Similarity Model, Including (a) Time Evolution of Turbulence Kinetic Energy at a Single Point in the Domain, (b) Time Evolution of Volume-Averaged Turbulence Kinetic Energy, and (c) Energy Spectrum. 97

15 Results From Forward Simulations With Static CL24, Including (a) Time Evolution of Turbulence Kinetic Energy at a Single Point in the Domain, (b) Time Evolution of Volume-Averaged Turbulence Kinetic Energy, and (c) Energy Spectrum. 98

Figure Page

16 Results From Forward Simulations With TF27, Including (a) Time Evolution of Turbulence Kinetic Energy at a Single Point in the Domain, (b) Time Evolution of Volume-Averaged Turbulence Kinetic Energy, and (c) Energy Spectrum. 99

17 Results From Forward Simulations With TF19, Including (a) Time Evolution of Turbulence Kinetic Energy at a Single Point in the Domain, (b) Time Evolution of Volume-Averaged Turbulence Kinetic Energy, and (c) Energy Spectrum. 100

18 Results From Forward Simulations With TF11, Including (a) Time Evolution of Turbulence Kinetic Energy at a Single Point in the Domain, (b) Time Evolution of Volume-Averaged Turbulence Kinetic Energy, and (c) Energy Spectrum. 101

19 Results From Forward Simulations With TF8, Including (a) Time Evolution of Turbulence Kinetic Energy at a Single Point in the Domain, (b) Time Evolution of Volume-Averaged Turbulence Kinetic Energy, and (c) Energy Spectrum. 102

20 Results From Forward Simulations With TF5, Including (a) Time Evolution of Turbulence Kinetic Energy at a Single Point in the Domain, (b) Time Evolution of Volume-Averaged Turbulence Kinetic Energy, and (c) Energy Spectrum. 103

21 Kinetic Energy Spectra $E(k)$ *(Left Column)* and Scalar Energy Spectra $E_\varphi(k)$ *(Right Column)* From High-*Re* DNS Dataset *(Upper Row)* and Low-*Re* DNS Dataset *(Lower Row).* 115

22 Locations of Test-Scale and LES-Scale Filters for $(k_{\widehat{\Delta}}, k_{\widetilde{\Delta}}) = (5, 10)$ in Kinetic Energy Spectrum $E(k)$ (Left) and Scalar Energy Spectrum $E_\varphi(k)$ (Right) From the High-Re DNS Dataset. 116

Figure Page

23 Typical Results for Subgrid Scalar Flux Component $z_1(\mathbf{x}, t)$ From *A Priori* Tests With the High-Re Dataset Using Box Filters With $(k_{\widehat{\Delta}}, k_{\widetilde{\Delta}}) = (5, 10)$. 117

24 Typical Results for Subgrid Scalar Energy Production $\Pi(\mathbf{x}, t)$ From *A Priori* Tests With the High-Re Dataset Using Box Filters With $(k_{\widehat{\Delta}}, k_{\widetilde{\Delta}}) = (5, 10)$. 118

25 PDFs for $z_1(\mathbf{x}, t)$ From *A Priori* Tests with High-Re Data Using Box Filters Having $(k_{\widehat{\Delta}}, k_{\widetilde{\Delta}}) = (5, 10)$, for $c_{BS,z} = 0$ in (8.11) *(Top)* and With Minimum Required $c_{BS,z}$ Value From Chapter 8 for Stable Forward Simulations *(Bottom)*. 119

26 PDFs for $\Pi(\mathbf{x}, t)$ From *A Priori* Tests With High-Re Data Using Box Filters Having $(k_{\widehat{\Delta}}, k_{\widetilde{\Delta}}) = (5, 10)$, for $c_{BS,z} = 0$ in (8.11) *(Top)* and With Minimum Required $c_{BS,z}$ Value From Chapter 8 for Stable Forward Simulations *(Bottom)*. 120

27 Locations of Test-Scale and LES-Scale Filters for $(k_{\widehat{\Delta}}, k_{\widetilde{\Delta}}) = (10, 20)$ in Kinetic Energy Spectrum $E(k)$ (left) and Scalar Energy Spectrum $E_\varphi(k)$ (Right) From the High-Re DNS Dataset. 121

28 Typical Results for Subgrid Scalar Flux Component $z_1(\mathbf{x}, t)$ From *A Priori* Tests With the High-Re Dataset Using Box Filters With $(k_{\widehat{\Delta}}, k_{\widetilde{\Delta}}) = (10, 20)$. 122

29 Typical Results for Subgrid Scalar Energy Production $\Pi(\mathbf{x}, t)$ From *A Priori* Tests With the High-Re Dataset Using Box Filters With $(k_{\widehat{\Delta}}, k_{\widetilde{\Delta}}) = (10, 20)$. 123

30 PDFs for $z_1(\mathbf{x}, t)$ From *A Priori* Tests with High-Re Data Using Box Filters Having $(k_{\widehat{\Delta}}, k_{\widetilde{\Delta}}) = (10, 20)$, for $c_{BS,z} = 0$ in (8.11) *(Top)* and With Minimum Required $c_{BS,z}$ Value From Chapter 8 for Stable Forward Simulations *(Bottom)*. 124

31 PDFs for $\Pi(\mathbf{x}, t)$ From *A Priori* Tests With High-Re Data Using Box Filters Having $(k_{\widehat{\Delta}}, k_{\widetilde{\Delta}}) = (10, 20)$, for $c_{BS,z} = 0$ in (8.11) *(Top)* and With Minimum Required $c_{BS,z}$ Value From Chapter 8 for Stable Forward Simulations *(Bottom)*. 125

Figure Page

32 Locations of Test-Scale and LES-Scale Filters for $(k_{\widehat{\Delta}}, k_{\widetilde{\Delta}}) = (20, 40)$ in Kinetic Energy Spectrum $E(k)$ (left) and Scalar Energy Spectrum $E_\varphi(k)$ (Right) From the High-Re DNS Dataset. 126

33 Typical Results for Subgrid Scalar Flux Component $z_1(\mathbf{x}, t)$ From *A Priori* Tests With the High-Re Dataset Using Box Filters With $(k_{\widehat{\Delta}}, k_{\widetilde{\Delta}}) = (20, 40)$. 127

34 Typical Results for Subgrid Scalar Energy Production $\Pi(\mathbf{x}, t)$ From *A Priori* Tests With the High-Re Dataset Using Box Filters With $(k_{\widehat{\Delta}}, k_{\widetilde{\Delta}}) = (20, 40)$. 128

35 PDFs for $z_1(\mathbf{x}, t)$ From *A Priori* Tests with High-Re Data Using Box Filters Having $(k_{\widehat{\Delta}}, k_{\widetilde{\Delta}}) = (20, 40)$, for $c_{BS,z} = 0$ in (8.11) *(Top)* and With Minimum Required $c_{BS,z}$ Value From Chapter 8 for Stable Forward Simulations *(Bottom)*. 129

36 PDFs for $\Pi(\mathbf{x}, t)$ From *A Priori* Tests With High-Re Data Using Box Filters Having $(k_{\widehat{\Delta}}, k_{\widetilde{\Delta}}) = (20, 40)$, for $c_{BS,z} = 0$ in (8.11) *(Top)* and With Minimum Required $c_{BS,z}$ Value From Chapter 8 for Stable Forward Simulations *(Bottom)*. 130

37 Locations of Test-Scale and LES-Scale Filters for $(k_{\widehat{\Delta}}, k_{\widetilde{\Delta}}) = (30, 60)$ in Kinetic Energy Spectrum $E(k)$ (left) and Scalar Energy Spectrum $E_\varphi(k)$ (Right) From the High-Re DNS Dataset. 131

38 Typical Results for Subgrid Scalar Flux Component $z_1(\mathbf{x}, t)$ From *A Priori* Tests With the High-Re Dataset Using Box Filters With $(k_{\widehat{\Delta}}, k_{\widetilde{\Delta}}) = (30, 60)$. 132

39 Typical Results for Subgrid Scalar Energy Production $\Pi(\mathbf{x}, t)$ From *A Priori* Tests With the High-Re Dataset Using Box Filters With $(k_{\widehat{\Delta}}, k_{\widetilde{\Delta}}) = (30, 60)$. 133

40 PDFs for $z_1(\mathbf{x}, t)$ From *A Priori* Tests with High-Re Data Using Box Filters Having $(k_{\widehat{\Delta}}, k_{\widetilde{\Delta}}) = (30, 60)$, for $c_{BS,z} = 0$ in (8.11) *(Top)* and With Minimum Required $c_{BS,z}$ Value From Chapter 8 for Stable Forward Simulations *(Bottom)*. 134

Figure Page

41 PDFs for $\Pi(\mathbf{x}, t)$ From *A Priori* Tests With High-Re Data Using Box Filters Having $(k_{\widehat{\Delta}}, k_{\widetilde{\Delta}}) = (30, 60)$, for $c_{BS,z} = 0$ in (8.11) *(Top)* and With Minimum Required $c_{BS,z}$ Value From Chapter 8 for Stable Forward Simulations *(Bottom)*. 135

42 Typical Results for Support Density Fields $G_{\Delta_\Gamma}(\mathbf{x}, t)$ at Various $k_{\Delta_\Gamma}/k_{\widetilde{\Delta}}$ for Subgrid Scalar Flux Fields $z_1(\mathbf{x}, t)$ From *A Priori* Tests With High-Re Dataset Using Box Filters Having $(k_{\widehat{\Delta}}, k_{\widetilde{\Delta}}) = (5, 10)$. 136

43 Typical Results for Support Density Fields $G_{\Delta_\Gamma}(\mathbf{x}, t)$ at Various $k_{\Delta_\Gamma}/k_{\widetilde{\Delta}}$ for Subgrid Scalar Energy Production Fields $\Pi(\mathbf{x}, t)$ From *A Priori* Tests With High-Re Dataset Using Box Filters Having $(k_{\widehat{\Delta}}, k_{\widetilde{\Delta}}) = (5, 10)$. 137

44 Typical Results for Support Density Fields $G_{\Delta_\Gamma}(\mathbf{x}, t)$ at Various $k_{\Delta_\Gamma}/k_{\widetilde{\Delta}}$ for Subgrid Scalar Flux Fields $z_1(\mathbf{x}, t)$ From *A Priori* Tests With High-Re Dataset Using Box Filters Having $(k_{\widehat{\Delta}}, k_{\widetilde{\Delta}}) = (10, 20)$. 138

45 Typical Results for Support Density Fields $G_{\Delta_\Gamma}(\mathbf{x}, t)$ at Various $k_{\Delta_\Gamma}/k_{\widetilde{\Delta}}$ for Subgrid Scalar Energy Production Fields $\Pi(\mathbf{x}, t)$ From *A Priori* Tests With High-Re Dataset Using Box Filters Having $(k_{\widehat{\Delta}}, k_{\widetilde{\Delta}}) = (10, 20)$. 139

46 Typical Results for Support Density Fields $G_{\Delta_\Gamma}(\mathbf{x}, t)$ at Various $k_{\Delta_\Gamma}/k_{\widetilde{\Delta}}$ for Subgrid Scalar Flux Fields $z_1(\mathbf{x}, t)$ From *A Priori* Tests With High-Re Dataset Using Box Filters Having $(k_{\widehat{\Delta}}, k_{\widetilde{\Delta}}) = (20, 40)$. 140

47 Typical Results for Support Density Fields $G_{\Delta_\Gamma}(\mathbf{x}, t)$ at Various $k_{\Delta_\Gamma}/k_{\widetilde{\Delta}}$ for Subgrid Scalar Energy Production Fields $\Pi(\mathbf{x}, t)$ From *A Priori* Tests With High-Re Dataset Using Box Filters Having $(k_{\widehat{\Delta}}, k_{\widetilde{\Delta}}) = (20, 40)$. 141

48 Typical Results for Support Density Fields $G_{\Delta_\Gamma}(\mathbf{x}, t)$ at Various $k_{\Delta_\Gamma}/k_{\widetilde{\Delta}}$ for Subgrid Scalar Flux Fields $z_1(\mathbf{x}, t)$ From *A Priori* Tests With High-Re Dataset Using Box Filters Having $(k_{\widehat{\Delta}}, k_{\widetilde{\Delta}}) = (30, 60)$. 142

Figure Page

49 Typical Results for Support Density Fields $G_{\Delta\Gamma}(\mathbf{x}, t)$ at Various $k_{\Delta\Gamma}/k_{\widetilde{\Delta}}$ for Subgrid Scalar Energy Production Fields $\Pi(\mathbf{x}, t)$ From *A Priori* Tests With High-Re Dataset Using Box Filters Having $(k_{\widehat{\Delta}}, k_{\widetilde{\Delta}}) = (30, 60)$. 143

50 Metrics for Scale-by-Scale Accuracy in Support Density $G_{\Delta\Gamma}(\mathbf{x}, t)$ for $z_i(\mathbf{x}, t)$ With $c_{BS,z} = 0$ in (8.11) and $(c_{BS,z})_{min}$ from Chapter 8 for Stable Forward Simulations, from *A Priori* Tests With High-Re Data Using Box Filters $(k_{\widehat{\Delta}}, k_{\widetilde{\Delta}}) = (5, 10)$. Smaller Values Correspond to Greater Accuracy. 144

51 Metrics for Scale-by-Scale Accuracy in Support Density $G_{\Delta\Gamma}(\mathbf{x}, t)$ for $\Pi(\mathbf{x}, t)$ With $c_{BS,z} = 0$ in (8.11) and $(c_{BS,z})_{min}$ from Chapter 8 for Stable Forward Simulations, from *A Priori* Tests with High-Re Data Using Box Filters $(k_{\widehat{\Delta}}, k_{\widetilde{\Delta}}) = (5, 10)$. Smaller Values Correspond to Greater Accuracy. 145

52 Metrics for Scale-by-Scale Accuracy in Support Density $G_{\Delta\Gamma}(\mathbf{x}, t)$ for $z_i(\mathbf{x}, t)$ With $c_{BS,z} = 0$ in (8.11) and $(c_{BS,z})_{min}$ from Chapter 8 for Stable Forward Simulations, from *A Priori* Tests With High-Re Data Using Box Filters $(k_{\widehat{\Delta}}, k_{\widetilde{\Delta}}) = (10, 20)$. Smaller Values Correspond to Greater Accuracy. 146

53 Metrics for Scale-by-Scale Accuracy in Support Density $G_{\Delta\Gamma}(\mathbf{x}, t)$ for $\Pi(\mathbf{x}, t)$ With $c_{BS,z} = 0$ in (8.11) and $(c_{BS,z})_{min}$ from Chapter 8 for Stable Forward Simulations, from *A Priori* Tests with High-Re Data Using Box Filters $(k_{\widehat{\Delta}}, k_{\widetilde{\Delta}}) = (10, 20)$. Smaller Values Correspond to Greater Accuracy. 147

54 Metrics for Scale-by-Scale Accuracy in Support Density $G_{\Delta\Gamma}(\mathbf{x}, t)$ for $z_i(\mathbf{x}, t)$ With $c_{BS,z} = 0$ in (8.11) and $(c_{BS,z})_{min}$ from Chapter 8 for Stable Forward Simulations, from *A Priori* Tests With High-Re Data Using Box Filters $(k_{\widehat{\Delta}}, k_{\widetilde{\Delta}}) = (20, 40)$. Smaller Values Correspond to Greater Accuracy. 148

Figure Page

55 Metrics for Scale-by-Scale Accuracy in Support Density $G_{\Delta_\Gamma}(\mathbf{x},t)$ for $\Pi(\mathbf{x},t)$ With $c_{BS,z}=0$ in (8.11) and $(c_{BS,z})_{min}$ from Chapter 8 for Stable Forward Simulations, from *A Priori* Tests with High-Re Data Using Box Filters $(k_{\widehat{\Delta}},\, k_{\widetilde{\Delta}}) = (20,\, 40)$. Smaller Values Correspond to Greater Accuracy. 149

56 Metrics for Scale-by-Scale Accuracy in Support Density $G_{\Delta_\Gamma}(\mathbf{x},t)$ for $z_i(\mathbf{x},t)$ With $c_{BS,z}=0$ in (8.11) and $(c_{BS,z})_{min}$ from Chapter 8 for Stable Forward Simulations, from *A Priori* Tests With High-Re Data Using Box Filters $(k_{\widehat{\Delta}},\, k_{\widetilde{\Delta}}) = (30,\, 60)$. Smaller Values Correspond to Greater Accuracy. 150

57 Metrics for Scale-by-Scale Accuracy in Support Density $G_{\Delta_\Gamma}(\mathbf{x},t)$ for $\Pi(\mathbf{x},t)$ With $c_{BS,z}=0$ in (8.11) and $(c_{BS,z})_{min}$ from Chapter 8 for Stable Forward Simulations, from *A Priori* Tests with High-Re Data Using Box Filters $(k_{\widehat{\Delta}},\, k_{\widetilde{\Delta}}) = (30,\, 60)$. Smaller Values Correspond to Greater Accuracy. 151

58 Locations of Test-Scale and LES-Scale Filters for $(k_{\widehat{\Delta}},\, k_{\widetilde{\Delta}}) = (5,\, 10)$ in Kinetic Energy Spectrum $E(k)$ (Left) and Scalar Energy Spectrum $E_\varphi(k)$ (Right) from the Low-Re DNS Dataset. 152

59 Typical Results for Subgrid Scalar Flux Component $z_1(\mathbf{x},t)$ from *A Priori* Tests With the Low-Re Dataset Using Box Filters With $(k_{\widehat{\Delta}},\, k_{\widetilde{\Delta}}) = (5,\, 10)$. 153

60 Typical Results for Subgrid Scalar Energy Production $\Pi(\mathbf{x},t)$ from *A Priori* Tests With the Low-Re Dataset Using Box Filters with $(k_{\widehat{\Delta}},\, k_{\widetilde{\Delta}}) = (5,\, 10)$. . 154

61 PDFs for $z_1(\mathbf{x},t)$ from *A Priori* Tests with Low-Re Data Using Box Filters Having $(k_{\widehat{\Delta}},\, k_{\widetilde{\Delta}}) = (5,\, 10)$, for $c_{BS,z}=0$ in (8.11) *(Top)* and With Minimum Required $c_{BS,z}$ Value from Chapter 8 for Stable Forward Simulations *(Bottom)*. 155

62 PDFs for $\Pi(\mathbf{x},t)$ from *A Priori* Tests with Low-Re Data Using Box Filters Having $(k_{\widehat{\Delta}},\, k_{\widetilde{\Delta}}) = (5,\, 10)$, for $c_{BS,z}=0$ in (8.11) *(Top)* and with Minimum Required $c_{BS,z}$ Value from Chapter 8 for Stable Forward Simulations *(Bottom)*. 156

Figure Page

63 Locations of Test-Scale and LES-Scale Filters for $(k_{\widehat{\Delta}}, k_{\widetilde{\Delta}}) = (10, 20)$ in Kinetic Energy Spectrum $E(k)$ (Left) and Scalar Energy Spectrum $E_\varphi(k)$ (Right) from the Low-Re DNS Dataset. 157

64 Typical Results for Subgrid Scalar Flux Component $z_1(\mathbf{x}, t)$ from *A Priori* Tests With the Low-Re Dataset Using Box Filters With $(k_{\widehat{\Delta}}, k_{\widetilde{\Delta}}) = (10, 20)$. 158

65 Typical Results for Subgrid Scalar Energy Production $\Pi(\mathbf{x}, t)$ from *A Priori* Tests With the Low-Re Dataset Using Box Filters with $(k_{\widehat{\Delta}}, k_{\widetilde{\Delta}}) = (10, 20)$. 159

66 PDFs for $z_1(\mathbf{x}, t)$ from *A Priori* Tests with Low-Re Data Using Box Filters Having $(k_{\widehat{\Delta}}, k_{\widetilde{\Delta}}) = (10, 20)$, for $c_{BS,z} = 0$ in (8.11) *(Top)* and With Minimum Required $c_{BS,z}$ Value from Chapter 8 for Stable Forward Simulations *(Bottom)*. 160

67 PDFs for $\Pi(\mathbf{x}, t)$ from *A Priori* Tests with Low-Re Data Using Box Filters Having $(k_{\widehat{\Delta}}, k_{\widetilde{\Delta}}) = (10, 20)$, for $c_{BS,z} = 0$ in (8.11) *(Top)* and with Minimum Required $c_{BS,z}$ Value from Chapter 8 for Stable Forward Simulations *(Bottom)*. 161

68 Locations of Test-Scale and LES-Scale Filters for $(k_{\widehat{\Delta}}, k_{\widetilde{\Delta}}) = (20, 40)$ in Kinetic Energy Spectrum $E(k)$ (Left) and Scalar Energy Spectrum $E_\varphi(k)$ (Right) from the Low-Re DNS Dataset. 162

69 Typical Results for Subgrid Scalar Flux Component $z_1(\mathbf{x}, t)$ from *A Priori* Tests With the Low-Re Dataset Using Box Filters With $(k_{\widehat{\Delta}}, k_{\widetilde{\Delta}}) = (20, 40)$. 163

70 Typical Results for Subgrid Scalar Energy Production $\Pi(\mathbf{x}, t)$ from *A Priori* Tests With the Low-Re Dataset Using Box Filters with $(k_{\widehat{\Delta}}, k_{\widetilde{\Delta}}) = (20, 40)$. 164

71 PDFs for $z_1(\mathbf{x}, t)$ from *A Priori* Tests with Low-Re Data Using Box Filters Having $(k_{\widehat{\Delta}}, k_{\widetilde{\Delta}}) = (20, 40)$, for $c_{BS,z} = 0$ in (8.11) *(Top)* and With Minimum Required $c_{BS,z}$ Value from Chapter 8 for Stable Forward Simulations *(Bottom)*. 165

Figure Page

72 PDFs for $\Pi(\mathbf{x}, t)$ from *A Priori* Tests with Low-Re Data Using Box Filters Having $(k_{\widehat{\Delta}}, k_{\widetilde{\Delta}}) = (20, 40)$, for $c_{BS,z} = 0$ in (8.11) *(Top)* and with Minimum Required $c_{BS,z}$ Value from Chapter 8 for Stable Forward Simulations *(Bottom)*. 166

73 Scalar Field Initial Condition in x, y, and z Mid-Planes of the Domain *(Upper Row)* and Typical Resulting Scalar Field $\varphi(\mathbf{x}, t)$ at Later Time *(Lower Row)*. 177

74 Domain-Averaged Scalar Energy $E_\varphi(t)$ (Upper Panel) and Corresponding Relative Scalar Energy $\Sigma_\varphi(t)$ (Lower Panel) from Basic Smagorinsky Model for $\boldsymbol{\tau}$ and Basic Smagorinsky Model for $\mathbf{z}$ (Case 1 in Table 11). 178

75 Similar to Lower Panel in Figure 74 but for Differing Levels of Energy Forcing and Initial Scalar Energy, Showing Scalar Energy Decay in Dimensional Time (Upper Panel) and Resulting Collapse in Properly Scaled Time (Lower Panel). 179

76 Scaled-Time Derivative of the Relative Scalar Energy $\Sigma_\varphi(\tau)$ in the Lower Panel of Figure 75. Corresponding Average Value Over $5 \leq \tau \leq 35$ and Associated 95% Uncertainty Level are Shown for Each Case in Table 10. . . . 180

77 Domain-Averaged Scalar Energy $E_\varphi(\tau)$ (top) and Corresponding Relative Scalar Energy $\Sigma_\varphi(\tau)$ (Bottom) from Basic Smagorinsky Model for $\boldsymbol{\tau}$ and Bardina Scale Similarity Model for $\mathbf{z}$ (Case 2 in Table 11) with $c_{BS,\tau} = 0$ and Various Levels of Added Dissipation Via $c_{BS,z}$ in (8.11). 181

78 Domain-Averaged Scalar Energy $E_\varphi(\tau)$ (Top) and Corresponding Relative Scalar Energy $\Sigma_\varphi(\tau)$ (Bottom) from Basic Smagorinsky Model for $\boldsymbol{\tau}$ and Dynamic Smagorinsky Model for $\mathbf{z}$ (Case 3 in Table 11) with $c_{BS,\tau} = 0$ and Various Levels of Added Dissipation Via $c_{BS,z}$ in (8.11). Simulations with $c_{BS,z} < 0.50$ Produced Blowup in the Scalar Energy. 182

79 Domain-Averaged Scalar Energy $E_\varphi(\tau)$ (Top) and Corresponding Relative Scalar Energy $\Sigma_\varphi(\tau)$ (Bottom) from Basic Smagorinsky Model for $\boldsymbol{\tau}$ and VF6 Representation for $\mathbf{z}$ (Case 4 in Table 11) with $c_{BS,\tau} = 0$ and Various Levels of Added Dissipation Via $c_{BS,z}$ in (8.11). Simulations with $c_{BS,z} < 0.20$ Produced Blowup in the Scalar Energy. 183

80 Domain-Averaged Scalar Energy $E_\varphi(\tau)$ (top) and Corresponding Relative Scalar Energy $\Sigma_\varphi(\tau)$ (Bottom) from TF5 Representation for $\boldsymbol{\tau}$ and Basic Smagorinsky Model for $\mathbf{z}$ (Case 5 in Table 11) with $c_{BS,\tau} = 0$ and $c_{BS,z} = 1$ in (8.11). 184

81 Domain-Averaged Scalar Energy $E_\varphi(\tau)$ (top) and Corresponding Relative Scalar Energy $\Sigma_\varphi(\tau)$ (Bottom) from TF5 Representation for $\boldsymbol{\tau}$ and Bardina Scale Similarity Model for $\mathbf{z}$ (Case 6 in Table 11) with $c_{BS,\tau} = 0$ and Various Levels of Added Dissipation Via $c_{BS,z}$ in (8.11). Simulations with $c_{BS,z} < 0.20$ Produced Blowup or Nonphysical Increase in the Scalar Energy. 185

82 Domain-Averaged Scalar Energy $E_\varphi(\tau)$ (Top) and Corresponding Relative Scalar Energy $\Sigma_\varphi(\tau)$ (Bottom) from TF5 Representation for $\boldsymbol{\tau}$ and Dynamic Smagorinsky Model for $\mathbf{z}$ (Case 7 in Table 11) with $c_{BS,\tau} = 0$ and Various Levels of Added Dissipation Via $c_{BS,z}$ in (8.11). Simulations with $c_{BS,z} < 0.90$ Produced Blowup or Nonphysical Increase in the Scalar Energy. 186

83 Domain-Averaged Scalar Energy $E_\varphi(\tau)$ (Top) and Corresponding Relative Scalar Energy $\Sigma_\varphi(\tau)$ (Bottom) from TF5 Representation for $\boldsymbol{\tau}$ and VF6 Representation for $\mathbf{z}$ (Case 8 in Table 11) with $c_{BS,\tau} = 0$ and Various Levels of Added Dissipation Via $c_{BS,z}$ in (8.11). Simulations with $c_{BS,z} < 0.80$ Produced Blowup in the Scalar Energy. 187

Figure Page

84 Domain-Averaged Scalar Energy $E_\varphi(\tau)$ (Top) and Corresponding Relative Scalar Energy $\Sigma_\varphi(\tau)$ (Bottom) from TF5 Representation for $\boldsymbol{\tau}$ and VF6 Representation for $\mathbf{z}$ (Case 9 in Table 11) with $c_{BS,\tau} = 0.15$ and Various Levels of Added Dissipation Via $c_{BS,z}$ in (8.11). Simulations with $c_{BS,z} < 0.60$ Produced Blowup or Nonphysical Increase in the Scalar Energy. 188

85 Domain-Averaged Scalar Energy $E_\varphi(\tau)$ (Top) and Corresponding Relative Scalar Energy $\Sigma_\varphi(\tau)$ (Bottom) from TF5 Representation for $\boldsymbol{\tau}$ and Dynamic Smagorinsky Model for $\mathbf{z}$ (Case 10 in Table 11) with $c_{BS,\tau} = 0.15$ and Various Levels of Added Dissipation Via $c_{BS,z}$ in (8.11). Simulations with $c_{BS,z} < 0.80$ Produced Blowup or Nonphysical Increase in the Scalar Energy. 189

86 PDFs of the Kinetic Energy Dissipation Rate from Forward Simulations Based on Traditional Closure with Basic Smagorinsky Models for Both $\boldsymbol{\tau}$ and $\mathbf{z}$ *(Red)*, Autonomic Closure with TF5 and VF6 Representations for $\boldsymbol{\tau}$ and $\mathbf{z}$ *(Blue)*, and Corresponding Filtered DNS *(Black)*. 197

87 PDFs of the Viscous Diffusion of Resolved Kinetic Energy in Forward Simulations Based on Traditional Closure with Basic Smagorinsky Models for Both $\boldsymbol{\tau}$ and $\mathbf{z}$ *(Red)*, Autonomic Closure with TF5 and VF6 Representations for $\boldsymbol{\tau}$ and $\mathbf{z}$ *(Blue)*, and Corresponding Filtered DNS *(Black)*. 198

88 PDFs of the Resolved Velocity in Forward Simulations Based on Traditional Closure with Basic Smagorinsky Models for Both $\boldsymbol{\tau}$ and $\mathbf{z}$ *(Red)*, Autonomic Closure with TF5 and VF6 Representations for $\boldsymbol{\tau}$ and $\mathbf{z}$ *(Blue)*, and Corresponding Filtered DNS *(Black)*. 199

89 PDFs of the Resolved Kinetic Energy in Forward Simulations Based on Traditional Closure with Basic Smagorinsky Models for Both $\boldsymbol{\tau}$ and $\mathbf{z}$ *(Red)*, Autonomic Closure with TF5 and VF6 Representations for $\boldsymbol{\tau}$ and $\mathbf{z}$ *(Blue)*, and Corresponding Filtered DNS *(Black)*. 200

Figure Page

90 PDFs of the Subgrid Production $P = \tau_{ij}\widetilde{S}_{ij}$ in Forward Simulations Based on Traditional Closure with Basic Smagorinsky Models for Both $\boldsymbol{\tau}$ and $\mathbf{z}$ *(Red)*, Autonomic Closure with TF5 and VF6 Representations for $\boldsymbol{\tau}$ and $\mathbf{z}$ *(Blue)*, and Corresponding Filtered DNS *(Black)*. 201

91 PDFs of the Kinetic Energy Transport by the Subgrid Stress in Forward Simulations Based on Traditional Closure with Basic Smagorinsky Models for Both $\boldsymbol{\tau}$ and $\mathbf{z}$ *(Red)*, Autonomic Closure with TF5 and VF6 Representations for $\boldsymbol{\tau}$ and $\mathbf{z}$ *(Blue)*, and Corresponding Filtered DNS *(Black)*. 202

92 PDFs of the Scalar Energy Transport Via Diffusion in Forward Simulations Based on Traditional Closure with Basic Smagorinsky Models for Both $\boldsymbol{\tau}$ and $\mathbf{z}$ *(Red)*, Autonomic Closure with TF5 and VF6 Representations for $\boldsymbol{\tau}$ and $\mathbf{z}$ *(Blue)*, and Corresponding Filtered DNS *(Black)*. 203

93 PDFs of the Scalar Energy Dissipation in Forward Simulations Based on Traditional Closure with Basic Smagorinsky Models for Both $\boldsymbol{\tau}$ and $\mathbf{z}$ *(Red)*, Autonomic Closure with TF5 and VF6 Representations for $\boldsymbol{\tau}$ and $\mathbf{z}$ *(Blue)*, and Corresponding Filtered DNS *(Black)*. 204

94 PDFs of Resolved Scalar Values in Forward Simulations Based on Traditional Closure with Basic Smagorinsky Models for Both $\boldsymbol{\tau}$ and $\mathbf{z}$ *(Red)*, Autonomic Closure with TF5 and VF6 Representations for $\boldsymbol{\tau}$ and $\mathbf{z}$ *(Blue)*, and Corresponding Filtered DNS *(Black)*. 205

95 PDFs of Resolved Scalar Energy in Forward Simulations Based on Traditional Closure with Basic Smagorinsky Models for Both $\boldsymbol{\tau}$ and $\mathbf{z}$ *(Red)*, Autonomic Closure with TF5 and VF6 Representations for $\boldsymbol{\tau}$ and $\mathbf{z}$ *(Blue)*, and Corresponding Filtered DNS *(Black)*. 206

Figure Page

96 PDFs of Scalar Energy Production $\Pi = z_i \frac{\partial \widetilde{\varphi}}{\partial x_i}$ in Forward Simulations Based on Traditional Closure with Basic Smagorinsky Models for Both $\boldsymbol{\tau}$ and $\mathbf{z}$ *(Red)*, Autonomic Closure with TF5 and VF6 Representations for $\boldsymbol{\tau}$ and $\mathbf{z}$ *(Blue)*, and Corresponding Filtered DNS *(Black)*. 207

97 PDFs of Scalar Energy Transport by the Subgrid Scalar Flux in Forward Simulations Based on Traditional Closure with Basic Smagorinsky Models for Both $\boldsymbol{\tau}$ and $\mathbf{z}$ *(Red)*, Autonomic Closure with TF5 and VF6 Representations for $\boldsymbol{\tau}$ and $\mathbf{z}$ *(Blue)*, and Corresponding Filtered DNS *(Black)*. 208

Chapter 1

INTRODUCTION

In applications involving turbulent flows, large eddy simulation (LES) is used to circumvent the impractical computational burden that would be associated with a direct numerical simulation (DNS). LES solves spatially filtered governing equations, and thus produces resulting fields that are resolved only to length scales as small as the filter scale, which typically is set implicitly by the local computational mesh size.

Early development and applications of LES focused primarily on simulating turbulent flows themselves, and then using the results to understand certain aspects of these flows and the turbulence physics in them. However, in most practical situations the underlying turbulent flow itself is not of primary interest. Instead it is other physical processes that are occurring within the turbulent flow – such as mixing of chemical constituents, highly exothermic combustion reactions, particle or droplet formation and transport, phase changes and interactions between phases, etc. – that are of primary interest. In most cases these physical processes can be strongly affected by details of the turbulence near the smallest resolved scales in the underlying flow. As a consequence, in such situations the LES must provide sufficiently high fidelity in its resulting filtered fields, even at or near the smallest resolved scales, in order for the physical processes that are of primary interest to be accurately simulated.

As high performance computing resources become more widely available, and as advances in methodologies such as wall treatments [1–4] are improving simulation accuracy, LES is being increasingly applied to such complex multiphysics turbulent flows [5–15], enabling simulations that address coupled physical processes such as scalar mixing [16–19], chemical reactions and heat transfer [20–22], phase changes [23, 24], droplet and particle dynamics [25, 26], and numerous other phenomena.

1.1 Governing Equations and Subgrid Terms

In such multiphysics problems, the relevant governing equations can each be expressed as a sum of linear and nonlinear terms, respectively $L(\mathbf{u},\varphi)$ and $N(\mathbf{u},\varphi)$, expressed in velocity and scalar fields, respectively $\mathbf{u}(\mathbf{x},t)$ and $\varphi(\mathbf{x},t)$, as

$$L(\mathbf{u},\varphi) + N(\mathbf{u},\varphi) = 0\,. \tag{1.1}$$

Applying a suitable spatial filter [27–30] denoted by $\widetilde{(\ )}$ that has characteristic length scale $\widetilde{\Delta}$, then (1.1) can be written in the filtered fields $\widetilde{\mathbf{u}}(\mathbf{x},t)$ and $\widetilde{\varphi}(\mathbf{x},t)$ as

$$L(\widetilde{\mathbf{u}},\widetilde{\varphi}) + N(\widetilde{\mathbf{u}},\widetilde{\varphi}) = -\left[\widetilde{N(\mathbf{u},\varphi)} - N(\widetilde{\mathbf{u}},\widetilde{\varphi})\right]\,, \tag{1.2}$$

where the left-hand side is of the same form as (1.1) but in the filtered variables $\widetilde{\mathbf{u}}$ and $\widetilde{\varphi}$, and the right-hand side consists of all subgrid terms that arise from the nonlinearities in $N(\mathbf{u},\varphi)$.

To solve such filtered governing equations, the subgrid terms on the right in (1.2) must be related to $\widetilde{\mathbf{u}}(\mathbf{x},t)$ and $\widetilde{\varphi}(\mathbf{x},t)$ to obtain a closed set of equations. Traditionally, this closure is done with prescribed models that involve substantial *ad hoc* treatments [27, 31–36]. Resulting errors from such models can be large even for subgrid terms such as the subgrid stress [14, 27, 31–33, 37–44] that are fundamental to LES.

1.2 The Subgrid Stress Tensor $\tau_{ij}(\mathbf{x},t)$

In the governing equation for conservation of momentum, the nonlinear product $u_i u_j$ in the advection term leads via (1.2) to a subgrid stress tensor of the form

$$\tau_{ij} \equiv \widetilde{u_i u_j} - \widetilde{u}_i \widetilde{u}_j\,, \tag{1.3}$$

with the corresponding form of the filtered momentum equation being

$$\frac{\partial \widetilde{u}_i}{\partial t} + \widetilde{u}_j \frac{\partial \widetilde{u}_i}{\partial x_j} = -\frac{1}{\rho}\frac{\partial \widetilde{p}}{\partial x_i} + \nu \frac{\partial^2 \widetilde{u}_i}{\partial x_j \partial x_j} - \frac{\partial \tau_{ij}}{\partial x_j}\,. \tag{1.4}$$

Widely used subgrid models that prescribe particular forms for τ_{ij} in terms of the resolved-scale variables include the basic Smagorinsky model [45], the dynamic

Smagorinsky model [31, 46–49], the Bardina scale-similarity model [31, 50–52], and mixed models [42–44, 53–57] that combine scale-similarity and dissipative models. However, all of these models have been shown in *a priori* tests to produce substantial errors in their representation of the subgrid stress field $\tau_{ij}(\mathbf{x}, t)$, thereby limiting the accuracy with which momentum and kinetic energy exchange are represented between resolved and subgrid scales in the simulation [3, 27, 31–33, 37].

Because the velocity field $\widetilde{\mathbf{u}}(\mathbf{x}, t)$ is determined primarily by the largest resolved scales, if simulating the velocity were the only objective then continued reliance on such traditional prescribed models might be acceptable, since the filter scale $\widetilde{\Delta}$ could simply be made sufficiently small, albeit at greater computational cost, so that errors introduced by the subgrid model would not substantially affect larger scales of the flow. However, as noted above, LES is being increasingly used to simulate not only the velocity field $\widetilde{\mathbf{u}}(\mathbf{x}, t)$, but also concurrent physical processes, many of which are determined primarily by the smallest resolved scales in $\widetilde{\mathbf{u}}(\mathbf{x}, t)$ and $\widetilde{\varphi}(\mathbf{x}, t)$. In such cases, inaccuracies in the corresponding subgrid models can create large errors in the resolved fields that are of interest. Achieving high fidelity in such multiphysics simulations may therefore require new approaches for representing subgrid terms, including τ_{ij} and other subgrid terms involved in the simulation, that are substantially more accurate across all resolved scales than are current prescribed models.

1.2.1 Resolved-Scale Kinetic Energy

Depending on how τ_{ij} in (1.3) and (1.4) is modeled, the resulting LES may not only be inaccurate near the smallest resolved scales, but the simulation may also become unstable in the sense that the resolved kinetic energy

$$k \equiv \frac{1}{2}\widetilde{u}_i\widetilde{u}_i \,, \tag{1.5}$$

associated with the resulting velocity field $\widetilde{\mathbf{u}}(\mathbf{x}, t)$ can increase without bound. Although the precise reasons for such instabilities remain poorly understood, certain

insights into the resulting $k(\mathbf{x},t)$ field can be gained from considering its governing equation and the associated kinetic energy subgrid production term within it.

1.2.2 Subgrid Production $P(\mathbf{x},t)$ of Resolved Kinetic Energy

From (1.4) and (1.5) the governing equation for $k(\mathbf{x},t)$ is obtained as

$$\frac{\partial k}{\partial t} + \widetilde{u}_j \frac{\partial k}{\partial x_j} = -\frac{\partial}{\partial x_j}\Big(\frac{1}{\rho}\big(\widetilde{p}\widetilde{u}_j\big) - 2\nu\big(\widetilde{u}_i\widetilde{S}_{ij}\big) + \big(\widetilde{u}_i\tau_{ij}\big)\Big) - 2\nu\widetilde{S}_{ij}\widetilde{S}_{ij} + \tau_{ij}\widetilde{S}_{ij}\,, \tag{1.6}$$

where

$$\widetilde{S}_{ij} \equiv \frac{1}{2}\Big(\frac{\partial \widetilde{u}_i}{\partial x_j} + \frac{\partial \widetilde{u}_j}{\partial x_i}\Big) \tag{1.7}$$

is the resolved-scale strain rate tensor. On the right-hand side of (1.6), the three terms in parentheses appear in divergence form and thus account, respectively, for the *conservative redistribution* of resolved-scale kinetic energy by *(i)* the normal stress due to pressure, *(ii)* the viscous stress, and *(iii)* the subgrid stress. The remaining viscous term on the right-hand side involves a square product and thus must always be negative; it accounts for viscous *dissipation* of the resolved-scale kinetic energy.

The rightmost term in (1.6), which can in general be positive or negative at various points and times in the simulation, accounts for the *subgrid production* of resolved-scale kinetic energy from interaction between the subgrid stress tensor $\tau_{ij}(\mathbf{x},t)$ and the resolved strain rate tensor $\widetilde{S}_{ij}(\mathbf{x},t)$. The importance of this term in the stability or instability of a simulation is widely recognized. Accordingly, the present study will pay particular attention to the kinetic energy subgrid production field, defined as

$$P(\mathbf{x},t) \equiv \tau_{ij}\widetilde{S}_{ij}\,, \tag{1.8}$$

associated with various ways of representing the subgrid stress $\tau_{ij}(\mathbf{x},t)$ in the resolved-scale variables.

1.3 The Subgrid Scalar Flux Vector $z_i(\mathbf{x},t)$

Analogous to the subgrid stress, in the governing equation for any conserved scalar quantity φ the nonlinear product $u_j\varphi$ in the advection term leads via (1.2) to a subgrid

scalar flux vector of the form

$$z_j \equiv \widetilde{u_j \varphi} - \widetilde{u}_j \widetilde{\varphi} \,, \tag{1.9}$$

with the corresponding form of the filtered scalar transport equation being

$$\frac{\partial \widetilde{\varphi}}{\partial t} + \widetilde{u}_j \frac{\partial \widetilde{\varphi}}{\partial x_j} = D \frac{\partial^2 \widetilde{\varphi}}{\partial x_j \partial x_j} - \frac{\partial z_j}{\partial x_j} \,, \tag{1.10}$$

where D is the scalar diffusivity.

There are widely used subgrid models that prescribe particular forms for the subgrid scalar flux z_i in terms of the resolved variables in the simulation. Most are direct analogs of corresponding prescribed models for the subgrid stress τ_{ij}, as discussed in Chapter 7 – the most common subgrid scalar flux model is obtained by direct analogy with the basic Smagorinsky model. However, as seen in Chapter 7, all of these prescribed models produce substantial errors in their representations of the subgrid scalar flux field $z_i(\mathbf{x}, t)$, thereby limiting the accuracy with which they can represent scalar mixing in the resolved scales and scalar energy exchange between resolved and subgrid scales, especially near the smallest resolved scales. In so doing they limit the accuracy with which physical processes involving scalar fields can be simulated in multiphysics LES.

1.3.1 Resolved-Scale Scalar Energy

Analogous to the role of the resolved-scale kinetic energy in (1.5) for understanding the accuracy of subgrid stress models, it is productive to similarly define the resolved-scale scalar energy as

$$E_\varphi \equiv \frac{1}{2} \widetilde{\varphi}^2 \,. \tag{1.11}$$

This allows the corresponding scalar energy transport equation to be obtained, from which insights can be gained into the effect of the subgrid scalar flux model for z_i on the resolved-scale scalar energetics in a simulation.

1.3.2 Subgrid Production $\Pi(\mathbf{x},t)$ of Resolved Scalar Energy

From (1.10) and (1.11), the governing equation for the scalar energy $E_\varphi(\mathbf{x},t)$ is obtained as

$$\frac{\partial E_\varphi}{\partial t} + \widetilde{u}_j \frac{\partial E_\varphi}{\partial x_j} = -\frac{\partial}{\partial x_j}\Big(- D\frac{\partial E_\varphi}{\partial x_j} + \widetilde{\varphi} z_j \Big) - D\frac{\partial \widetilde{\varphi}}{\partial x_j}\frac{\partial \widetilde{\varphi}}{\partial x_j} + z_j \frac{\partial \widetilde{\varphi}}{\partial x_j} \,. \tag{1.12}$$

On the right-hand side of (1.12), the two terms in the parenthesis appear in divergence form and thus account for the *conservative redistribution* of resolved-scale scalar energy by *(i)* the scalar diffusive flux and *(ii)* the subgrid scalar flux. The remaining diffusive term on the right-hand side involves a square product and thus must always be negative; it accounts for the diffusive *dissipation* of the resolved scalar energy, and is commonly called the scalar energy dissipation rate.

The rightmost term in (1.12), which can in general be positive or negative at various points and times in the simulation, accounts for the *subgrid production* of resolved-scale scalar energy from interaction between the subgrid scalar flux vector $z_j(\mathbf{x},t)$ and the resolved scalar gradient vector $\partial\widetilde{\varphi}/\partial x_j(\mathbf{x},t)$. Analogous to the kinetic energy subgrid production field in (1.8), the present study will pay particular attention to this scalar energy subgrid production field, defined as

$$\Pi(\mathbf{x},t) \equiv z_j \frac{\partial \widetilde{\varphi}}{\partial x_j} \,, \tag{1.13}$$

and how it relates to various ways of representing the subgrid scalar flux $z_i(\mathbf{x},t)$ in the resolved-scale variables.

1.4 Autonomic Closure and Subgrid Representations for τ_{ij} and z_i

In contrast to traditional *prescribed* models noted above for the subgrid stress τ_{ij} and subgrid scalar flux z_i, an entirely different approach to subgrid closures, termed "autonomic closure", has recently been proposed [58–62]. Autonomic closure is described in detail in Chapter 2. It circumvents the need to specify a particular fixed parametric closure relation for any subgrid term, and instead allows a fully-adaptive

self-optimizing closure methodology. This approach to subgrid closure is autonomic in the sense that the simulation itself determines the optimal relation at each point and time between the subgrid term and the resolved-scale variables in the simulation. In some respects, autonomic closure can be regarded as a high-dimensional dynamic closure approach that avoids the narrow prescribed relations used in various traditional prescribed closure models [31, 46, 47].

Autonomic closure can be *nonparametric* in the sense that the generalized representation for the subgrid term is formulated in the resolved primitive variables of the simulation. Alternatively, it can be *parametric* in the sense that the generalized representation is written in various parameters, presumed to be appropriate for the subgrid term, that can be formed from the primitive variables. In both cases, a substantial number of degrees of freedom in the generalized representation allows the representation to adapt to widely varying local turbulence conditions, including the local degrees of nonlinearity, nonlocality, nonequilibrium, and other characteristics of the turbulence state at each point and time in the simulation.

Since fully dynamic implementations of autonomic closure must, as described below, solve a local system identification problem at each point and time in the simulation to determine the local coefficients in the underlying generalized representation, this can potentially make the computational cost of autonomic closure substantially higher than that of traditional closure based on prescribed subgrid models. That is certainly the case when the number of degrees of freedom in the generalized representation of a subgrid term is very large, as has been the case in prior studies [58–62]. However if, as in the present study, the underlying generalized representations are restricted to tensorally-correct parametric forms, then the number of degrees of freedom becomes far smaller without loss of generality in the representation, and the computational cost can then become comparable to that of traditional dynamic closures based on far more restrictive prescribed models.

The present study therefore focuses on formulating, testing and implementing tensorally-correct generalized representations for τ_{ij} and z_i in autonomic closure of LES. It uses *a priori* tests to determine the fundamental accuracy of each such generalized representation, and then assesses their resulting computational stability in forward simulations. From those results, it then demonstrates substantially improved accuracy in *a posteriori* tests of autonomic closure for τ_{ij} and z_i in large eddy simulations of turbulent conserved scalar mixing.

1.5 *A Priori* Tests of Subgrid Representations

A priori tests of subgrid models have long been used to directly determine the accuracy with which a given closure represents its corresponding subgrid term. Such tests begin with DNS fields, which are filtered to produce pseudo-LES fields that then serve as inputs to the subgrid model. At the same time, the DNS fields permit exact evaluation of the subgrid term at every point in the field. The resulting exact subgrid fields are then compared with the subgrid fields obtained from the subgrid model. The comparisons can be done on a *statistical* basis, which addresses only the distribution of values without regard to similarities or differences in the structure of the exact and modeled fields, and can also be done on a *structural* basis, in which the detailed spatial structure of the exact and modeled fields are directly compared.

Although such *a priori* tests give direct insights into the accuracy of a given subgrid closure, they do not address whether the subgrid closure – when implemented in an LES code and used in a forward simulation – will allow the simulation to remain stable or will lead to computational instability, in which the kinetic energy or the scalar energy increase without bound. For example, several classical subgrid models for τ_{ij} that are deemed to perform reasonably well in *a priori* tests, including the Bardina scale similarity model, lead to nearly immediate computational "blow-up" when they are implemented in a forward simulation. For this reason, *a priori* tests allow comparisons of the relative accuracy of various subgrid closures, but such tests

alone cannot assess the computational stability of the closure. The latter requires so-called *a posteriori* tests, in which the closure is implemented in an LES code and used in forward simulations.

The present study uses *a priori* tests to assess the accuracy of various tensorally-correct generalized representations for τ_{ij} and z_i in autonomic closure, and to compare the resulting accuracies with those of traditional prescribed closure models. From the resulting insights, it identifies representations that are accurate yet efficient enough from a computational perspective to enable their practical use for forward simulations when implemented in an LES code.

1.6 Forward Runs, Subgrid Energetics, and Computational Stability

Assessing the computational stability of any generalized representation for autonomic closure, or of any traditional prescribed subgrid model, requires the closure approach to be implemented in an LES code and tested in forward runs. However, not all LES codes can provide equally objective assessments of computational stability. Different codes may be based on substantially different numerical methods, including relatively low-order spatial differencing schemes that can introduce sufficient artificial dissipation (dispersion error) to make an otherwise unstable subgrid model appear to be inherently stable. Thus, to objectively assess the inherent stability or instability of any closure approach requires forward runs with an LES code based on numerical methods that effectively eliminate all or most such artificial dissipation.

The pseudo-spectral method is particularly well suited for such assessments of closure stability. It is well known that this method can be viewed as the limit of finite differences with infinite order of accuracy. With this method, dispersion errors are essentially eliminated, enabling the inherent subgrid energetics of the closure approach to determine the resulting stability or instability of the simulation. However the common use of Fourier basis functions restricts such pseudo-spectral codes to domains having periodic boundary conditions. That nevertheless allows simulations of

homogeneous isotropic turbulence in periodic domains, in which naturally-occurring large differences in the local turbulence state at various points across the domain and various times throughout the simulation enable robust assessments of the inherent stability or instability of any given closure approach.

For this reason, the present study uses a pseudo-spectral LES code that is based on Fourier collocation spectral methods for the spatial discretization, which thereby eliminates the stabilizing effects of artificial dissipation that would result from low-order spatial differencing methods, and uses an explicit fourth-order Runge-Kutta scheme for time advancement. As a consequence, this is an exceedingly challenging code from the perspective of closure stability, and effectively requires a subgrid closure approach to be manifestly stable in order to obtain stable forward simulations.

1.7 *A Posteriori* Tests of Subgrid Representations

A posteriori tests of subgrid closures are based on the resulting resolved fields obtained from a forward simulation with a sufficiently high-order LES code that implements the particular closure approach. As described above, the assessment of whether the simulation remains stable or not is the most basic result from an *a posteriori* test. But beyond that, the resolved fields obtained from a stable simulation can be examined in detail to gain insights into whether one closure approach gives more accurate resolved fields than does another closure approach. Aside from assessing closure stability, such insights regarding accuracy are the primary purpose of *a posteriori* tests.

A particularly useful way to do this is to compare statistics obtained from forward simulations using various closure models against corresponding statistics obtained from filtering the fields produced by DNS of the same test problem. By using conserved scalar mixing in homogeneous isotropic turbulence in a periodic domain as the test problem, obtaining the requisite DNS fields is well within computational

reach. The resulting filtered DNS statistics then provide the "truth data" against which corresponding LES results using any chosen closure approach can be compared.

This study conducts such *a posteriori* tests for conserved scalar mixing in homogeneous isotropic turbulence, which provides statistics for both the velocity field and the scalar field, as well as joint velocity-scalar statistics, for comparison against the corresponding filtered DNS statistics. In these tests, the turbulence is forced at large scales to maintain statistical stationarity in the underlying turbulent flow, while the scalar field is statistically unstationary and thus continually progresses toward asymptotic homogenization. It will be seen in Chapter 9 that use of the present tensorally-correct representations for τ_{ij} and z_i in autonomic closure provides substantially more accurate *a posteriori* results for scalar mixing statistics than do conventional prescribed closure models.

1.8 Present Study

1.8.1 Objectives

The present study seeks to demonstrate, for the first time, practical LES based on a fully dynamic implementation of autonomic closure for the subgrid stress τ_{ij}. It also seeks to extend this to demonstrate, for the first time, a fully dynamic implementation of autonomic closure for the subgrid scalar flux z_i. It further seeks to combine these fully dynamic implementations of autonomic closure for τ_{ij} and z_i and thereby demonstrate, for the first time, practical LES of turbulent conserved scalar mixing via fully dynamic autonomic closure. In so doing, it seeks to demonstrate that autonomic closure is a viable approach to replace traditional prescribed subgrid models in practical LES of multiphysics turbulent flow problems. It further seeks to show that the results from autonomic closure can be substantially more accurate than those from traditional prescribed subgrid models, especially for physical processes that are sensitive to phenomena at or near the smallest resolved scales in the simulation.

To achieve this, the study seeks to leverage the inherent computational efficiency made possible by tensorally-correct generalized representations in terms of parametric quantities for both the subgrid stress and the subgrid scalar flux. Toward that end it seeks to use the fundamental representation theory of Smith (1971) to develop tensorally-correct generalized parametric representations for τ_{ij} and z_i. It also seeks to assess the accuracy of these representations via *a priori* tests, and to compare with the corresponding accuracy from alternative nonparametric representations and from traditional prescribed subgrid models. It further seeks to understand the computational stability of these tensorally-correct parametric representations for τ_{ij} and z_i, including the extent to which any added stabilization is needed in any of them to ensure computational stability, and to compare against the added stabilization needed in traditional prescribed subgrid models. From these results it then seeks to conduct the first practical LES of turbulent conserved scalar mixing via a fully dynamic implementation of autonomic closure, and to conduct *a posteriori* assessments of the resulting accuracy in comparision to traditional prescribed subgrid models.

1.8.2 Organization of the Dissertation

The remainder of the dissertation is organized as follows:

- Chapter 2 describes the autonomic closure methodology for both the subgrid stress τ_{ij} and the subgrid scalar flux z_i. It first outlines how generalized representations for these subgrid terms are expressed in the resolved variables at the LES-filter scale and at a test-filter scale, and points to Chapter 3 for a complete description of tensorally-correct representations for these subgrid terms. It then describes how the required local system identification problem is solved at each point and time in the simulation, using test-scale filtering and the resulting test-scale subgrid terms to determine the local coefficients in any such generalized representation. It then outlines how the coefficient values obtained at the test-filter scale are rescaled to the LES-filter

scale, using fundamental inertial-range scaling concepts based on the dimensions of each tensor basis element, and points to Chapter 4 for a complete description of this fully general rescaling procedure.

- Chapter 3 then uses complete and minimal tensor representation theory to develop tensorally-correct generalized representations for the subgrid stress tensor $\boldsymbol{\tau} = \tau_{ij}$ and for the subgrid scalar flux vector $\mathbf{z} = z_i$. It first summarizes the representation theory of Smith (1971) and shows how it provides the complete and minimal set of tensor basis elements $\mathbf{m}_i$ for any representation. It then uses this to develop complete and minimal tensorally-correct parametric and nonparametric representations for the subgrid stress $\boldsymbol{\tau}$, and compares these with traditional prescribed subgrid stress models. It also develops tensorally-correct parametric and nonparametric representations for the subgrid scalar flux $\mathbf{z}$ via this fundamental representation theory, and compares these with traditional prescribed subgrid models.

- Chapter 4 then provides a complete description of the procedure for rescaling coefficients in the generalized representations for the subgrid stress tensor $\boldsymbol{\tau}$ and subgrid scalar flux vector $\mathbf{z}$ from the test-filter scale to the LES-filter scale. It first goes through a simple example for a generalized representation of $\boldsymbol{\tau}$ entirely in terms of the strain rate tensor $\mathbf{S}$, to show how this is based on the dimensions of each basis element $\mathbf{m}_i$ in the generalized representation. It then develops a general result for the LES-scale to test-scale coefficient ratio that can be used for any term in any generalized representation for the subgrid stress $\boldsymbol{\tau}$, and a corresponding general result for any term in any generalized representation for the subgrid scalar flux vector $\mathbf{z}$.

- Chapter 5 then assesses the accuracy of each tensorally-correct generalized representation from Chapter 3 for the subgrid stress $\boldsymbol{\tau}$ in autonomic closure via *a priori* tests, and compares to the accuracy of traditional prescribed subgrid models. It pays particular attention to the accuracy in the resulting subgrid production field

$P(\mathbf{x}, t)$ associated with each generalized representation and each prescribed subgrid model. These comparisons include not only the magnitudes of the stress and production fields, but also the detailed spatial structure in these fields. From those results, it confirms the tensorally-correct representation for $\boldsymbol{\tau}$ denoted herein as "TF5" provides the most efficient results with the smallest number of coefficients.

- Chapter 6 then conducts forward simulations with each representation in Chapters 3 and 5 for the subgrid stress $\boldsymbol{\tau}$. It determines the minimum level of stabilization needed to achieve long-time stability in simulations, and compares with the minimum stabilization needed for each of the traditional prescribed subgrid models. From those results it identifies the tensorally-correct and parametric TF5 representation for $\boldsymbol{\tau}$ as being both accurate in *a priori* tests and fully stable by itself in forward simulations without needing *any* added stabilization.

- Chapter 7 uses *a priori* tests to assess the accuracy of each representation developed in Chapter 3 for the subgrid scalar flux $\mathbf{z}$ in autonomic closure, and compares to the accuracy from traditional prescribed subgrid models. It also quantifies how the accuracy found in these *a priori* tests depends on the LES filter scale and test filter scale relative to the inertial and dissipative scale ranges. From these results it identifies one of the tensorally-correct parametric representations for $\mathbf{z}$, herein denoted the "VF6" representation, as providing the most accurate results.

- Chapter 8 then presents results from forward simulations of turbulent conserved scalar mixing to assess the computational stability of autonomic closure based on the TF5 representation for the subgrid stress $\boldsymbol{\tau}$ and the VF6 representation for the subgrid scalar flux $\mathbf{z}$. In particular, it determines the resulting minimum required level of stabilization for the combined TF5/VF6 representations, and compares with the corresponding minimum levels of stabilization needed for various combinations of traditional prescribed subgrid models for $\boldsymbol{\tau}$ and $\mathbf{z}$, including the basic Smagorinsky

model, the dynamic Smagorinsky model, and the Bardina scale-similarity model. Whereas the TF5 representation for the subgrid stress $\boldsymbol{\tau}$ is found in Chapter 6 to be inherently stable by itself, all of the models for the subgrid scalar flux $\mathbf{z}$ are found to require at least some level of added stabilization.

- Chapter 9 then goes beyond assessing the stability of these representations for the subgrid stress $\boldsymbol{\tau}$ and subgrid scalar flux $\mathbf{z}$, by conducting *a posteriori* tests of turbulent conserved scalar mixing to assess the *accuracy* of results obtained from forward simulations of autonomic closure using the combined TF5/VF6 representations. It also conducts corresponding *a posteriori* tests for traditional closure based on prescribed subgrid models for $\boldsymbol{\tau}$ and $\mathbf{z}$ of the basic Smagorinsky form, and additionally conducts DNS of the same turbulent conserved scalar mixing problem. Then it compares the resulting statistics of the velocity, scalar, and joint velocity-scalar fields from autonomic closure using the TF5/VF6 representations with those from traditional closure via prescribed subgrid models and from the filtered DNS results. Those comparisons show a substantial increase in accuracy of LES based on autonomic closure using the combined TF5/VF6 representations for $\boldsymbol{\tau}$ and $\mathbf{z}$, compared to LES based on the traditional prescribed subgrid models.

- Chapter 10 summarizes major conclusions from this study.

Chapter 2

THE AUTONOMIC CLOSURE METHODOLOGY

2.1 The General Autonomic Closure Methodology

Autonomic closure of LES is based on (1) highly generalized representations of subgrid terms, each having a sufficient number of degrees of freedom to allow the local relation between the subgrid term and the resolved variables to adapt freely to the local turbulence state, (2) a local system identification problem at a test-filter scale in which test-scale values of the subgrid term can be obtained from corresponding local test-filtered variables and used to express the generalized representation at the test-filter scale, (3) solution of the local system identification problem as an overdetermined system formed by expressing the generalized test-scale representation at a sufficient number of local reference points, to determine the test-scale coefficients associated with the degrees of freedom in the generalized representation, (4) rescaling of the resulting local coefficients from the test-filter scale to the LES-filter scale, using inertial-range scaling relations, and (5) using the resulting local coefficients at the LES-filter scale in the generalized representation to evaluate the subgrid term from the resolved variables.

Thus, autonomic closure is fundamentally based on scale similarity, which implies that the local relation between any *unknown* LES-scale subgrid term and the LES-filtered variables can be obtained from the local relation between the *known* test-scale subgrid term and the test-filtered variables, via inertial-range rescaling of coefficients in the generalized representation from the test-filter scale to the LES-filter scale.

Because autonomic closure is based on highly generalized representations of subgrid terms, as described in Section 2.2, it circumvents the need to specify a prescribed model for any subgrid term, and instead allows a fully-adaptive self-optimizing closure

methodology, in which the simulation itself determines the optimal relation at each point and time between each subgrid term and the resolved variables. Autonomic closure can be thought of as a high-dimensional dynamic closure approach based on generalized representations having far more degrees of freedom than the narrow prescribed relations used in current dynamic models, such as the single coefficient in the dynamic Smagorinsky model. As a result, autonomic closure can adapt far more freely to widely varying local turbulence conditions, including the local degrees of nonlinearlity, nonlocality, nonequilibrium, and other characteristics of the turbulence state at each point and time in the simulation.

2.1.1 Representations for the Subgrid Stress τ_{ij}

In autonomic closure, the local subgrid stress $\tau_{ij} \equiv \widetilde{u_i u_j} - \widetilde{u}_i \widetilde{u}_j$ is related to the local resolved variables $\widetilde{\mathbf{u}}$ and $\widetilde{p}$ at the LES-filter scale through a highly generalized representation having a sufficient number of degrees of freedom to enable the wide adaptability of this relation as the local turbulence state changes. As described in Section 2.2, with each degree of freedom there is an associated coefficient, the value of which depends on the local turbulence state and is free to change. For any local turbulence state, the corresponding complete set of coefficient values in the generalized representation defines the particular local relation between the local subgrid stress and the local resolved variables.

This generalized representation can be expressed in any desired form, and since it has many degrees of freedom it does not specify a particular relation between the subgrid stress and the resolved variables. Instead it represents a broad *class* of possible relations, with any particular relation corresponding to a particular set of values of the coefficients. This generalized representation may be expressed in *nonparametric* form in terms of the resolved variables, or it may be expressed in *parametric* form in terms of derived quantities that can be evaluated from the resolved variables.

Thus the generalized representation for $\boldsymbol{\tau} \equiv \tau_{ij}$, denoted $\widetilde{\mathcal{F}}$, can be expressed

parametrically or nonparametrically in terms of $\widetilde{\mathbf{u}}$ and $\widetilde{p}$ as

$$\boldsymbol{\tau}(\mathbf{x},t) \approx \boldsymbol{\tau}^{\mathcal{F}}(\mathbf{x},t) \equiv \widetilde{\mathcal{F}}\left[\ \widetilde{\mathbf{u}}(\mathbf{x}+\mathbf{x}',t),\ \widetilde{p}(\mathbf{x}+\mathbf{x}',t)\ \ \forall\, \mathbf{x}' \in \widetilde{\mathbf{S}}\ \right], \tag{2.1}$$

where $\widetilde{\mathbf{S}}$ is a set of points $\mathbf{x}'$ that define a stencil with separation $\widetilde{\Delta}$ on the LES grid.

Analogous to τ_{ij}, local test stresses $T_{ij} \equiv \widehat{\widetilde{u}_i\widetilde{u}_j} - \widehat{\widetilde{u}}_i\widehat{\widetilde{u}}_j$ can be obtained from the resolved velocities $\widetilde{u}_i$ by applying a test filter $\widehat{(\ )}$ [27–32, 42–49, 53, 54] having a length scale $\widehat{\Delta} \geq \widetilde{\Delta}$. Since $\widetilde{\mathcal{F}}$ reflects the local turbulence state at $\mathbf{x}$ via (2.1), then in the same way that τ_{ij} is related to $\widetilde{u}_i$ and $\widetilde{p}$ on $\widetilde{\mathbf{S}}$, so also should T_{ij} be related to $\widehat{\widetilde{u}}_i$ and $\widehat{\widetilde{p}}$ on the corresponding stencil $\widehat{\mathbf{S}}$ with separation $\widehat{\Delta}$. As a result, $\mathbf{T} \equiv T_{ij}$ will follow the same generalized representation as $\boldsymbol{\tau}$ in (2.1), but in the test-filtered variables, namely

$$\mathbf{T}(\mathbf{x},t) \approx \mathbf{T}^{\mathcal{F}}(\mathbf{x},t) \equiv \widehat{\mathcal{F}}\left[\ \widehat{\widetilde{\mathbf{u}}}(\mathbf{x}+\mathbf{x}',t),\ \widehat{\widetilde{p}}(\mathbf{x}+\mathbf{x}',t)\ \ \forall\, \mathbf{x}' \in \widehat{\mathbf{S}}\ \right]. \tag{2.2}$$

The central principle in autonomic closure is that the known values of $\mathbf{T}$, $\widehat{\widetilde{\mathbf{u}}}$, and $\widehat{\widetilde{p}}$ in (2.2) can be used to determine the local form of $\widehat{\mathcal{F}}$ at $\mathbf{x}$, as described in Section 2.3. The resulting $\widehat{\mathcal{F}}$ then determines $\widetilde{\mathcal{F}}$ in (2.1) by inertial-range rescaling of the coefficients from the test-filter scale to the LES-filter scale, as described in Section 2.4. The resulting $\widetilde{\mathcal{F}}$ and the resolved variables $\widetilde{\mathbf{u}}$ and $\widetilde{p}$ then determine $\boldsymbol{\tau}$ via (2.1).

2.1.2 Representations for the Subgrid Scalar Flux z_i

Analogous to the generalized representation for the subgrid stress, in autonomic closure the local subgrid scalar flux z_i is related to the local resolved variables $\widetilde{\mathbf{u}}$ and $\widetilde{\varphi}$ at the LES-filter scale through its own highly generalized representation, which also has a sufficient number of degrees of freedom to enable it to adapt widely as the local turbulence state changes. As described in Section 2.2, there is a coefficient associated with each degree of freedom, the value of which depends on the local turbulence state and is free to change. For any local turbulence state, the corresponding complete set of coefficient values in the generalized representation defines the particular local relation between the local subgrid scalar flux z_i and the local resolved variables $\widetilde{\mathbf{u}}$ and

$\widetilde{\varphi}$. The generalized representation representing this broad *class* of possible relations can be expressed in *nonparametric* form in terms of the resolved variables $\widetilde{\mathbf{u}}$ and $\widetilde{\varphi}$, or in *parametric* form in terms of derived quantities that can be evaluated from these resolved variables.

Thus the generalized representation for $\mathbf{z} \equiv z_i$, denoted $\widetilde{\mathcal{J}}$, can be expressed parametrically or nonparametrically in terms of $\widetilde{\mathbf{u}}$ and $\widetilde{\varphi}$ as

$$\mathbf{z}(\mathbf{x},t) \approx \mathbf{z}^{\mathcal{J}}(\mathbf{x},t) \equiv \widetilde{\mathcal{J}}\left[\ \widetilde{\mathbf{u}}(\mathbf{x}+\mathbf{x}',t),\ \widetilde{\varphi}(\mathbf{x}+\mathbf{x}',t)\ \ \forall\, \mathbf{x}' \in \widetilde{\mathbf{S}}\ \right], \tag{2.3}$$

where $\widetilde{\mathbf{S}}$ is a set of points $\mathbf{x}'$ that define a stencil with separation $\widetilde{\Delta}$ on the LES grid.

Analogous to z_i, local test scalar fluxes $Z_i \equiv \widehat{\widetilde{u}_i\widetilde{\varphi}} - \widehat{\widetilde{u}}_i\widehat{\widetilde{\varphi}}$ can be obtained from the resolved $\widetilde{u}_i$ and $\widetilde{\varphi}$ by applying a test filter $\widehat{(\ )}$ [27–32, 42–49, 53, 54] having a length scale $\widehat{\Delta} \geq \widetilde{\Delta}$. Since $\widetilde{\mathcal{J}}$ reflects the local turbulence state at $\mathbf{x}$ via (2.3), then in the same way that z_i is related to $\widetilde{u}_i$ and $\widetilde{\varphi}$ on $\widetilde{\mathbf{S}}$, so also should Z_i be related to $\widehat{\widetilde{u}}_i$ and $\widehat{\widetilde{\varphi}}$ on the corresponding stencil $\widehat{\mathbf{S}}$ with separation $\widehat{\Delta}$. Therefore $\mathbf{Z} \equiv Z_i$ follows the same generalized representation as $\mathbf{z}$ in (2.3), but in the test-filtered variables, namely

$$\mathbf{Z}(\mathbf{x},t) \approx \mathbf{Z}^{\mathcal{J}}(\mathbf{x},t) \equiv \widehat{\mathcal{J}}\left[\ \widehat{\widetilde{\mathbf{u}}}(\mathbf{x}+\mathbf{x}',t),\ \widehat{\widetilde{\varphi}}(\mathbf{x}+\mathbf{x}',t)\ \ \forall\, \mathbf{x}' \in \widehat{\mathbf{S}}\ \right]. \tag{2.4}$$

The same central principle in autonomic closure applies here to the subgrid scalar flux, namely that the known values of $\mathbf{Z}$, $\widehat{\widetilde{\mathbf{u}}}$, and $\widehat{\widetilde{\varphi}}$ in (2.4) can be used to determine the local form of $\widehat{\mathcal{J}}$ at $\mathbf{x}$ as described in Section 2.3, and then the resulting $\widehat{\mathcal{J}}$ determines $\widetilde{\mathcal{J}}$ in (2.3) by inertial-range rescaling of the coefficients from the test-filter scale to the LES-filter scale as described in Section 2.4. The resulting $\widetilde{\mathcal{J}}$ and the resolved variables $\widetilde{\mathbf{u}}$ and $\widetilde{\varphi}$ then determine $\mathbf{z}$ via (2.3).

2.2 Tensorally-Correct Representations for $\mathcal{F}$ and $\mathcal{J}$

Autonomic closure requires a generalized representation $\mathcal{F}$ for the subgrid stress in (2.1) and the corresponding test stress in (2.2). If the simulation includes conserved scalars then it also requires a generalized representation $\mathcal{J}$ for the subgrid scalar flux

in (2.3) and the corresponding test scalar flux in (2.4). While these representations must have sufficient degrees of freedom to let them adapt freely to changes in the local turbulence state, if the number of degrees of freedom is too large then fully dynamic implementations of autonomic closure will be too computationally burdensome.

This motivates the use of tensorally-correct representations for $\mathcal{F}$ and $\mathcal{J}$, in which each of the resulting degrees of freedom is *required* by the frame invariance properties of the tensor or vector quantity being represented. Such representations are *efficient* in the sense that they ensure each degree of freedom is required for the quantity being represented, given the quantities on which it is assumed to depend. The framework for determining tensorally-correct representations is called representation theory.

Chapter 3 uses the complete and minimal representation theory of Smith (1971) [63] to construct tensorally-correct representations for the stress tensor and the scalar flux vector. The Smith (1971) representation theory is *complete*, in the sense that its tensor and vector bases suffice to represent *any* tensor or vector quantity. It has also been shown by Pennisi & Trovato (1987) [64] to be *minimal*, in the sense that there can be no other complete tensor and vector bases consisting of fewer basis elements.

The generalized representations $\mathcal{F}$ and $\mathcal{J}$ are expressed as sums over these minimal tensor or vector basis elements, with each basis element multiplied by a separate coefficient h that is determined by solving a local system identification problem at the test-filter scale, as described in Section 2.3. It is the resulting full set of these coefficients, denoted $\mathbf{h}$, that adapts the generalized representation to the local turbulence state. In fully dynamic implementations of autonomic closure, new coefficients $\mathbf{h}$ are determined at every point and time in the simulation.

2.3 Solution of the Local System Identification Problem

For the particular turbulence state at $\mathbf{x}$, the particular coefficient values in the generalized representations $\widehat{\mathcal{F}}$ in (2.2) and $\widehat{\mathcal{J}}$ in (2.4) are obtained by solving a local system identification problem in the immediate vicinity of $\mathbf{x}$. This involves solving an

overdetermined system formed by expressing the generalized test-scale representation at a sufficient number of local reference points in the vicinity of $\mathbf{x}$ to determine the test-scale coefficients associated with the degrees of freedom in $\widehat{\mathcal{F}}$. The procedure is described below for $\widehat{\mathcal{F}}$, and a completely analogous procedure is used for $\widehat{\mathcal{J}}$.

The generalized test-scale representation $\widehat{\mathcal{F}}$ involves a substantial number N of degrees of freedom, each of which has a test-scale coefficient $\widehat{h}$ associated with it, the value of which depends on the local turbulence state. The complete local set of N coefficients forms the test-scale coefficient vector $\widehat{\mathbf{h}}$. In a tensorally-correct generalized representation, the coefficient vector $\widehat{\mathbf{h}}$ must be the same for all components of $T_{ij} \equiv \widehat{\widetilde{u}_i \widetilde{u}_j} - \widehat{\widetilde{u}}_i \widehat{\widetilde{u}}_j$, which are known from the $\widehat{\widetilde{\mathbf{u}}}$ and $\widehat{\widetilde{p}}$ values. Thus (2.2) can be equivalently written at $\mathbf{x}$ for each of the six independent components of $\mathbf{T}$ as

$$T_{ij} \approx T_{ij}^{\mathcal{F}} = \widehat{\mathbf{v}}_{ij}\, \widehat{\mathbf{h}}\,, \tag{2.5}$$

where $\widehat{\mathbf{v}}_{ij}$ is the length-N row vector containing the known values of all terms in $\widehat{\mathcal{F}}$ for that ij-component of $\mathbf{T}$ from the test-filtered variables $\widehat{\widetilde{\mathbf{u}}}$ and $\widehat{\widetilde{p}}$ at all points on the stencil $\widehat{\mathbf{S}}$, and where $\widehat{\mathbf{h}}$ is the length-N column vector containing the coefficients of all the terms in $\widehat{\mathcal{F}}$. Grouping all six independent ij-components of $\mathbf{T}$, (2.5) can be written as

$$\mathbf{T} \approx \mathbf{T}^{\mathcal{F}} = \widehat{\mathbf{v}}\, \widehat{\mathbf{h}}\,, \tag{2.6}$$

where $\mathbf{T}$ is a length-6 column vector containing the six T_{ij} components at $\mathbf{x}$, and $\widehat{\mathbf{v}}$ is a $6 \times N$ matrix, each row of which is the corresponding length-N vector $\widehat{\mathbf{v}}_{ij}$ in (2.5).

Placing the stencil $\widehat{\mathbf{S}}$ at each of M reference points $(\mathbf{x}_1, \ldots, \mathbf{x}_M)$ within a local bounding box containing the current point of interest $\mathbf{x}$, in which variations in the turbulence state embodied in $\widehat{\mathcal{F}}$ are taken to be negligible, defines a $6M \times N$ matrix $\widehat{\mathbf{V}} \equiv [\widehat{\mathbf{v}}(\mathbf{x}_1), \ldots, \widehat{\mathbf{v}}(\mathbf{x}_M)]$. With $\boldsymbol{\Upsilon}$ denoting the corresponding $6M$-length column vector consisting of the known T_{ij} values at the M reference points, from (2.6) this gives

$$\boldsymbol{\Upsilon} \approx \boldsymbol{\Upsilon}^{\mathcal{F}} = \widehat{\mathbf{V}}\, \widehat{\mathbf{h}}\,. \tag{2.7}$$

Since the vector $\boldsymbol{\Upsilon}$ and the matrix $\widehat{\mathbf{V}}$ are known, the system in (2.7) may be solved by any number of means. The present study uses a damped least-squares optimization [60] of the form

$$\widehat{\mathbf{h}} = \left(\widehat{\mathbf{V}}^{\mathsf{T}}\widehat{\mathbf{V}} + \lambda\mathbf{I}\right)^{-1}\widehat{\mathbf{V}}^{\mathsf{T}}\boldsymbol{\Upsilon}\,, \tag{2.8}$$

where λ is the damping coefficient. When $M/N \gg 1$, prior work [61, 62] has shown that the value of λ is relatively unimportant over a wide range of sufficiently small values, and thus the value $\lambda = 10^{-3}$ is used. By contrast, when $M/N \leq \mathcal{O}(1)$, this is set $\lambda = 10^{-1}$ to avoid over-fitting of the coefficients.

Once the local test-scale coefficients $\widehat{\mathbf{h}}$ have been determined via (2.8), they are rescaled from the test-filter scale to the LES-filter scale as described in Section 2.3 to produce the corresponding LES-scale coefficients $\widetilde{\mathbf{h}}$. Those coefficients can then be used to evaluate the local subgrid stress τ_{ij}, since in the same way that (2.2) could be written in the form in (2.5), so also can (2.1) be written as

$$\tau_{ij} \approx \tau_{ij}^{\mathcal{F}} = \widetilde{\mathbf{v}}\,\widetilde{\mathbf{h}}\,, \tag{2.9}$$

where $\widetilde{\mathbf{v}}$ is the length-N row vector containing the known values of all terms in $\widetilde{\mathcal{F}}$ from the resolved variables $\widetilde{\mathbf{u}}$ and $\widetilde{p}$ at all points on the stencil $\widetilde{\mathbf{S}}$.

In fully dynamic implementations of autonomic closure, new coefficients $\widetilde{\mathbf{h}}$ are found at each point and time in the simulation, by solving this system identification problem at each $(\mathbf{x}, t)$ to evaluate $\tau_{ij}(\mathbf{x}, t)$.

2.4 Coefficient Rescaling from Test-Filter Scale to LES-Filter Scale

The generalized representations in (2.1), (2.2), (2.3) and (2.4) are, when practical, expressed as complete and minimal sums over dimensional tensor or vector basis elements $\mathbf{m}_i$, and the coefficient h_i associated with each basis element has dimensions that are implied by the dimensions of that basis element. Thus when transferring coefficients from the test-filter scale to the LES-filter scale, the coefficients must be rescaled so that in *nondimensional* form the generalized representations at both

scales are *identical*. The requirement that, in nondimensional form, the generalized representations $\widehat{\mathcal{F}}$ and $\widetilde{\mathcal{F}}$ for the stress, and $\widehat{\mathcal{J}}$ and $\widetilde{\mathcal{J}}$ for the scalar flux, must be identical at the test-filter scale and the LES-filter scale is the precise statement of scale similarity on which autonomic closure is based.

Chapter 4 details the procedure for rescaling the coefficients in these representations. At the test-filter scale in (2.2) and (2.4), each basis element is nondimensionalized with the test-filter length scale $\widehat{\Delta}$ and with the characteristic test-scale velocity $\widehat{U}$ and test-scale scalar value $\widehat{Y}$. Similarly, at the LES-filter scale in (2.1) and (2.3), each basis element in these representations is nondimensionalized with the LES-filter length scale $\widetilde{\Delta}$ and with the characteristic LES-scale velocity $\widetilde{U}$ and scalar value $\widetilde{Y}$. Classical inertial-range scaling relates $\widetilde{U}/\widehat{U}$ and $\widetilde{Y}/\widehat{Y}$ to $\widetilde{\Delta}/\widehat{\Delta}$. Equating each nondimensional basis element in the LES-scale representation, including its coefficient $\widetilde{h}$, with the corresponding nondimensional basis element in the test-scale representation, including its coefficient $\widehat{h}_i$, then gives $\widetilde{h}_i/\widehat{h}_i = (\widetilde{\Delta}/\widehat{\Delta})^{p_i}$, where the scaling exponent p_i depends on the dimensions of the basis element $\mathbf{m}_i$. The resulting $\widetilde{h}_i/\widehat{h}_i$ ratios for all the basis elements allow the complete set of coefficients $\widehat{\mathbf{h}}$ from the test-scale representation, based on $(\widetilde{\Delta}/\widehat{\Delta})$, to determine the complete set of coefficients $\widetilde{\mathbf{h}}$ in the LES-scale representation.

2.5 Implementations of Autonomic Closure

Autonomic closure is meant to be applied in a fully dynamic manner, in which new coefficients are obtained at each point and time in the simulation, as described above. It will be seen in following chapters that, for tensorally-correct forms of the generalized representations, the number of coefficients involved can be small enough while maintaining sufficient generality in the underlying subgrid representations that such fully dynamic implementations are entirely feasible from the perspective of the required computational burden.

However, it is conceivable that for some types of representations, and especially for

representations that are not tensorally correct, the associated computational burden may be too large to enable a fully dynamic implementation. In such cases there are at least two options. The first is a *zonal* dynamic implementation, in which the computational domain is divided into a set of defined spatial zones, and at each time step a set of coefficients is found for each zone. The zonal nature reduces the number of times that the coefficients need to be determined throughout the simulation. The second option is a *static* implementation, in which coefficients are determined ahead of time, for example from simulations of a similar nature as the problem at hand, and then applied in a static sense throughout the simulation.

While such zonal or static implementations may be useful for certain applications of autonomic closure, when using tensorally-correct forms of the underlying generalized representations – as is the focus of the present study – then the number of coefficients that must be determined at each point and time in the simulation can be small enough that a fully dynamic implementation is entirely feasible from the perspective of the required computational burden.

Chapter 3

COMPLETE AND MINIMAL TENSOR REPRESENTATIONS

Representation theory formally provides the most general expression for any tensor quantity, such as the subgrid stress tensor $\boldsymbol{\tau}$ or subgrid scalar flux vector $\mathbf{z}$, in terms of any set of tensors $\mathbf{A}_k$ $(k = 1, \ldots, N)$ and vectors $\mathbf{v}_l$ $(l = 1, \ldots, M)$ in a way that preserves the frame-invariance properties of the tensor quantity. With regard to frame rotation and reflection invariance, for any proper orthogonal tensor $\mathbf{Q}$ (i.e., $Q_{ik}Q_{kj} = \delta_{ij}$ with $\det \mathbf{Q} = \pm 1$) that transforms Cartesian coordinate frame $\mathbf{x}$ into a new Cartesian frame $\mathbf{x}'$ as $x'_i = Q_{ij}x_j$, the tensors $\boldsymbol{\tau}$ and $\boldsymbol{\tau'}$ in the two frames must be related as $\tau'_{ij} = Q_{ik}\,\tau_{kl}\,Q^T_{lj}$, and the invariants $\mathrm{I} = \tau_{ii}$, $\mathrm{II} = \tau_{ij}\tau_{ji}$, and $\mathrm{III} = \tau_{ij}\tau_{jk}\tau_{ki}$ must be the same in both coordinate frames.

Smith (1971) [63] provides a *complete* representation theory for tensors up to rank-two, meaning its tensor polynomial bases formed from $\mathbf{A}_k$ and $\mathbf{v}_l$ is sufficient to represent *any* such tensor quantity. Pennisi & Trovato (1987) [64] subsequently proved that this representation is *minimal*, meaning there can be no *smaller* tensor polynomial basis set that is complete.

This complete and minimal representation theory allows fully generalized representations for $\mathcal{F}$ and $\mathcal{J}$ in (2.1), (2.2), (2.3) and (2.4) to be obtained. Their underlying tensor polynomial bases can be formulated in vectors such as the velocity $\mathbf{u}$ and scalar gradient $\nabla\varphi$, in tensors such as the resolved strain rate $\mathbf{S}$ and rotation rate $\mathbf{R}$, where

$$\mathbf{S} = S_{ij} = \frac{1}{2}\left(\frac{\partial u_i}{\partial x_j} + \frac{\partial u_j}{\partial x_i}\right) \tag{3.1a}$$

$$\mathbf{R} = R_{ij} = \frac{1}{2}\left(\frac{\partial u_i}{\partial x_j} - \frac{\partial u_j}{\partial x_i}\right) \tag{3.1b}$$

and even in tensor gradients such as $\nabla\mathbf{S}$ and $\nabla\mathbf{R}$. The resulting generalized representations $\mathcal{F}$ and $\mathcal{J}$ are guaranteed to be complete and minimal. The minimality

guarantees the resulting tensor polynomial representations involve the smallest possible number of coefficients, and the completeness guarantees there is no loss of generality in the representations despite their minimality.

3.1 Rank-Two Tensor Representations

Following Smith (1971) [63] we seek the most general representation f of a rank-two tensor $\mathbf{B}$ in terms of any assumed set of rank-two tensors $\mathbf{A}_k$ $(k = 1, \ldots, N)$, namely

$$\mathbf{B} = f\big(\mathbf{A}_k\big)\,, \tag{3.2}$$

that satisfies the symmetry, translation, rotation and reflection invariance of rank-two symmetric tensor. Translational invariance is enforced by requiring f to depend only on velocity gradients. With regard to frame invariance, if $\mathbf{Q}$ is a proper orthogonal tensor that transforms Cartesian coordinate frame $\mathbf{x}$ into a new Cartesian frame $\mathbf{x}'$, then this requires

$$\mathbf{B}' = \mathbf{Q}\,\mathbf{B}\,\mathbf{Q}^T = f\big(\mathbf{Q}\,\mathbf{A}_k\,\mathbf{Q}^T\big)\,, \tag{3.3}$$

in such a way that the three tensor invariants of $\mathbf{B}'$, namely $\mathrm{I} = \mathbf{B}'_{ii}$, $\mathrm{II} = \mathbf{B}'_{ij}\mathbf{B}'_{ji}$, and $\mathrm{III} = \mathbf{B}'_{ij}\mathbf{B}'_{jk}\mathbf{B}'_{ki}$, are the same as those of $\mathbf{B}$. Note since $\mathbf{B}$ is a rank-two tensor, for each $\mathbf{A}$ in (3.3) it is understood that $\mathbf{Q}\mathbf{A}\mathbf{Q}^T = Q_{ik}\,A_{kl}\,Q^T_{lj}$ so that $\mathbf{A}$ is contracted with both $\mathbf{Q}$ and $\mathbf{Q}^T$. The general approach for obtaining the complete and minimal tensor polynomial representation f is given in Refs. [63], [64], [65] and [66].

The N tensors $\mathbf{A}_k$ are each separated into symmetric and anti-symmetric parts as

$$\text{symmetric part:} \qquad \mathbf{M}_i \equiv \frac{1}{2}\big(\mathbf{A}_i + \mathbf{A}_i^T\big) \quad i = 1, 2, \ldots, m \leq N \tag{3.4a}$$

$$\text{anti-symmetric part:} \qquad \mathbf{W}_p \equiv \frac{1}{2}\big(\mathbf{A}_p - \mathbf{A}_p^T\big) \quad p = 1, 2, \ldots, w \leq N \tag{3.4b}$$

Similarly, $\mathbf{B} = f(\mathbf{A}_k)$ is separated into symmetric and anti-symmetric parts as

$$\text{symmetric part:} \qquad \mathbf{B}_S \equiv \frac{1}{2}\big(\mathbf{B} + \mathbf{B}^T\big) \tag{3.5a}$$

$$\text{anti-symmetric part:} \qquad \mathbf{B}_A \equiv \frac{1}{2}\big(\mathbf{B} - \mathbf{B}^T\big) \tag{3.5b}$$

from which $\mathbf{B}$ can then be reconstructed as $\mathbf{B} = \mathbf{B}_S + \mathbf{B}_A$.

Following Smith (1971), Pennisi and Trovato (1987), and Itskov (2007), the symmetric part $\mathbf{B}_S$ can be a function only of the following invariant symmetric rank-2 tensor polynomial bases

$$\mathbf{m}_S^{(0)} = \mathbf{I} \tag{3.6a}$$

$$\mathbf{m}_S^{(1,i)} = \mathbf{M}_i \tag{3.6b}$$

$$\mathbf{m}_S^{(2,i)} = \mathbf{M}_i^2 \tag{3.6c}$$

$$\mathbf{m}_S^{(3,ij)} = \mathbf{M}_i\mathbf{M}_j + \mathbf{M}_j\mathbf{M}_i \tag{3.6d}$$

$$\mathbf{m}_S^{(4,ij)} = \mathbf{M}_i^2\mathbf{M}_j + \mathbf{M}_j\mathbf{M}_i^2 \tag{3.6e}$$

$$\mathbf{m}_S^{(5,ij)} = \mathbf{M}_i\mathbf{M}_j^2 + \mathbf{M}_j^2\mathbf{M}_i \tag{3.6f}$$

$$\mathbf{m}_S^{(6,p)} = \mathbf{W}_p^2 \tag{3.6g}$$

$$\mathbf{m}_S^{(7,pq)} = \mathbf{W}_p\mathbf{W}_q - \mathbf{W}_q\mathbf{W}_p \tag{3.6h}$$

$$\mathbf{m}_S^{(8,pq)} = \mathbf{W}_p^2\mathbf{W}_q - \mathbf{W}_q\mathbf{W}_p^2 \tag{3.6i}$$

$$\mathbf{m}_S^{(9,pq)} = \mathbf{W}_p\mathbf{W}_q^2 - \mathbf{W}_q^2\mathbf{W}_p \tag{3.6j}$$

$$\mathbf{m}_S^{(10,ip)} = \mathbf{M}_i\mathbf{W}_p - \mathbf{W}_p\mathbf{M}_i \tag{3.6k}$$

$$\mathbf{m}_S^{(11,ip)} = \mathbf{W}_p\mathbf{M}_i\mathbf{W}_p \tag{3.6l}$$

$$\mathbf{m}_S^{(12,ip)} = \mathbf{M}_i^2\mathbf{W}_p - \mathbf{W}_p\mathbf{M}_i^2 \tag{3.6m}$$

$$\mathbf{m}_S^{(13,ip)} = \mathbf{W}_p\mathbf{M}_i\mathbf{W}_p^2 - \mathbf{W}_p^2\mathbf{M}_i\mathbf{W}_p \tag{3.6n}$$

for all $i < j = 1, 2, \ldots, m$ and all $p < q = 1, 2, \ldots, w$. The symmetric part of $\mathbf{B}$ is then a tensor polynomial formed by the sum over all the tensor bases in (3.6), with each term weighted by its own coefficient h.

Similarly, the anti-symmetric part $\mathbf{B}_A$ can be a function only of the following invariant rank-2 anti-symmetric tensor polynomial bases

$$\mathbf{m}_A^{(1,i)} = \mathbf{W}_p \tag{3.7a}$$

$$\mathbf{m}_A^{(2,pq)} = \mathbf{W}_p\mathbf{W}_q - \mathbf{W}_q\mathbf{W}_p \tag{3.7b}$$

$$\mathbf{m}_A^{(3,ij)} = \mathbf{M}_i\mathbf{M}_j - \mathbf{M}_j\mathbf{M}_i \tag{3.7c}$$

$$\mathbf{m}_A^{(4,ij)} = \mathbf{M}_i^2\mathbf{M}_j - \mathbf{M}_j\mathbf{M}_i^2 \tag{3.7d}$$

$$\mathbf{m}_A^{(5,ij)} = \mathbf{M}_i\mathbf{M}_j^2 - \mathbf{M}_j^2\mathbf{M}_i \tag{3.7e}$$

$$\mathbf{m}_A^{(6,ij)} = \mathbf{M}_i\mathbf{M}_j\mathbf{M}_i^2 - \mathbf{M}_i^2\mathbf{M}_j\mathbf{M}_i \tag{3.7f}$$

$$\mathbf{m}_A^{(7,ij)} = \mathbf{M}_j\mathbf{M}_i\mathbf{M}_j^2 - \mathbf{M}_j^2\mathbf{M}_i\mathbf{M}_j \tag{3.7g}$$

$$\begin{aligned}\mathbf{m}_A^{(8,ijk)} &= \mathbf{M}_i\mathbf{M}_j\mathbf{M}_k + \mathbf{M}_j\mathbf{M}_k\mathbf{M}_i + \mathbf{M}_k\mathbf{M}_i\mathbf{M}_j \\ &\quad - \mathbf{M}_j\mathbf{M}_i\mathbf{M}_k - \mathbf{M}_i\mathbf{M}_k\mathbf{M}_j - \mathbf{M}_k\mathbf{M}_j\mathbf{M}_i\end{aligned} \tag{3.7h}$$

$$\mathbf{m}_A^{(9,ip)} = \mathbf{M}_i\mathbf{W}_p + \mathbf{W}_p\mathbf{M}_i \tag{3.7i}$$

$$\mathbf{m}_A^{(10,ip)} = \mathbf{M}_i\mathbf{W}_p^2 - \mathbf{W}_p^2\mathbf{M}_i \tag{3.7j}$$

for all $i < j = 1, 2, \ldots, m$ and all $p < q = 1, 2, \ldots, w$. The anti-symmetric part of $\mathbf{B}$ is then a tensor polynomial formed by the sum over all the tensor bases in (3.7), with each term weighted by its own coefficient h.

Smith (1971) showed the symmetric and anti-symmetric tensor polynomial bases in (3.6) and (3.7) to be *complete*, meaning that any $\mathbf{B}_S$ and $\mathbf{B}_A$ can be written as a linear sum of the corresponding polynomial terms $\mathbf{m}_S^{(\alpha)}$ and $\mathbf{m}_A^{(\alpha)}$, each weighted by a corresponding coefficient h. However, a complete tensor polynomial basis is not *minimal* if it is reducible to an even smaller basis set that suffices to represent any rank-2 polynomial $\mathbf{B}$. This arises from the fact that there may be tensor polynomial relations among various terms in the basis set that allow the number of tensor products in the basis set to be further reduced. Such relations are generally called Rivlin identities that result from the generalized Cayley-Hamilton theorem

$$\mathbf{A}_k^n - I_A^{(1)}\mathbf{A}_k^{(n-1)} + I_A^{(2)}\mathbf{A}_k^{(n-2)} + \ldots + (-1)^n I_A^{(n)}\mathbf{I} = 0 \tag{3.8}$$

where the $I_A^{(i)}$ are scalar invariants of $\mathbf{A}$ defined as $I_A^{(1)} = tr(\mathbf{A})$, $2I_A^{(2)} = tr(\mathbf{A})^2 - tr(\mathbf{A}^2)$, $\ldots$, $nI = det(\mathbf{A})$. By differentiating (3.8) repeatedly with respect to $\mathbf{A}$, numerous

Rivlin identities can be generated in the form of relations among tensor products of various orders.

Pennisi & Trovato (1987) proved the irreducibility of Smith's (1971) tensor bases in (3.6) and (3.7), thereby establishing these as a *complete* and *minimal* basis. Previously a number of rank-2 tensor polynomial bases had been proposed that were complete but were not minimal. Zemach (1998) discusses completeness and minimality of tensor polynomial bases, and Itskov (2007) uses modern tensor notation and algebra to more clearly derive the complete and minimal bases in (3.5) and (3.6) than was done by Smith (1971). Even complete and minimal bases may not appear unique, since Rivlin identities may allow terms in one basis to be expressed equivalently but differently in another basis. The minimality of a basis simply means that there is no other basis that can be complete and have a smaller number of basis tensors $\mathbf{m}^{(k)}$.

3.1.1 Representation of $\boldsymbol{\tau}$ in $\mathbf{S}$

In this case, $N = 1$ and the only tensor involved in the representation is $\mathbf{A}_1 = \mathbf{S}$. Thus except for $\mathbf{M}_1 = \mathbf{S}$ all the other $\mathbf{M}_i$ are zero, and all the $\mathbf{W}_p$ are zero. Since τ_{ij} is symmetric, its representation is entirely in the symmetric bases $\mathbf{m}_S$ in (3.6), and of these only the following are not zero.

$$\begin{aligned} \mathbf{m}_S^{(0)} &= \mathbf{I} \\ \mathbf{m}_S^{(1)} &= \mathbf{S} \\ \mathbf{m}_S^{(2)} &= \mathbf{S^2} \end{aligned} \tag{3.9}$$

As a result the complete and minimal representation for $\boldsymbol{\tau}$ in $\mathbf{S}$ is

$$\boldsymbol{\tau} = h_0\,\mathbf{I} + h_1\,\mathbf{S} + h_2\,\mathbf{S}^2 \tag{3.10}$$

where the coefficients h_0, h_1 and h_2 are scalars. In representation theory these can at most be functions of the finite set of scalar invariants formable from $\mathbf{I}$, $\mathbf{S}$, and $\mathbf{S}^2$. Traditional prescribed subgrid models are based on conjectures regarding how

the coefficients depend on these invariants or on other parameters that are presumed relevant. For example, Smagorinsky models force $h_2 \equiv 0$ and prescribe a dimensional relation for h_1 in terms of $\widetilde{\Delta}$ and $\mathbf{S}$; the basic Smagorinsky model fixes the value of the constant in that relation, while in the dynamic Smagorinsky model the constant is allowed to vary. In contrast, if autonomic closure were done with the representation for $\boldsymbol{\tau}$ in (3.10), the coefficients h_0, h_1 and h_2 would be determined dynamically at each point and time in the simulation, as described in Chapter 2.

3.1.2 Representations of $\boldsymbol{\tau}$ in S and R

In this case, $N = 2$ and the only tensors involved in the representation are $\mathbf{A}_1 = \mathbf{S}$ and $\mathbf{A}_1 = \mathbf{R}$. As a result, except for $\mathbf{M}_1 = \mathbf{S}$ and $\mathbf{W}_1 = \mathbf{R}$ all the other $\mathbf{M}_i$ and $\mathbf{W}_p$ are zero. Since τ_{ij} is symmetric its representation is entirely in the symmetric bases $\mathbf{m}_S$ in (3.6), and of these all $\mathbf{m}_S^{(k)} \equiv 0$ except

$$\begin{aligned} \mathbf{m}_S^{(0)} &= \mathbf{I} & \mathbf{m}_S^{(10)} &= \mathbf{SR} - \mathbf{RS} \\ \mathbf{m}_S^{(1)} &= \mathbf{S} & \mathbf{m}_S^{(11)} &= \mathbf{RSR} \\ \mathbf{m}_S^{(2)} &= \mathbf{S^2} & \mathbf{m}_S^{(12)} &= \mathbf{S^2R} - \mathbf{RS^2} \\ \mathbf{m}_S^{(6)} &= \mathbf{R^2} & \mathbf{m}_S^{(13)} &= \mathbf{RSR^2} - \mathbf{R^2SR} \end{aligned} \tag{3.11}$$

The stress $\boldsymbol{\tau}$ is then a sum of these eight tensor bases, each with a coefficient h, as

$$\begin{aligned} \boldsymbol{\tau} = h_0\,\mathbf{I} + h_1\,\mathbf{S} + h_2\,\mathbf{S}^2 + h_3\,\mathbf{R}^2 + h_4\,(\mathbf{SR} - \mathbf{RS}) + h_5\,\mathbf{RSR} \\ + h_6\,(\mathbf{S^2R} - \mathbf{RS^2}) + h_7\,(\mathbf{RSR^2} - \mathbf{R^2SR}) \end{aligned} \tag{3.12}$$

In autonomic closure, these eight coefficients h_i are determined dynamically as described in Chapter 2. Importantly, the eight tensor bases in (3.11) and (3.12) are guaranteed to be a complete and minimal representation for $\boldsymbol{\tau}$ in $\mathbf{S}$ and $\mathbf{R}$. The tensor form in (3.12) in eight coefficients will be referred to as TF8.

Previous work [58–61] has shown that subgrid stress representations extending only up to second order products of local velocities are sufficient to provide high accuracy in *a priori* tests of autonomic closure. That motivates a further tensorally-correct

representation, in which (3.12) is truncated to remove terms involving third- and higher-order tensor products. Doing so provides a further representation for the subgrid stress $\boldsymbol{\tau}$ as

$$\boldsymbol{\tau} = h_0\,\mathbf{I} + h_1\,\mathbf{S} + h_2\,\mathbf{S}^2 + h_3\,\mathbf{R}^2 + h_4\,(\mathbf{SR} - \mathbf{RS}) \tag{3.13}$$

The representation in (3.13) is not complete, since it was truncated from the complete and minimal form in (3.12), but it is tensorally correct. The tensor form in (3.13) in five coefficients will be referred to as TF5.

A different tensorally-correct representation for $\boldsymbol{\tau}$ in terms of $\mathbf{S}$ and $\mathbf{R}$, involving 11 tensor bases, has been used in fluid dynamics for over three decades, namely

$$\begin{aligned}\boldsymbol{\tau} = {} & h_0\,\mathbf{I} + h_1\,\mathbf{S} + h_2\,\mathbf{S}^2 + h_3\,\mathbf{R}^2 + h_4\,(\mathbf{SR} - \mathbf{RS}) + h_5\,(\mathbf{S^2R} - \mathbf{RS^2}) \\ & + h_6\,(\mathbf{SR^2} + \mathbf{R^2S}) + h_7\,(\mathbf{S^2R^2} + \mathbf{R^2S^2}) + h_8\,(\mathbf{SRS^2} - \mathbf{S^2RS}) \\ & + h_9\,(\mathbf{RSR^2} - \mathbf{R^2SR}) + h_{10}\,(\mathbf{RS^2R^2} - \mathbf{R^2S^2R})\end{aligned} \tag{3.14}$$

This was originated by Lumley (1970) [67] and put in this form by Pope (1974) [68], prior to the Smith (1971) formulation of the complete and minimal representation theory. It has subsequently been used by Lund & Novikov (1992) [69], Gatski & Speziale (1993) [70], and others to model the turbulent stress in Reynolds-averaged turbulence simulations, and to propose traditional prescribed closure models for the subgrid stress in LES. Yet the representation in (3.14) involves 11 tensor bases in $\mathbf{S}$ and $\mathbf{R}$, extending to fifth-order tensor products, whereas the complete and minimal representation in (3.12) involves only eight tensor bases and extends to only fourth-order tensor products.

It is likely that the tensor basis in (3.14) is complete, however it cannot be minimal since the basis in (3.12) from the Smith (1971) generalized formulation for complete and minimal tensor representation in $\mathbf{S}$ and $\mathbf{R}$ involves fewer terms. There may be Rivlin identities that relate the fifth-order tensor products in (3.14) to fourth- and lower-order products as in (3.12), but that alone would only reduce the 11 tensor

bases in (3.14) by one. This suggests there may be other relations that can reduce this representation to the same number of bases as in (3.12).

Indeed, Lund & Novikov (1992) [69] showed that, under the additional assumption that the strain rate $\mathbf{S}$ is not in an axisymmetric state (i.e., when $\mathbf{S}$ does not have repeated eigenvalues) and when the vorticity vector corresponding to $\mathbf{R}$ is not aligned with any of the strain rate eigenvectors, then the number of *independent* tensor bases in (3.14) is reduced from eleven to six, and the number of independent scalar invariants on which the coefficients for these bases can depend is reduced from seven to five. While the assumptions involved in that reduction will not apply in a fully general representation, it suggests there are ways to reduce (3.14) to the same number of tensor bases as in the minimal and complete representation in (3.12).

It does not appear to be widely known in the fluid dynamics community that (3.14) is not a minimal basis [65, 67, 68, 70–74], and that the tensor basis in (3.12) – obtained from the general tensor basis formulation of Smith (1971) in Section 3.1 – is complete and minimal for representing τ_{ij} in terms of $\mathbf{S}$ and $\mathbf{R}$.

Despite (3.14) not being a minimal tensor basis, Section 5.1.3.2 uses *a priori* tests to assess its accuracy as a generalized representation for $\boldsymbol{\tau}$. That representation is the sum over the 11 tensor bases, each weighted by a corresponding coefficient h that is determined as part of the autonomic closure methodology. That tensor form in 11 coefficients will be referred to as TF11.

3.1.3 Representations of $\boldsymbol{\tau}$ in S, R, ∇S and ∇R

In this case, in addition to

$$\mathbf{A}_1 = \mathbf{S} \equiv S_{ij} \tag{3.15a}$$

$$\mathbf{A}_2 = \mathbf{R} \equiv R_{ij} \tag{3.15b}$$

this section also uses $\nabla\mathbf{S} \equiv \partial S_{ij}/\partial x_k$ and $\nabla\mathbf{R} \equiv \partial R_{ij}/\partial x_k$ to formulate tensorally-correct representations for $\boldsymbol{\tau}$. Importantly, $\nabla\mathbf{S}$ and $\nabla\mathbf{R}$ are rank-3 tensors. The

Smith (1971) complete and minimal representation theory [63] does not apply to rank-3 tensors, and there is no general formulation for a rank-2 tensor polynomial representation in terms of rank-2 and rank-3 tensors that would apply to this situation [75].

However, prior work [59–62] has shown that $\boldsymbol{\tau}$ can be accurately represented by generalized representations that extend only up to second order in velocity component products. For that reason, this study forms rank-2 tensors from $\nabla\mathbf{S}$ and $\nabla\mathbf{R}$, via contractions of the form of $\nabla\mathbf{S}^{\alpha}$, $\nabla\mathbf{R}^{\beta}$, and $\nabla\mathbf{S}^{\gamma}\nabla\mathbf{R}^{\delta}$, and includes the resulting rank-2 tensors with $\mathbf{S}$ and $\mathbf{R}$ in the tensors $\mathbf{A}_k$ that are used in the general formulation in Section 3.1.

3.1.3.1 Rank-2 contractions involving only $\nabla\mathbf{S}^{\alpha}$

Since $\nabla\mathbf{S}$ is a rank-3 tensor, this section determines the powers α that contract $\nabla\mathbf{S}^{\alpha}$ to a rank-2 tensor. For any α, $\nabla\mathbf{S}^{\alpha}$ involves 3α indices, so two of these must be the free indices i and j, and the remaining indices must be repeated in integer m pairs. Thus allowable values of $\alpha > 1$ must satisfy $3\alpha - 2 = 2m$ for integer $m \geq 1$, which is the case only for $\alpha = 2, 4, 6, \ldots$. For $\alpha = 2$ there are eight possible tensor products of the form $\nabla\mathbf{S}^2$, namely

$$\begin{gathered}\frac{\partial S_{kk}}{\partial x_i}\frac{\partial S_{ll}}{\partial x_j}, \quad \frac{\partial S_{kl}}{\partial x_i}\frac{\partial S_{kl}}{\partial x_j}, \quad \frac{\partial S_{ik}}{\partial x_k}\frac{\partial S_{lj}}{\partial x_l}, \quad \frac{\partial S_{ik}}{\partial x_l}\frac{\partial S_{lj}}{\partial x_k} \\ \frac{\partial S_{ik}}{\partial x_k}\frac{\partial S_{ll}}{\partial x_j}, \quad \frac{\partial S_{ik}}{\partial x_l}\frac{\partial S_{kl}}{\partial x_j}, \quad \frac{\partial S_{kk}}{\partial x_i}\frac{\partial S_{lj}}{\partial x_l}, \quad \frac{\partial S_{kl}}{\partial x_i}\frac{\partial S_{kj}}{\partial x_l}\end{gathered} \tag{3.16}$$

For each of $\alpha = 4, 6, \ldots$ there are far larger numbers of tensor products of the form $\nabla\mathbf{S}^{\alpha}$ that can form rank-2 symmetric tensors. Many of these may be reducible via the equivalent of Rivlin identities among them, though for rank-3 tensors there appears to be no equivalent of the Cayley-Hamilton theorem from which to obtain such identities. Such an approach could potentially lead to a *minimal* tensor polynomial basis set. However, while there are efficiencies gained from a tensor representation in a minimal basis, there is no loss of generality if a non-minimal basis is used. Moreover,

lacking the equivalent of a Cayley-Hamilton theorem for rank-3 tensors leaves open the question of whether it is even possible for there to be a *finite* set of tensor products $\nabla\mathbf{S}^\alpha$ that can form rank-2 symmetric tensors.

Thus, while including such higher tensor products $\nabla\mathbf{S}^\alpha$ for $\alpha > 2$ may be necessary to obtain a *complete* tensor polynomial basis set, even if only the $\nabla\mathbf{S}^2$ products are included in the representation of $\boldsymbol{\tau}$ they will allow effects of $\nabla\mathbf{S}$ to be reflected in the subgrid stress. The complete set of unique second-order rank-2 contractions $\nabla\mathbf{S}^2$ consists of

$$\mathbf{A}_3 = \frac{\partial S_{kk}}{\partial x_i}\frac{\partial S_{ll}}{\partial x_j} \tag{3.17a}$$

$$\mathbf{A}_4 = \frac{\partial S_{kl}}{\partial x_i}\frac{\partial S_{kl}}{\partial x_j} \tag{3.17b}$$

$$\mathbf{A}_5 = \frac{\partial S_{ik}}{\partial x_k}\frac{\partial S_{lj}}{\partial x_l} \tag{3.17c}$$

$$\mathbf{A}_6 = \frac{\partial S_{ik}}{\partial x_l}\frac{\partial S_{lj}}{\partial x_k} \tag{3.17d}$$

$$\mathbf{A}_7 = \frac{\partial S_{ik}}{\partial x_k}\frac{\partial S_{ll}}{\partial x_j} \tag{3.17e}$$

$$\mathbf{A}_8 = \frac{\partial S_{ik}}{\partial x_l}\frac{\partial S_{kl}}{\partial x_j} \tag{3.17f}$$

$$\mathbf{A}_9 = \frac{\partial S_{kk}}{\partial x_i}\frac{\partial S_{lj}}{\partial x_l} \tag{3.17g}$$

$$\mathbf{A}_{10} = \frac{\partial S_{kl}}{\partial x_i}\frac{\partial S_{kj}}{\partial x_l} \tag{3.17h}$$

3.1.3.2 Rank-2 contractions involving only $\nabla\mathbf{R}^\beta$

Because in Section 3.1 the tensors $\mathbf{A}_k$ are identified without regard to their symmetry, since $\nabla\mathbf{R}$ is a rank-3 tensor it is possible by direct analogy with the rank-2 contractions $\nabla\mathbf{S}^2$ in (3.17a-h) to write corresponding rank-2 contractions $\nabla\mathbf{R}^2$. However, due to the anti-symmetry of $\mathbf{R}$, $R_{kk} \equiv 0$ even when $S_{kk} \neq 0$, and this

eliminates three of the eight corresponding contractions $\nabla\mathbf{R}^2$, leaving only

$$\mathbf{A}_{11} = \frac{\partial R_{kl}}{\partial x_i}\frac{\partial R_{kl}}{\partial x_j} \tag{3.18a}$$

$$\mathbf{A}_{12} = \frac{\partial R_{ik}}{\partial x_k}\frac{\partial R_{lj}}{\partial x_l} \tag{3.18b}$$

$$\mathbf{A}_{13} = \frac{\partial R_{ik}}{\partial x_l}\frac{\partial R_{lj}}{\partial x_k} \tag{3.18c}$$

$$\mathbf{A}_{14} = \frac{\partial R_{ik}}{\partial x_l}\frac{\partial R_{kl}}{\partial x_j} \tag{3.18d}$$

$$\mathbf{A}_{15} = \frac{\partial R_{kl}}{\partial x_i}\frac{\partial R_{kj}}{\partial x_l} \tag{3.18e}$$

3.1.3.3 Rank-2 contractions involving $\nabla\mathbf{S}^\gamma\nabla\mathbf{R}^\delta$

Because $\nabla\mathbf{S}$ and $\nabla\mathbf{R}$ are both rank-3 tensors it is again possible by direct analogy with the rank-2 contractions in (3.17a-h) to write corresponding second-order rank-2 mixed contractions $\nabla\mathbf{S}\nabla\mathbf{R}$. Contractions involving R_{kk} are again eliminated since $R_{kk} \equiv 0$, but in this case this eliminates only two of the eight contractions. Additionally, the symmetry of $\mathbf{S}$ and the anti-symmetry of $\mathbf{R}$ require $S_{kl}R_{kl} \equiv 0$, but due to resulting chain-rule terms this does not eliminate any of the remaining six contractions. Thus, retaining only second-order rank-2 mixed contractions $\nabla\mathbf{S}\nabla\mathbf{R}$ leaves

$$\mathbf{A}_{16} = \frac{\partial S_{kl}}{\partial x_i}\frac{\partial R_{kl}}{\partial x_j} \tag{3.19a}$$

$$\mathbf{A}_{17} = \frac{\partial S_{ik}}{\partial x_k}\frac{\partial R_{lj}}{\partial x_l} \tag{3.19b}$$

$$\mathbf{A}_{18} = \frac{\partial S_{ik}}{\partial x_l}\frac{\partial R_{lj}}{\partial x_k} \tag{3.19c}$$

$$\mathbf{A}_{19} = \frac{\partial S_{ik}}{\partial x_l}\frac{\partial R_{kl}}{\partial x_j} \tag{3.19d}$$

$$\mathbf{A}_{20} = \frac{\partial S_{kk}}{\partial x_i}\frac{\partial R_{lj}}{\partial x_l} \tag{3.19e}$$

$$\mathbf{A}_{21} = \frac{\partial S_{kl}}{\partial x_i}\frac{\partial R_{kj}}{\partial x_l} \tag{3.19f}$$

3.1.3.4 Symmetric and antisymmetric tensors $\mathbf{M}_k$ and $\mathbf{W}_p$

The symmetric and anti-symmetric parts of each of the tensor elements $\mathbf{A}_k$ in (3.15), (3.17), (3.18), and (3.19) are formed via (3.4a,b). Some of the resulting symmetric parts $\mathbf{M}_k$ are duplicates upon addition in (3.4a), and thus are listed only once, and some of the resulting anti-symmetric parts $\mathbf{W}_k$ are zero upon subtraction in (3.4b). The resulting unique symmetric parts are

$$\mathbf{M}_1 = S_{ij} \tag{3.20a}$$

$$\mathbf{M}_2 = \frac{\partial S_{kk}}{\partial x_i}\frac{\partial S_{ll}}{\partial x_j} \tag{3.20b}$$

$$\mathbf{M}_3 = \frac{\partial S_{kl}}{\partial x_i}\frac{\partial S_{kl}}{\partial x_j} \tag{3.20c}$$

$$\mathbf{M}_4 = \frac{\partial S_{ik}}{\partial x_k}\frac{\partial S_{lj}}{\partial x_l} \tag{3.20d}$$

$$\mathbf{M}_5 = \frac{\partial S_{ik}}{\partial x_l}\frac{\partial S_{lj}}{\partial x_k} \tag{3.20e}$$

$$\mathbf{M}_6 = \frac{1}{2}\left(\frac{\partial S_{ik}}{\partial x_k}\frac{\partial S_{ll}}{\partial x_j} + \frac{\partial S_{ll}}{\partial x_j}\frac{\partial S_{ik}}{\partial x_k}\right) \tag{3.20f}$$

$$\mathbf{M}_7 = \frac{1}{2}\left(\frac{\partial S_{ik}}{\partial x_l}\frac{\partial S_{kl}}{\partial x_j} + \frac{\partial S_{kl}}{\partial x_i}\frac{\partial S_{jk}}{\partial x_l}\right) \tag{3.20g}$$

$$\mathbf{M}_8 = \frac{\partial R_{kl}}{\partial x_i}\frac{\partial R_{kl}}{\partial x_j} \tag{3.20h}$$

$$\mathbf{M}_9 = \frac{\partial R_{ik}}{\partial x_k}\frac{\partial R_{lj}}{\partial x_l} \tag{3.20i}$$

$$\mathbf{M}_{10} = \frac{\partial R_{ik}}{\partial x_k}\frac{\partial R_{lj}}{\partial x_l} \tag{3.20j}$$

$$\mathbf{M}_{11} = \frac{1}{2}\left(\frac{\partial R_{ik}}{\partial x_l}\frac{\partial R_{kl}}{\partial x_j} + \frac{\partial R_{kl}}{\partial x_i}\frac{\partial R_{jk}}{\partial x_l}\right) \tag{3.20k}$$

$$\mathbf{M}_{12} = \frac{1}{2}\left(\frac{\partial S_{ik}}{\partial x_k}\frac{\partial R_{lj}}{\partial x_l} + \frac{\partial R_{li}}{\partial x_l}\frac{\partial S_{jk}}{\partial x_k}\right) \tag{3.20l}$$

$$\mathbf{M}_{13} = \frac{1}{2}\left(\frac{\partial S_{ik}}{\partial x_l}\frac{\partial R_{lj}}{\partial x_k} + \frac{\partial R_{li}}{\partial x_k}\frac{\partial S_{jk}}{\partial x_l}\right) \tag{3.20m}$$

$$\mathbf{M}_{14} = \frac{1}{2}\left(\frac{\partial S_{kk}}{\partial x_i}\frac{\partial R_{lj}}{\partial x_l} + \frac{\partial R_{li}}{\partial x_l}\frac{\partial S_{kk}}{\partial x_j}\right) \tag{3.20n}$$

$$\mathbf{M}_{15} = \frac{1}{2}\left(\frac{\partial S_{kl}}{\partial x_i}\frac{\partial R_{kj}}{\partial x_l} + \frac{\partial R_{ki}}{\partial x_l}\frac{\partial S_{kl}}{\partial x_j}\right) \tag{3.20o}$$

Thus there are $m = 15$ symmetric parts that can be formed from the tensor elements $\mathbf{A}_k$ in (3.15)-(3.18). Similarly, the resulting unique non-zero anti-symmetric parts are

$$\mathbf{W}_1 = R_{ij} \tag{3.21a}$$

$$\mathbf{W}_2 = \frac{1}{2}\left(\frac{\partial S_{ik}}{\partial x_k}\frac{\partial S_{ll}}{\partial x_j} - \frac{\partial S_{ll}}{\partial x_i}\frac{\partial S_{jk}}{\partial x_k}\right) \tag{3.21b}$$

$$\mathbf{W}_3 = \frac{1}{2}\left(\frac{\partial S_{ik}}{\partial x_l}\frac{\partial S_{kl}}{\partial x_j} - \frac{\partial S_{kl}}{\partial x_i}\frac{\partial S_{jk}}{\partial x_l}\right) \tag{3.21c}$$

$$\mathbf{W}_4 = \frac{1}{2}\left(\frac{\partial S_{kk}}{\partial x_i}\frac{\partial S_{lj}}{\partial x_l} - \frac{\partial S_{li}}{\partial x_l}\frac{\partial S_{kk}}{\partial x_j}\right) \tag{3.21d}$$

$$\mathbf{W}_5 = \frac{1}{2}\left(\frac{\partial R_{ik}}{\partial x_l}\frac{\partial R_{kl}}{\partial x_j} - \frac{\partial R_{kl}}{\partial x_i}\frac{\partial R_{jk}}{\partial x_l}\right) \tag{3.21e}$$

$$\mathbf{W}_6 = \frac{1}{2}\left(\frac{\partial R_{kl}}{\partial x_i}\frac{\partial R_{kj}}{\partial x_l} - \frac{\partial R_{ki}}{\partial x_l}\frac{\partial R_{kl}}{\partial x_j}\right) \tag{3.21f}$$

$$\mathbf{W}_7 = \frac{1}{2}\left(\frac{\partial S_{kl}}{\partial x_i}\frac{\partial R_{kl}}{\partial x_j} - \frac{\partial R_{kl}}{\partial x_i}\frac{\partial S_{kl}}{\partial x_j}\right) \tag{3.21g}$$

$$\mathbf{W}_8 = \frac{1}{2}\left(\frac{\partial S_{ik}}{\partial x_k}\frac{\partial R_{lj}}{\partial x_l} - \frac{\partial R_{li}}{\partial x_l}\frac{\partial S_{jk}}{\partial x_k}\right) \tag{3.21h}$$

$$\mathbf{W}_9 = \frac{1}{2}\left(\frac{\partial S_{ik}}{\partial x_l}\frac{\partial R_{lj}}{\partial x_k} - \frac{\partial R_{li}}{\partial x_k}\frac{\partial S_{jk}}{\partial x_l}\right) \tag{3.21i}$$

$$\mathbf{W}_{10} = \frac{1}{2}\left(\frac{\partial S_{ik}}{\partial x_l}\frac{\partial R_{kl}}{\partial x_j} - \frac{\partial R_{kl}}{\partial x_i}\frac{\partial S_{jk}}{\partial x_l}\right) \tag{3.21j}$$

$$\mathbf{W}_{11} = \frac{1}{2}\left(\frac{\partial S_{kk}}{\partial x_i}\frac{\partial R_{lj}}{\partial x_l} - \frac{\partial R_{li}}{\partial x_l}\frac{\partial S_{kk}}{\partial x_j}\right) \tag{3.21k}$$

$$\mathbf{W}_{12} = \frac{1}{2}\left(\frac{\partial S_{kl}}{\partial x_i}\frac{\partial R_{kj}}{\partial x_l} - \frac{\partial R_{ki}}{\partial x_l}\frac{\partial S_{kl}}{\partial x_j}\right) \tag{3.21l}$$

Thus there are $w = 12$ anti-symmetric parts that can be formed from the tensor elements $\mathbf{A}_k$ in (3.15)-(3.18).

3.1.3.5 Symmetric rank-2 tensor polynomial basis $\mathbf{m}_S^{(k)}$

From the general formulation in Section 3.1, any symmetric rank-2 tensor can be expressed as a tensor polynomial in the frame-invariant symmetric rank-2 bases $\mathbf{m}_S^{(k)}$ given in (3.6a-n). These are based on the rank-2 symmetric tensors $\mathbf{M}_i$ for $i = 1, 2, \ldots, 15$ in (3.20), and on the rank-2 anti-symmetric tensors $\mathbf{W}_p$ for $p = 1, 2, \ldots, 12$ in (3.21). The resulting number of $\mathbf{m}_S^{(k)}$ is large. For instance, the first few $\mathbf{m}_S^{(k,\alpha)}$ for $k = 0, 1, 2, 3, ..., 13$ are given by

$$k = 0 \qquad \mathbf{m}_S^{(0)} = \mathbf{I} \tag{3.22a}$$

$$k = 1 \qquad \mathbf{m}_S^{(1,1)} = \mathbf{M}_1 \tag{3.22b}$$

$$\mathbf{m}_S^{(1,2)} = \mathbf{M}_2 \tag{3.22c}$$

$$\vdots$$

$$\mathbf{m}_S^{(1,15)} = \mathbf{M}_{15} \tag{3.22d}$$

$$k = 2 \qquad \mathbf{m}_S^{(2,1)} = \mathbf{M}_1^2 \tag{3.22e}$$

$$\mathbf{m}_S^{(2,2)} = \mathbf{M}_2^2 \tag{3.22f}$$

$$\vdots$$

$$\mathbf{m}_S^{(2,15)} = \mathbf{M}_{15}^2 \tag{3.22g}$$

$$k = 3 \qquad \mathbf{m}_S^{(3,1)} = \mathbf{M_1 M_2} + \mathbf{M_2 M_1} \tag{3.22h}$$

$$\mathbf{m}_S^{(3,2)} = \mathbf{M_1 M_3} + \mathbf{M_3 M_1} \tag{3.22i}$$

$$\mathbf{m}_S^{(3,3)} = \mathbf{M_1 M_4} + \mathbf{M_4 M_1} \tag{3.22j}$$

$$\vdots$$

$$\mathbf{m}_S^{(3,14)} = \mathbf{M_1 M_{15}} + \mathbf{M_{15} M_1} \tag{3.22k}$$

$$\mathbf{m}_S^{(3,15)} = \mathbf{M_2 M_3} + \mathbf{M_3 M_2} \tag{3.22l}$$

$$\mathbf{m}_S^{(3,16)} = \mathbf{M_2 M_4} + \mathbf{M_4 M_2} \tag{3.22m}$$

$$\mathbf{m}_S^{(3,17)} = \mathbf{M_2 M_5} + \mathbf{M_5 M_2} \tag{3.22n}$$

$$\vdots$$

$$\mathbf{m}_S^{(3,30)} = \mathbf{M_2 M_{15}} + \mathbf{M_{15} M_2} \tag{3.22o}$$

$$\vdots$$

$$\mathbf{m}_S^{(3,108)} = \mathbf{M_{14} M_{15}} + \mathbf{M_{15} M_{14}} \tag{3.22p}$$

It is easy to determine how many $\mathbf{m}_S^{(k,\alpha)}$ there are, given that $i < j = 1, 2, \ldots, 15$ and $p < q = 1, 2, \ldots, 12$. Specifically

$$\mathbf{m}_S^{(0)} : 1 \tag{3.23a}$$

$$\mathbf{m}_S^{(1,\alpha)} : 15 \tag{3.23b}$$

$$\mathbf{m}_S^{(2,\alpha)} : 15 \tag{3.23c}$$

$$\mathbf{m}_S^{(3,\alpha)} : (15^2 - 15)/2 = 105 \tag{3.23d}$$

$$\mathbf{m}_S^{(4,\alpha)} : (15^2 - 15)/2 = 105 \tag{3.23e}$$

$$\mathbf{m}_S^{(5,\alpha)} : (15^2 - 15)/2 = 105 \tag{3.23f}$$

$$\mathbf{m}_S^{(6,\alpha)} : 12 \tag{3.23g}$$

$$\mathbf{m}_S^{(7,\alpha)} : (12^2 - 12)/2 = 66 \tag{3.23h}$$

$$\mathbf{m}_S^{(8,\alpha)} : (12^2 - 12)/2 = 66 \tag{3.23i}$$

$$\mathbf{m}_S^{(9,\alpha)} : (12^2 - 12)/2 = 66 \tag{3.23j}$$

$$\mathbf{m}_S^{(10,\alpha)} : 15 \cdot 12 = 180 \tag{3.23k}$$

$$\mathbf{m}_S^{(11,\alpha)} : 15 \cdot 12 = 180 \tag{3.23l}$$

$$\mathbf{m}_S^{(12,\alpha)} : 15 \cdot 12 = 180 \tag{3.23m}$$

$$\mathbf{m}_S^{(13,\alpha)} : 15 \cdot 12 = 180 \tag{3.23n}$$

Thus the total number of invariant symmetric rank-2 tensor polynomial bases $\mathbf{m}_S^{(k)}$ in (3.6a-n) is 1276. This is far too large to allow use of this tensorally-correct generalized representation in a fully dynamic implementation of autonomic closure. In a *static*

implementation of autonomic closure based on this generalized representation, these 1276 coefficients would need to be determined just once in advance of the simulation. Yet even in such a static implementation, a substantial computational burden may come from the large number of tensor component multiplications required at every point in the simulation to calculate the $\mathbf{m}_S^{(k)}$ in (3.19a-p) via the $\mathbf{M}_i$ in (3.20a-o) and the $\mathbf{W}_p$ in (3.21a-l).

3.1.3.6 Truncation to second-order tensor products

Chapter 5 shows that truncating a nonparametric series representation in the local velocities to retain velocity products only up to second order (*i.e.*, CL24) is sufficient to obtain excellent representations for the subgrid stress and the associated subgrid production. Anticipating that at least comparable accuracy will be obtained if (3.22a-p) are similarly truncated to retain at most second-order products of velocities, it is necessary to determine where velocity products of various orders appear in each of the tensor bases $\mathbf{m}_S^{(\alpha)}$.

The strain rate $\mathbf{S}$ and rotation rate $\mathbf{R}$ are each linear in the velocity components u_i, and therefore $\mathbf{M}_1$ in (3.20a) and $\mathbf{W}_1$ in (3.21a) are each linear in the velocities. The remaining $\mathbf{M}_i$ in (3.20b-r) and $\mathbf{W}_p$ in (3.21b-l) all involve rank-2 contractions of the forms $\nabla\mathbf{S}^2$, $\nabla\mathbf{R}^2$, and $\nabla\mathbf{S}\nabla\mathbf{R}$, and therefore are second-order in the velocity components u_i. From these, the order of the velocity products in each of the tensor bases $\mathbf{m}_S^{(\alpha)}$ in (3.6a-n) can be readily determined. Zeroth-order velocity products appear only in $\mathbf{m}_S^{(0)} \equiv \mathbf{I}$. First-order velocity products appear only in $\mathbf{m}_S^{(1)}$, since only $\mathbf{M}_1$ and $\mathbf{W}_1$ are linear in the velocities, and $\mathbf{M}_1$ appears linearly in $\mathbf{m}_S^{(1)}$ while $\mathbf{W}_1$ enters only via tensor products of second order or higher in (3.6g-n). Second-order velocity products are present only in $\mathbf{m}_S^{(1)}$ for $i > 1$, in $\mathbf{m}_S^{(2)}$ for $i = 1$, in $\mathbf{m}_S^{(6)}$ for $p = 1$, and in $\mathbf{m}_S^{(10)}$ for $i = p = 1$. All other terms in (3.22) are of order three or higher in the velocity components.

Thus the representation for $\boldsymbol{\tau}$ in the tensor bases in (3.22a-p) can be truncated to

retain only terms that are up to second-order in the velocities, which gives

$$\boldsymbol{\tau} = h_0\mathbf{I} + \underbrace{h_1\mathbf{m}_S^{(1,1)}}_{\mathbf{S}} + \underbrace{\sum_{\alpha=2}^{15} h_{1,\alpha}\mathbf{m}_S^{(1,\alpha)}}_{\nabla\mathbf{S}^2,\,\nabla\mathbf{R}^2,\,\nabla\mathbf{S}\nabla\mathbf{R}} + \underbrace{h_{16}\mathbf{m}_S^{(2,1)}}_{\mathbf{S}^2} + \underbrace{h_{17}\mathbf{m}_S^{(6,1)}}_{\mathbf{R}^2} + \underbrace{h_{18}\mathbf{m}_S^{(10,1)}}_{(\mathbf{SR}-\mathbf{RS})} \tag{3.24}$$

The four non-gradient terms in (3.24) can be expressed directly in $\mathbf{S}$ and $\mathbf{R}$ as indicated above, and from (3.6b) $\mathbf{m}_S^{(1,\alpha)}$ in the gradient terms is simply equal to $\mathbf{M}_{(\alpha)}$ in (3.20b-r), allowing (3.24) to be written as

$$\begin{aligned}\boldsymbol{\tau} = {} & h_0\mathbf{I} + h_1\mathbf{S} + h_{16}\mathbf{S}^2 + h_{17}\mathbf{R}^2 + h_{18}(\mathbf{SR}-\mathbf{RS}) \\ & + \underbrace{\sum_{\alpha=2}^{7} h_\alpha\mathbf{M}_{(\alpha)}}_{\nabla\mathbf{S}^2} + \underbrace{\sum_{\alpha=8}^{11} h_\alpha\mathbf{M}_{(\alpha)}}_{\nabla\mathbf{R}^2} + \underbrace{\sum_{\alpha=12}^{15} h_\alpha\mathbf{M}_{(\alpha)}}_{\nabla\mathbf{S}\nabla\mathbf{R}}\end{aligned} \tag{3.25}$$

The form of $\boldsymbol{\tau}$ in (3.25) with the $\mathbf{M}_{(\alpha)}$ in (3.20) involves 19 terms and 19 corresponding coefficients, and is the most general tensorally-correct representation for τ_{ij} when the stress is taken to depend on $\mathbf{I}$, $\mathbf{S}$, $\mathbf{R}$, $\nabla\mathbf{S}^2$, $\nabla\mathbf{R}^2$, and $\nabla\mathbf{S}\nabla\mathbf{R}$ in terms that extend up to second order in the velocity components u_i. Section 5.1.3.1 uses *a priori* tests to assess the accuracy of this generalized representation for $\boldsymbol{\tau}$ as the sum over the 19 tensor bases in (3.25), each weighted by a corresponding coefficient h that is determined as part of the autonomic closure methodology. That tensor form in 19 coefficients will be referred to as TF19.

3.2 Vector Representations

Following Smith (1971) [63] we seek the most general representation f of any vector $\mathbf{z}$, such as the subgrid scalar flux, in terms of any assumed set of rank-two tensors $\mathbf{A}_k$ ($k = 1, \ldots, N$) and vectors $\mathbf{v}_l$ ($l = 1, \ldots, P$), namely

$$\mathbf{z} = f\left(\mathbf{A}_k, \mathbf{v}_l\right), \tag{3.26}$$

that satisfies the translation, rotation and reflection invariance of a rank-one tensor (*i.e.*, a vector). Translational invariance is enforced by requiring f to depend only on

velocity gradients in the case of parametric representations, and on relative velocities in the case of nonparametric representations. With regard to frame invariance, since $\mathbf{z}$ is a vector, for any proper orthogonal tensor $\mathbf{Q}$ that transforms Cartesian frame $\mathbf{x}$ into a new Cartesian frame $\mathbf{x}'$, then this requires

$$\mathbf{z}' = \mathbf{Q}\,\mathbf{z} = f\big(\mathbf{Q}\,\mathbf{A}_k\,\mathbf{Q}^T, \mathbf{Q}\,\mathbf{v}_l\big) \tag{3.27}$$

in such a way that the sole tensor invariant of $\mathbf{z}'$, namely $\mathrm{I} = z_i' z_i'$, is the same as that for $\mathbf{z}$. For each $\mathbf{v}$ in (3.27) it is understood that $\mathbf{Q}\mathbf{v} = Q_{ij} v_j$.

The N tensors $\mathbf{A}_k$ are each separated into symmetric and anti-symmetric parts as

$$\text{symmetric part:} \qquad \mathbf{M}_i \equiv \frac{1}{2}\big(\mathbf{A}_k + \mathbf{A}_k^T\big) \quad i = 1, 2, \ldots, m \leq N \tag{3.28a}$$

$$\text{anti-symmetric part:} \qquad \mathbf{W}_p \equiv \frac{1}{2}\big(\mathbf{A}_k - \mathbf{A}_k^T\big) \quad p = 1, 2, \ldots, w \leq N \tag{3.28b}$$

From $\mathbf{M}_i$, $\mathbf{W}_p$ and $\mathbf{v}_l$ the complete and minimal vector basis is given by Smith (1971) as

$$\mathbf{m}^{(1,l)} = \mathbf{v}_l \tag{3.29a}$$

$$\mathbf{m}^{(2,il)} = \mathbf{M}_i \mathbf{v}_l \tag{3.29b}$$

$$\mathbf{m}^{(3,il)} = \mathbf{M}_i^2 \mathbf{v}_l \tag{3.29c}$$

$$\mathbf{m}^{(4,ijl)} = \big(\mathbf{M}_i \mathbf{M}_j - \mathbf{M}_j \mathbf{M}_i\big)\mathbf{v}_l \tag{3.29d}$$

$$\mathbf{m}^{(5,pl)} = \mathbf{W}_p \mathbf{v}_l \tag{3.29e}$$

$$\mathbf{m}^{(6,pl)} = \mathbf{W}_p^2 \mathbf{v}_l \tag{3.29f}$$

$$\mathbf{m}^{(7,pql)} = \big(\mathbf{W}_p \mathbf{W}_q - \mathbf{W}_q \mathbf{W}_p\big)\mathbf{v}_l \tag{3.29g}$$

$$\mathbf{m}^{(8,pql)} = \big(\mathbf{M}_i \mathbf{W}_p - \mathbf{W}_p \mathbf{M}_i\big)\mathbf{v}_l \tag{3.29h}$$

for all $i < j = 1, \ldots, m$, all $p < q = 1, \ldots, w$, and $l = 1, \ldots, P$. This produces a total of $1 + m(m+1) + w(w+1)$ vector bases $\mathbf{m}^{(\alpha)}$ in (3.29). The complete and minimal representation for $\mathbf{z}$ is the sum over all these vector bases, each having a coefficient that is determined as part of the autonomic closure methodology.

3.2.1 Representation of z in $\nabla\varphi$, S, and R

Assuming the subgrid scalar flux vector $\mathbf{z}$ at any point $\mathbf{x}$ depends only on the scalar gradient vector $\nabla\varphi$ and the strain rate and rotation rate tensors $\mathbf{S}$ and $\mathbf{R}$, then $l = 1$ with

$$\mathbf{v}_1 = \nabla\varphi \tag{3.30}$$

and $N = 2$ with $\mathbf{A}_k = \{\mathbf{S}, \mathbf{R}\}$, giving

$$\mathbf{M}_1 = \mathbf{S} \tag{3.31a}$$

$$\mathbf{M}_2 = 0 \tag{3.31b}$$

$$\mathbf{W}_1 = 0 \tag{3.31c}$$

$$\mathbf{W}_2 = \mathbf{R} \tag{3.31d}$$

The complete and minimal vector basis in (3.29) then is

$$\mathbf{m}^{(1)} = \nabla\varphi \tag{3.32a}$$

$$\mathbf{m}^{(2)} = \mathbf{S}\,\nabla\varphi \tag{3.32b}$$

$$\mathbf{m}^{(3)} = \mathbf{S}^2\,\nabla\varphi \tag{3.32c}$$

$$\mathbf{m}^{(4)} = 0 \tag{3.32d}$$

$$\mathbf{m}^{(5)} = \mathbf{R}\,\nabla\varphi \tag{3.32e}$$

$$\mathbf{m}^{(6)} = \mathbf{R}^2\,\nabla\varphi \tag{3.32f}$$

$$\mathbf{m}^{(7)} = 0 \tag{3.32g}$$

$$\mathbf{m}^{(8)} = (\mathbf{SR} - \mathbf{RS})\,\nabla\varphi \tag{3.32h}$$

There are six non-zero vector bases $\mathbf{m}^{(\alpha)}$ in (3.32), so the resulting complete and minimal representation of the subgrid scalar flux $\mathbf{z}$ in $\mathbf{S}$, $\mathbf{R}$, and $\nabla\varphi$ is

$$\mathbf{z} = h_0\,\nabla\varphi + h_1\,\mathbf{S}\nabla\varphi + h_2\,\mathbf{S}^2\nabla\varphi + h_3\,\mathbf{R}\nabla\varphi + h_4\,\mathbf{R}^2\nabla\varphi + h_5\,(\mathbf{SR} - \mathbf{RS})\,\nabla\varphi \tag{3.33}$$

This vector form in six coefficients will be referred to as VF6. Section 7.3.1 uses *a priori* tests to assess the accuracy of this generalized representation for $\mathbf{z}$ as the

sum of the six terms in (3.33), each weighted by a corresponding coefficient that is determined as part of the autonomic closure methodology.

3.2.2 Representations of z in $\nabla\varphi$ and u

In this case, the subgrid scalar flux $\mathbf{z}$ at any point $\mathbf{x}$ is assumed to depend on the scalar gradient $\nabla\varphi$ at $\mathbf{x}$ and the velocities in the immediate vicinity of $\mathbf{x}$. First we consider the absolute velocities on a $3 \times 3 \times 3$ stencil centered on $\mathbf{x}$. These are converted to relative velocities by subtracting the stencil-center velocity to enforce Galilean invariance, and the resulting relative velocities $\mathbf{u}_l$ ($l = 1, \ldots, 27$) can then be used with $\nabla\varphi$ to form a complete and minimal representation for $\mathbf{z}$.

We first try using the 27 relative velocities $\mathbf{u}_l$ to form all possible rank-two tensors from their outer products $\mathbf{u}_i \otimes \mathbf{u}_j$ for $i = 1, \ldots, 27$ and $j = 1, \ldots, 27$, where the outer product is defined as

$$\mathbf{a} \otimes \mathbf{b} = \begin{pmatrix} a_1 b_1 & a_1 b_2 & a_1 b_3 \\ a_2 b_1 & a_2 b_2 & a_2 b_3 \\ a_3 b_1 & a_3 b_2 & a_3 b_3 \end{pmatrix}. \tag{3.34}$$

For each i and j, the associated $\mathbf{u}_i \otimes \mathbf{u}_j$ corresponds to a rank-two tensor $\mathbf{A}_k$ in Section 3.2. Since $\mathbf{u}_i \otimes \mathbf{u}_j$ is not ij-symmetric, there are $N = 27^2 = 729$ such tensors. In principle these tensors $\mathbf{A}_k$ ($k = 1, \ldots, 729$) could be used in (3.28) to form $\mathbf{M}_i$ and $\mathbf{W}_p$, which together with $\mathbf{v}_1 = \nabla\varphi$ could be used in (3.29) to obtain a corresponding complete and minimal generalized representation for $\mathbf{z}$. However, the resulting number of vector bases $\mathbf{m}^{(\alpha)}$, and thus the corresponding number of coefficients in the associated generalized representation, would be far too large for use in a fully dynamic implementation of autonomic closure.

An alternative is to restrict the set of $\mathbf{A}_k$ to only the $N = 27$ collocated ($i = j$) outer products ($\mathbf{u}_i \otimes \mathbf{u}_i$). In that case $\mathbf{A}_k = \mathbf{A}_k^T$, so from (3.28) there will be $m = 27$ unique $\mathbf{M}_i$, and since then all the $\mathbf{W}_p \equiv 0$ we have $w = 0$. As a result, from (3.29)

this will produce $1 + m(m+1) + w(w+1) = 757$ vector bases $\mathbf{m}^{(\alpha)}$, which is also far too large for use in fully dynamic autonomic closure.

Another alternative is to use the smallest spatially unbiased stencil, which would consist of just $P = 6$ points centered around $\mathbf{x}$. Even then, $\mathbf{u}_i \otimes \mathbf{u}_j$ for $i = 1, \ldots, 6$ and $j = 1, \ldots, 6$ would produce 36 rank-two tensors $\mathbf{A}_k$. However, recognizing that $\mathbf{A}_{(ij)} = \mathbf{A}_{(ji)}^T$ because $(\mathbf{u}_i \otimes \mathbf{u}_j) = (\mathbf{u}_j \otimes \mathbf{u}_i)^T$, there would be only $m = 18$ unique $\mathbf{M}_i$ and $w = 18$ unique $\mathbf{W}_p$ in (3.28). From (3.29) this would produce a total of $1 + m(m+1) + w(w+1) = 343$ vector bases $\mathbf{m}^{(\alpha)}$. That is still far too large for use in a fully dynamic implementation of autonomic closure.

These two alternatives suggest combining the smallest spatially unbiased stencil, consisting of $P = 6$ points, with the restricted set of $\mathbf{A}_k$ formed from the corresponding $N = 6$ collocated outer products $(\mathbf{u}_i \otimes \mathbf{u}_i)$. In that case, from (3.28) there will be $m = 6$ unique $\mathbf{M}_i$, and again $w = 0$ since all the $\mathbf{W}_p \equiv 0$. From (3.29) this will produce $1 + m(m+1) + w(w+1) = 43$ vector bases $\mathbf{m}^{(\alpha)}$, and thus 43 associated coefficients. Such a representation for $\mathbf{z}$ is still relatively large for use in a fully dynamic implementation of autonomic closure, compared to the VF6 representation in (3.33), which involves only six tensor bases and thus six coefficients.

Thus, all four of the alternatives described above produce tensorally-correct generalized representations for $\mathbf{z}$ in terms of $\nabla\varphi$ and $\mathbf{u}$, but all of them are too large for implementation in fully dynamic autonomic closure. Therefore, we instead consider an *ad hoc* vector form that is *not* derived from the Smith (1971) formulation for complete and minimal representations, namely a contraction of $(\mathbf{u}_i \otimes \mathbf{u}_i)$ with $\nabla\varphi$ of the form

$$\mathbf{z} = h_0 \mathbf{I}_v + \sum_{i=1}^{P=27} h_i (\mathbf{u}_i \otimes \mathbf{u}_i) \nabla\varphi \ , \tag{3.35}$$

where $\mathbf{I}_v$ is the unit vector. This vector form involves nominally 27 coefficients, and will be referred to as VF27b. Section 7.2.2 uses *a priori* tests to assess the accuracy of this generalized representation for $\mathbf{z}$.

3.2.3 Representations of z in φ and u

Recognizing from Section 3.2.2 that tensorally-correct representations of $\mathbf{z}$ in $\nabla\varphi$ and $\mathbf{u}$ are not viable for fully dynamic implementations of autonomic closure, an *ad hoc* representation of $\mathbf{z}$ in φ and $\mathbf{u}$ is considered of the form

$$\mathbf{z} = h_0 \mathbf{I}_v + \sum_{m=1}^{P=27} h_m \mathbf{u}_m \, \varphi \ . \tag{3.36}$$

This also involves nominally 27 coefficients, and will be referred to as VF27a. Section 7.2.1 uses *a priori* tests to assess the accuracy of this generalized representation for $\mathbf{z}$.

3.2.4 Representations of z in φ, $\nabla\varphi$, and u

Since tensorally-correct representations for $\mathbf{z}$ in φ, $\nabla\varphi$ and $\mathbf{u}$ are not viable in autonomic closure, a further *ad hoc* representation of $\mathbf{z}$ in these quantities is considered that combines VF27a and VF27, of the form

$$\mathbf{z} = h_0 \mathbf{I}_v + \sum_{m=1}^{P=27} \left(h_m \mathbf{u}_m \, \varphi + h_{m+27} \left(\mathbf{u}_m \otimes \mathbf{u}_m \right) \nabla\varphi \right) \ . \tag{3.37}$$

This involves nominally 54 coefficients and will be referred to as VF54. Section 7.2.3 uses *a priori* tests to assess the accuracy of this generalized representation for $\mathbf{z}$.

Chapter 4

COEFFICIENT RESCALING FROM TEST- TO LES-FILTER SCALE

Because the generalized representations in (2.1), (2.2), (2.3) and (2.4) are, when practical, expressed as complete and minimal sums over dimensional tensor or vector basis elements $\mathbf{m}_i$, as discussed in Chapter 3, the coefficient h_i associated with each basis element has dimensions that are implied by the dimensions of that basis element. Thus when transferring coefficients from the test-filter scale to the LES-filter scale, the coefficients must be rescaled so that in *nondimensional* form the generalized representations at both scales are *identical*. The requirement that, in nondimensional form, the generalized representations $\widehat{\mathcal{F}}$ and $\widetilde{\mathcal{F}}$ for the stress, and $\widehat{\mathcal{J}}$ and $\widetilde{\mathcal{J}}$ for the scalar flux, must be the same at the test-filter scale and the LES-filter scale is the precise statement of scale similarity on which autonomic closure is based.

This chapter details the procedure for rescaling the coefficients in these representations. At the test-filter scale in (2.2) and (2.4), each basis element is nondimensionalized with the test-filter length scale $\widehat{\Delta}$ and with the characteristic test-scale velocity $\widehat{U}$ and test-scale scalar value $\widehat{Y}$. Similarly, at the LES-filter scale in (2.1) and (2.3), each basis element in these representations is nondimensionalized with the LES-filter length scale $\widetilde{\Delta}$ and with the characteristic LES-scale velocity $\widetilde{U}$ and scalar value $\widetilde{Y}$. Classical inertial-range scaling relates $\widetilde{U}/\widehat{U}$ and $\widetilde{Y}/\widehat{Y}$ to $\widetilde{\Delta}/\widehat{\Delta}$. Equating each nondimensional basis element in the LES-scale representation, including its coefficient $\widetilde{h}_i$, with the corresponding nondimensional basis element in the test-scale representation, including its coefficient $\widehat{h}_i$, then gives $\widetilde{h}_i/\widehat{h}_i = (\widetilde{\Delta}/\widehat{\Delta})^{p_i}$, where the scaling exponent p_i depends on the dimensions of the basis element. The resulting $\widetilde{h}_i/\widehat{h}_i$ ratios for all the basis elements $\mathbf{m}_i$ allow the set of coefficients $\widehat{\mathbf{h}}$ from the test-scale representation to be used with $(\widetilde{\Delta}/\widehat{\Delta})$ to determine the set of coefficients $\widetilde{\mathbf{h}}$ in the LES-scale representation.

4.1 General Methodology

To describe the general principle for rescaling the coefficients in any given generalized representation for $\boldsymbol{\tau}$, consider the subgrid stress representation in (3.10), where $\boldsymbol{\tau}$ is represented solely in $\mathbf{S}$. At the LES-filter scale and test-filter scale this is

$$\boldsymbol{\tau} = \widetilde{h}_0\,\mathbf{I} + \widetilde{h}_1\,\widetilde{\mathbf{S}} + \widetilde{h}_2\,\widetilde{\mathbf{S}}^2 \tag{4.1a}$$

$$\mathbf{T} = \widehat{h}_0\,\mathbf{I} + \widehat{h}_1\,\widehat{\mathbf{S}} + \widehat{h}_2\,\widehat{\mathbf{S}}^2 \tag{4.1b}$$

The coefficients $\widetilde{h}_i$ and $\widehat{h}_i$ in (4.1a,b) are not dimensionless, since the stress on the left of each equation has dimensions U^2, and the strain rate on the right of each equation has dimensions (U/Δ).

Using $\widetilde{U}$ and $\widehat{U}$ to respectively denote local characteristic velocities at the LES-scale and the test-scale, and $\widetilde{\Delta}$ and $\widehat{\Delta}$ to denote the corresponding characteristic length at each of these scales, (4.1) can be equivalently written in nondimensional form as

$$\frac{\boldsymbol{\tau}}{\widetilde{U}^2} = c_0\,\mathbf{I} + c_1\,\frac{\widetilde{\mathbf{S}}}{(\widetilde{U}/\widetilde{\Delta})} + c_2\,\frac{\widetilde{\mathbf{S}}^2}{(\widetilde{U}/\widetilde{\Delta})^2} \tag{4.2a}$$

$$\frac{\mathbf{T}}{\widehat{U}^2} = c_0\,\mathbf{I} + c_1\,\frac{\widehat{\mathbf{S}}}{(\widehat{U}/\widehat{\Delta})} + c_2\,\frac{\widehat{\mathbf{S}}^2}{(\widehat{U}/\widehat{\Delta})^2} \tag{4.2b}$$

where the coefficients c_i are now dimensionless and therefore independent of scale. Rearranging (4.2) as

$$\tau = (c_0\,\widetilde{U}^2)\,\mathbf{I} + (c_1\,\widetilde{U}\widetilde{\Delta})\,\widetilde{\mathbf{S}} + (c_2\,\widetilde{\Delta}^2)\,\widetilde{\mathbf{S}}^2 + \cdots \tag{4.3a}$$

$$\mathbf{T} = (c_0\,\widehat{U}^2)\,\mathbf{I} + (c_1\,\widehat{U}\widehat{\Delta})\,\widehat{\mathbf{S}} + (c_2\,\widehat{\Delta}^2)\,\widehat{\mathbf{S}}^2 + \cdots \tag{4.3b}$$

and then comparing (4.3) to (4.1) shows

$$\widetilde{h}_0 = (c_0\,\widetilde{U}^2) \qquad \widetilde{h}_1 = (c_1\,\widetilde{U}\widetilde{\Delta}) \qquad \widetilde{h}_2 = (c_2\,\widetilde{\Delta}^2) \tag{4.4a}$$

$$\widehat{h}_0 = (c_0\,\widehat{U}^2) \qquad \widehat{h}_1 = (c_1\,\widehat{U}\widehat{\Delta}) \qquad \widehat{h}_2 = (c_2\,\widehat{\Delta}^2) \tag{4.4b}$$

Since the c_i are the same at both scales, (4.4) gives

$$\frac{\widetilde{h}_0}{\widehat{h}_0} = \left(\frac{\widetilde{U}}{\widehat{U}}\right)^2 \qquad \frac{\widetilde{h}_1}{\widehat{h}_1} = \left(\frac{\widetilde{U}}{\widehat{U}}\right)\left(\frac{\widetilde{\Delta}}{\widehat{\Delta}}\right) \qquad \frac{\widetilde{h}_2}{\widehat{h}_2} = \left(\frac{\widetilde{\Delta}}{\widehat{\Delta}}\right)^2 \tag{4.5}$$

Section 4.4 shows that classical inertial-range scaling arguments require

$$\left(\frac{\widetilde{U}}{\widehat{U}}\right) = \left(\frac{\widetilde{\Delta}}{\widehat{\Delta}}\right)^{1/3}, \tag{4.6}$$

which with (4.5) gives the coefficient ratios as

$$\frac{\widetilde{h}_0}{\widehat{h}_0} = \left(\frac{\widetilde{\Delta}}{\widehat{\Delta}}\right)^{2/3} \qquad \frac{\widetilde{h}_1}{\widehat{h}_1} = \left(\frac{\widetilde{\Delta}}{\widehat{\Delta}}\right)^{4/3} \qquad \frac{\widetilde{h}_2}{\widehat{h}_2} = \left(\frac{\widetilde{\Delta}}{\widehat{\Delta}}\right)^{2} \tag{4.7}$$

Once values of the local test-scale coefficients $\widehat{h}_0$, $\widehat{h}_1$ and $\widehat{h}_2$ have been determined by solving the local system identification problem, as described in Section 2.3, corresponding values of the LES-scale coefficients $\widetilde{h}_0$, $\widetilde{h}_1$ and $\widetilde{h}_2$ can then be obtained from the scaling ratios in (4.7).

Although the general methodology for coefficient rescaling is shown above for the generalized representation in (4.1), the same procedure can be applied to find coefficient scaling ratios analogous to those in (4.7) for any generalized representation.

4.2 Rescaling for Subgrid Stress Representations

Section 4.1 shows that the rescaling from the test-scale to the LES-scale for the coefficient h_i associated with any term in a $\boldsymbol{\tau}$ representation is independent of all the other terms in the representation, and depends only on the dimensions of the tensor basis element $\mathbf{m}_i$ associated with that term. Consequently, a completely general form for rescaling the coefficient associated with any term in any stress representation can be obtained, as shown below.

As shown in Chapter 3, generalized representations for $\boldsymbol{\tau}$ and $\mathbf{T}$ are sums over a set of the tensor basis elements $\mathbf{m}$ associated with that representation. Thus any such generalized representation can be written as

$$\boldsymbol{\tau} = \sum_{\alpha} \widetilde{h}_\alpha \, \mathbf{m}_\alpha \tag{4.8a}$$

$$\mathbf{T} = \sum_{\alpha} \widehat{h}_{\alpha}\, \mathbf{m}_{\alpha} \tag{4.8b}$$

where the $\widetilde{h}_{\alpha}$ and $\widehat{h}_{\alpha}$ are dimensional. Now consider any i-th term, namely

$$\boldsymbol{\tau} = \cdots + \widetilde{h}_i\, \mathbf{m}_i + \cdots \tag{4.9a}$$

$$\mathbf{T} = \cdots + \widehat{h}_i\, \mathbf{m}_i + \cdots \tag{4.9b}$$

where the dimensions of the corresponding basis element $\mathbf{m}_i$ are

$$\mathbf{m}_i \sim \left[\frac{L^n}{T^m}\right] \sim U^m\, \Delta^{n-m} \tag{4.10}$$

and where U and Δ are the characteristic velocity and length scales associated with that scale. When (4.9) are made nondimensional with U and Δ, namely

$$\frac{\boldsymbol{\tau}}{\widetilde{U}^2} = \cdots + c_i\, \frac{\mathbf{m}_i}{\widetilde{U}^m \widetilde{\Delta}^{n-m}} + \cdots \tag{4.11a}$$

$$\frac{\mathbf{T}}{\widehat{U}^2} = \cdots + c_i\, \frac{\mathbf{m}_i}{\widehat{U}^m \widehat{\Delta}^{n-m}} + \cdots \tag{4.11b}$$

then the coefficients are now nondimensional and therefore scale-independent, and thus denoted by c_i . Multiplying in (4.11) by U^2 gives

$$\boldsymbol{\tau} = \cdots + c_i\, \frac{\mathbf{m}_i}{\widetilde{U}^{m-2} \widetilde{\Delta}^{n-m}} + \cdots \tag{4.12a}$$

$$\mathbf{T} = \cdots + c_i\, \frac{\mathbf{m}_i}{\widehat{U}^{m-2} \widehat{\Delta}^{n-m}} + \cdots \tag{4.12b}$$

Equating each term in (4.12) with the corresponding term in (4.9) gives

$$\widetilde{h}_i = \frac{c_i}{\widetilde{U}^{m-2} \widetilde{\Delta}^{n-m}} \tag{4.13a}$$

$$\widehat{h}_i = \frac{c_i}{\widehat{U}^{m-2} \widehat{\Delta}^{n-m}} \tag{4.13b}$$

Since the c_i are scale-independent, (4.13) gives

$$\frac{\widetilde{h}_i}{\widehat{h}_i} = \left(\frac{\widetilde{U}}{\widehat{U}}\right)^{2-m} \left(\frac{\widetilde{\Delta}}{\widehat{\Delta}}\right)^{m-n} , \tag{4.14}$$

and from Section 4.3 classical inertial-range scaling requires

$$\frac{\widetilde{U}}{\widehat{U}} = \left(\frac{\widetilde{\Delta}}{\widehat{\Delta}}\right)^{1/3} , \tag{4.15}$$

which therefore gives

$$\frac{\widetilde{h}_i}{\widehat{h}_i} = \left(\frac{\widetilde{\Delta}}{\widehat{\Delta}}\right)^{\frac{2}{3}(m+1)-n} , \tag{4.16}$$

The coefficient scaling ratio in (4.16) is completely general for any term in any stress representation. It can be applied to any particular term in any particular representation via the n and m associated with the dimensions of the corresponding basis element $\mathbf{m}_i$ in (4.10). The corresponding test-scale coefficient $\widehat{h}_i$ obtained from solution of the local system identification problem, as described in Section 2.3, can then be used in (4.16) to obtain the corresponding LES-scale coefficient $\widetilde{h}_i$.

4.3 Inertial-Range Scaling for $\widetilde{U}/\widehat{U}$

At the test-filter scale and LES-filter scale the corresponding stress, $\mathbf{T}$ or $\boldsymbol{\tau}$, scales on dimensional grounds with the square of the corresponding characteristic velocity $\widehat{U}$ or $\widetilde{U}$, as seen in (4.2), where

$$\widetilde{U} \equiv \widetilde{\Delta} \cdot \widetilde{\langle \mathrm{q}^2 \rangle}^{1/2} \tag{4.17a}$$

$$\widehat{U} \equiv \widehat{\Delta} \cdot \widehat{\langle \mathrm{q}^2 \rangle}^{1/2} \tag{4.17b}$$

where q can be any dimensionally-correct and Galilean-invariant quantity that in (4.17) characterizes the velocities at that scale; e.g., $\mathrm{q}^2 \sim [\mathbf{S}^2 + \mathbf{R}^2]$ or any other suitable choice for which the dimensions of q are $[L^0/T^1]$, as required in (4.17).

Since any general quantity q having dimensions $[L^n/T^m]$ has an associated energy spectrum $Q(k)$ for which

$$\langle q^2 \rangle = \int_0^\infty Q(k)\, dk , \tag{4.18}$$

the dimensions of the spectrum Q must be $[L^{2n+1}/T^{2m}]$. Following classical inertial-range scaling arguments, in the inertial range $Q(k)$ will depend on the average

kinetic energy dissipation rate $\epsilon \sim [L^2/T^3]$ and wavenumber $k \sim [1/T]$, and thus on dimensional grounds Q must scale as

$$Q(k) \sim \epsilon^{\frac{2}{3}m}\, k^{\frac{4}{3}m-(2n+1)} \tag{4.19}$$

Since in (4.17) q has dimensions $[L^0/T^1]$, namely $n = 0$ and $m = 1$, its energy spectrum must scale as

$$Q(k) \sim \epsilon^{2/3}\, k^{1/3} \tag{4.20}$$

Integrating this spectrum up to $k_{\widetilde{\Delta}}$ and $k_{\widehat{\Delta}}$ then gives

$$\widetilde{\langle \mathrm{q}^2 \rangle} \sim \int_0^{k_{\widetilde{\Delta}}} \epsilon^{2/3}\, k^{1/3}\, dk \sim \epsilon^{2/3}\, k_{\widetilde{\Delta}}^{4/3} \tag{4.21a}$$

$$\widehat{\langle \mathrm{q}^2 \rangle} \sim \int_0^{k_{\widehat{\Delta}}} \epsilon^{\frac{2}{3}}\, k^{1/3}\, dk \sim \epsilon^{2/3}\, k_{\widehat{\Delta}}^{4/3} \tag{4.21b}$$

Then from (4.17) and (4.21) the ratio $\widetilde{U}/\widehat{U}$ is

$$\frac{\widetilde{U}}{\widehat{U}} \;=\; \frac{\widetilde{\Delta} \cdot \widetilde{\langle \mathrm{q}^2 \rangle}^{1/2}}{\widehat{\Delta} \cdot \widehat{\langle \mathrm{q}^2 \rangle}^{1/2}} \;=\; \frac{\widetilde{\Delta}}{\widehat{\Delta}} \cdot \frac{\left(\epsilon^{\frac{2}{3}}\, k_{\widetilde{\Delta}}^{4/3}\right)^{1/2}}{\left(\epsilon^{\frac{2}{3}}\, k_{\widehat{\Delta}}^{4/3}\right)^{1/2}} \;=\; \frac{\widetilde{\Delta}}{\widehat{\Delta}} \cdot \left(\frac{\widehat{\Delta}}{\widetilde{\Delta}}\right)^{2/3} \tag{4.22}$$

and therefore

$$\frac{\widetilde{U}}{\widehat{U}} = \left(\frac{\widetilde{\Delta}}{\widehat{\Delta}}\right)^{1/3} \tag{4.23}$$

4.4 Rescaling for Subgrid Scalar Flux Representations

Analogous to Section 4.2, a similarly general form for rescaling the coefficient associated with any term in any scalar flux representation can be obtained. As shown in Chapter 3, generalized representations for $\mathbf{z}$ and $\mathbf{z}$ are sums over a set of the tensor basis elements $\mathbf{m}$ associated with the scalar flux representation. Thus any generalized representation can be written as

$$\mathbf{z} = \sum_\alpha \widetilde{h}_\alpha\, \mathbf{m}_\alpha \tag{4.24a}$$

$$\mathbf{Z} = \sum_\alpha \widehat{h}_\alpha\, \mathbf{m}_\alpha \tag{4.24b}$$

where the $\widetilde{h}_\alpha$ and $\widehat{h}_\alpha$ are dimensional. Now consider any i-th term, namely

$$\mathbf{z} = \cdots + \widetilde{h}_i \, \mathbf{m}_i + \cdots \tag{4.25a}$$

$$\mathbf{Z} = \cdots + \widehat{h}_i \, \mathbf{m}_i + \cdots \tag{4.25b}$$

where, using A to denote the dimensions of the scalar φ, the dimensions of the corresponding basis element $\mathbf{m}_i$ are

$$\mathbf{m}_i \sim \left[A^p \, \frac{L^n}{T^m} \right] \sim Y^p \, U^m \, \Delta^{n-m} \, , \tag{4.26}$$

and where Y, U and Δ are characteristic scalar, velocity and length scales associated with that scale. When (4.25) are made nondimensional with Y, U and Δ, namely

$$\frac{\mathbf{z}}{\widetilde{Y}^2} = \cdots + c_i \, \frac{\mathbf{m}_i}{\widetilde{Y}^p \, \widetilde{U}^m \widetilde{\Delta}^{n-m}} + \cdots \tag{4.27a}$$

$$\frac{\mathbf{Z}}{\widehat{Y}^2} = \cdots + c_i \, \frac{\mathbf{m}_i}{\widehat{Y}^p \, \widehat{U}^m \widehat{\Delta}^{n-m}} + \cdots \tag{4.27b}$$

then the coefficients c_i are now nondimensional and therefore scale-independent. Multiplying in (4.27) by Y^2 gives

$$\mathbf{z} = \cdots + c_i \, \frac{\mathbf{m}_i}{\widetilde{Y}^{p-2} \, \widetilde{U}^m \widetilde{\Delta}^{n-m}} + \cdots \tag{4.28a}$$

$$\mathbf{Z} = \cdots + c_i \, \frac{\mathbf{m}_i}{\widehat{Y}^{p-2} \, \widehat{U}^m \widehat{\Delta}^{n-m}} + \cdots \tag{4.28b}$$

Equating each term in (4.28) with the corresponding term in (4.25) gives

$$\widetilde{h}_i = \frac{c_i}{\widetilde{Y}^{p-2} \widetilde{U}^m \widetilde{\Delta}^{n-m}} \tag{4.29a}$$

$$\widehat{h}_i = \frac{c_i}{\widehat{Y}^{p-2} \widehat{U}^m \widehat{\Delta}^{n-m}} \tag{4.29b}$$

Since the c_i are scale-independent, (4.13) gives

$$\frac{\widetilde{h}_i}{\widehat{h}_i} = \left(\frac{\widetilde{Y}}{\widehat{Y}} \right)^{2-p} \left(\frac{\widetilde{U}}{\widehat{U}} \right)^{-m} \left(\frac{\widetilde{\Delta}}{\widehat{\Delta}} \right)^{m-n} . \tag{4.30}$$

From Section 4.3

$$\frac{\widetilde{U}}{\widehat{U}} = \left(\frac{\widetilde{\Delta}}{\widehat{\Delta}} \right)^{1/3} , \tag{4.31}$$

and from Section 4.5 classical inertial-range scaling requires

$$\frac{\widetilde{Y}}{\widehat{Y}} = \left(\frac{\widetilde{\Delta}}{\widehat{\Delta}} \right)^{1/3} , \tag{4.32}$$

therefore

$$\frac{\widetilde{h}_i}{\widehat{h}_i} = \left(\frac{\widetilde{\Delta}}{\widehat{\Delta}} \right)^{\frac{2}{3}(m+1)-n-\frac{1}{3}p} , \tag{4.33}$$

The coefficient scaling ratio in (4.33) is completely general for any term in any scalar flux representation. It can be applied to any particular term in any particular representation via the n, m, and p associated with the dimensions of the corresponding basis element $\mathbf{m}_i$ in (4.26). The corresponding test-scale coefficient $\widehat{h}_i$ obtained from solution of the local system identification problem, as described in Section 2.3, can then be used in (4.33) to obtain the corresponding LES-scale coefficient $\widetilde{h}_i$.

4.5 Inertial-Range Scaling for $\widetilde{Y}/\widehat{Y}$

Analogous to (4.17), at the test-filter scale and LES-filter scale the corresponding scalar flux, $\mathbf{Z}$ or $\mathbf{z}$, scales on dimensional grounds with the square of the corresponding characteristic scalar value $\widehat{Y}$ or $\widetilde{Y}$, where we take

$$\widetilde{Y} \equiv \widetilde{\Delta} \cdot \langle \widetilde{\nabla\varphi \cdot \nabla\varphi} \rangle^{1/2} \tag{4.34a}$$

$$\widehat{Y} \equiv \widehat{\Delta} \cdot \langle \widehat{\nabla\varphi \cdot \nabla\varphi} \rangle^{1/2} \tag{4.34b}$$

where $\nabla\varphi$ is the scalar gradient. Using A to denote the dimension of the scalar φ, then the scalar gradient $\nabla\varphi$ has the dimensions $[A^1/L^1]$, and thus $\nabla\varphi \cdot \nabla\varphi$ has the dimensions $[A^2/L^2]$, as required in (4.34).

We define the inertial-range spectrum $\Sigma(k)$ for the energy $\nabla\varphi \cdot \nabla\varphi$ associated with the scalar gradient, namely

$$\langle \nabla\varphi \cdot \nabla\varphi \rangle = \int_0^\infty \Sigma(k)\, dk , \tag{4.35}$$

thus the dimensions of Σ must be $[A^2/L^1]$. Following classical inertial-range scaling arguments, in the inertial range $\Sigma(k)$ will depend on the scalar energy dissipation rate

$\chi \equiv D\nabla\varphi \cdot \nabla\varphi$, the kinetic energy dissipation rate ϵ, and the wavenumber k, namely

$$\Sigma(k) = f(\chi, \epsilon, k) \; . \tag{4.36}$$

Since χ has dimensions of $[A^2/T^1]$, ϵ has dimensions of $[L^2/T^3]$, k has dimensions of $[1/L^1]$ and Σ has dimensions of $[A^2/L^1]$, dimensional consistency in (4.36) requires

$$\Sigma(k) \sim \chi \, \epsilon^{-1/3} \, k^{1/3} \; . \tag{4.37}$$

Integrating this spectrum up to $k_{\widetilde{\Delta}}$ and $k_{\widehat{\Delta}}$ then gives

$$\widetilde{\langle \nabla\varphi \cdot \nabla\varphi \rangle} \sim \int_0^{k_{\widetilde{\Delta}}} \chi \, \epsilon^{-1/3} \, k^{1/3} \, dk \sim \chi \, \epsilon^{-1/3} \, k_{\widetilde{\Delta}}^{4/3} \tag{4.38a}$$

$$\widehat{\langle \nabla\varphi \cdot \nabla\varphi \rangle} \sim \int_0^{k_{\widehat{\Delta}}} \chi \, \epsilon^{-1/3} \, k^{1/3} \, dk \sim \chi \, \epsilon^{-1/3} \, k_{\widehat{\Delta}}^{4/3} \tag{4.38b}$$

Then from (4.34) and (4.38) the ratio $\widetilde{Y}/\widehat{Y}$ is

$$\frac{\widetilde{Y}}{\widehat{Y}} \; = \; \frac{\widetilde{\Delta} \cdot \widetilde{\langle \nabla\varphi \cdot \nabla\varphi \rangle}^{\,1/2}}{\widehat{\Delta} \cdot \widehat{\langle \nabla\varphi \cdot \nabla\varphi \rangle}^{\,1/2}} \; = \; \frac{\widetilde{\Delta}}{\widehat{\Delta}} \cdot \frac{\left(\chi \, \epsilon^{-1/3} \, k_{\widetilde{\Delta}}^{4/3} \right)^{1/2}}{\left(\chi \, \epsilon^{-1/3} \, k_{\widehat{\Delta}}^{4/3} \right)^{1/2}} \; = \; \frac{\widetilde{\Delta}}{\widehat{\Delta}} \cdot \left(\frac{\widehat{\Delta}}{\widetilde{\Delta}} \right)^{2/3} \; , \tag{4.39}$$

and therefore

$$\frac{\widetilde{Y}}{\widehat{Y}} = \left(\frac{\widetilde{\Delta}}{\widehat{\Delta}} \right)^{1/3} \; . \tag{4.40}$$

Chapter 5

A PRIORI TESTS: SUBGRID STRESS REPRESENTATIONS

Results from prior work [58–62] have shown that autonomic closure for the subgrid stress can provide a significant improvement over traditional closures based on prescribed subgrid stress models in terms of the accuracy with which they represent the structure and magnitude of the momentum and energy exchange fields between resolved and unresolved scales. While that improved accuracy does not guarantee stability in forward simulations, it does suggest that it may be possible for some representations of the subgrid stress in autonomic closure to be stable with only minimal limiters, added dissipation, or other *ad hoc* treatments to provide stability. This chapter uses *a priori* tests to assess the fundamental accuracy of subgrid stress representations for use in autonomic closure. The stability of these subgrid stress representations is then assessed in Chapter 6 using forward simulations.

5.1 Subgrid Stress Representations

The subgrid stress representations assessed in this chapter can be grouped into *nonparametric* and *parametric* representations. Nonparametric stress representations are expressed directly in the test-filtered velocities on the stencil $\widehat{\mathbf{S}}$ at the test-filter scale $\widehat{\Delta}$, and in the LES-filtered velocities on the stencil $\widetilde{\mathbf{S}}$ at the LES-filter scale $\widetilde{\Delta}$. Parametric stress representations are formulated in quantities that can be obtained from these velocities on the stencils $\widehat{\mathbf{S}}$ and $\widetilde{\mathbf{S}}$, including the strain rate tensor $\widehat{S}_{ij}$ and rotation rate tensor $\widehat{R}_{ij}$ at the test-filter scale, and $\widetilde{S}_{ij}$ and $\widetilde{R}_{ij}$ at the LES-filter scale, and in some cases may even including gradients of these quantities, as discussed in Chapter 3. In general, the advantage of tensorally-correct parametric representations is that they provide as much tensorally-valid information as a nonparametric representation, but with substantially fewer terms in the representation and thus with fewer

coefficients that must be determined via the local system identification problem as described in Section 2.3, which makes them more computationally efficient.

5.1.1 Traditional Prescribed Models for τ_{ij}

The prescribed models that are considered in the *a priori* tests in this chapter, and in the forward simulations in Chapter 6, include the basic Smagorinsky model, the dynamic Smagorinsky model [31, 46–49], and the Bardina scale similarity model [31, 50–52]. The basic Smagorinsky model has long been used in LES, in part because it is known to be manifestly stable. The dynamic Smagorinsky model is also widely used in LES, though it is known to be unstable and thus must be artificially stabilized by some means. The Bardina model is also often used, but it too is known to be unstable and thus is typically used in mixed models, where it is combined with the basic Smagorinsky model to achieve computational stability.

5.1.1.1 Basic Smagorinsky model

The basic Smagorinsky model is a simple eddy-viscosity model based on the gradient transport hypothesis, and thus it models the subgrid stress as

$$\tau_{ij} = -\nu_{sgs}\,\widetilde{S}_{ij}\,, \tag{5.1}$$

where ν_{sgs} is assumed to depend only on the LES-filter length scale $\widetilde{\Delta}$ and the local strain rate magnitude $|\widetilde{S}| = (\widetilde{S}_{ij}\widetilde{S}_{ij})^{1/2}$. Thus on dimensional grounds $\nu_{sgs} = C_S\widetilde{\Delta}^2|\widetilde{S}|$, and therefore the representation for the subgrid stress is

$$\tau_{ij} = -C_S\widetilde{\Delta}^2|\widetilde{S}|\,\widetilde{S}_{ij}\,, \tag{5.2}$$

which in tensor notation is

$$\boldsymbol{\tau} = -C_S\widetilde{\Delta}^2|\widetilde{\mathbf{S}}|\,\widetilde{\mathbf{S}}\,. \tag{5.3}$$

The coefficient C_S is the called Smagorinsky constant, and is typically chosen based on an average of values that best match commonly used reference cases. The present study uses $C_S = 0.173$.

The resulting subgrid production of resolved kinetic energy in (1.8) is $P = \boldsymbol{\tau} : \mathbf{S}$, and from (5.3) this gives

$$P = -C_S \widetilde{\Delta}^2 |\widetilde{\mathbf{S}}|^2 \,, \tag{5.4}$$

which for $C_S > 0$ is always *negative*, and thus from (1.6) acts to *reduce* the kinetic energy in the resolved scales of the simulation. As a result, the basic Smagorinsky model is purely *dissipative*, and consequently it is manifestly stable in forward simulations. For that reason, it is often combined with unstable subgrid stress representations in order to provide additional dissipation to achieve stability in forward runs.

5.1.1.2 Dynamic Smagorinsky model

The dynamic Smagorinsky model is derived from the basic Smagorinsky model in (5.2), but allows the value of C_S to vary in such a way that it can take on locally positive or negative values in the simulation, and thereby produce positive and negative values of subgrid production. Specifically, C_S is calculated dynamically using information at a test filter scale $\widehat{(\,)}$ having length scale $\widehat{\Delta}$. It first defines

$$N_{ij} \equiv \widehat{\widetilde{u_i u_j}} - \widehat{\widetilde{u}}_i \widehat{\widetilde{u}}_j \,, \tag{5.5}$$

and represents this with a basic Smagorinsky model as in (5.2), namely

$$N_{ij} = -C_S \widehat{\Delta}^2 |\widehat{\widetilde{S}}| \, \widehat{\widetilde{S}}_{ij} \,. \tag{5.6}$$

It also represents the subgrid stress

$$\tau_{ij} \equiv \widetilde{u_i u_j} - \widetilde{u}_i \widetilde{u}_j \,, \tag{5.7}$$

with the basic Smagorinsky model in (5.2), namely

$$\tau_{ij} = -C_S \widetilde{\Delta}^2 |\widetilde{S}| \, \widetilde{S}_{ij} \,, \tag{5.8}$$

Applying the test filter $\widehat{(\,)}$ to (5.8) gives

$$\widehat{\tau}_{ij} = -C_S \widetilde{\Delta}^2 \widehat{|\widetilde{S}| \, \widetilde{S}_{ij}} \,. \tag{5.9}$$

Subtracting (5.9) from (5.6) gives

$$L_{ij} \equiv N_{ij} - \widehat{\tau_{ij}} = C_S M_{ij} \tag{5.10}$$

where

$$M_{ij} \equiv \widehat{\widetilde{\Delta}^2 |\widetilde{S}| \, \widetilde{S}_{ij}} - \widehat{\Delta}^2 \, |\widehat{\widetilde{S}}| \, \widehat{\widetilde{S}}_{ij} \, . \tag{5.11}$$

Contracting (5.10) with M_{ij} and dividing then gives

$$C_S = \frac{L_{ij} M_{ij}}{M_{kl} M_{kl}} \tag{5.12}$$

The resulting C_S from (5.12) can be positive or negative, and is then used in (5.8) to determine the local value of the subgrid stress as

$$\boldsymbol{\tau} = -C_S \widetilde{\Delta}^2 |\widetilde{\mathbf{S}}| \, \widetilde{\mathbf{S}} \, . \tag{5.13}$$

Since C_S can be positive or negative, the resulting subgrid production

$$P = -C_S \widetilde{\Delta}^2 |\widetilde{\mathbf{S}}|^2 \, , \tag{5.14}$$

can also be positive or negative.

5.1.1.3 Bardina scale similarity model

The Bardina scale similarity model applies a test filter $\widehat{(\ )}$ having length scale $\widehat{\Delta}$ to the LES-filtered velocities $\widetilde{u}_i$ to define a test stress

$$T_{ij} \equiv \widehat{\widetilde{u}_i \widetilde{u}_j} - \widehat{\widetilde{u}}_i \, \widehat{\widetilde{u}}_j \, . \tag{5.15}$$

It then takes the local subgrid stress to be directly proportional to the local test stress, namely

$$\tau_{ij} = C_B T_{ij} \, , \tag{5.16}$$

or equivalently

$$\boldsymbol{\tau} = C_B \mathbf{T}_{ij} \, . \tag{5.17}$$

The constant C_B is typically chosen based on an average of values that best match commonly used reference cases. The present study uses $C_B = 0.45$.

5.1.2 Nonparametric Representations for Autonomic Closure

Nonparametric representations are formulated in the resolved primitive variables of the simulation, and thus for the subgrid stress $\boldsymbol{\tau}$ are written in the resolved velocities $\mathbf{u}$. Results from *a priori* tests of two nonparametric representations for $\boldsymbol{\tau}$ are presented in this chapter.

5.1.2.1 CL24 representation

Prior work [61, 62] developed a nonparametric subgrid stress representation, referred to as CL24, that consists of all first- and second-order combinations of collocated velocity components on a $3 \times 3 \times 3$ stencil. Each component of the subgrid stress is separately represented as a sum of 244 terms, with each term having an associated coefficient h_i. Such a representation is not tensorally correct, but it involves a sufficiently large number of degrees of freedom that it nevertheless has been found in *a priori* tests to accurately represent subgrid stress fields $\tau_{ij}(\mathbf{x}, t)$ and associated subgrid production fields $P(\mathbf{x}, t)$. However, the number of coefficients involved in this CL24 representation is too large to be practical for use in fully dynamic implementations of autonomic closure, though it can be applied in static implementations.

5.1.2.2 TF27 representation

A tensorally-correct nonparametric representation for the subgrid stress in the collocated velocity components on a $3 \times 3 \times 3$ stencil is possible by forming the set of $m = 1, \ldots, 27$ tensors $(\mathbf{u}_m \otimes \mathbf{u}_m)$, where $\mathbf{u}_m$ are the relative velocities at the stencil points and $\otimes$ denotes the outer product in (3.34), as

$$\boldsymbol{\tau} = h_0 \mathbf{I} + \sum_{m=1}^{27} h_m (\mathbf{u}_m \otimes \mathbf{u}_m). \tag{5.18}$$

As in all tensorally-correct representations, the same set of coefficients h_m applies to all six components of the subgrid stress $\boldsymbol{\tau} \equiv \tau_{ij}$. While this representation is tensorally correct, it is not complete in the sense described in Chapter 3. It does, however,

involve only 27 nontrivial coefficients and therefore from a computational perspective is efficient enough for use in fully dynamic implementations of autonomic closure. This tensorally-correct form in 27 coefficients is referred to as TF27.

5.1.3 Parametric Representations for Autonomic Closure

Parametric representations are formulated in derived quantities that can be evaluated from the resolved variables in the simulation. For the subgrid stress, these include the strain rate and rotation rate tensors $\mathbf{S}$ and $\mathbf{R}$, and their gradients $\nabla\mathbf{S}$ and $\nabla\mathbf{R}$. Chapter 3 shows how the tensor representation theory of Smith (1971) [63] can be used to obtain complete and minimal representations for $\boldsymbol{\tau}$ in these parametric quantities, and how the resulting complete representations can be truncated to reduce the number of coefficients involved. Results from *a priori* tests of four parametric representations for $\boldsymbol{\tau}$ are presented in this chapter.

5.1.3.1 TF19 representation

Section 3.1.3 showed that the complete and minimal representation for the subgrid stress tensor $\boldsymbol{\tau}$ in tensor products of $\mathbf{S}$, $\mathbf{R}$, and rank-2 contractions of $\nabla\mathbf{S}$ and $\nabla\mathbf{R}$ would consist of 1276 terms. This number of coefficients h_i is far too large for practical implementation in fully dynamic autonomic closure. That section also showed that if tensor products extending only up to second order in the velocities are retained then this produces a tensorally-correct representation for $\boldsymbol{\tau}$ that involves only 19 coefficients, namely

$$\begin{aligned}\boldsymbol{\tau}_{ij} = {} & h_0\mathbf{I} + h_1\mathbf{S} + h_{16}\mathbf{S}^2 + h_{17}\mathbf{R}^2 + h_{18}(\mathbf{SR}-\mathbf{RS}) \\ & + \underbrace{\sum_{\alpha=2}^{7} h_\alpha \mathbf{M}_\alpha}_{\nabla\mathbf{S}^2} + \underbrace{\sum_{\alpha=8}^{11} h_\alpha \mathbf{M}_\alpha}_{\nabla\mathbf{R}^2} + \underbrace{\sum_{\alpha=12}^{15} h_\alpha \mathbf{M}_\alpha}_{\nabla\mathbf{S}\nabla\mathbf{R}}\end{aligned} \tag{5.19}$$

where M_2 through M_{15} are given in (3.20). From a computational perspective is efficient enough for use in fully dynamic implementations of autonomic closure. This tensorally-correct form in 19 coefficients is referred to as TF19.

5.1.3.2 TF11 representation

Section 3.1.2 shows that, when $\boldsymbol{\tau}$ is represented solely in $\mathbf{S}$ and $\mathbf{R}$, without their gradients, then the number of terms in any complete representation is substantially reduced. It notes that one such representation was originally proposed by Lumley (1970) [67] and Pope (1975) [68], independent of the Smith (1971) [63] formulation for complete and minimal tensor representations, and has since been widely used (e.g., Gatski & Speziale 1993 [70]) to represent nonlinear models for $\boldsymbol{\tau}$ in the form

$$\begin{aligned}\boldsymbol{\tau} = h_0\,\mathbf{I} + h_1\,\mathbf{S} + h_2\,\mathbf{S}^2 + h_3\,\mathbf{R}^2 + h_4\,(\mathbf{SR}-\mathbf{RS}) + h_5\,(\mathbf{S^2R}-\mathbf{RS^2}) \\ + h_6\,(\mathbf{SR^2}+\mathbf{R^2S}) + h_7\,(\mathbf{S^2R^2}+\mathbf{R^2S^2}) + h_8\,(\mathbf{SRS^2}-\mathbf{S^2RS}) \\ + h_9\,(\mathbf{RSR^2}-\mathbf{R^2SR}) + h_{10}\,(\mathbf{RS^2R^2}-\mathbf{R^2S^2R})\end{aligned} \tag{5.20}$$

This representation is tensorally complete, but it is not minimal. It involves 11 coefficients and thus from a computational perspective is efficient enough for use in fully dynamic implementations of autonomic closure. This tensorally-correct form in 11 coefficients is referred to as TF11.

5.1.3.3 TF8 representation

Unlike TF11 in (5.20), which is not based on the Smith (1971) [63] theory for complete and minimal tensor representations, Section 3.1.2 shows that an alternative representation for $\boldsymbol{\tau}$ in $\mathbf{S}$ and $\mathbf{R}$ can be obtained from the Smith (1971) theory as

$$\begin{aligned}\boldsymbol{\tau} = h_0\,\mathbf{I} + h_1\,\mathbf{S} + h_2\,\mathbf{S}^2 + h_3\,\mathbf{R}^2 + h_4\,(\mathbf{SR}-\mathbf{RS}) + h_5\,\mathbf{RSR} \\ + h_6\,(\mathbf{S^2R}-\mathbf{RS^2}) + h_7\,(\mathbf{RSR^2}-\mathbf{R^2SR})\end{aligned} \tag{5.21}$$

This is tensorally-correct and is a complete and minimal representation that involves only 8 coefficients, so from a computational perspective it is efficient enough for use in fully dynamic implementations of autonomic closure. This tensorally-correct form in 8 coefficients is referred to as TF8.

5.1.3.4 TF5 representation

As noted in Section 3.1.2, the fact that the CL24 has been found to accurately represent the subgrid stress even though it involves only velocity products up to second order suggests a further representation in which the tensor products of third and higher orders are truncated. This gives

$$\boldsymbol{\tau} = h_0\,\mathbf{I} + h_1\,\mathbf{S} + h_2\,\mathbf{S}^2 + h_3\,\mathbf{R}^2 + h_4\,(\mathbf{SR} - \mathbf{RS}) \tag{5.22}$$

Since this involves only five coefficients, from a computational perspective it is the most efficient of all these representations for use in fully dynamic implementations of autonomic closure. This tensorally-correct representation in five coefficients is referred to as TF5.

5.2 *A Priori* Tests: Comparisons of τ_{ij} Representations

As described in Section 1.5, *a priori* tests are the most direct way to determine the *accuracy* of the $\tau_{ij}(\mathbf{x}, t)$ fields and their associated subgrid production fields $P(\mathbf{x}, t)$ that result from any given subgrid stress representation. Such tests allow direct comparisons of the fields produced by the subgrid stress representation and the corresponding exact fields. Although *a priori* tests do not address the computational *stability* of the stress representation – that is addressed via forward simulations in Chapter 6 – they provide complete information on the accuracy of the representation.

These *a priori* tests used Direct Numerical Simulation (DNS) data for homogeneous isotropic turbulence at $Re_\lambda = 433$ from the Johns Hopkins Turbulence Database [76, 77]. The velocity fields on the 1024^3 DNS grid were first downsampled onto a uniformly spaced 256^3 grid with grid spacing Δ to produce $\mathbf{u}(\mathbf{x}, t)$. These velocity fields were then filtered in the spectral domain with a spectrally sharp LES-scale filter $\widetilde{(\ )}$ having cutoff wavenumber at $k_{\widetilde{\Delta}} = 40$ to produce the pseudo-LES velocity fields $\widetilde{\mathbf{u}}(\mathbf{x}, t)$. From the resulting $\widetilde{\mathbf{u}}(\mathbf{x}, t)$ and the original $\mathbf{u}(\mathbf{x}, t)$ together with the LES-scale filter $\widetilde{(\ )}$, the true subgrid stress field $\tau_{ij}(\mathbf{x}, t)$ was then constructed as $\tau_{ij} = \widetilde{u_i u_j} - \widetilde{u}_i \widetilde{u}_j$.

The pseudo-LES velocity fields $\widetilde{\mathbf{u}}(\mathbf{x},t)$ were then test-filtered in the spectral domain with a spectrally sharp test-scale filter $\widehat{(\ )}$ having cutoff wavenumber at $k_{\widehat{\Delta}} = 20$ to produce test-filtered velocity fields $\widehat{\widetilde{\mathbf{u}}}(\mathbf{x},t)$. From the resulting test-filtered velocities $\widetilde{\mathbf{u}}(\mathbf{x},t)$ and the LES-filtered velocities $\widetilde{\mathbf{u}}(\mathbf{x},t)$ together with the test-scale filter $\widehat{(\ )}$, the test stress fields $T_{ij}(\mathbf{x},t)$ was then constructed as $T_{ij} = \widehat{\widetilde{u}_i}\widehat{\widetilde{u}_j} - \widehat{\widetilde{u}}_i\widehat{\widetilde{u}}_j$. These test stresses are the inputs for solving of the local system identification problem at each point $\mathbf{x}$, as described in Section 2.3, which determines the local set of coefficients $\mathbf{h}$. The resulting local coefficients at $\mathbf{x}$ are then used in the generalized subgrid stress representation $\mathcal{F}$ to determine the resulting local subgrid stresses $\tau_{ij}^{\mathcal{F}}(\mathbf{x})$. This is repeated at every point $\mathbf{x}$ in the 256^3 field to produce the subgrid stress field $\tau_{ij}^{\mathcal{F}}(\mathbf{x},t)$, which is then compared with the true subgrid stress field $\tau_{ij}(\mathbf{x},t)$.

Figure 1 shows the kinetic energy spectrum computed from the 256^3 velocity field $\mathbf{u}(\mathbf{x},t)$, which shows the expected $k^{-5/3}$ inertial range extends to the maximum wavenumber $k_{max} = 128$. The figure also shows the cutoff wavenumbers at $k_{\widetilde{\Delta}} = 40$ for the LES-filtered velocity fields and at $k_{\widehat{\Delta}} = 20$ for test-filtered velocity fields, confirming that both are well within the inertial range. As a result, the classical inertial-range scaling used in section 4.2 are clearly valid.

Figures 2, 3 and 4 show typical *a priori* test results from traditional prescribed models for the subgrid stress $\tau_{ij}(\mathbf{x},t)$, including the basic Smagorinsky model in Section 5.1.1.1, the dynamic Smagorinsky model in Section 5.1.1.2, and the Bardina scale similarity model in Section 5.1.1.3. Figure 2 shows results for a typical normal stress component $\tau_{11}(\mathbf{x},t)$, Figure 3 shows results for a typical shear stress component $\tau_{12}(\mathbf{x},t)$, and Figure 4 shows results for the corresponding subgrid production $P(\mathbf{x},t) = \tau_{ij}\,\widetilde{S}_{ij}$. In each case, the resulting field from the corresponding traditional prescribed model must be compared with the corresponding true field in the uppermost panel of each figure. It is apparent in these figures that both the basic and dynamic Smagorinsky models give remarkably poor representations for the subgrid stresses

and the subgrid production. The Bardina scale similarity model is substantially more accurate, especially in the subgrid production field $P(\mathbf{x}, t)$ in Figure 4, though there are clear differences apparent between it and the true production field in the uppermost panel.

Figures 5, 6 and 7 show corresponding typical *a priori* test results from atonomic closure using *nonparametric* generalized representations for the subgrid stress $\tau_{ij}(\mathbf{x}, t)$, including static and fully dynamic implementations of the 244-term CL24 representation in Section 5.1.2.1, and fully dynamic implementation of the 27-term TF27 representation in Section 5.1.2.2. Figure 5 shows results for a typical normal stress component $\tau_{11}(\mathbf{x}, t)$, Figure 6 shows results for a typical shear stress component $\tau_{12}(\mathbf{x}, t)$, and Figure 7 shows results for the corresponding subgrid production $P(\mathbf{x}, t) = \tau_{ij}\, \widetilde{S}_{ij}$. In each case, the resulting field from the corresponding nonparametric generalized representation must be compared with the corresponding true field in the uppermost panel of each figure. The static and dynamic CL24 representation is not tensorally correct, yet both show relatively good agreement with the corresponding true field in the uppermost panel of each figure, especially for the subgrid production field $P(\mathbf{x}, t)$ in Figure 7. More importantly, the results from the tensorally-correct TF27 representation, despite involving only 27 coefficients, are substantially more accurate than those from the two 244-term CL24 representations. This shows one of the main benefits from the use of tensorally-correct representations in autonomic closure. Moreover, comparing the bottommost panels in Figures 4 and 7 with the corresponding true field in the uppermost panels shows that the TF27 representation gives substantially more accurate results for the subgrid production field than does the Bardina scale similarity model.

Figures 8, 9 and 10 show corresponding typical *a priori* test results from atonomic closure using *parametric* generalized representations for the subgrid stress $\tau_{ij}(\mathbf{x}, t)$, including fully dynamic implementations of the 19-term TF19 representation in

Section 5.1.3.1, the 11-term TF11 representation in Section 5.1.3.2, the 8-term TF8 representation in Section 5.1.3.3, and the 5-term TF5 representation in Section 5.1.3.4. Figure 8 shows results for a typical normal stress component $\tau_{11}(\mathbf{x}, t)$, Figure 9 shows results for a typical shear stress component $\tau_{12}(\mathbf{x}, t)$, and Figure 10 shows results for the corresponding subgrid production $P(\mathbf{x}, t) = \tau_{ij}\, \widetilde{S}_{ij}$. In each case, the resulting field from the corresponding nonparametric generalized representation must be compared with the corresponding true field in the uppermost panel of each figure. Unlike the other generalized representations in these figures, the results from TF19 – which is the only representation that includes terms accounting for $\nabla\mathbf{S}$ and $\nabla\mathbf{R}$ – show excessive fine-scale features and excessively large positive and negative values. The reasons for this have not been determined.

More importantly, in comparison with the results from the traditional prescribed models for the subgrid stress in Figures 2, 3, and 4, the TF11, TF8, and TF5 representations in Figures 8, 9, and 10 show remarkably good agreement with the corresponding true field in the uppermost panel of each figure. This is attributed to the larger number of degrees of freedom in these tensorally-correct representations. Equally important is the observation that there is little, if any, loss of accuracy in the results from the TF11, TF8, and TF5 representations as the number of degrees of freedom decreases from 11 to 5. The fact that the TF5 representation is essentially as accurate as are representations having larger numbers of degrees of freedom is consistent with the observation that retaining terms up to only second-order in velocity products in nonparametric representations such as CL24 is sufficient to obtain accurate results for subgrid stress and subgrid production fields.

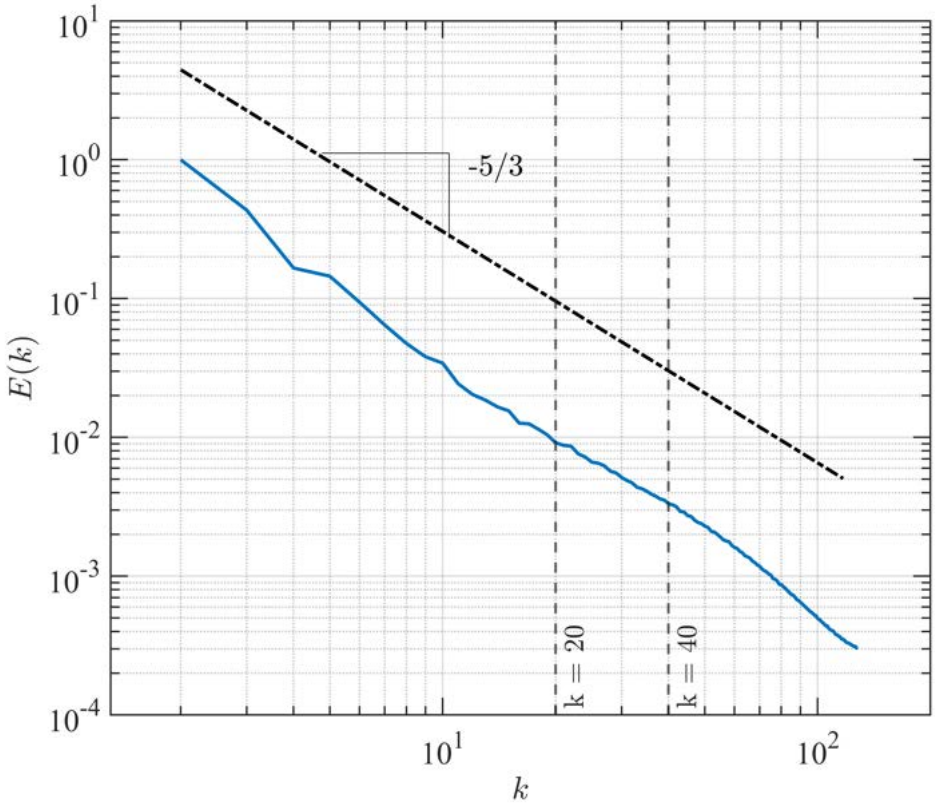

Figure 1. Inertial-range kinetic energy spectrum $E(k)$ from the Johns Hopkins DNS data used in the present *a priori* tests, showing LES-filter wavenumber $k_{\widetilde{\Delta}} = 40$ and test-filter wavenumber $k_{\widehat{\Delta}} = 20$.

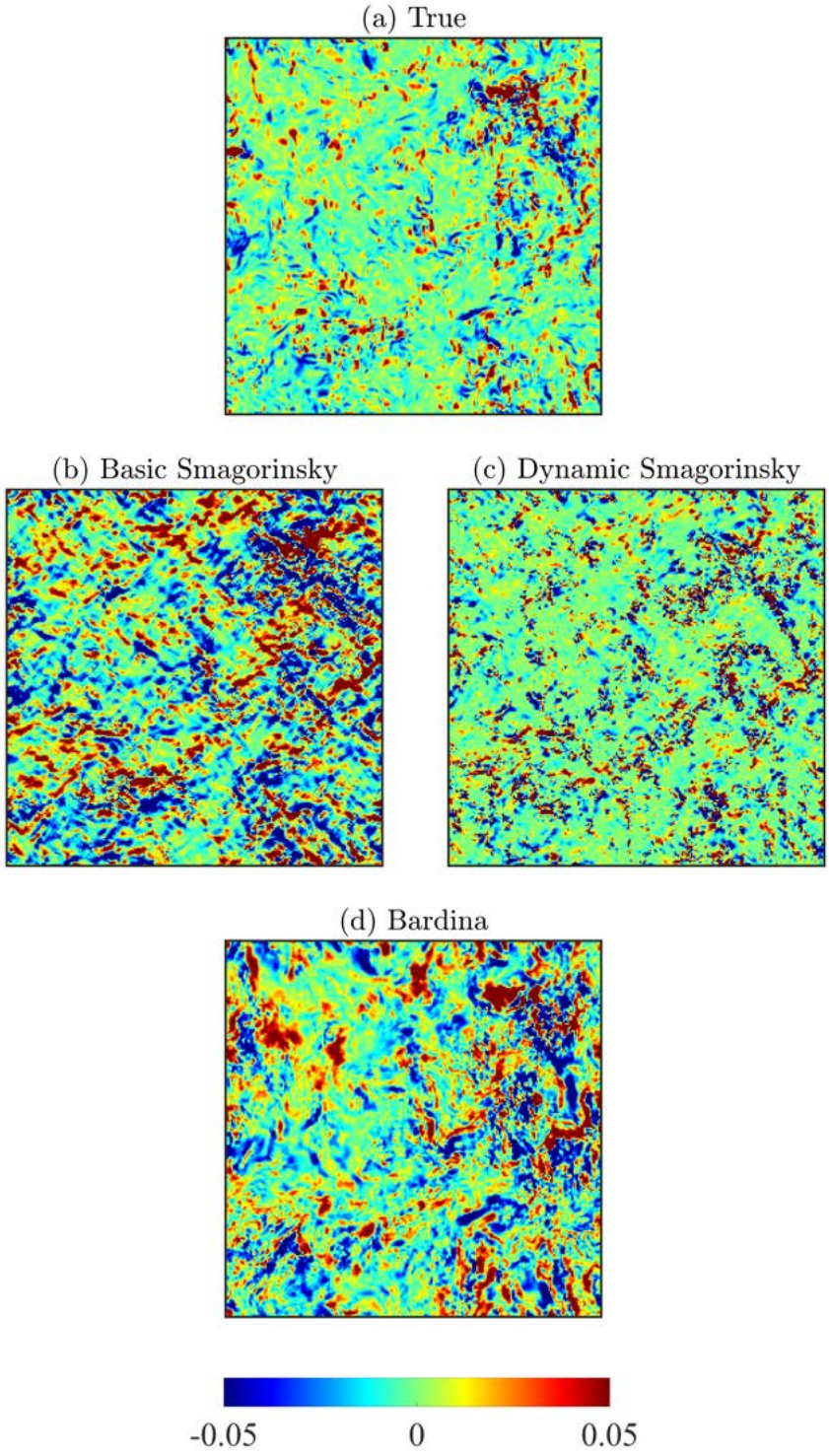

Figure 2. Typical results from *a priori* tests of traditional *prescribed* models for τ_{ij}, showing a *normal* stress component τ_{11} in a typical plane.

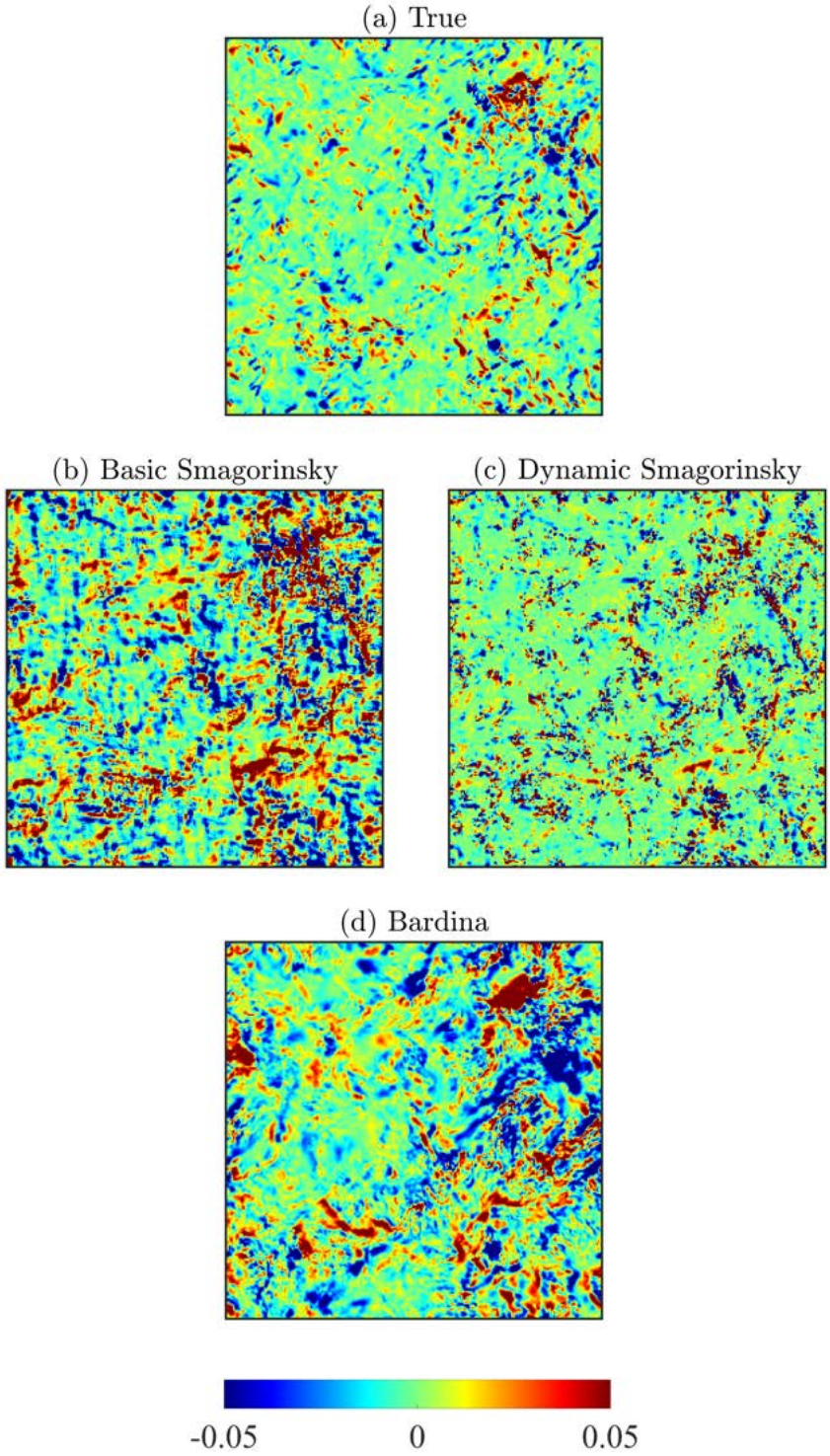

Figure 3. Similar to Fig. 2 but showing results from traditional *prescribed* models for a *shear* stress component τ_{12} in the same plane.

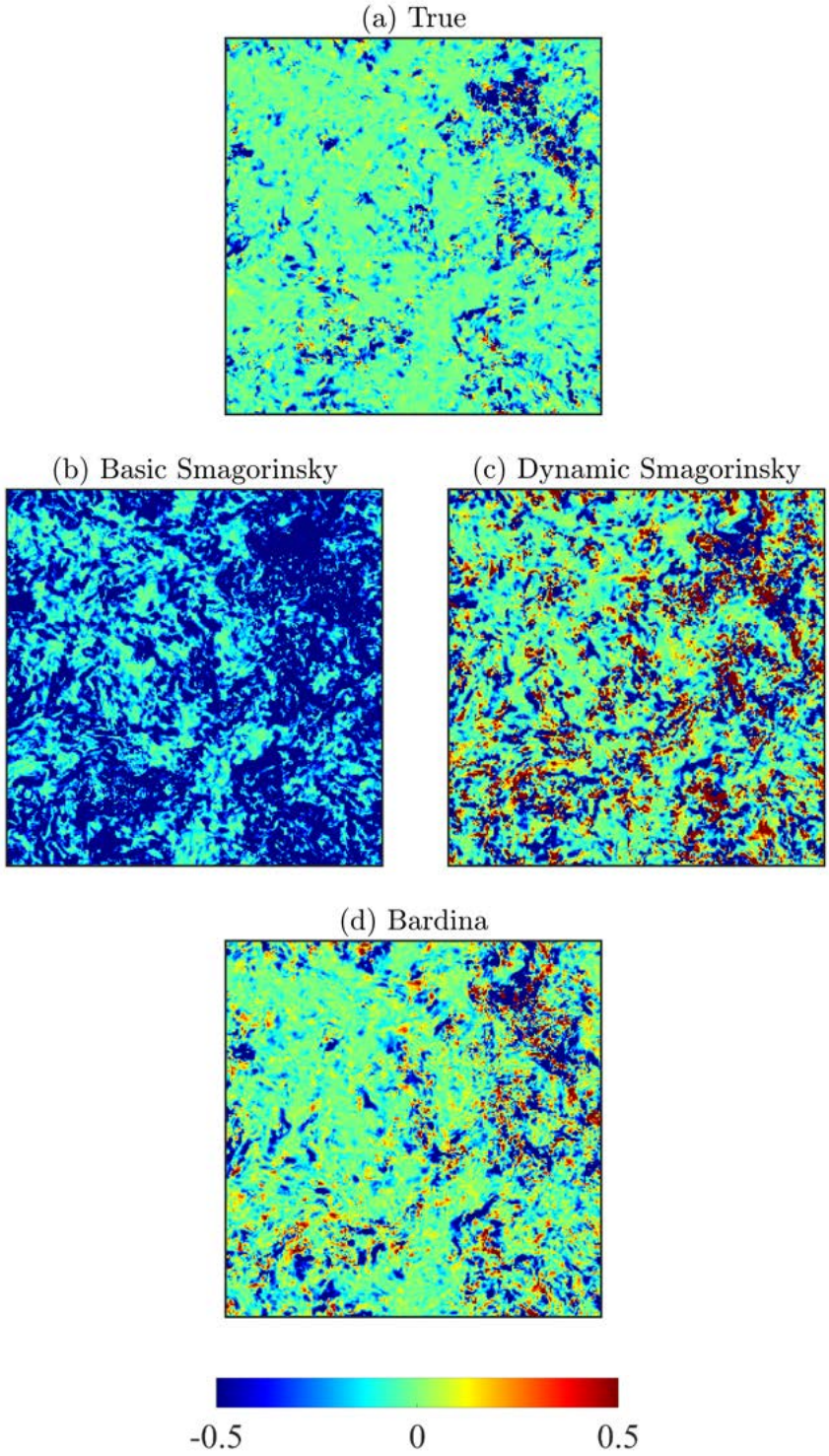

Figure 4. Similar to Figs. 2 and 3 but showing results from traditional *prescribed* models for the *subgrid production* P in the same plane.

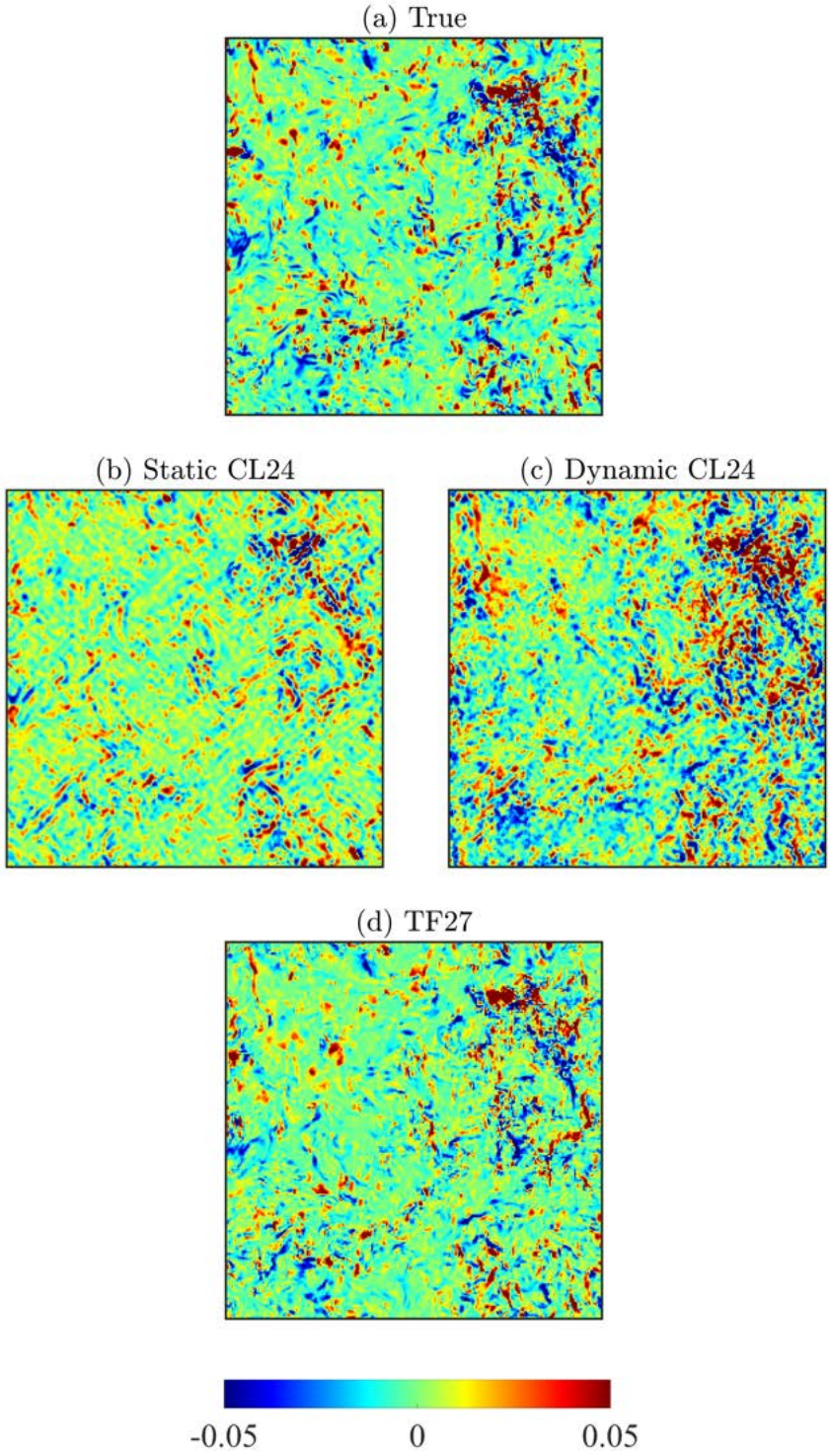

Figure 5. Typical results from *a priori* tests of *nonparametric* representations for τ_{ij} in autonomic closure, showing a *normal* stress component τ_{11} in a typical plane. Note CL24 is not tensorally correct, whereas TF27 is tensorally correct.

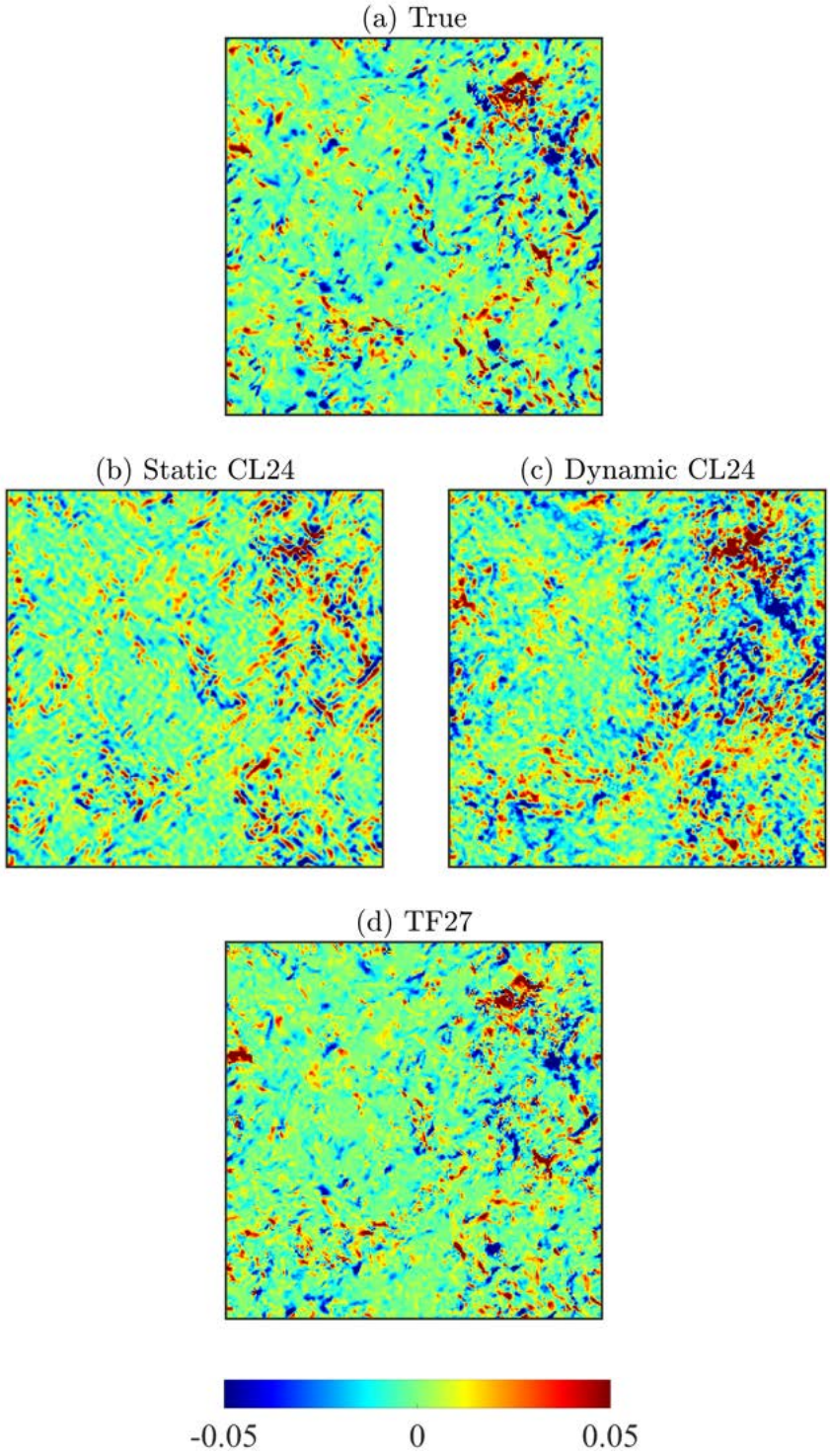

Figure 6. Similar to Fig. 5 but showing results from *nonparametric* representations of a *shear* stress component τ_{12} in autonomic closuree. Note CL24 is not tensorally correct, whereas TF27 is tensorally correct.

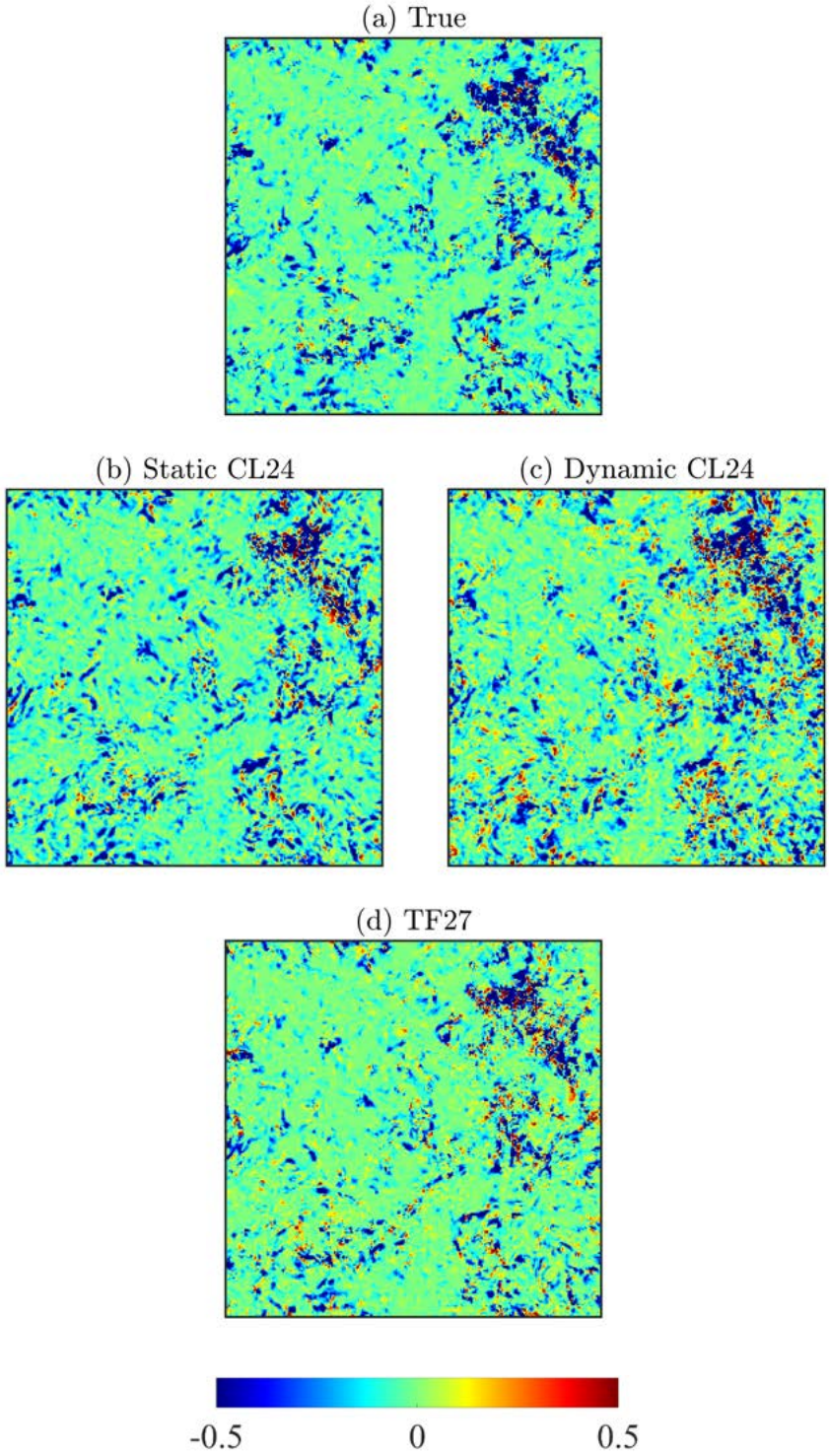

Figure 7. Similar to Figs. 5 and 6 but showing results from *nonparametric* representations for the *subgrid production* P in autonomic closure. Note CL24 is not tensorally correct, whereas TF27 is tensorally correct.

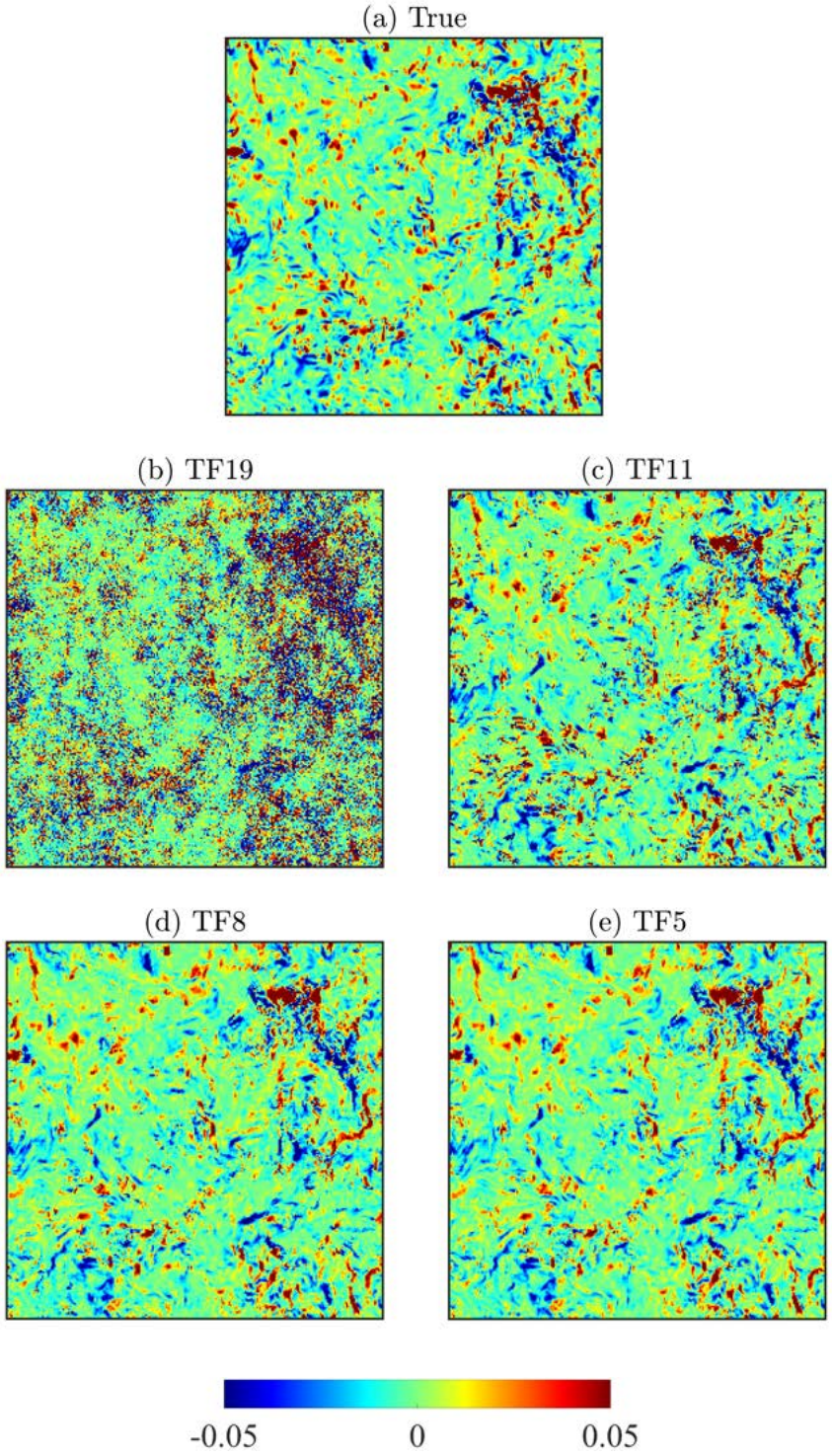

Figure 8. Typical results from *a priori* tests of *parametric* representations of τ_{ij} in autonomic closure, showing a *normal* stress component τ_{11} in a typical plane. TF19, TF11, TF8, and TF5 are all tensorally-correct representations.

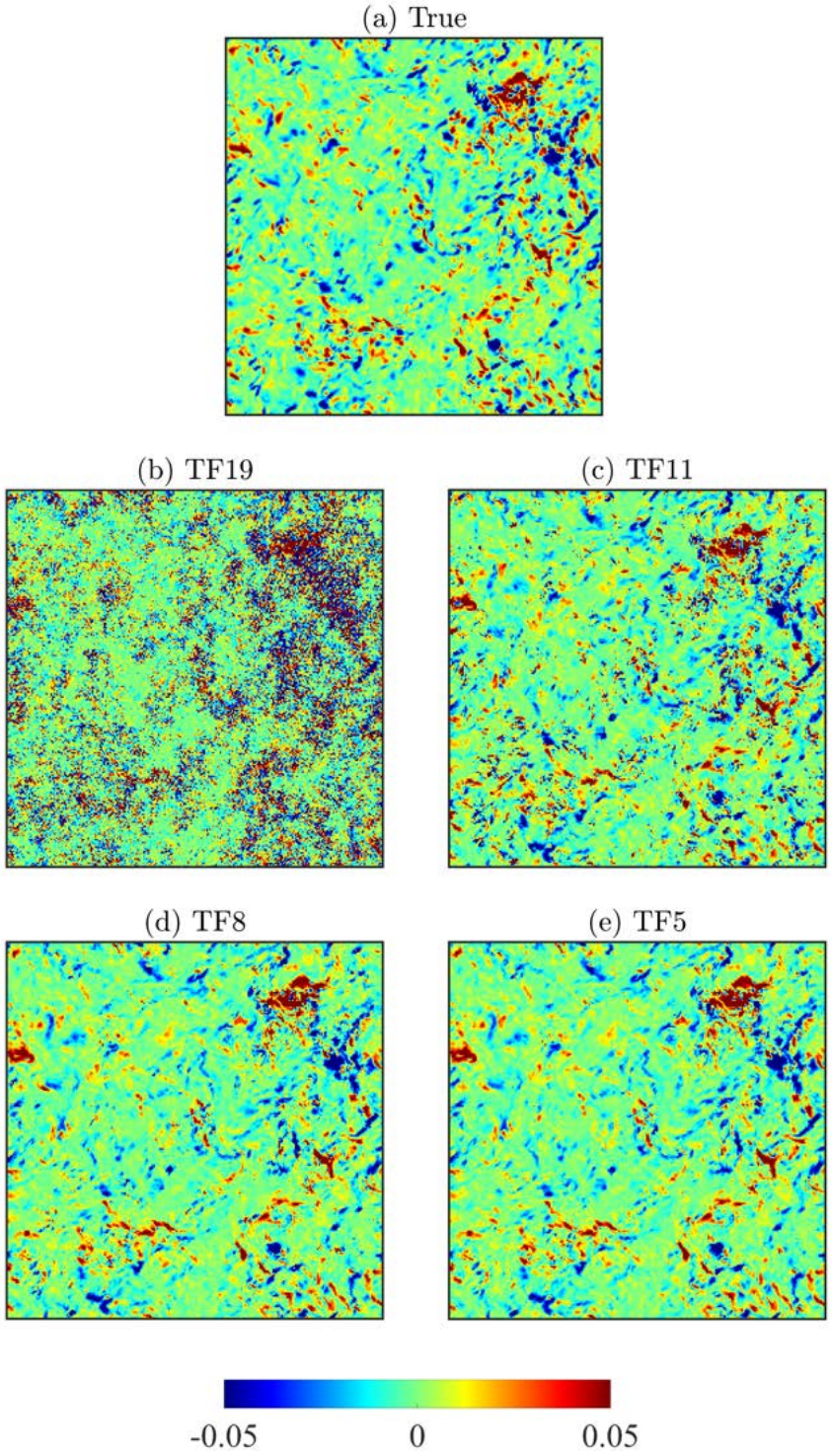

Figure 9. Similar to Fig. 8 but showing results from *parametric* representations of a *shear* stress component τ_{12} in autonomic closure. TF19, TF11, TF8, and TF5 are all tensorally-correct representations.

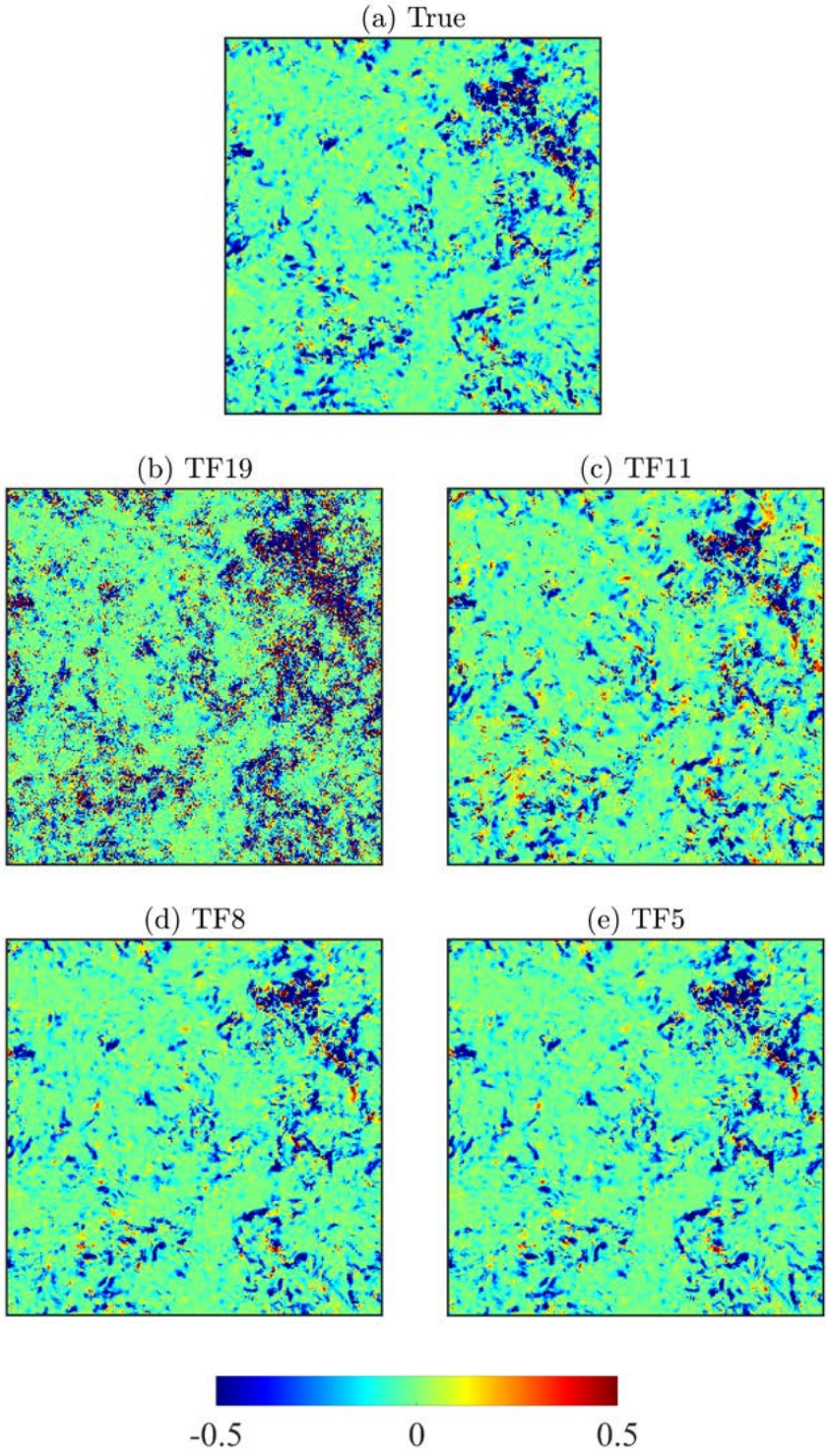

Figure 10. Similar to Figs. 8 and 9 but showing results from *parametric* representations for the *subgrid production* P in autonomic closure. TF19, TF11, TF8, and TF5 are all tensorally-correct representations.

Chapter 6

STABILITY OF SUBGRID STRESS REPRESENTATIONS

While *a priori* tests such as those in Chapter 5 are the most direct way to determine the *accuracy* of any traditional prescribed model for the subgrid stress τ_{ij}, or of any generalized representation for τ_{ij} in autonomic closure, assessing the computational *stability* of any of these forms for τ_{ij} requires its implementation in an LES code to enable forward simulations. However, as noted in Section 1.6, the numerical methods on which the underlying LES code is based must be be sufficiently non-dissipative (non-dispersive) to allow the inherent stability of the τ_{ij} closure to be assessed. This chapter uses a high-order pseudo-spectral code to assess the inherent stability or instability of autonomic closure based on each of the generalized representations for which *a priori* results are presented in Chapter 5, and also assesses the corresponding stability or instability of each of the traditional prescribed models for τ_{ij}. In particular, for each it determines the minimum amount of added dissipation, if any, that is needed to achieve computational stability, as well as the amount of added dissipation, if any, that is needed to produce clear $k^{-5/3}$ inertial-range scaling in the kinetic energy spectrum $E(k)$ extending up to or near the smallest resolved scales in the simulation.

6.1 The Pseudo-Spectral LES Code

These forward simulations were done using SpectralLES, a high-order pseudo-spectral LES code developed at CU Boulder. The present study implemented autonomic closure in this code for each of the generalized representations for τ_{ij} in Sections 5.1.2 and 5.1.3, as well as traditional closure with each of the prescribed models for τ_{ij} in Section 5.1.1. The code was used to simulate homogeneous isotropic turbulence in a periodic domain, discretized on a 64^3 grid with side lengths $L = 2\pi$ and having periodic boundary conditions in all three directions, with a non-dimensional viscosity

$\nu = 1.85(10^{-4})$. Fourier collocation methods were used for the spatial discretization and an explicit fourth-order Runge Kutta scheme was employed for time advancement. The turbulence is sustained by a spectrally-truncated linear energy forcing at wavenumbers $2 \leq k < 4$ with a non-dimensional energy input rate of 0.103. De-aliasing was performed by explicitly filtering the velocity fields with a spectrally sharp filter at $k = 30$ to remove all contributions from doubly and triply aliased wavenumbers. Each simulation was run sufficiently long past the startup phase and well into the statistically stationary phase, and thereby produced homogeneous isotropic turbulence that was uncontaminated by the initial conditions. The inherently high-order nature of this pseudo-spectral code guarantees numerical dissipation to be insignificant in comparison to the kinetic energy production resulting from the subgrid stress model.

Two reference cases were first simulated to clarify the energetics involved in such simulations and provide baseline results for comparison with results from subgrid stress representations in autonomic closure and prescribed models in traditional closure. The first is a case where no subgrid stress model was used. This was done by literally setting $\boldsymbol{\tau} \equiv 0$ in the LES code, while leaving all other parameters as described above. Since the subgrid stress is zero, the subgrid production $P \equiv \boldsymbol{\tau} : \mathbf{S}$ is also zero, meaning that no kinetic energy can be transferred out of the resolved scales into subgrid scales. Instead, the only mechanism for removing kinetic energy from the simulation is the viscous dissipation rate $-2\nu\widetilde{S}_{ij}\widetilde{S}_{ij}$ in (1.6). As a consequence, in such a simulation the velocity gradients in $\widetilde{S}_{ij}$ must increase until the resulting viscous dissipation rate is sufficient to balance the energy input rate at the largest scales.

Figure 11 presents results from such a simulation, where panel (a) shows the kinetic energy $\frac{1}{2}\,\widetilde{\mathbf{u}} \cdot \widetilde{\mathbf{u}}$ versus time at a typical point $\mathbf{x}$ in the domain, panel (b) shows the time evolution of the volume-averaged kinetic energy $\left\langle \frac{1}{2}\,\widetilde{\mathbf{u}} \cdot \widetilde{\mathbf{u}} \right\rangle_V$, and Figure 11$(c)$ shows the resulting kinetic energy spectrum $E(k)$. Figure 11(a) verifies that the simulation ran stably for more than 55 characteristic time scales (k/ϵ) before being intentionally

stopped, while Figure 11(b) verifies that the simulation remained stable across all points in the domain. Figure 11(c) clarifies how the energetics adjust when $\boldsymbol{\tau} \equiv 0$, as described above. In particular, since aliasing has been removed, a "bottleneck" occurs in the small scales, where the energy accumulates until the velocity gradients at these small scales become large enough to produce a sufficiently large viscous dissipation rate to balance the rate at which energy is input at the largest scales. The pseudo-spectral code remains stable in such $\boldsymbol{\tau} \equiv 0$ simulations despite the resulting exceedingly high accumulation of energy near the smallest scales of the simulation.

The second reference case is a simulation with the basic Smagorinsky model for the subgrid stress. As noted in (5.4), this traditional prescribed model is purely dissipative, thus providing a guaranteed-stable baseline case against which the other simulations may be compared. Furthermore, due to its inherently dissipative nature, the basic Smagorinsky model is often combined with other higher-accuracy models that may be unstable by themselves to produce mixed models that will be computationally stable in forward simulations. Results obtained from the pseudo-spectral LES code with the basic Smagorinsky model are shown in Figure 12, where the panels are arranged the same way as in Figure 11 and in Figures 13-20. Figure 12(a) shows that the simulation was again run for more than 55 characteristic time scales (k/ϵ) before being intentionally stopped. Comparing Figure 12(a, b) with the corresponding panels in Figure 11 shows how the subgrid dissipation in the basic Smagorinsky model alters the energetics at a typical point and averaged over the domain. Importantly, in Figure 12(c) the energy spectrum $E(k)$ shows that there is little or no inertial range, due to the dissipative roll-off occuring over a very wide range of wavenumbers k in the highly dissipative basic Smagorinsky subgrid model.

With insights from these references cases, the next section examines the stability of $\boldsymbol{\tau}$ representations in forward simulations with this pseudo-spectral LES code.

6.2 Computational Stability of Subgrid Stress Representations

Each of the aforementioned τ_{ij} representations in Section 5.1.1 for traditional closure, and in Sections 5.1.2 and 5.1.3 for autonomic closure, have been implemented in the pseudo-spectral LES code and used in forward simulations. As in Figures 11 and 12, for each case the kinetic energy $\frac{1}{2}\,\widetilde{\mathbf{u}}\cdot\widetilde{\mathbf{u}}$ at a typical point in the domain and its average $\left\langle \frac{1}{2}\,\widetilde{\mathbf{u}}\cdot\widetilde{\mathbf{u}} \right\rangle_V$ over the whole domain were used to assess the resulting computational stability, and for stable cases the resulting kinetic energy spectrum $E(k)$ was used to assess how accurately it produces the required $k^{-5/3}$ inertial-range scaling. Additionally, the computational time required for LES with each stable representation was determined to assess its computational cost and practicality.

With the exception of the purely dissipative basic Smagorinsky model, all the prescribed models for τ_{ij} in traditional closure led to unstable simulations, and most of the generalized representations for τ_{ij} in autonomic closure also produced unstable simulations. For this reason, each of the τ_{ij} representations was implemented in a mixed model by combining it with the purely dissipative basic Smagorinsky model as

$$\tau_{ij} = (1 - c_{BS})\,\tau_{ij}^{R} + c_{BS}\,\tau_{ij}^{BS} \tag{6.1}$$

where τ_{ij}^{R} is the subgrid stress from the representation being considered, τ_{ij}^{BS} is the subgrid stress from basic Smagorinsky model, and $0 \leq c_{BS} \leq 1$ is an adjustable constant that controls how much dissipation is being added by the basic Smagorinsky part of the mixed model. When $c_{BS} = 0$ then the basic Smagorinsky part is "turned off", and as c_{BS} is increased the inherent dissipation from the basic Smagorinsky part increases to assist with computational stability.

For each representation, beginning at a relatively large value that ensures stability, c_{BS} was systematically decreased to determine the minimum value that provides sufficient added dissipation from the basic Smagorinsky part in (6.1) to achieve stable long-time forward simulations. Further, for stable cases the value of c_{BS} was

determined that provides "good" $k^{-5/3}$ inertial-range scaling in the resulting $E(k)$. Since "goodness" of the energy spectrum was assessed visually and thus to some extent is subjective, in some cases a range of such c_{BS} values is reported.

The remainder of this section provides an overview of the results obtained in regard to computational stability of each subgrid stress representation for traditional closure or for autonomic closure. Detailed results for each representation and closure method are then presented in following sections.

Table 1 summarizes the main results found from these forward simulations with each subgrid stress representation and closure approach. The first two entries are for traditional closure using prescribed subgrid models for τ_{ij}, including the dynamic Smagorinsky model in Section 5.1.1.2 and the Bardina scale similarity model in Section 5.1.1.3. The remaining entries are for autonomic closure based on various generalized representations for τ_{ij}. The first of these is the non-tensorally-correct CL24 representation [61, 62] summarized in Section 5.1.2.1. The others are all tensorally-correct representations, including TF27 in Section 5.1.2.2, TF19 in Section 5.1.3.1, TF11 in Section 5.1.3.2, TF8 in Section 5.1.3.3, and TF5 in Section 5.1.3.4.

The results in Table 1 show that two subgrid stress representations in autonomic closure are stable in forward simulations without *any* added dissipation, namely with $c_{BS} = 0$. These are the static CL24 representation and the dynamic TF5 representation. Furthermore, these two manifestly stable representations for the subgrid stress in autonomic closure also require only comparatively small amounts of additional dissipation to achieve a "good" energy spectrum $E(k)$. This can be contrasted with the minimum added dissipation needed for stability in traditional closure with the dynamic Smagorinsky model and with the Bardina scale similarity model, which respectively needed 40% and 5% added dissipation from the basic Smagorinsky model part in (6.1) to achieve stability, but needed large amounts of added dissipation to achieve a "good" $E(k)$.

Another important consideration in comparing these closure methods is the computational cost of each. Table 2 gives the average run-time required for one computational time step with each of these subgrid stress representations. The run-time per time step varies slightly, so an average was taken of run-time per time step in the statistically stationary phase of each forward simulation. Since there are many computational factors that can affect the run-time per time step, all of these forward simulations were done on the same ASU Agave cluster with the same amount of memory, number of processors, and type of processors in an attempt to make these comparisons as meaningful as possible.

As expected, Table 2 shows the implementations of autonomic closure based on τ_{ij} representations involving large numbers of degrees of freedom, such as TF27 and TF19, were computationally expensive. At the other extreme, the run-time per time step with the static CL24 representation was comparable to that of traditional models.

Most importantly however, the run-time per time step in a fully dynamic implementation of autonomic closure based on the TF5 representation for the subgrid stress is only slightly more than three times longer than for traditional closure with the dynamic Smagorinsky model. Yet as can be seen by comparing Figures 2-4 with Figures 8-11, the TF5 representation produces far more accurate subgrid stress fields and subgrid production fields than does the dynamic Smagorinsky model. Additionally, since the TF5 representation in autonomic closure requires only a small amount of added dissipation from the basic Smagorinsky part in (6.1) to achieve a good $E(k)$, whereas the dynamic Smagorinsky model in traditional closure requires at least 50% of the subgrid stress in (6.1) to come from the clearly inaccurate basic Smagorinsky model (see Figures 2-4), the difference in accuracy between the two in forward simulations is even far larger. Especially in multiphysics problems that require high accuracy in the resolved fields, the factor of three longer run-time per time step may be entirely acceptable to gain this substantially increased accuracy.

6.2.1 Traditional Closure with Prescribed Models

6.2.1.1 Dynamic Smagorinsky model

Figure 13 shows results from forward simulations with the dynamic Smagorinsky model for various levels of added dissipation via c_{BS} in (6.1). The minimum value for which a stable simulation was possible was $c_{BS} = 0.40$, which corresponds to 40% added dissipation from the basic Smagorinsky part. As can best be seen in Figure 13(b), with this level the added dissipation the simulation is barely stable, as evident from the large spikes in the kinetic energy versus time at a typical point, and the corresponding kinetic energy spectrum $E(k)$ in Figure 13(d) accordingly shows a large "bottleneck" of energy at high wavenumbers.

Figure 13(b) shows that c_{BS} must be further increased until 50% or more of the dissipation comes from the basic Smagorinsky part to eliminate the sharp spikes in the kinetic energy versus time at a typical point. Even at these large c_{BS} values, the spectrum $E(k)$ in Figure 13(d) does not show a clear $k^{-5/3}$ inertial-range scaling.

6.2.1.2 Bardina scale similarity model

Figure 14 shows corresponding results from forward simulations with the Bardina scale similarity model for various levels of added dissipation via c_{BS} in (6.1). As seen in Table 1, the model is unstable without any added dissipation, but requires only 5% added dissipation to become stable. However, the associated energy spectrum $E(k)$ in Figure 14(d) shows large "bottlenecks" of energy near both the test-scale wavenumber and the LES-scale wavenumber. For the spectrally sharp filters used in this study, the nature of the Bardina scale similarity model as described in Section 5.1.1.3 inherently creates large steps in its resulting $E(k)$ at these two wavenumbers, since it represents the subgrid stresses as being simply proportional to the test-scale stresses. Even with increasing c_{BS} values, the resulting steps in $E(k)$ at $k_{\widehat{\Delta}}$ become increasingly larger in this prescribed model for traditional closure.

6.2.2 Autonomic Closure with Nonparametric Representations

6.2.2.1 CL24 representation

Figure 15 shows results from forward simulations with a static implementation of autonomic closure based on the nonparametric CL24 representation [61, 62]. These simulations are stable even with no added dissipation, though in that case the kinetic energy spectrum $E(k)$ in Figure 15(c) shows a significant "bottleneck" at high wavenumbers. However, adding even 5% added dissipation via $c_{BS} = 0.05$ in (6.1) removes most of this "bottleneck", and with just 10% added dissipation the resulting $E(k)$ in Figure 15(c) shows clear $k^{-5/3}$ inertial-range scaling over the entire range of resolved scales in the simulation. This is what the energy spectrum should look like from a large eddy simulation that properly transfers momentum and energy within the resolved scales and between the resolved and subgrid scales.

6.2.2.2 TF27 representation

Figure 16 and Table 3 show results from forward simulations with a fully dynamic implementation of autonomic closure based on the nonparametric TF27 representation. This is solving the local system identification to determine 27 coefficients at each point and time in the simulation. This is computationally expensive, as seen in Table 2, so the simulation was run for a shorter duration before being intentionally stopped. This representation requires a minimum of 20% added dissipation from the basic Smagorinsky model in (6.1) to be computationaly stable. As seen in Figure 16(c) there is only a small "bottleneck" in the spectrum $E(k)$ with this level of stabilization, and increasing the added dissipation via c_{BS} to 25-30% produces clear $k^{-5/3}$ inertial-range scaling over the entire range of resolved scales in the simulation. As also seen from autonomic closure with CL24 in Section 6.2.2.1, this is what the energy spectrum should look like from a large eddy simulation that properly transfers momentum and energy within the resolved scales and between the resolved and subgrid scales.

6.2.3 Autonomic Closure with Parametric Representations

6.2.3.1 TF19 representation

Figure 17 and Table 4 show results from forward simulations with a fully dynamic implementation of autonomic closure based on the parametric TF19 representation. This still involves 19 coefficients, so the local system identification to determine these at each point and time in the simulation is computationally expensive, as seen in Table 2. While TF19 involves substantially fewer coefficients than TF27, it requires the additional cost of computing all the gradients of $\mathbf{S}$ and $\mathbf{R}$ and the resulting tensor products of their components. For this reason, the simulation was run for a shorter duration before being intentionally stopped. As seen in Figure 17, the TF19 representation requires just 5% added dissipation from the basic Smagorinsky model in (6.1) to be computationaly stable. Figure 17(c) shows there is only a relatively small "bottleneck" in $E(k)$ with this level of stabilization, and increasing the added dissipation via c_{BS} to 10-15% produces clear $k^{-5/3}$ inertial-range scaling over the entire range of resolved scales in the simulation. As seen from autonomic closure with the CL24 and TF27 representations in Sections 6.2.2.1 and 6.2.2.2, this is what the energy spectrum should look like from a simulation that properly transfers momentum and energy within the resolved scales and between the resolved and subgrid scales.

6.2.3.2 TF11 representation

Figure 18 and Table 5 show results from forward simulations with a fully dynamic implementation of autonomic closure based on the parametric TF11 representation. Since only 11 coefficients are involved in this generalized representation for the subgrid stress, solving the local system identification to determine these coefficients at each point and time in the simulation is substantially faster than for TF27 or TF19, but is still computationally expensive as seen in Table 2. For this reason the simulation was run for only about 45 characteristic time scales before being intentionally stopped. As

seen in Figure 18 and Table 5, the TF11 representation requires a minimum of 30% added dissipation from the basic Smagorinsky model in (6.1) to be computationaly stable, though Figure 18(b) shows it is only marginally stable at this level of added dissipation. With 35% added dissipation it is fully stable. The corresponding $E(k)$ in Figure 18(c), from a simulation with TF11 that remained stable, shows a roughly $k^{-5/3}$ inertial-range scaling over the entire range of resolved scales. With increasing levels of added dissipation, the resulting $E(k)$ for TF11 is only weakly affected, and for all cases it follows $k^{-5/3}$ more closely than does the dynamic Smagorinsky model in Figure 13 or the Bardina scale similarity model in Figure 14.

6.2.3.3 TF8 representation

Figure 19 and Table 6 show results from forward simulations with a fully dynamic implementation of autonomic closure based on the parametric TF8 generalized representation for the subgrid stress. It involves 8 coefficients, and Table 2 shows that solving the local system identification to determine these coefficients at each point and time in the simulation is still computationally expensive. For this reason the simulation was run only for about 45 characteristic time scales before being intentionally stopped.

Recall from Section 3.1.2 that both TF11 and TF8 represent the subgrid stress solely in tensorally-correct products of $\mathbf{S}$ and $\mathbf{R}$, though TF8 was obtained from the complete and minimal tensor representation theory of Smith (1971) [63], whereas TF11 was not. As a result, TF11 is likely to also be complete but it cannot be minimal. This suggests that whereas TF8 is more computationally efficient than TF11, both representations are likely to be similarly accurate. Indeed this was seen in the *a priori* tests in Figures 8, 9 and 10, and suggests that TF8 is likely perform similarly to TF11 in forward simulations.

This is in fact verified by comparing the results in Figure 19 with those in Figure 19. The TF8 representation is requires a minimum of 25% added dissipation from the basic Smagorinsky model in (6.1) to be computationaly stable, though Figure 19(b)

shows it to also be only marginally stable at this level of added dissipation. With 30% added dissipation it is fully stable. At this level of added dissipation, the energy spectrum $E(k)$ in Figure 19(c) shows a roughly $k^{-5/3}$ inertial-range scaling over the entire range of resolved scales, and as seen for TF11 in Figure 18(c) the spectrum is only weakly affected as the level of added dissipation is increased.

6.2.3.4 TF5 representation

Figure 20 and Table 7 shows results from forward simulations with a fully dynamic implementation of autonomic closure based on the parametric TF5 representation for the subgrid stress. These simulations are stable even with no added dissipation, though in that case the kinetic energy spectrum $E(k)$ in Figure 20(c) shows a significant "bottleneck" at high wavenumbers. However, introducing just 10-15% added dissipation via c_{BS} in (6.1) removes most of this "bottleneck", and the resulting $E(k)$ in Figure 20(c) shows clear $k^{-5/3}$ inertial-range scaling over the entire range of resolved scales in the simulation. This is what the energy spectrum should look like from a large eddy simulation that properly transfers momentum and energy within the resolved scales and between the resolved and subgrid scales.

TF5 involves just five coefficients, and therefore solving the local system identification problem to determine these five coefficients at each point and time in the simulation is computationally efficient. As seen in Table 2, the run-time per time step in these forward simulations based on a fully dynamic implementation of autonomic closure with the TF5 representation for the subgrid stress is only slightly more than three times longer than for traditional closure with the dynamic Smagorinsky model.

Yet as discussed at the end of Section 6.2, comparing Figures 2-4 with Figures 8-11 shows that the TF5 representation produces far more accurate subgrid stress fields and subgrid production fields than does the dynamic Smagorinsky model. Furthermore, the TF5 representation in autonomic closure is seen in Figure 20 to require only a small amount of added dissipation from the basic Smagorinsky part in (6.1) to achieve

a good $E(k)$, whereas the dynamic Smagorinsky model in traditional closure is seen in Figure 13 to require at least 50% of the subgrid stress in (6.1) to come from the clearly inaccurate basic Smagorinsky model (see Figures 2-4). As a consequence, the difference in accuracy between traditional closure with the dynamic Smagorinsky model and fully dynamic autonomic closure with the TF5 representation, at the levels of added stabilization for each that are required for stable forward simulations, is even far larger than was seen in the *a priori* tests by comparing the dynamic Smagorinsky results in Figures 2-4 with the TF5 results in Figures 8-10. In simulations that require high accuracy in the resolved fields, the factor of three longer run-time per time step may be entirely acceptable to gain this substantially increased accuracy.

Lastly, note it is interesting that 30% added dissipation is needed for stability in the TF8 representation and 35% added dissipation is needed for the TF11 representation, but 0% is needed for the TF5 representation and just 5-10% appears to be needed for the TF19 representation. This could suggest that using higher-order velocity products, such as the 4th-order products in the TF8 representation and 5th-order products in the TF11 representation, may make subgrid stress representations more unstable, since the TF5 and TF19 representations involve only 2nd-order products of velocities.

Table 1. Stabilization Requirements for Each Subgrid Stress Representation

Subgrid Stress Representation	$(c_{BS})_{min}$ Required for Stability	$(c_{BS})_{min}$ Required for "Good" $E(k)$
Dynamic Smagorinsky	40%	50-55%
Bardina Scale Similarity	5%	25-50%
Static CL24	0%	5-10%
Dynamic TF27	20%	20-25%
Dynamic TF19	5%	10%
Dynamic TF11	35%	35%
Dynamic TF8	30%	30%
Dynamic TF5	0%	10-15%

Table 2. Run-time per Time Step

Subgrid Stress Method	Run-time per Time Step (s)
No Model	0.7
Basic Smagorinsky	0.9
Dynamic Smagorinsky	2.8
Bardina Scale Similarity	1.1
Static CL24	1.2
Dynamic TF27	150
Dynamic TF19	130
Dynamic TF11	45
Dynamic TF8	24
Dynamic TF5	9.5

Table 3. Computational Stability of TF27 Representation

BS Amount	Result	Blow-up Time
0%	Blow-up	$t = 0.47$
5%	Blow-up	$t = 0.72$
10%	Blow-up	$t = 0.81$
15%	Blow-up	$t = 1.40$
20%	Stable	$t \to \infty$
25%	Stable	$t \to \infty$
30%	Stable	$t \to \infty$
35%	Stable	$t \to \infty$
40%	Stable	$t \to \infty$
45%	Stable	$t \to \infty$
50%	Stable	$t \to \infty$

Table 4. Computational Stability of TF19 Representation

BS Amount	Result	Blow-up Time
0%	Blow-up	$t = 1.53$
5%	Stable	$t \to \infty$
10%	Stable	$t \to \infty$
15%	Stable	$t \to \infty$
20%	Stable	$t \to \infty$

Table 5. Computational Stability of TF11 Representation

BS Amount	Result	Blow-up Time
20%	Blow-up	$t = 0.47$
25%	Blow-up	$t = 1.14$
30%	Blow-up	$t = 13.0$
35%	Stable	$t \to \infty$
40%	Stable	$t \to \infty$
45%	Stable	$t \to \infty$

Table 6. Computational Stability of TF8 Representation

BS Amount	Result	Blow-up Time
0%	Blow-up	$t = 0.47$
5%	Blow-up	$t = 0.50$
10%	Blow-up	$t = 0.86$
15%	Blow-up	$t = 2.03$
20%	Blow-up	$t = 5.44$
25%	Blow-up	$t = 13.0$
30%	Stable	$t \to \infty$
35%	Stable	$t \to \infty$
40%	Stable	$t \to \infty$
45%	Stable	$t \to \infty$
50%	Stable	$t \to \infty$

Table 7. Computational Stability of TF5 Representation

BS Amount	Result	Blow-up Time
0%	Stable	$t \to \infty$
5%	Stable	$t \to \infty$
10%	Stable	$t \to \infty$
15%	Stable	$t \to \infty$

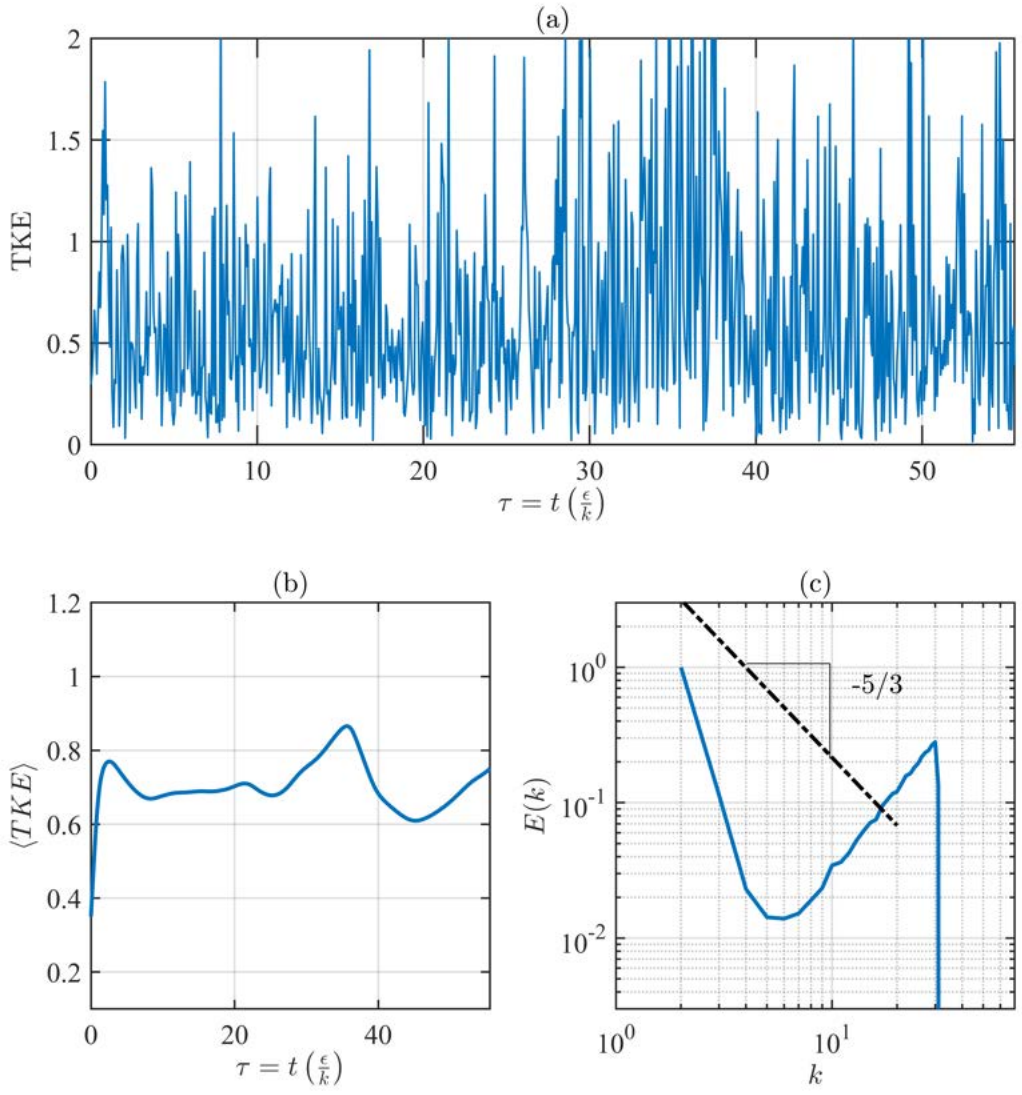

Figure 11. Results from forward simulations with no subgrid stress model, including (a) time evolution of turbulence kinetic energy at a single point in the domain, (b) time evolution of volume-averaged turbulence kinetic energy, and (c) energy spectrum.

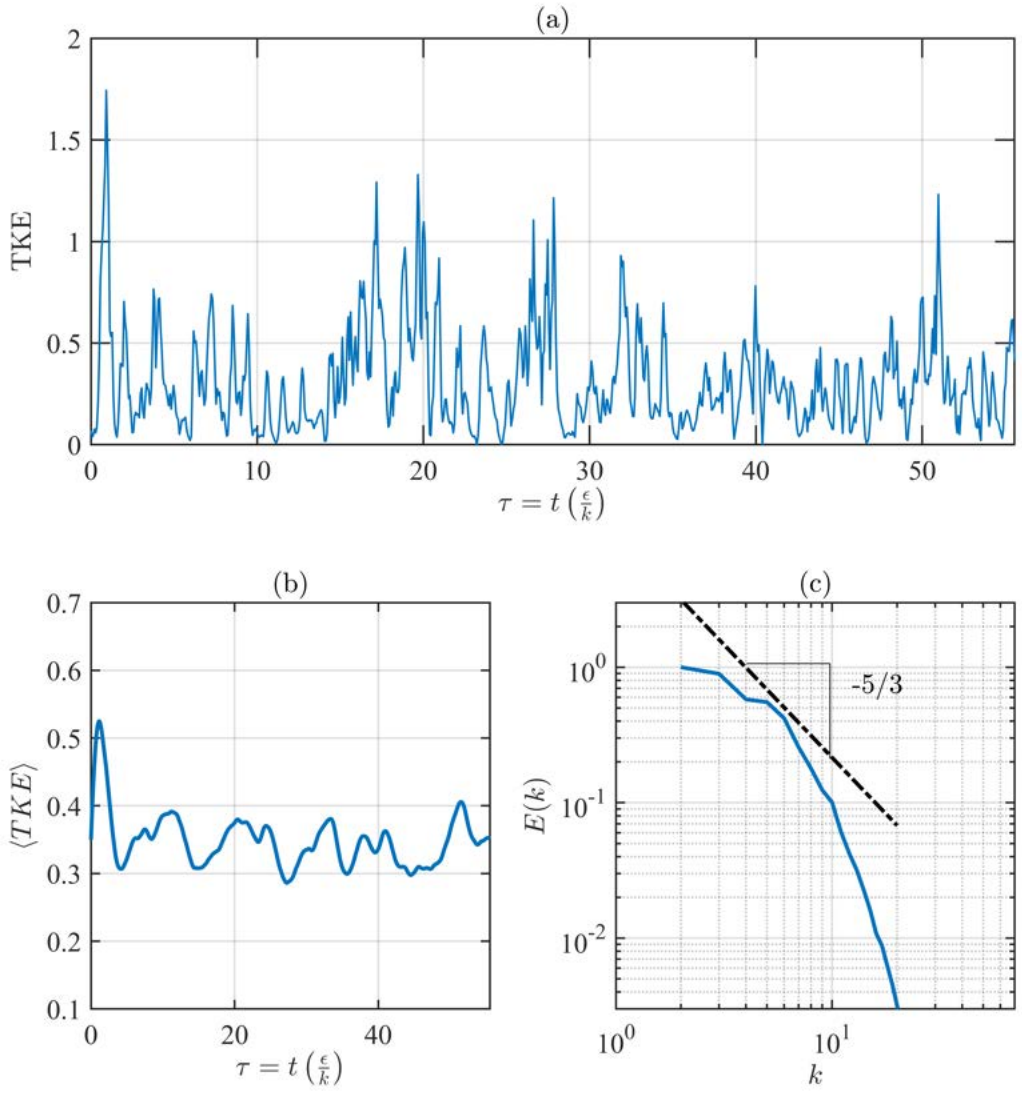

Figure 12. Results from forward simulations with the basic Smagorinsky model, including (a) time evolution of turbulence kinetic energy at a single point in the domain, (b) time evolution of volume-averaged turbulence kinetic energy, and (c) energy spectrum.

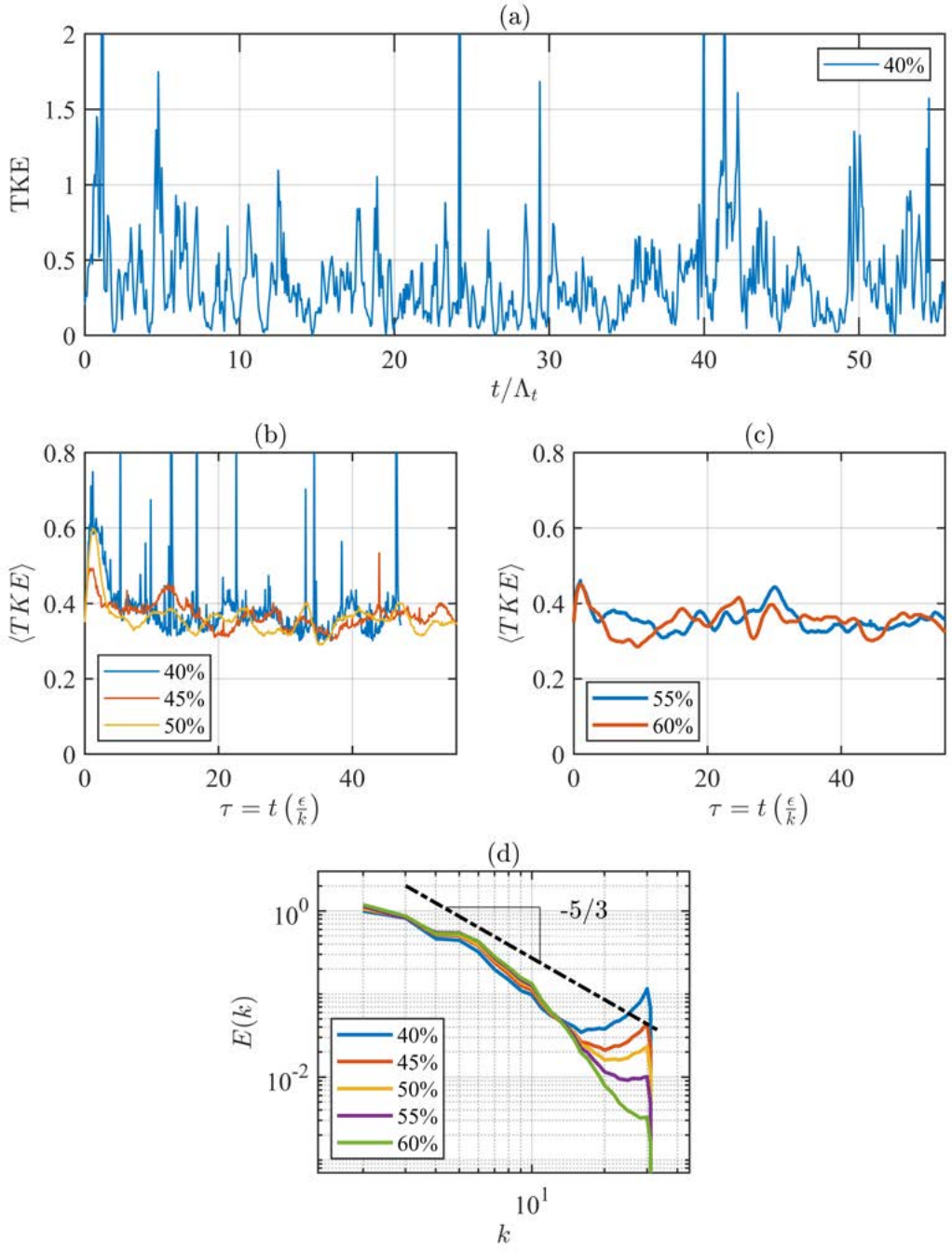

Figure 13. Results from forward simulations with the dynamic Smagorinsky model, including (a) time evolution of turbulence kinetic energy at a single point in the domain, (b) time evolution of volume-averaged turbulence kinetic energy, and (c) energy spectrum.

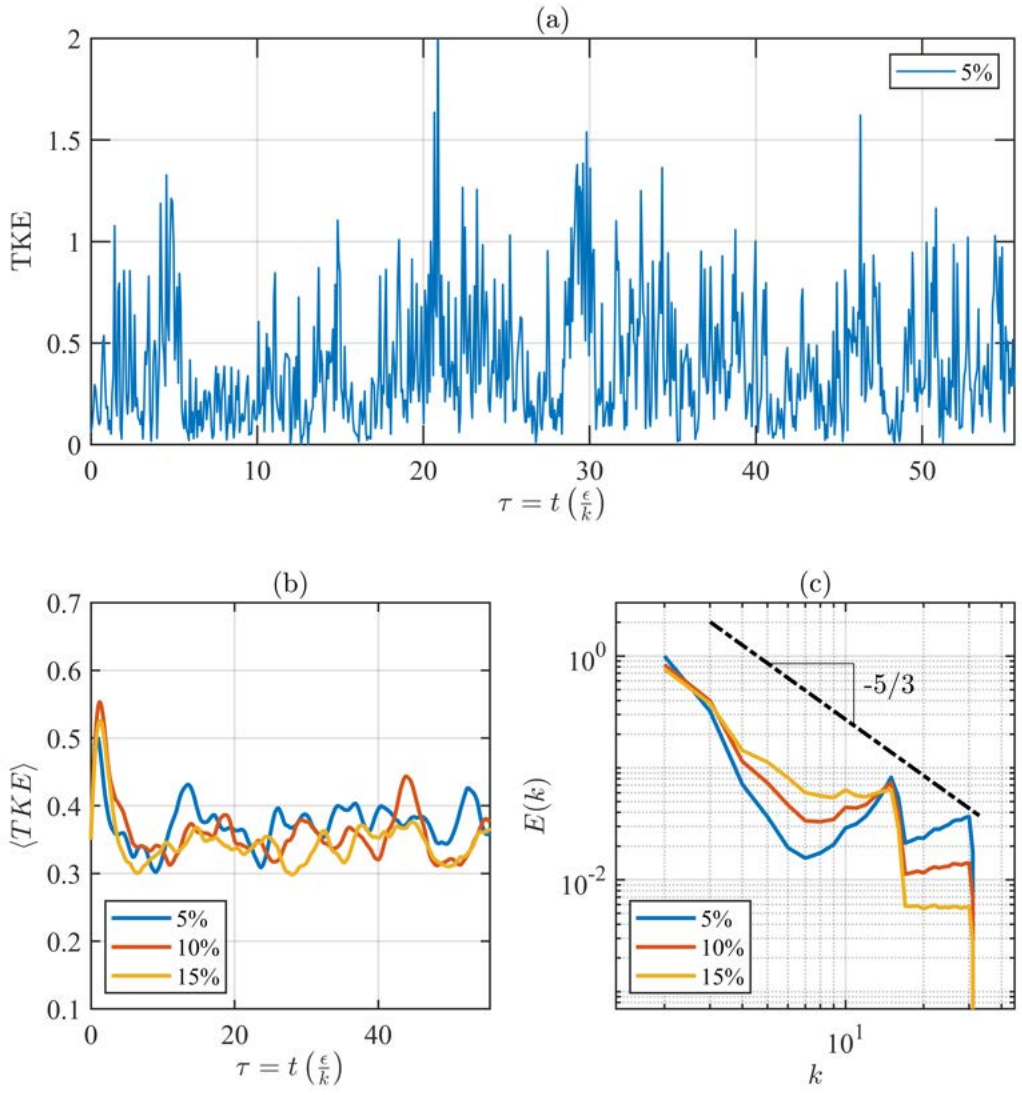

Figure 14. Results from forward simulations with the Bardina scale similarity model, including (a) time evolution of turbulence kinetic energy at a single point in the domain, (b) time evolution of volume-averaged turbulence kinetic energy, and (c) energy spectrum.

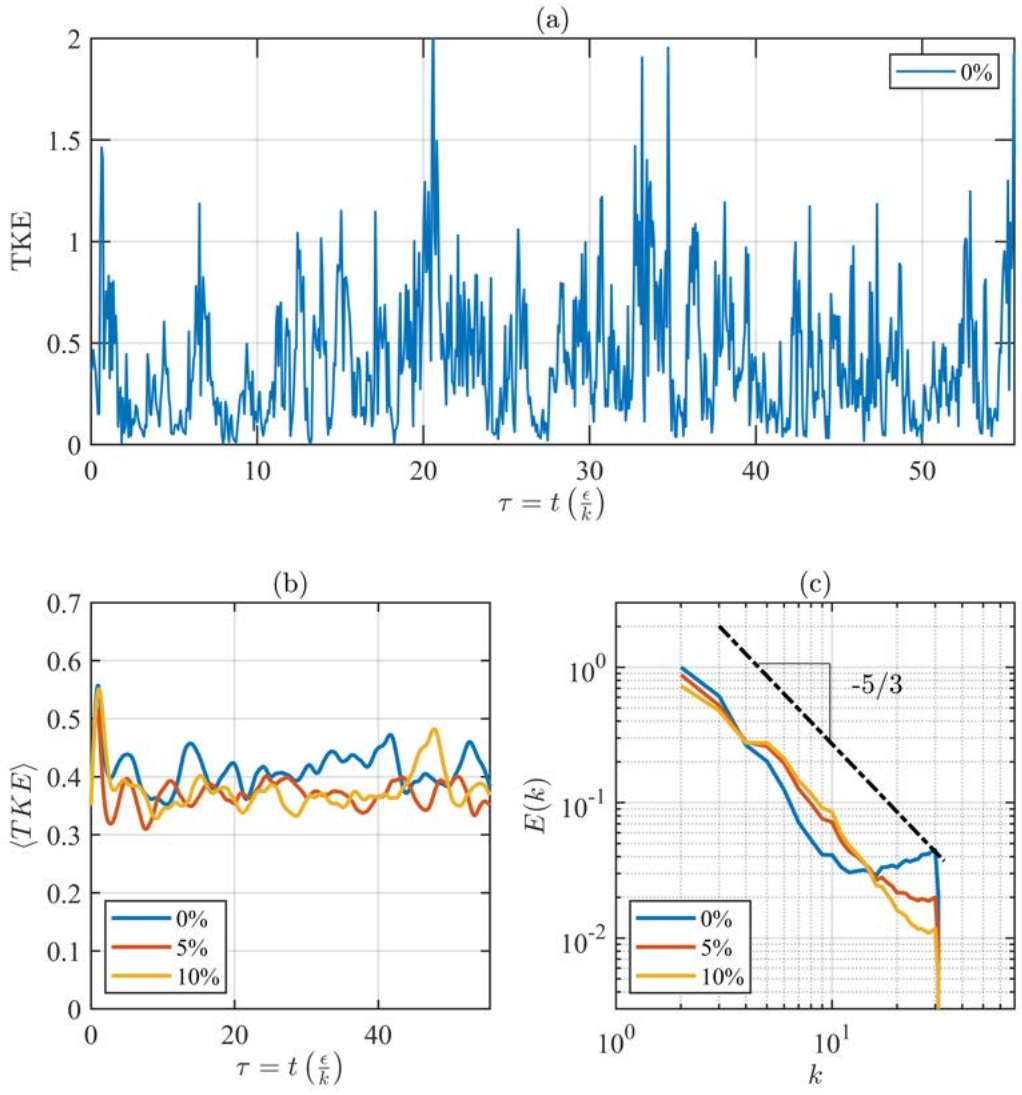

Figure 15. Results from forward simulations with static CL24, including (a) time evolution of turbulence kinetic energy at a single point in the domain, (b) time evolution of volume-averaged turbulence kinetic energy, and (c) energy spectrum.

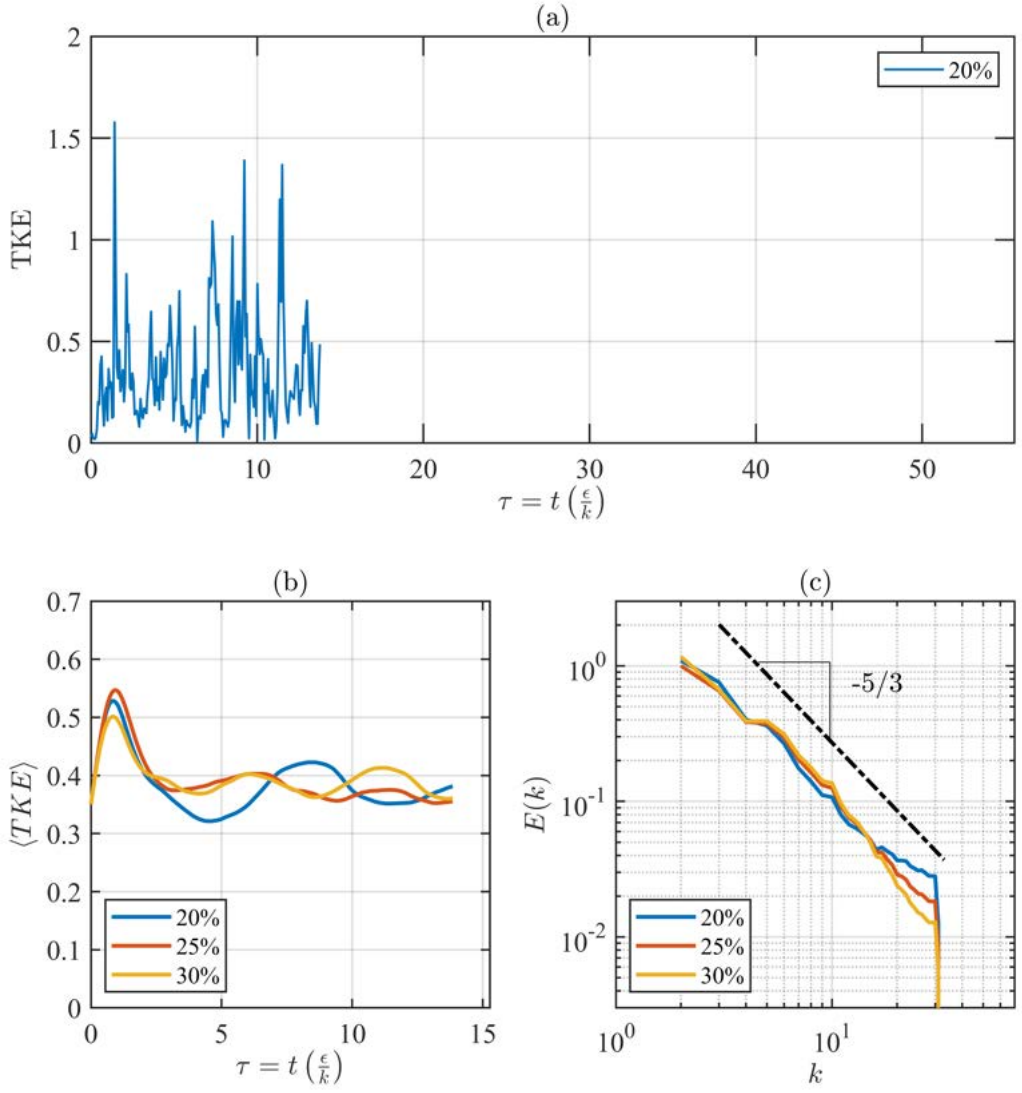

Figure 16. Results from forward simulations with TF27, including (a) time evolution of turbulence kinetic energy at a single point in the domain, (b) time evolution of volume-averaged turbulence kinetic energy, and (c) energy spectrum.

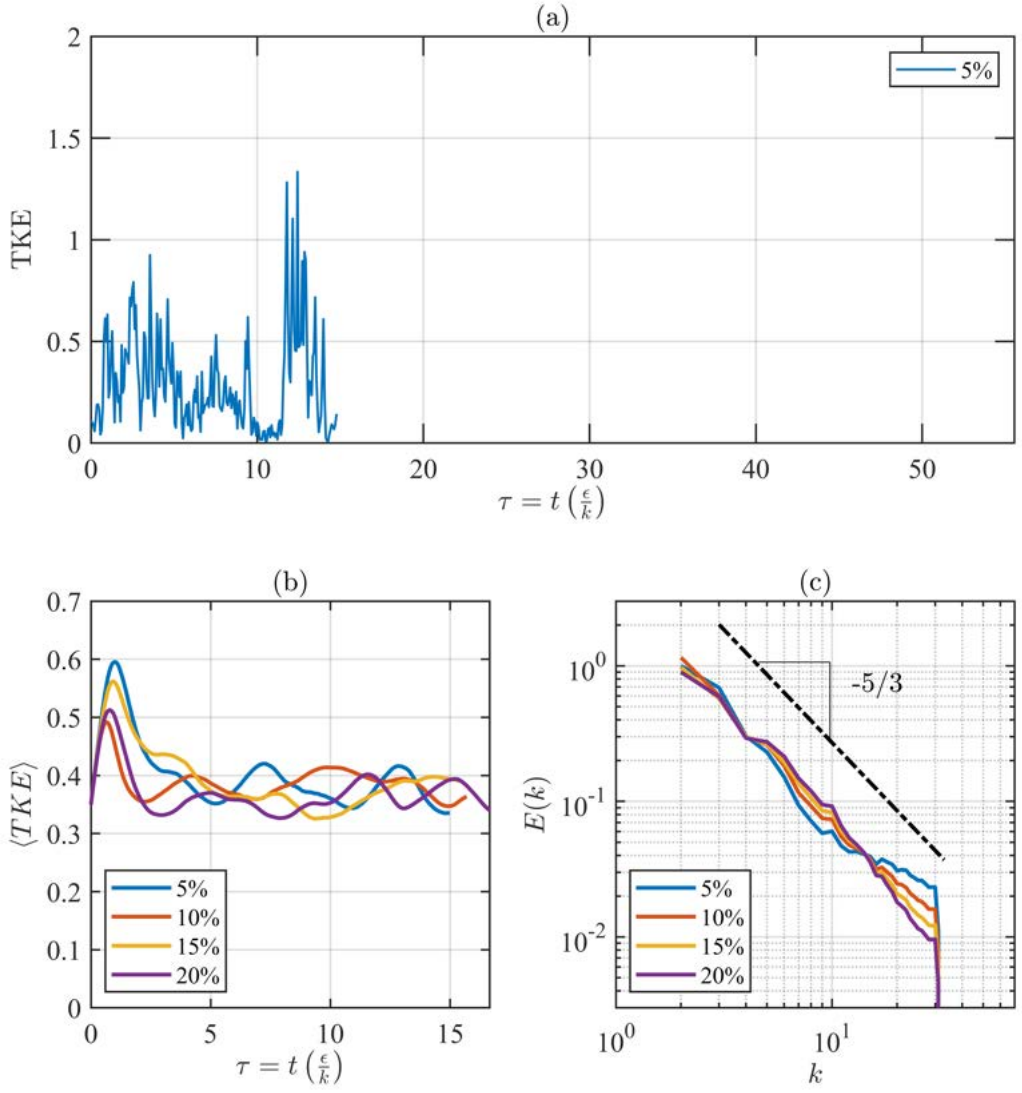

Figure 17. Results from forward simulations with TF19, including (a) time evolution of turbulence kinetic energy at a single point in the domain, (b) time evolution of volume-averaged turbulence kinetic energy, and (c) energy spectrum.

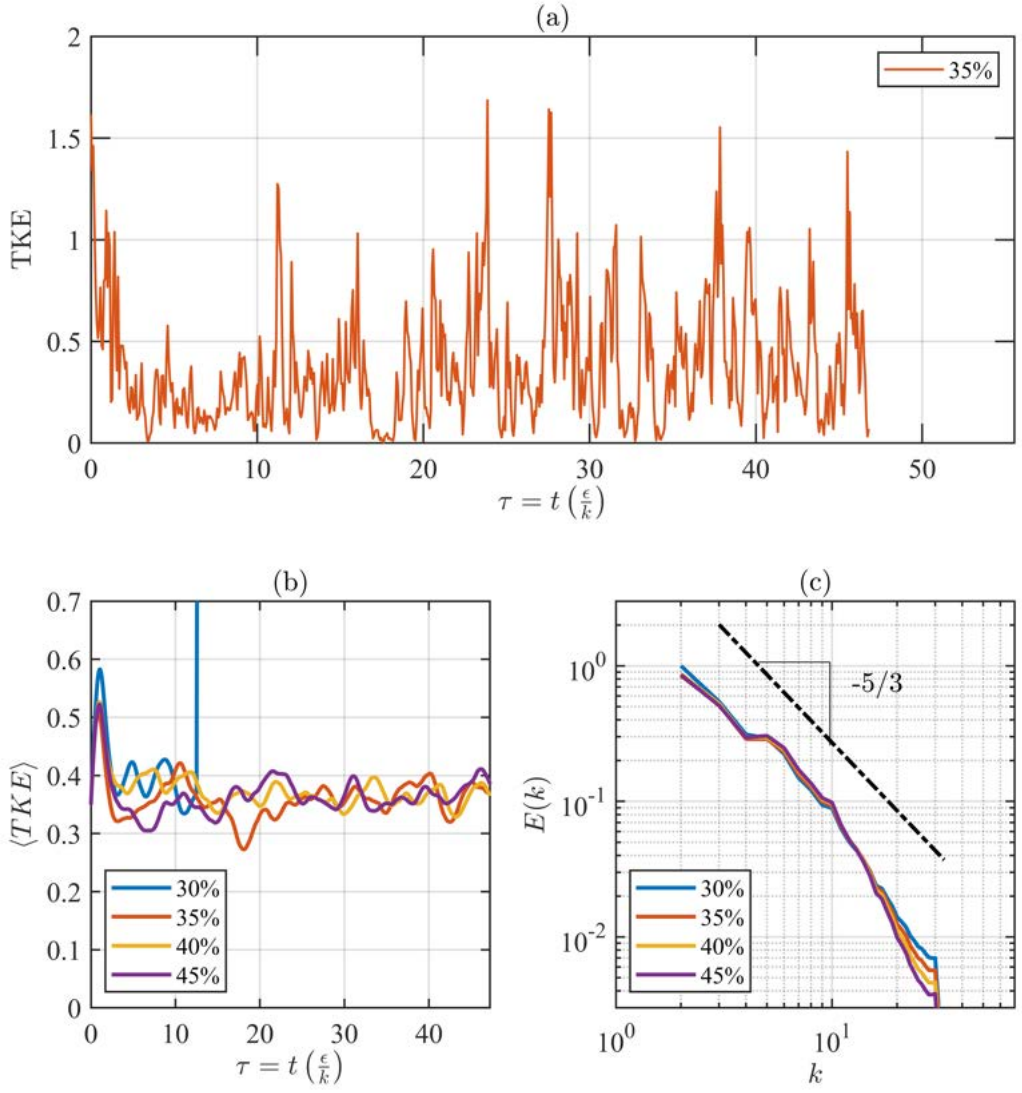

Figure 18. Results from forward simulations with TF11, including (a) time evolution of turbulence kinetic energy at a single point in the domain, (b) time evolution of volume-averaged turbulence kinetic energy, and (c) energy spectrum.

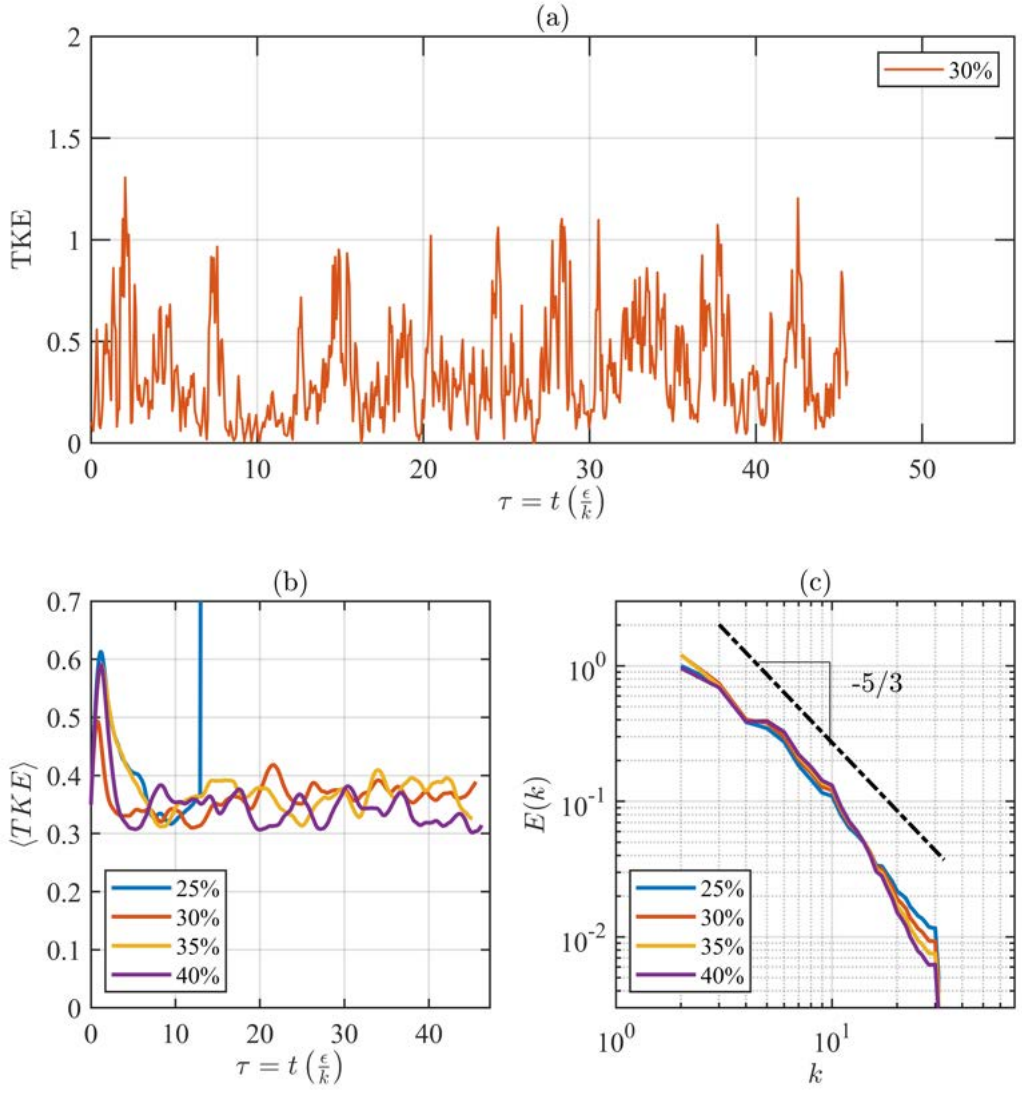

Figure 19. Results from forward simulations with TF8, including (a) time evolution of turbulence kinetic energy at a single point in the domain, (b) time evolution of volume-averaged turbulence kinetic energy, and (c) energy spectrum.

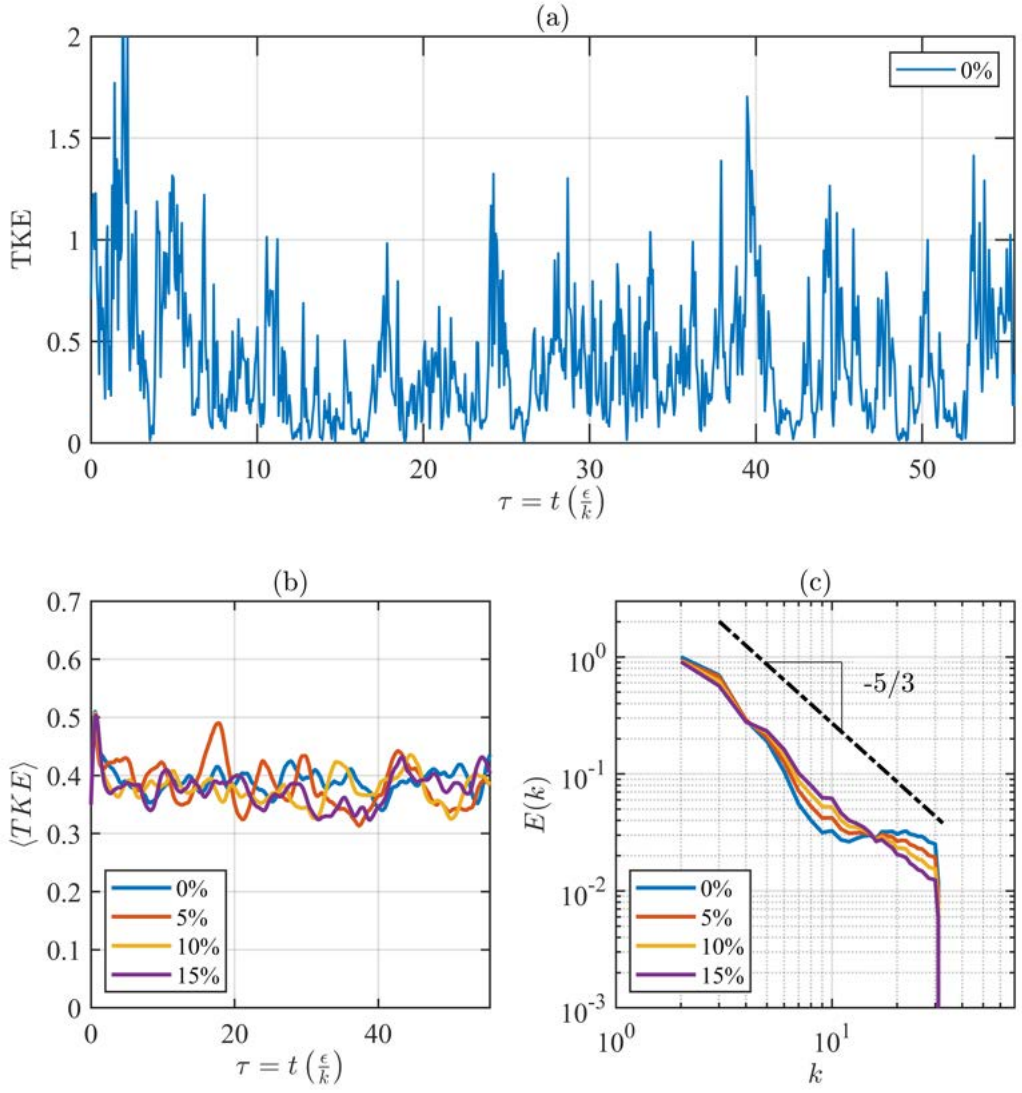

Figure 20. Results from forward simulations with TF5, including (a) time evolution of turbulence kinetic energy at a single point in the domain, (b) time evolution of volume-averaged turbulence kinetic energy, and (c) energy spectrum.

Chapter 7

A PRIORI TESTS: SUBGRID SCALAR FLUX REPRESENTATIONS

Analogous to the results from *a priori* tests presented in Chapter 5 to assess the accuracy of subgrid stress representations, here corresponding results are presented to assess the accuracy of subgrid scalar flux representations. Such *a priori* tests are the most direct way to determine the *accuracy* of any representation. Forward simulations to assess their computational stability are presented in Chapter 8.

The subgrid scalar flux representations in this chapter include prescribed models of the type used in traditional closure, and nonparametric and parametric representations for use in autonomic closure. Nonparametric subgrid scalar flux representations are expressed directly in the velocities $\mathbf{u}$ and scalar values φ on the stencil $\widehat{\mathbf{S}}$ at the test-filter scale $\widehat{\Delta}$, and on the stencil $\widetilde{\mathbf{S}}$ at the LES-filter scale $\widetilde{\Delta}$. Parametric representations are formulated in quantities that can be obtained from these velocities and scalar values on these stencils, including the strain rate tensor S_{ij} and rotation rate tensor R_{ij}, and the scalar gradient vector $\partial\varphi/\partial x_i$. Tensorally-correct parametric representations can provide as much tensorally-valid information as a nonparametric representation, but with substantially fewer terms in the representation and thus with fewer coefficients that must be determined via solution of the local system identification problem. This can make tensorally-correct parametric representations more computationally efficient, but this chapter first seeks to determine how the accuracy of such representations compares to nonparametric representations and traditional prescribed models.

7.1 Prescribed Models for Traditional Closure

The prescribed models for the subgrid scalar flux $z_i = \widetilde{u_i\,\varphi} - \widetilde{u}_i\,\widetilde{\varphi}$ that are considered in this chapter, and in the forward simulations in Chapter 8, include a basic Smagorinsky model, a dynamic Smagorinsky, and a Bardina scale similarity model.

Each of these is developed through direct analogy with the corresponding prescribed model for the subgrid stress in Section 5.1.1, as described below.

7.1.1 Basic Smagorinsky Model

For the subgrid scalar flux, the corresponding basic Smagorinsky model is also a linear eddy-viscosity model based on the gradient transport hypothesis, and thus relates the subgrid scalar flux to the scalar gradient as

$$z_i = -\nu_{sgf} \frac{\partial \widetilde{\varphi}}{\partial x_i} \tag{7.1}$$

where ν_{sgf} is assumed to depend only on the LES-filter length scale $\widetilde{\Delta}$ and the local strain rate magnitude $|\widetilde{S}| = (\widetilde{S}_{ij}\widetilde{S}_{ij})^{1/2}$. Thus on dimensional grounds $\nu_{sgf} = C_Z \widetilde{\Delta}^2 |\widetilde{S}|$, where C_Z is the Smagorinski constant for the subgrid scalar flux, and thus the representation for the subgrid scalar flux is

$$z_i = -C_Z \, \widetilde{\Delta}^2 \, |\widetilde{S}| \, \frac{\partial \widetilde{\varphi}}{\partial x_i} \,, \tag{7.2}$$

or equivalently in tensor notation

$$\mathbf{z} = -C_Z \, \widetilde{\Delta}^2 \, |\widetilde{S}| \, \nabla \varphi \,. \tag{7.3}$$

The value of C_Z is typically chosen based on an average of values that best match commonly used reference cases. The present study uses $C_Z = 0.173$.

The subgrid production of resolved scalar energy in (1.13) is $\Pi = \mathbf{z} \cdot \nabla \varphi$, and from (7.3) this gives

$$\Pi = -C_Z \, \widetilde{\Delta}^2 \, |\widetilde{S}| \, (\nabla \varphi \cdot \nabla \varphi) \,, \tag{7.4}$$

which for $C_Z > 0$ is always *negative*, and thus in (1.12) acts to *reduce* the scalar energy in the resolved scales of the simulation. As a result, the basic Smagorinsky model for z_i is purely *dissipative*, and consequently it is manifestly stable in forward simulations. For that reason, it is often combined with unstable subgrid scalar flux representations to provide additional dissipation to achieve stability in forward runs.

7.1.2 Dynamic Smagorinsky Model

The dynamic Smagorinsky model for the subgrid scalar flux is derived from the basic Smagorinsky model in (7.2), but allows the C_Z value to vary in such a way that it can take on locally positive or negative values in the simulation, thereby producing positive and negative values of Π in (7.4). It first defines

$$Z_i = \widehat{\widetilde{u}_i \widetilde{\varphi}} - \widehat{\widetilde{u}}_i \widehat{\widetilde{\varphi}}, \tag{7.5}$$

via a test filter scale $\widehat{(\ )}$ having length scale $\widehat{\Delta}$, analogous to

$$z_i \equiv \widetilde{u_i \varphi} - \widetilde{u}_i \widetilde{\varphi} \tag{7.6}$$

at the LES-filter scale $\widetilde{(\ )}$ having length scale $\widetilde{\Delta}$. It then represents both z_i and Z_i with the basic Smagorinsky model in (7.2) as

$$z_i = -C_Z \widetilde{\Delta}^2 |\widetilde{S}| \frac{\partial \widetilde{\varphi}}{\partial x_i} \tag{7.7}$$

and

$$Z_i = -C_Z \widehat{\Delta}^2 |\widehat{\widetilde{S}}| \frac{\partial \widehat{\widetilde{\varphi}}}{\partial x_i}. \tag{7.8}$$

Applying the test filter $\widehat{(\ )}$ to z_i gives

$$\widehat{z_i} = -C_Z \widetilde{\Delta}^2 \widehat{|\widetilde{S}| \frac{\partial \widetilde{\varphi}}{\partial x_i}}. \tag{7.9}$$

Subtracting (7.9) from (7.8) gives

$$L_i \equiv Z_i - \widehat{z_i} = C_Z M_i \tag{7.10}$$

where

$$M_i \equiv \widetilde{\Delta}^2 \widehat{|\widetilde{S}| \frac{\partial \widetilde{\varphi}}{\partial x_i}} - \widehat{\Delta}^2 |\widehat{\widetilde{S}}| \frac{\partial \widehat{\widetilde{\varphi}}}{\partial x_i}. \tag{7.11}$$

Contracting (7.10) with M_i and dividing then gives

$$C_Z = \frac{L_i M_i}{M_k M_k} \tag{7.12}$$

The resulting C_Z from (7.12) can be positive or negative, and is then used in (7.2) to determine the local value of the subgrid scalar flux. Since C_Z can be positive or negative, the resulting subgrid production Π in (7.4) can also be positive or negative.

7.1.3 Bardina Scale Similarity Model

The Bardina scale similarity model for the subgrid scalar flux applies a test filter $\widehat{(\,)}$ having length scale $\widehat{\Delta}$ to the LES-filtered velocities $\widetilde{u}_i$ and scalar values $\widetilde{\varphi}$ to define a test scalar flux

$$Z_i = \widehat{\widetilde{u}_i\,\widetilde{\varphi}} - \widehat{\widetilde{u}}_i\,\widehat{\widetilde{\varphi}}\,. \tag{7.13}$$

It then takes the local subgrid scalar flux to be directly proportional to the local test scalar flux, namely

$$z_i = C_B Z_i\,. \tag{7.14}$$

The constant C_B is typically chosen based on an average of values that best match commonly used reference cases. The present study uses $C_B = 0.45$.

7.2 Nonparametric Representations for Autonomic Closure

Nonparametric representations are formulated in the resolved primitive variables of the simulation, and thus for the subgrid scalar flux $\mathbf{z}$ are written in the resolved velocities $\mathbf{u}$ and scalar values φ. Section 3.2 applied the complete and minimal tensor representation of Smith (1971) [63] to develop three nonparametric representations for the subgrid scalar flux.

7.2.1 VF27a Representation

Section 3.2.3 developed an *ad hoc* 27-term representation in the velocities $\mathbf{u}$ and scalar values φ on a $3 \times 3 \times 3$ stencil centered on $\mathbf{x}$ as

$$\mathbf{z} = h_0\,\mathbf{I_v} + \sum_{m=1}^{27} h_m\,\mathbf{u}_m\,\varphi\,. \tag{7.15}$$

7.2.2 VF27b Representation

Section 3.2.2 developed another 27-term representation in the velocities $\mathbf{u}$ on a $3 \times 3 \times 3$ stencil centered on $\mathbf{x}$, together with the scalar gradient $\nabla\varphi$ at $\mathbf{x}$, as

$$\mathbf{z} = h_0\mathbf{I_v} + \sum_{m=1}^{27} h_m(\mathbf{u}_m \otimes \mathbf{u}_m)\nabla\varphi\,, \tag{7.16}$$

where $\otimes$ is the outer product in (3.34).

7.2.3 VF54 Representation

Section 3.2.4 developed a 54-term representation from VF27a and VF27b for use on a $3 \times 3 \times 3$ stencil centered on $\mathbf{x}$ as

$$\mathbf{z} = h_0 \mathbf{I}_v + \sum_{m=1}^{P=27} \left(h_m \mathbf{u}_m \, \varphi + h_{m+27} \left(\mathbf{u}_m \otimes \mathbf{u}_m \right) \nabla \varphi \right) . \tag{7.17}$$

7.3 Parametric Representations for Autonomic Closure

Parametric representations are formulated in derived quantities that can be evaluated from the resolved variables in the simulation. For the subgrid scalar flux $\mathbf{z}$, these include the strain rate and rotation rate tensors $\mathbf{S}$ and $\mathbf{R}$, and the scalar gradient vector $\nabla \varphi$. Results from only one parametric representation for the subgrid scalar flux are presented in this chapter.

7.3.1 VF6 Representation

Section 3.2 shows how the tensor representation theory of Smith (1971) [63] leads to the complete and minimal tensorally-corrrect representation parametric representation for the subgrid scalar flux $\mathbf{z}$ in $\mathbf{S}$, $\mathbf{R}$, and $\nabla \varphi$ as

$$\mathbf{z} = h_0 \, \nabla \varphi + h_1 \, \mathbf{S} \nabla \varphi + h_2 \, \mathbf{S}^2 \nabla \varphi + h_3 \, \mathbf{R} \nabla \varphi + h_4 \, \mathbf{R}^2 \nabla \varphi + h_5 \left(\mathbf{SR} - \mathbf{RS} \right) \nabla \varphi \tag{7.18}$$

In addition to being tensorally-correct, despite being complete this scalar flux representation involves only six coefficients.

7.4 Metrics for Assessing Accuracy in *A Priori* Tests

In analyzing results from *a priori* tests there is a need for more precise and useful means of quantifying accuracy beyond just average values and statistical distributions. For example, Figures 2-10 from such tests of the subgrid stress show obvious structural similarities in fields such as the subgrid production $P(\mathbf{x}, t)$, even in many of the detailed features of these fields, including regions where large positive and negative

values are concentrated. Yet point-by-point differences between two apparently highly similar fields are large, due to the high intermittency in these fields. This led prior work [61] to develop metrics $\mathcal{M}_1$ and $\mathcal{M}_2$ based on the structure of the spatial support on which large production magnitudes are concentrated.

The support of a field is the subset of the domain on which the field values are substantially non-zero. Following [61], the support on which large magnitudes of production are concentrated is defined by thresholding the absolute value of the field at a fixed fraction γ of its *rms*. This defines the support field $\Sigma(\mathbf{x}, t)$ that is either zero or one, depending on whether the absolute value of the production is below or above the threshold. Thus points where $\Sigma = 1$ are on the support of large production magnitudes.

The support field can be separated into different scales to allow scale-by-scale comparison. From the support $\Sigma(\mathbf{x}, t)$, a corresponding support-density field $G(\mathbf{x}, t)$ is defined as

$$G(\mathbf{x}, t) \equiv \int_V \Sigma(\mathbf{x}', t)\Gamma_\Delta(|\mathbf{x} - \mathbf{x}'|)\mathbf{x}', \tag{7.19}$$

where $\Gamma_\Delta(|\mathbf{x} - \mathbf{x}'|)$ is a convolution filter kernel with filter length scale Δ_Γ. Standard Gaussian filters are used for Γ_Δ in (7.19). Whereas the support $\Sigma(\mathbf{x}, t)$ is a discontinuous binary-valued field, the support-density $G(\mathbf{x}, t)$ is a continuous real-valued field to which standard error measures can be applied. These G fields can be used to accurately identify the locations, sizes, and shapes of the regions in which large subgrid values are concentrated.

Successive filter length scales Δ_Γ in (7.19) allow scale-dependent structure in the support-density fields to be determined. Comparisons at the same filter scale between true support-density fields G^F and those obtained from the subgrid model allow for quantitative assessment of the accuracy at any given scale in the field. Using successive filter length scales allows for the creation of two metrics used to quantitatively compare

spatial structure. At any scale-ratio $\Delta_\Gamma/\widetilde{\Delta}$ these metrics are defined as

$$\mathcal{M}_1 \equiv \frac{\langle G'(\mathbf{x},t)G'^F(\mathbf{x},t)\rangle_V}{\langle G'(\mathbf{x},t)\rangle_V^{1/2}\langle G'^F(\mathbf{x},t)\rangle_V^{1/2}} \quad \text{and} \quad \mathcal{M}_2 \equiv \sqrt{\frac{\langle\big[G(\mathbf{x},t)-G^F(\mathbf{x},t)\big]^2\rangle_V}{\langle\big[G(\mathbf{x},t)\big]^2\rangle_V}} \tag{7.20}$$

where $\mathcal{M}_1$ is the correlation between the modeled fields $G(\mathbf{x},t)$ and the true fields $G^F(\mathbf{x},t)$, and $\mathcal{M}_2$ is the normalized *rms* difference between the two. Note $\mathcal{M}_1 \to 1$ as the two support-density fields become perfectly correlated, and $\mathcal{M}_2 \to 0$ as the two support-density fields become identical. The changes in these metrics with the scale-ratio allow quantitative comparisons of the support-density fields.

7.5 Comparisons of *A Priori* Test Results

A priori tests determine the accuracy of $\mathbf{z}(\mathbf{x},t)$ fields and their associated production fields $\Pi(\mathbf{x},t)$ for any subgrid scalar flux representation. Such tests allow direct comparisons of the fields produced by the subgrid scalar flux representation and the corresponding exact fields. While such tests do not address the computational stability of these representations – that is addressed via forward simulations in Chapter 8 – they provide complete information on the accuracy of such representations.

Such *a priori* tests were conducted with the three prescribed models for traditional closure in Section 7.1, with the three representations for autonomic closure in Section 7.2, and with the tensorally-correct complete and minimal representation for autonomic closure in Section 7.3. Direct numerical simulation (DNS) data from two simulations of conserved scalar mixing in homogeneous isotropic turbulence were used to these tests. The first, provided by Professor P.K. Yeung, was generated with a pseudo-spectral DNS code [78] at $Re_\lambda = 140$ and $Sc = 1$, and is referred to herein as the high-Re dataset. The first, provided by by Dr. Colin Towery, was generated with the Athena-RFX DNS code [79, 80] at $Re_\lambda = 35$ and $Sc = 1$, and is referred to herein as the low-Re dataset.

As described in Section 2.4 and Chapter 4, coefficients in the autonomic closure methodology must be rescaled from the test-filter scale to the LES-filter scale based

on scale similarity and inertial-range scaling. This suggests that both the LES-filter and test-filter length scales, $\widetilde{\Delta}$ and $\widehat{\Delta}$, must be in the inertial scale-range to achieve accurate results from autonomic closure. However, it is unclear how strongly the resulting accuracy will degrade one or both filter scales enters the dissipation scale-range. The high-*Re* and low-*Re* datasets allow this to be tested, by choosing the corresponding spectrally-sharp cutoff wavenumbers $k_{\widetilde{\Delta}}$ and $k_{\widehat{\Delta}}$ as shown in Tables 8 and 9. Based on the kinetic energy spectra $E(k)$ and scalar energy spectra $E_\varphi(k)$ for the two datasets in Figure 21, for each case these Tables note whether both cutoff wavenumbers are in the inertial range, (Inertial), one is in the inertial range and one in the dissipative range (Transitional), or both are in the dissipative range (Dissipative).

Results from these *a priori* tests of the subgrid scalar flux representations from the high-*Re* dataset are shown in Figures 22-40, and from the low-*Re* dataset are shown in Figures 58-71. For each subgrid scalar flux representation, the results from these *a priori* tests include *(i)* comparisons of typical planes from subgrid scalar flux fields $z_i(\mathbf{x}, t)$ and subgrid scalar energy production fields $\Pi(\mathbf{x}, t)$, *(ii)* comparisons of probability density functions for each field from each representation, and *(iii)* subgrid production support density fields $G(\mathbf{x}, t)$ and metrics $\mathcal{M}_1$ and $\mathcal{M}_2$ obtained from them for each field from each representation.

Moreover for each of these subgrid scalar flux representations, the forward simulations in Chapter 8 determine the minimum added scalar dissipation that is needed for a computational stable simulation. Accordingly, the probability density functions in Figures 25-41 and the metrics $\mathcal{M}_1$ and $\mathcal{M}_2$ in Figures 42-57 for each field from each representation show results *without* and *with* this minimum added dissipation. In so doing, these results show the accuracy that is achieved with each representation by itself and when it is implemented with the minimum added dissipation in a forward simulation.

In these results, it can be seen in the high-Re cases that the tensorally correct,

complete, and minimal VF6 representation performs best among all the generalized representations for autonomic closure, far outperforming the dynamic Smagorinsky model and showing some improvement over the Bardina scale similarity model. The traditional models interestingly seem to perform better for the subgrid scalar flux here than they did for the subgrid stress in Chapter 3, relative to the respective true fluxes and stresses.

Comparing results for the various cutoff wavenumbers $(k_{\widehat{\Delta}}, k_{\widetilde{\Delta}})$ in Tables 8 and 9 reveals that, except for the $(30, 60)$ and $(5, 10)$ cases in the high-Re dataset, all other cases appear to be about equally accurate. Regarding the $(30, 60)$ case, both these cutoff wavenumbers can be seen in Figure 37 to clearly be in the dissipative range, so the inertial-range rescaling of the coefficients in autonomic closure is expected to fail. Regarding the $(5, 10)$ case, energy input in the high-Re simulations was via forcing at $k = 2$ and 3, so based on Figure 22 the test filter at $k = 5$ was potentially contaminated by this forcing, leading to inaccurate results.

Comparing the probability density functions for the subgrid scalar energy production Π shows that the VF6 representation accurately represents scalar energy transfer from the resolved scales into the subgrid scale, called "forward scatter", but that it produces excessive "backscatter" of scalar energy from the subgrid scales into the resolved scales. Figures 31 and 36 for $(k_{\widetilde{\Delta}}, k_{\widehat{\Delta}})$ = (20,10) and (40,20), respectively, are of particular importance in this regard. They show that, with and without the minimum added dissipation needed for stable forward simulations, the Bardina scale similarity model is generally about as accurate in representing the subgrid scalar energy production Π as is the VF6 representation, and both these representations are far more accurate than the basic or dynamic Smagorinsky models.

Results for support density fields are shown in Figures 42-49, and for the corresponding support-density metrics $\mathcal{M}_1$ and $\mathcal{M}_2$ in Figures 50-57. These are largely consistent with what is seen in the $z_i(\mathbf{x}, t)$ and $\Pi(\mathbf{x}, t)$ fields and in the probability

density functions resulting from them. The VF6 representation for autonomic closure performs best in producing the correct spatial structure in subgrid scalar energy production $\Pi(\mathbf{x}, t)$ across all scales. It is somewhat more accurate in this regard than the Bardina scale similarity model, and far more accurate than the basic or dynamic Smagorinsky models.

Results from the low-Re data are not as useful as those from the high-Re dataset, since the low-Re nature of that simulation leads to only a very limited inertial range. However those results do generally confirm and support the observations from the high-Re dataset that the VF6 representation is the most accurate in representing the subgrid scalar fields $z_i(\mathbf{x}, t)$ and subgrid scalar energy production fields $\Pi(\mathbf{x}, t)$ among all the representations considered in these *a priori* tests.

Test and LES Filter Lengths	$E(k)$ from High-Re Data	$E_\varphi(k)$ from High-Re Data
$(k_{\widehat{\Delta}},k_{\widetilde{\Delta}}) = (5,10)$	Inertial	Inertial
$(k_{\widehat{\Delta}},k_{\widetilde{\Delta}}) = (10,20)$	Transition	Inertial
$(k_{\widehat{\Delta}},k_{\widetilde{\Delta}}) = (20,40)$	Dissipative	Transition
$(k_{\widehat{\Delta}},k_{\widetilde{\Delta}}) = (30,60)$	Dissipative	Dissipative

Table 8. Spectral ranges in the kinetic energy spectrum $E(k)$ and scalar energy spectrum $E_\varphi(k)$ where wavenumbers corresponding to test-scale ($\widehat{\Delta}$) and LES-scale ($\widetilde{\Delta}$) filters are located for the high-Re DNS dataset.

Test and LES Filter Lengths	$E(k)$ from Low-Re Data	$E_\varphi(k)$ from Low-Re Data
$(k_{\widehat{\Delta}},k_{\widetilde{\Delta}}) = (5,10)$	Transition	Inertial
$(k_{\widehat{\Delta}},k_{\widetilde{\Delta}}) = (10,20)$	Dissipative	Dissipative
$(k_{\widehat{\Delta}},k_{\widetilde{\Delta}}) = (20,40)$	Dissipative	Dissipative

Table 9. Spectral ranges in the kinetic energy spectrum $E(k)$ and scalar energy spectrum $E_\varphi(k)$ where wavenumbers corresponding to test-scale ($\widehat{\Delta}$) and LES-scale ($\widetilde{\Delta}$) filters are located for the high-Re DNS dataset.

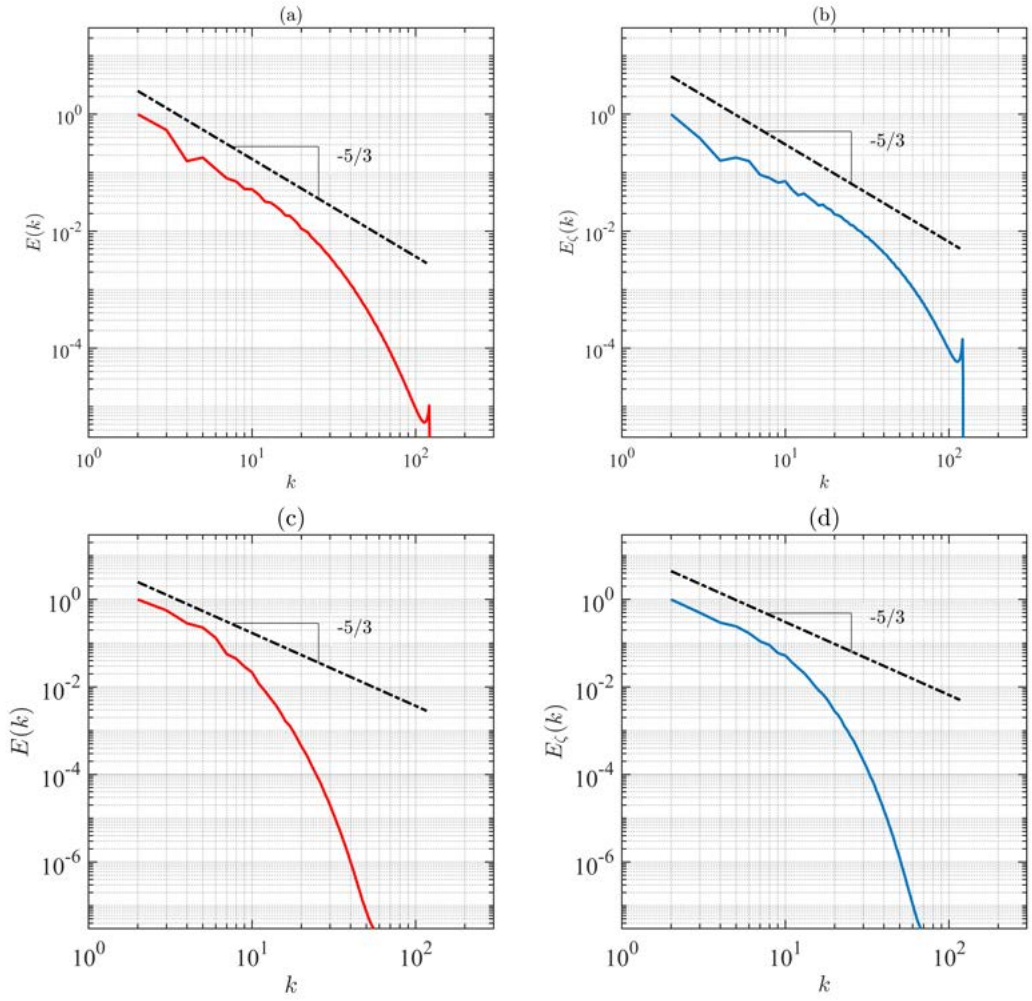

Figure 21. Kinetic energy spectra $E(k)$ *(left column)* and scalar energy spectra $E_\varphi(k)$ *(right column)* from high-Re DNS dataset *(upper row)* and low-Re DNS dataset *(lower row)*.

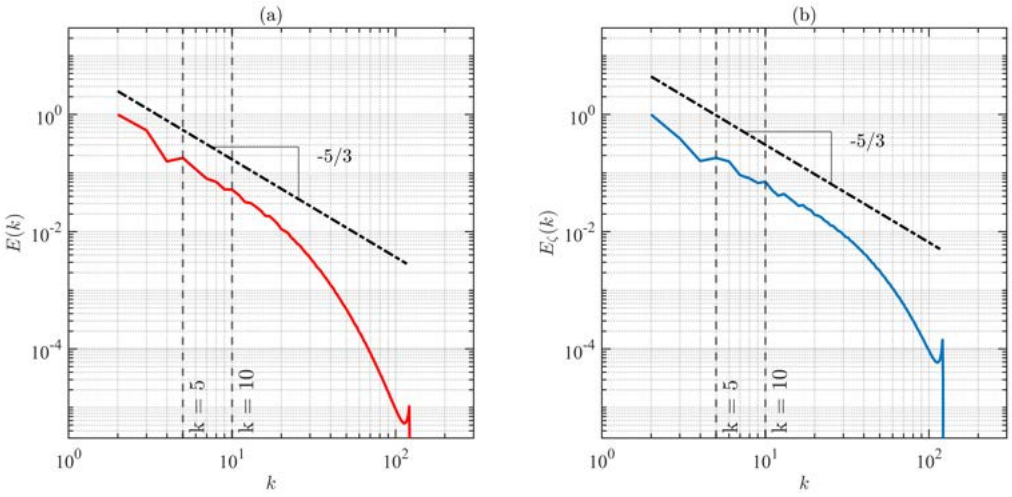

Figure 22. Locations of test-scale and LES-scale filters for $(k_{\widehat{\Delta}}, k_{\widetilde{\Delta}}) = (5, 10)$ in kinetic energy spectrum $E(k)$ (left) and scalar energy spectrum $E_\varphi(k)$ (right) from the high-Re DNS dataset.

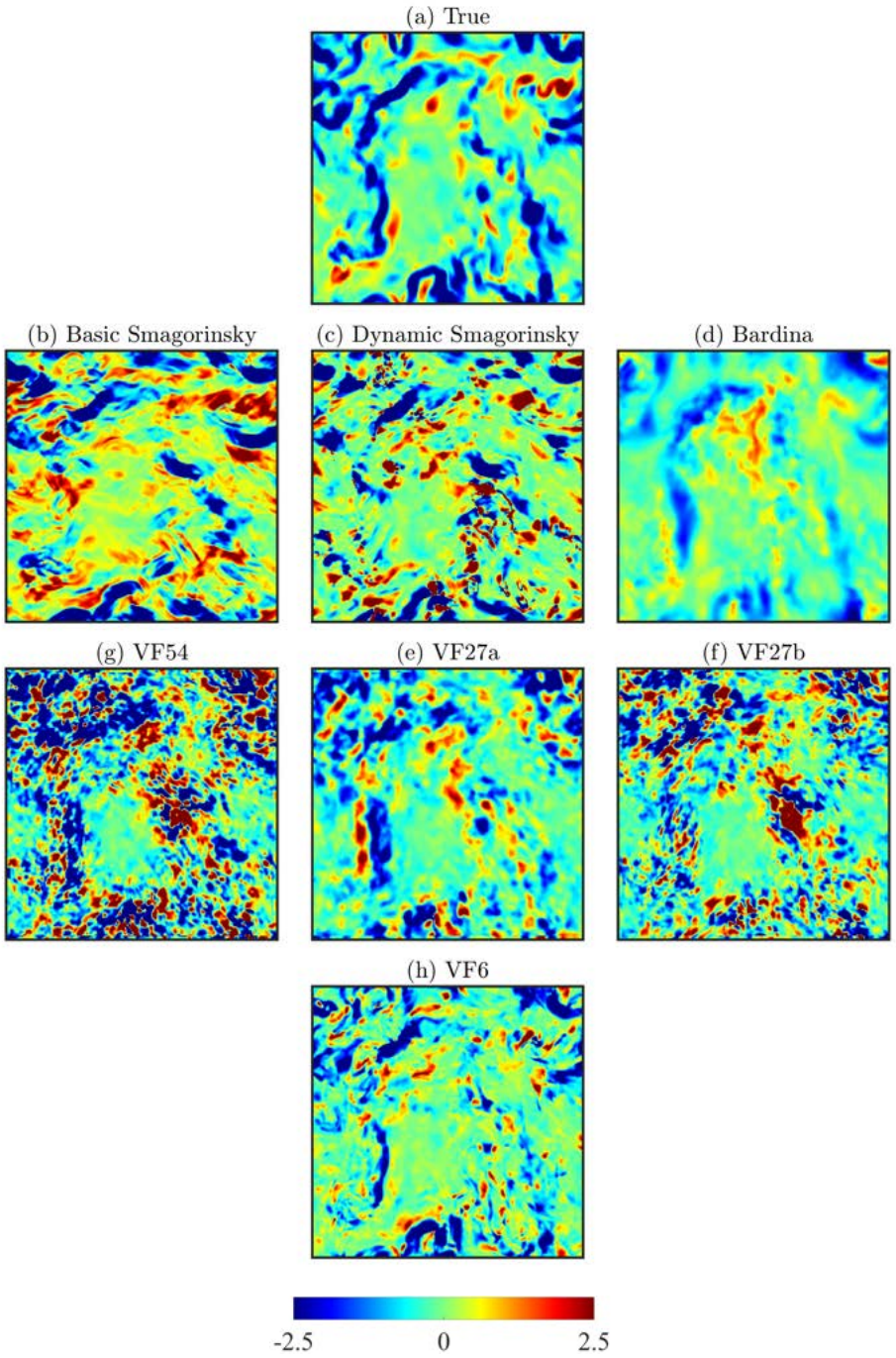

Figure 23. Typical results for subgrid scalar flux component $z_1(\mathbf{x}, t)$ from *a priori* tests with the high-Re dataset using box filters with $(k_{\widehat{\Delta}}, k_{\widetilde{\Delta}}) = (5, 10)$.

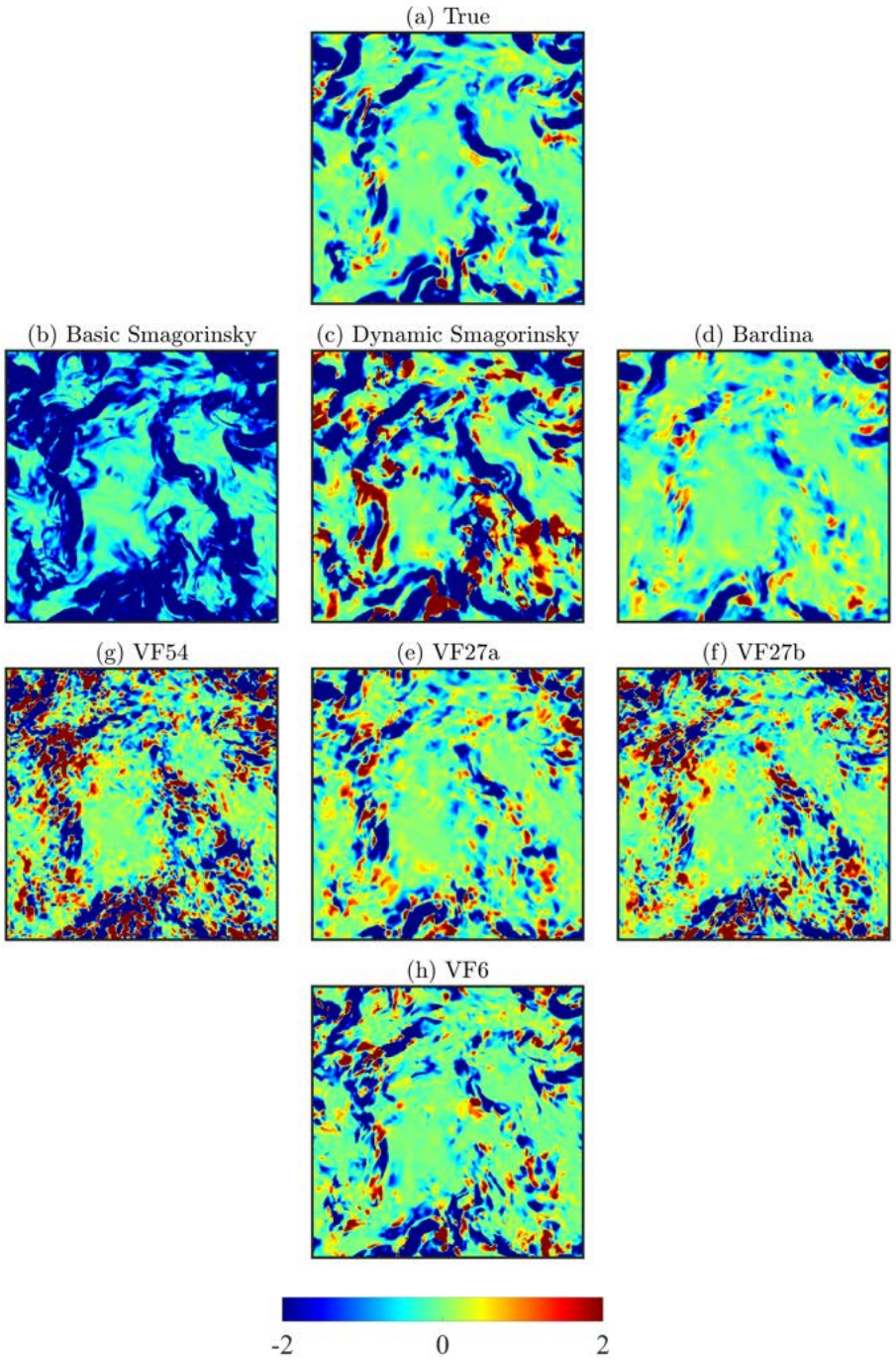

Figure 24. Typical results for subgrid scalar energy production $\Pi(\mathbf{x}, t)$ from *a priori* tests with the high-Re dataset using box filters with $(k_{\widehat{\Delta}}, k_{\widetilde{\Delta}}) = (5, 10)$.

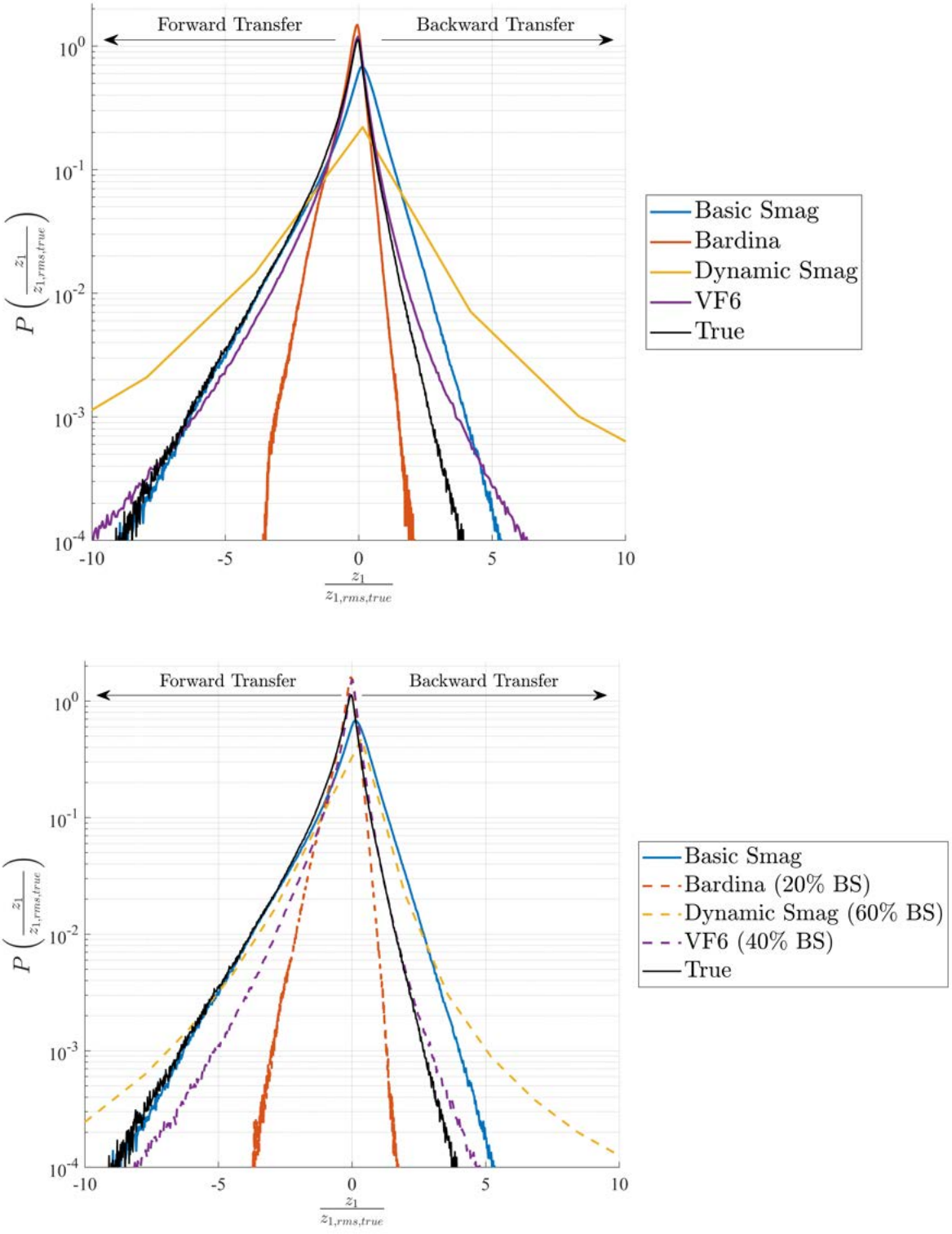

Figure 25. PDFs for $z_1(\mathbf{x}, t)$ from *a priori* tests with high-Re data using box filters having $(k_{\widehat{\Delta}},\, k_{\widetilde{\Delta}}) = (5,\, 10)$, for $c_{BS,z} = 0$ in (8.11) *(top)* and with minimum required $c_{BS,z}$ value from Chapter 8 for stable forward simulations *(bottom)*.

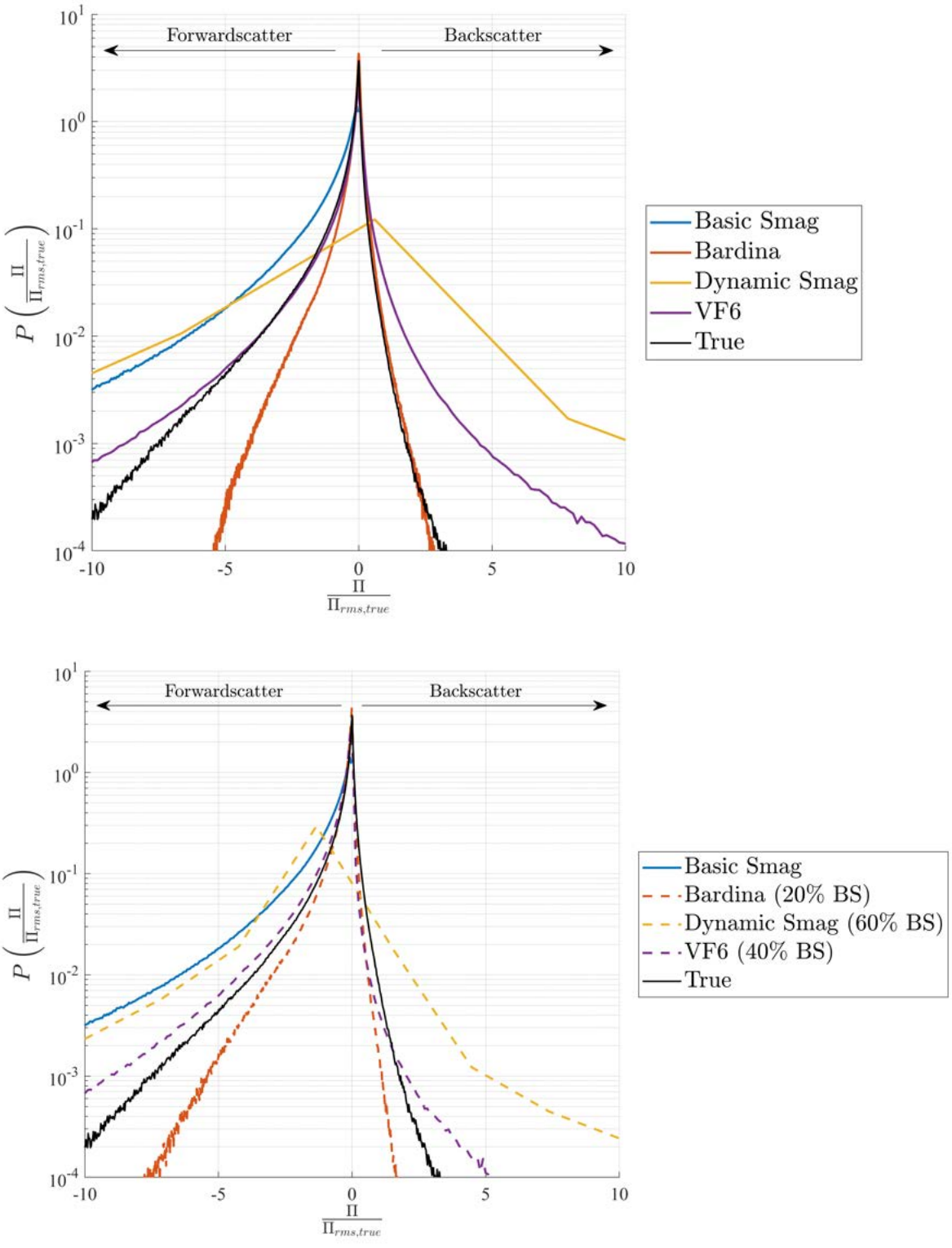

Figure 26. PDFs for $\Pi(\mathbf{x}, t)$ from *a priori* tests with high-Re data using box filters having $(k_{\widehat{\Delta}},\, k_{\widetilde{\Delta}}) = (5,\, 10)$, for $c_{BS,z} = 0$ in (8.11) *(top)* and with minimum required $c_{BS,z}$ value from Chapter 8 for stable forward simulations *(bottom)*.

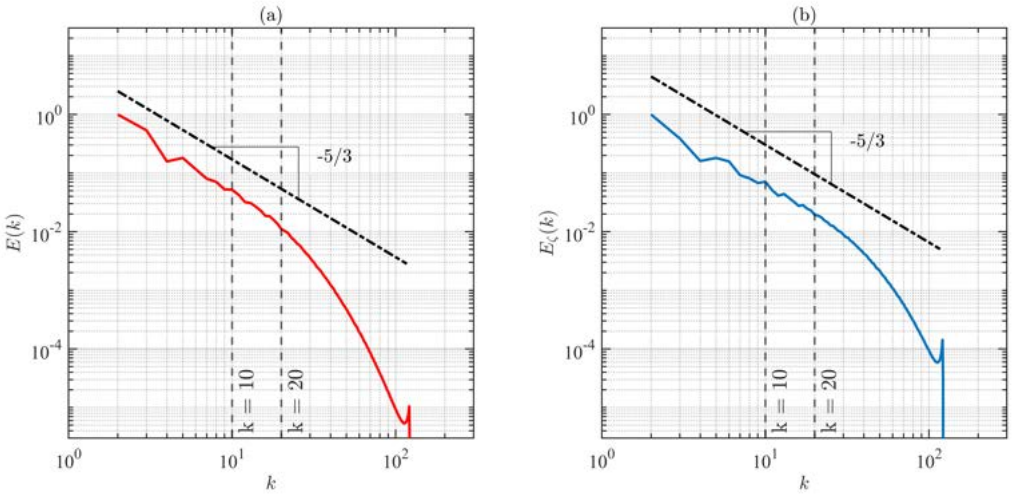

Figure 27. Locations of test-scale and LES-scale filters for $(k_{\widehat{\Delta}}, k_{\widetilde{\Delta}}) = (10, 20)$ in kinetic energy spectrum $E(k)$ (left) and scalar energy spectrum $E_\varphi(k)$ (right) from the high-Re DNS dataset.

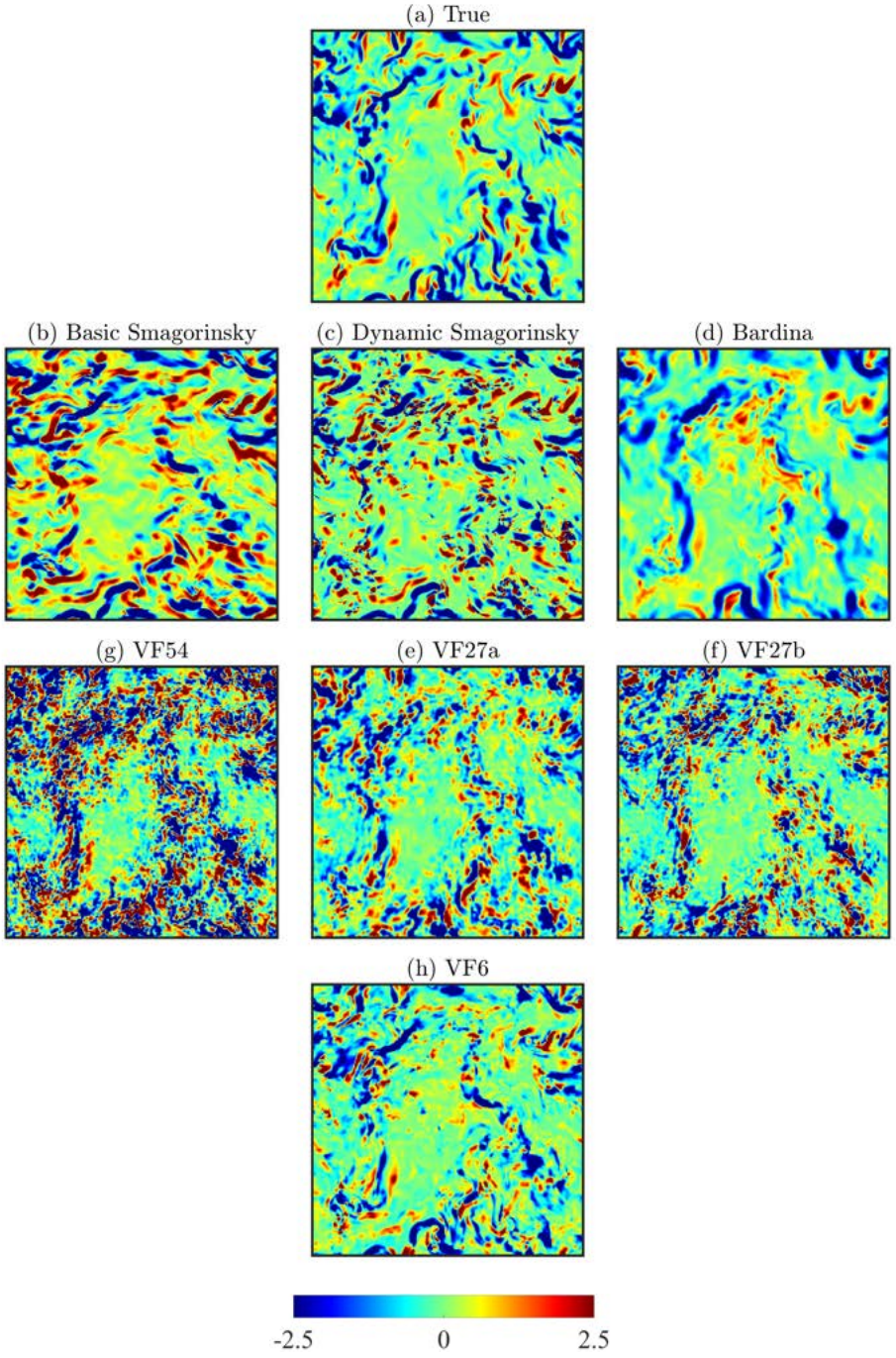

Figure 28. Typical results for subgrid scalar flux component $z_1(\mathbf{x}, t)$ from *a priori* tests with the high-Re dataset using box filters with $(k_{\widehat{\Delta}}, k_{\widetilde{\Delta}}) = (10, 20)$.

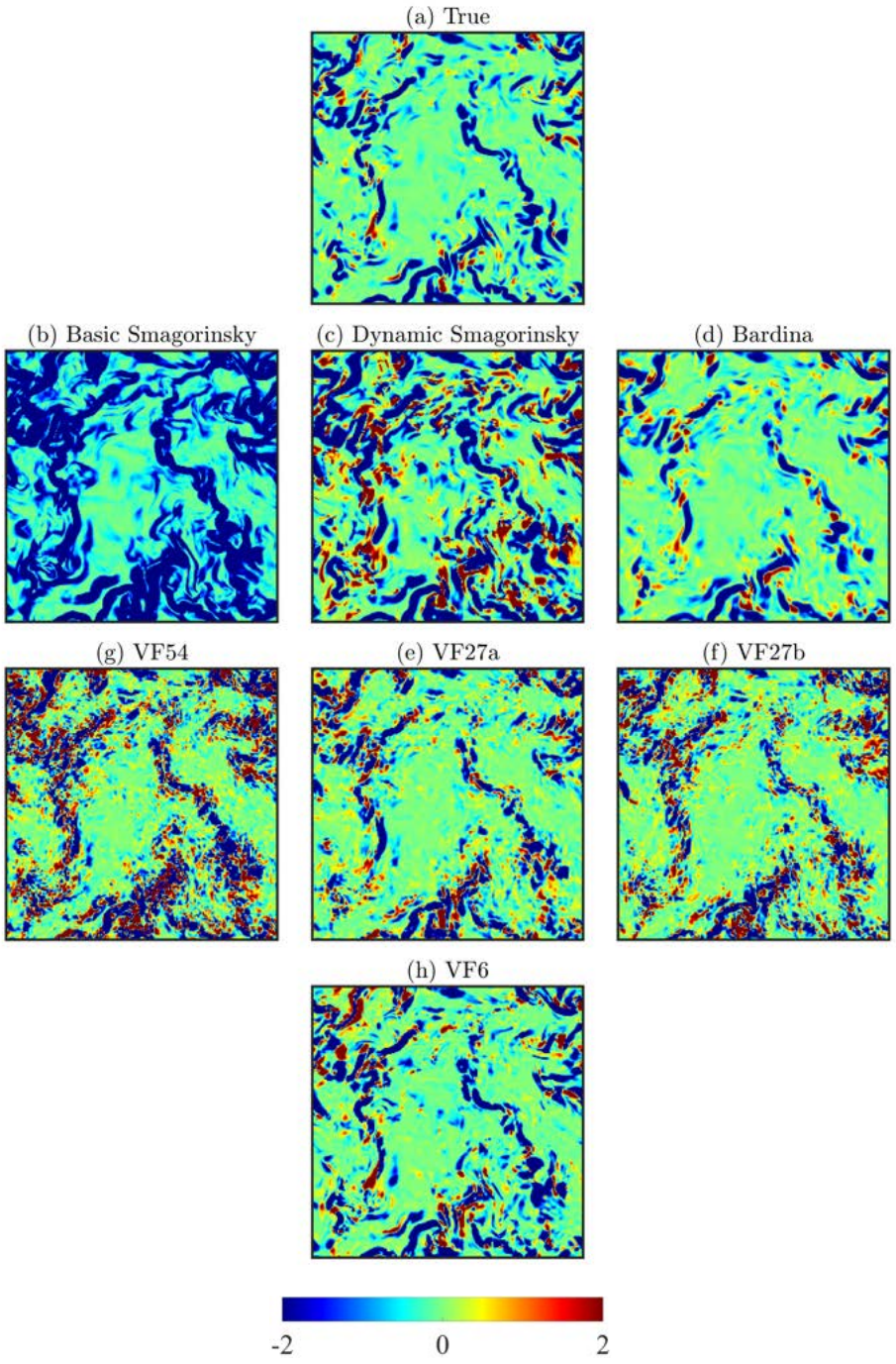

Figure 29. Typical results for subgrid scalar energy production $\Pi(\mathbf{x}, t)$ from *a priori* tests with the high-Re dataset using box filters with $(k_{\widehat{\Delta}}, k_{\widetilde{\Delta}}) = (10, 20)$.

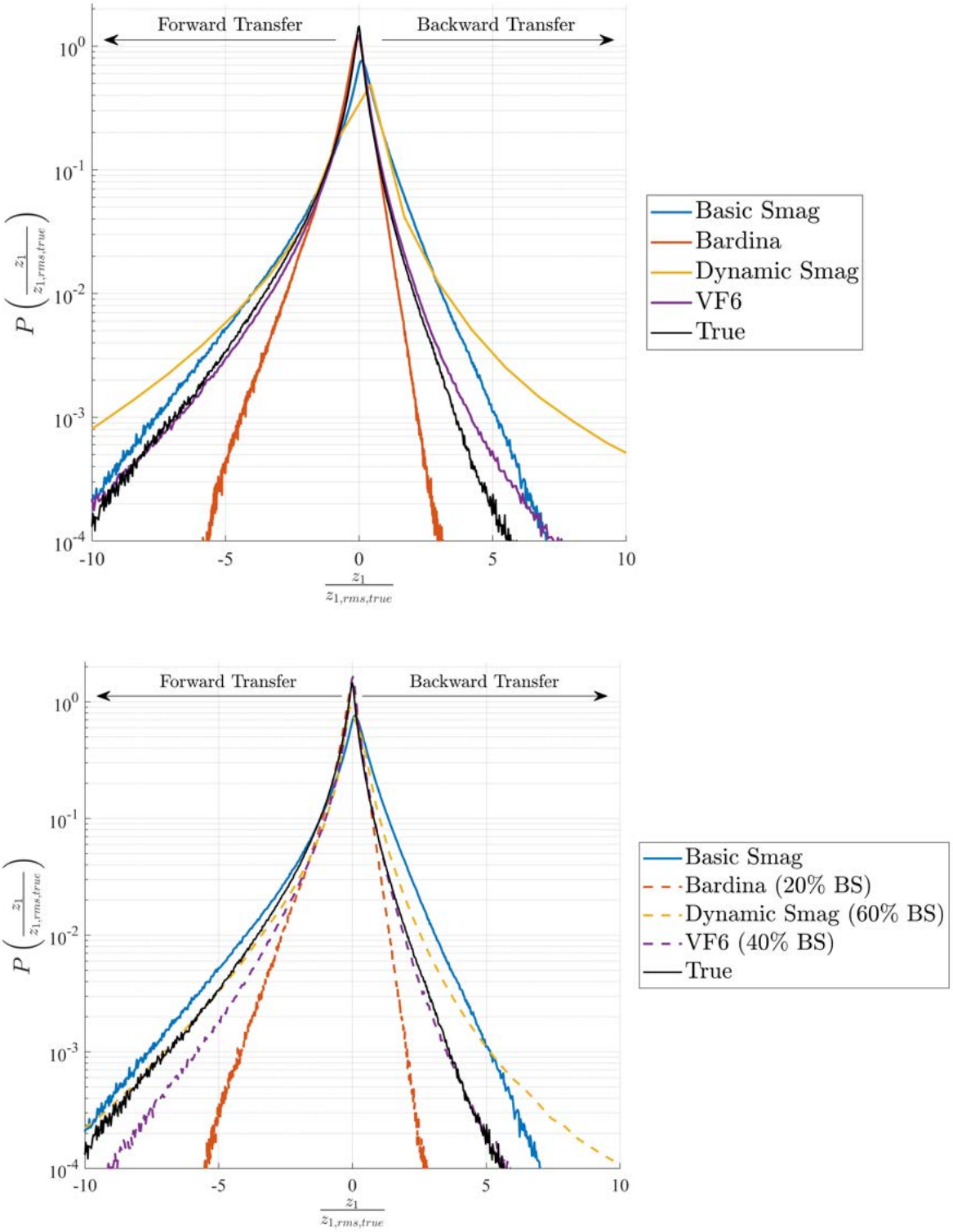

Figure 30. PDFs for $z_1(\mathbf{x}, t)$ from *a priori* tests with high-Re data using box filters having $(k_{\widehat{\Delta}},\, k_{\widetilde{\Delta}}) = (10,\, 20)$, for $c_{BS,z} = 0$ in (8.11) *(top)* and with minimum required $c_{BS,z}$ value from Chapter 8 for stable forward simulations *(bottom)*.

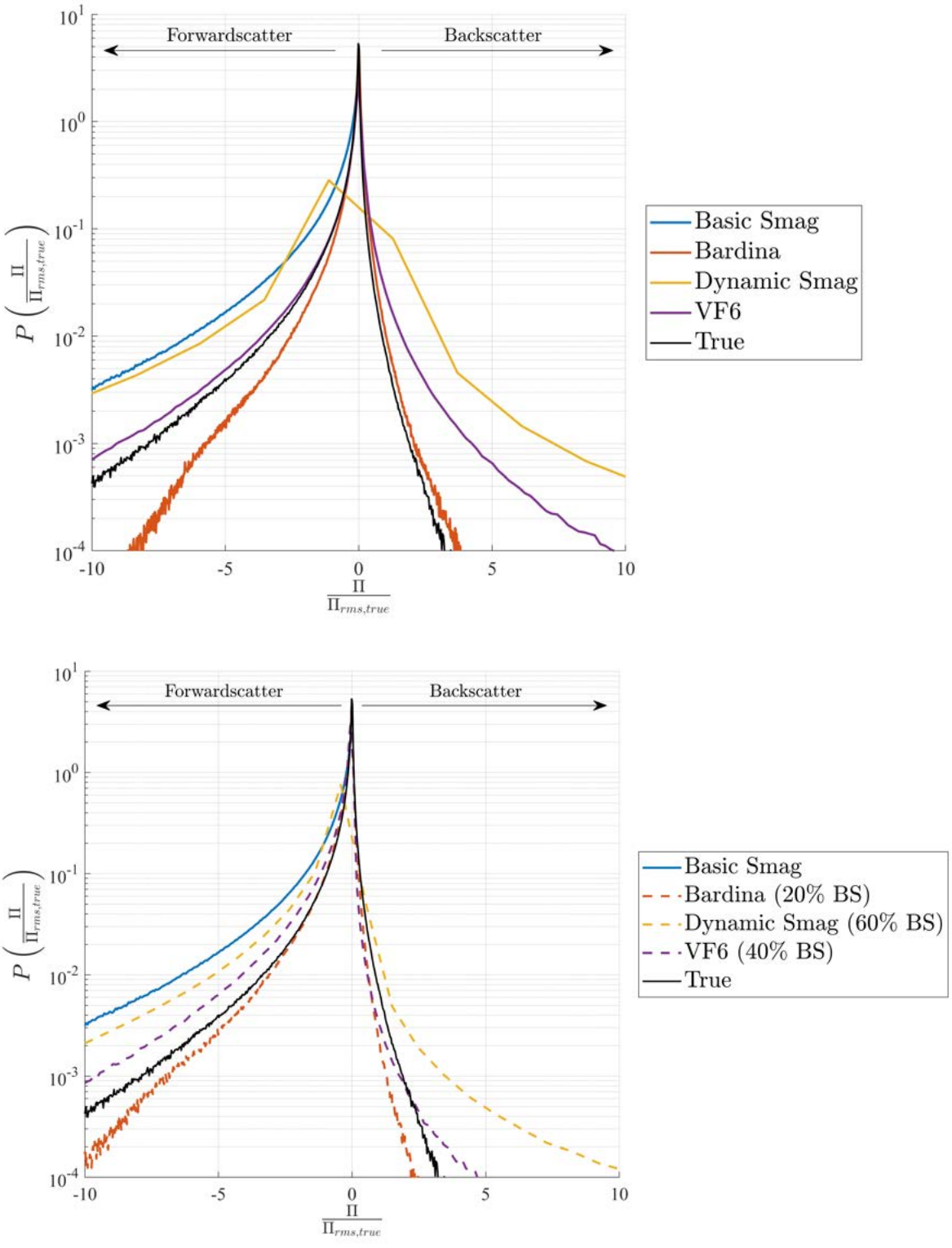

Figure 31. PDFs for $\Pi(\mathbf{x}, t)$ from *a priori* tests with high-Re data using box filters having $(k_{\widehat{\Delta}}, k_{\widetilde{\Delta}}) = (10, 20)$, for $c_{BS,z} = 0$ in (8.11) *(top)* and with minimum required $c_{BS,z}$ value from Chapter 8 for stable forward simulations *(bottom)*.

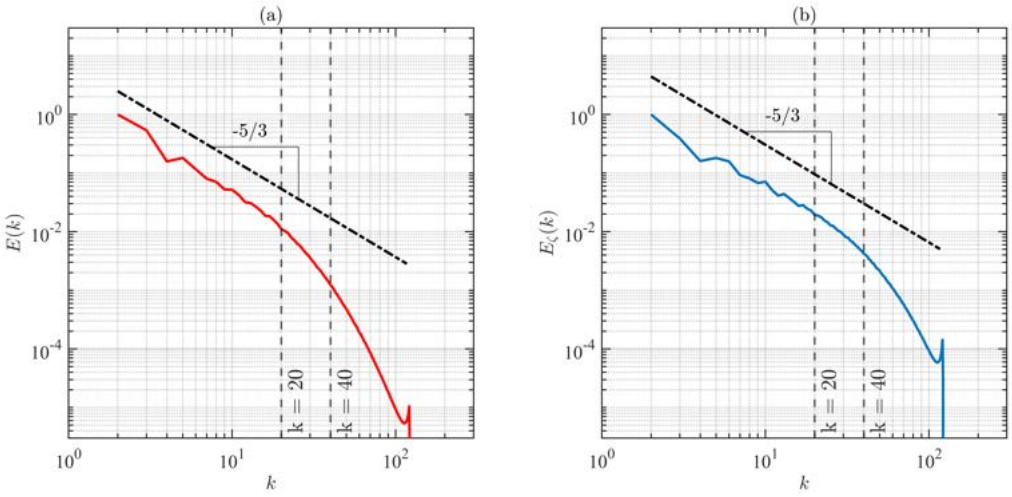

Figure 32. Locations of test-scale and LES-scale filters for $(k_{\widehat{\Delta}}, k_{\widetilde{\Delta}}) = (20, 40)$ in kinetic energy spectrum $E(k)$ (left) and scalar energy spectrum $E_\varphi(k)$ (right) from the high-Re DNS dataset.

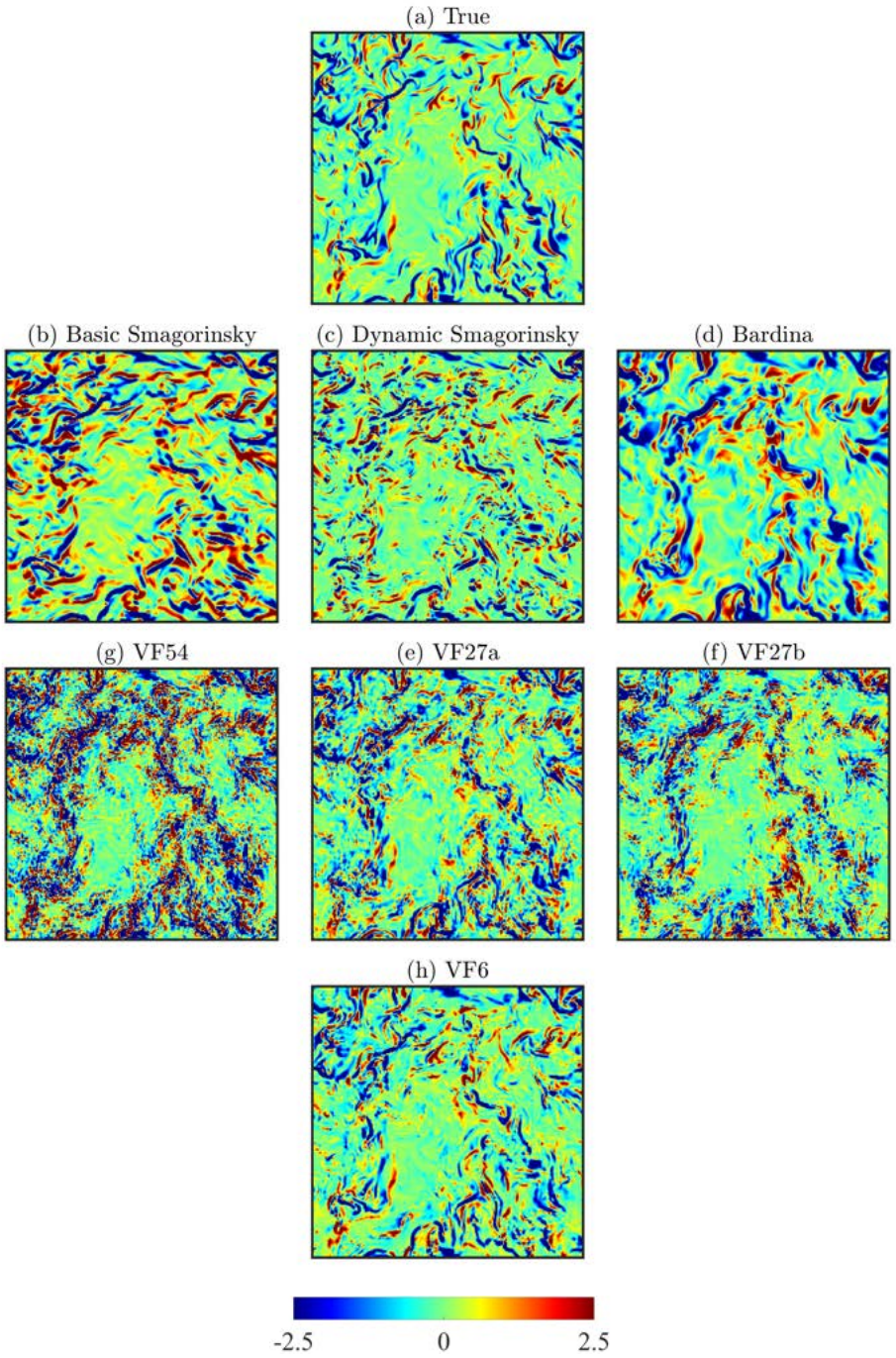

Figure 33. Typical results for subgrid scalar flux component $z_1(\mathbf{x}, t)$ from *a priori* tests with the high-Re dataset using box filters with $(k_{\widehat{\Delta}}, k_{\widetilde{\Delta}}) = (20, 40)$.

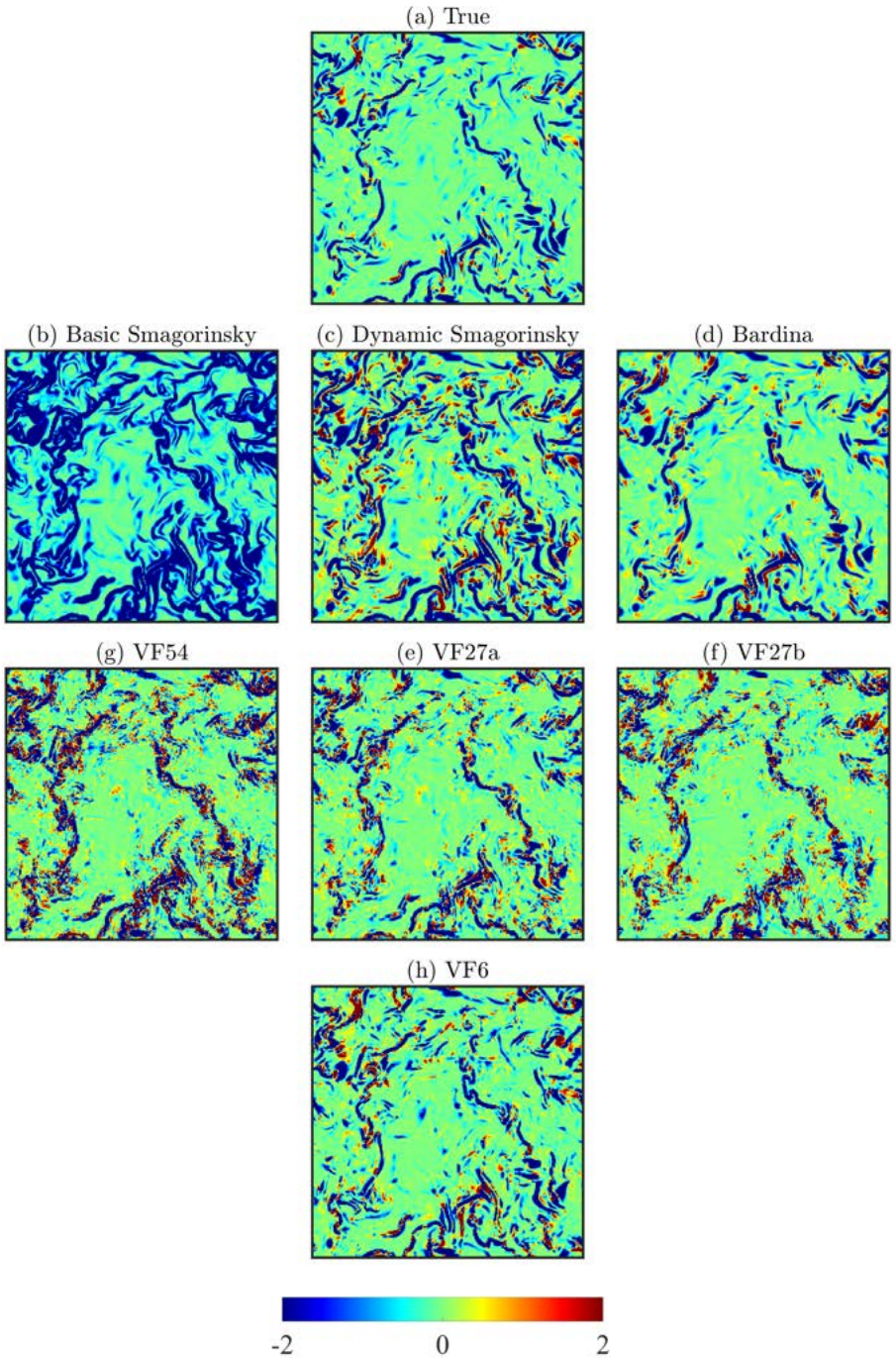

Figure 34. Typical results for subgrid scalar energy production $\Pi(\mathbf{x}, t)$ from *a priori* tests with the high-Re dataset using box filters with $(k_{\widehat{\Delta}}, k_{\widetilde{\Delta}}) = (20, 40)$.

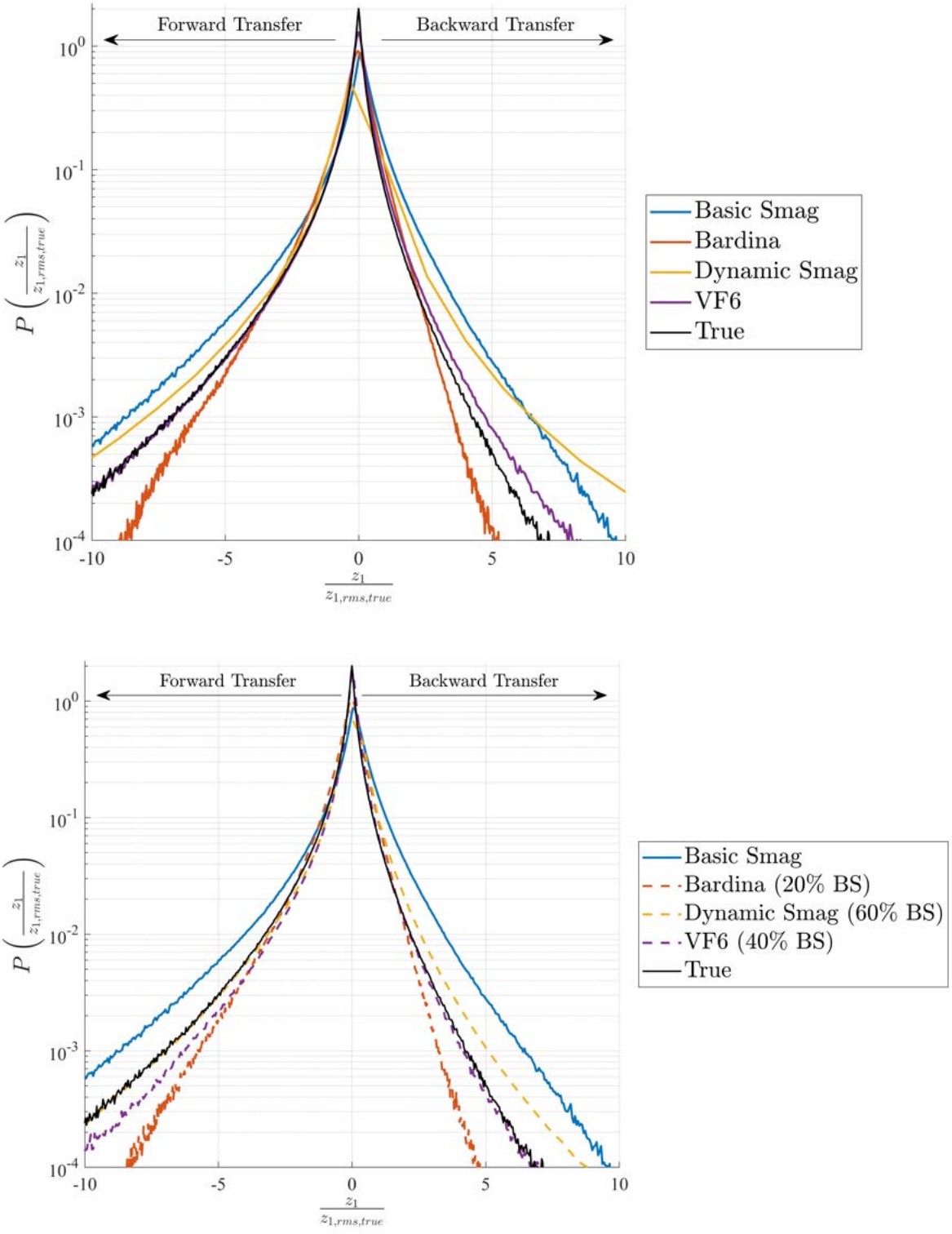

Figure 35. PDFs for $z_1(\mathbf{x}, t)$ from *a priori* tests with high-Re data using box filters having $(k_{\widehat{\Delta}},\, k_{\widetilde{\Delta}}) = (20,\, 40)$, for $c_{BS,z} = 0$ in (8.11) *(top)* and with minimum required $c_{BS,z}$ value from Chapter 8 for stable forward simulations *(bottom)*.

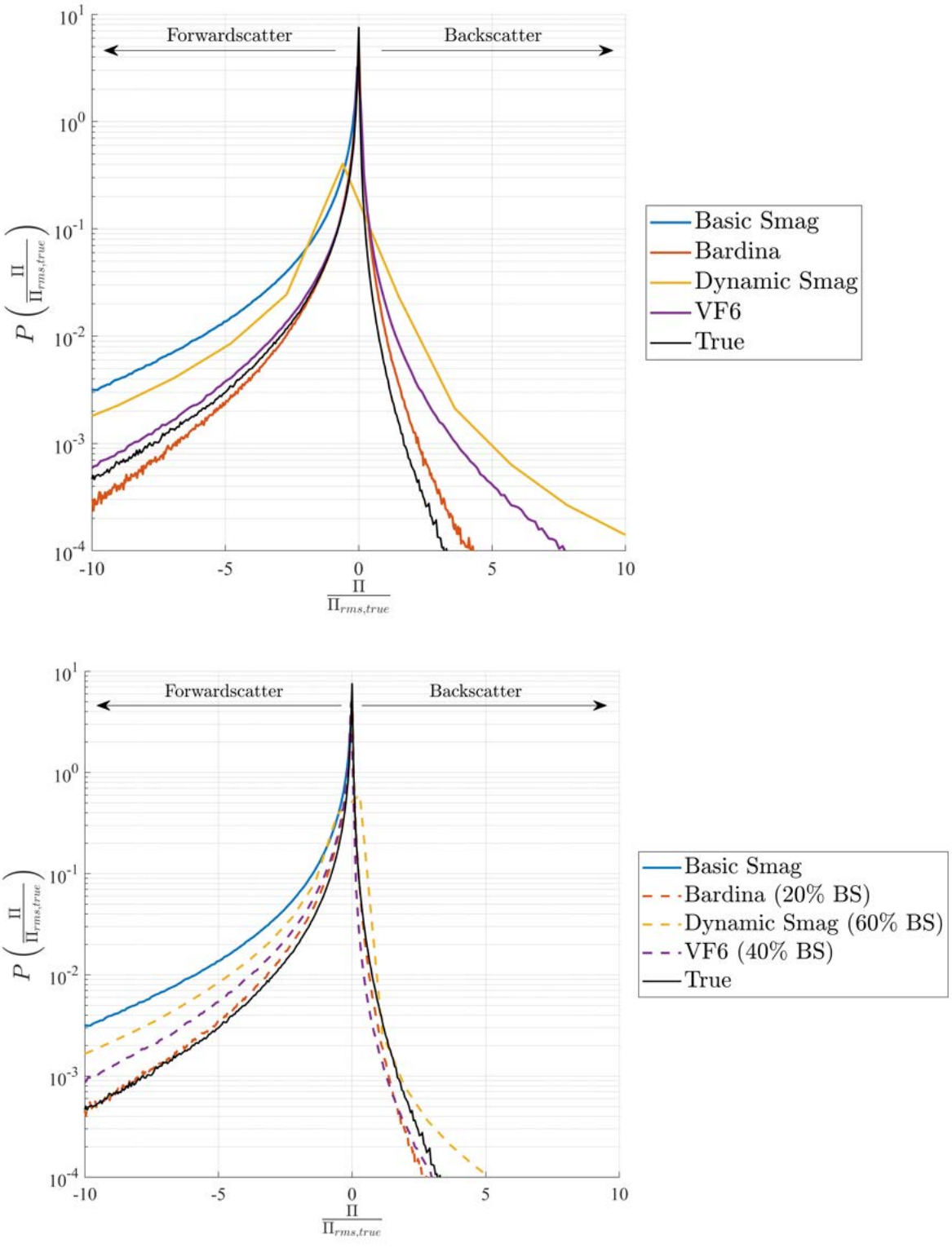

Figure 36. PDFs for $\Pi(\mathbf{x}, t)$ from *a priori* tests with high-Re data using box filters having $(k_{\widehat{\Delta}}, k_{\widetilde{\Delta}}) = (20, 40)$, for $c_{BS,z} = 0$ in (8.11) *(top)* and with minimum required $c_{BS,z}$ value from Chapter 8 for stable forward simulations *(bottom)*.

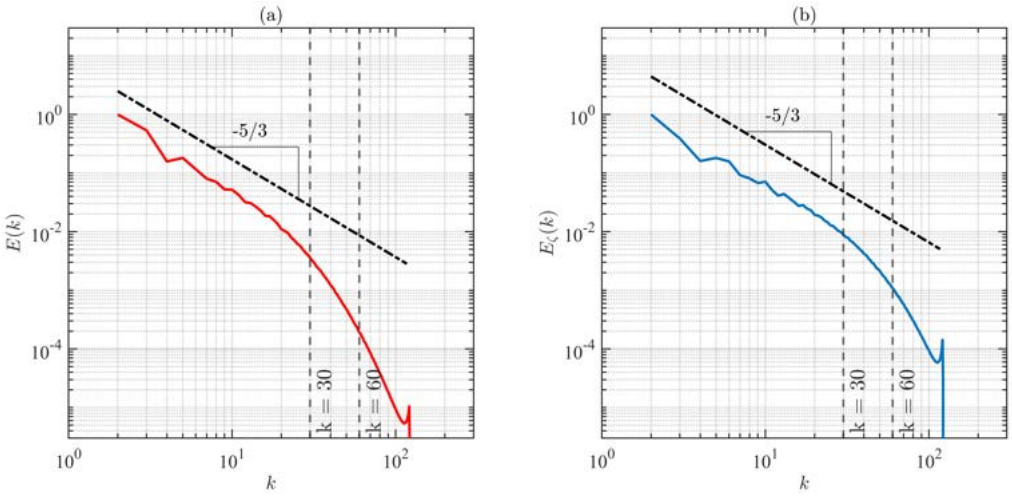

Figure 37. Locations of test-scale and LES-scale filters for $(k_{\widehat{\Delta}}, k_{\widetilde{\Delta}}) = (30, 60)$ in kinetic energy spectrum $E(k)$ (left) and scalar energy spectrum $E_\varphi(k)$ (right) from the high-Re DNS dataset.

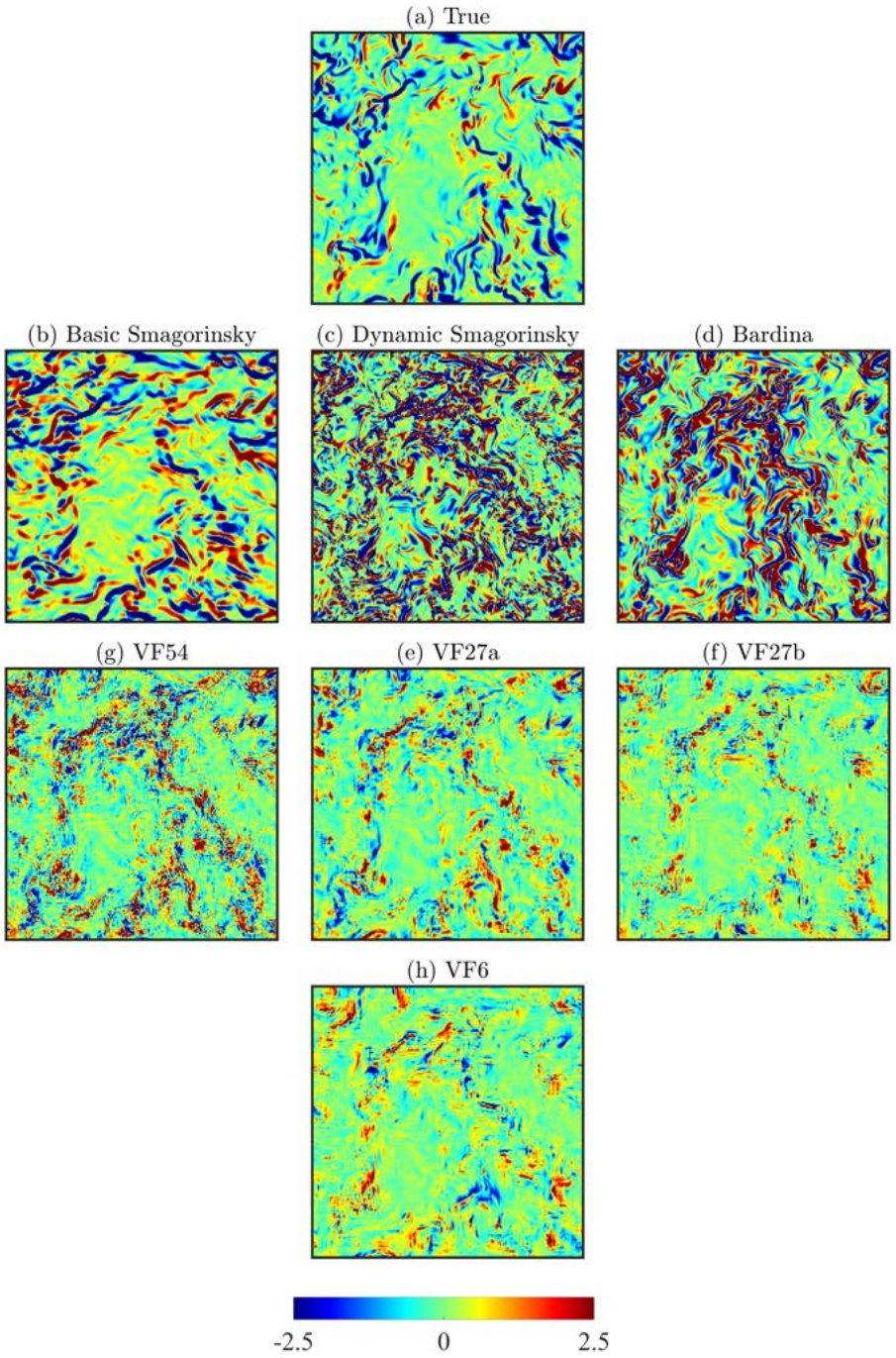

Figure 38. Typical results for subgrid scalar flux component $z_1(\mathbf{x}, t)$ from *a priori* tests with the high-Re dataset using box filters with $(k_{\widehat{\Delta}}, k_{\widetilde{\Delta}}) = (30, 60)$.

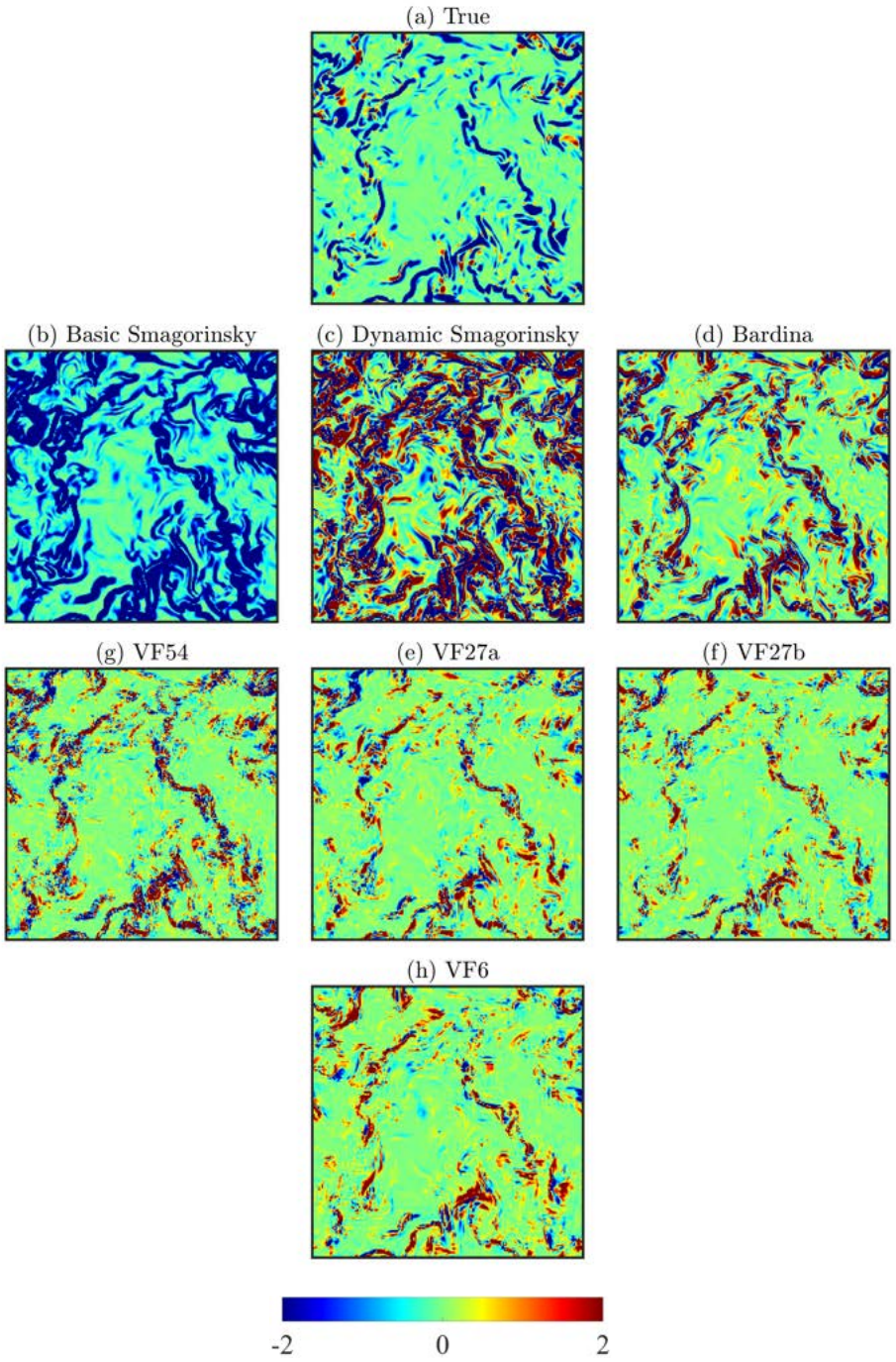

Figure 39. Typical results for subgrid scalar energy production $\Pi(\mathbf{x}, t)$ from *a priori* tests with the high-Re dataset using box filters with $(k_{\widehat{\Delta}}, k_{\widetilde{\Delta}}) = (30, 60)$.

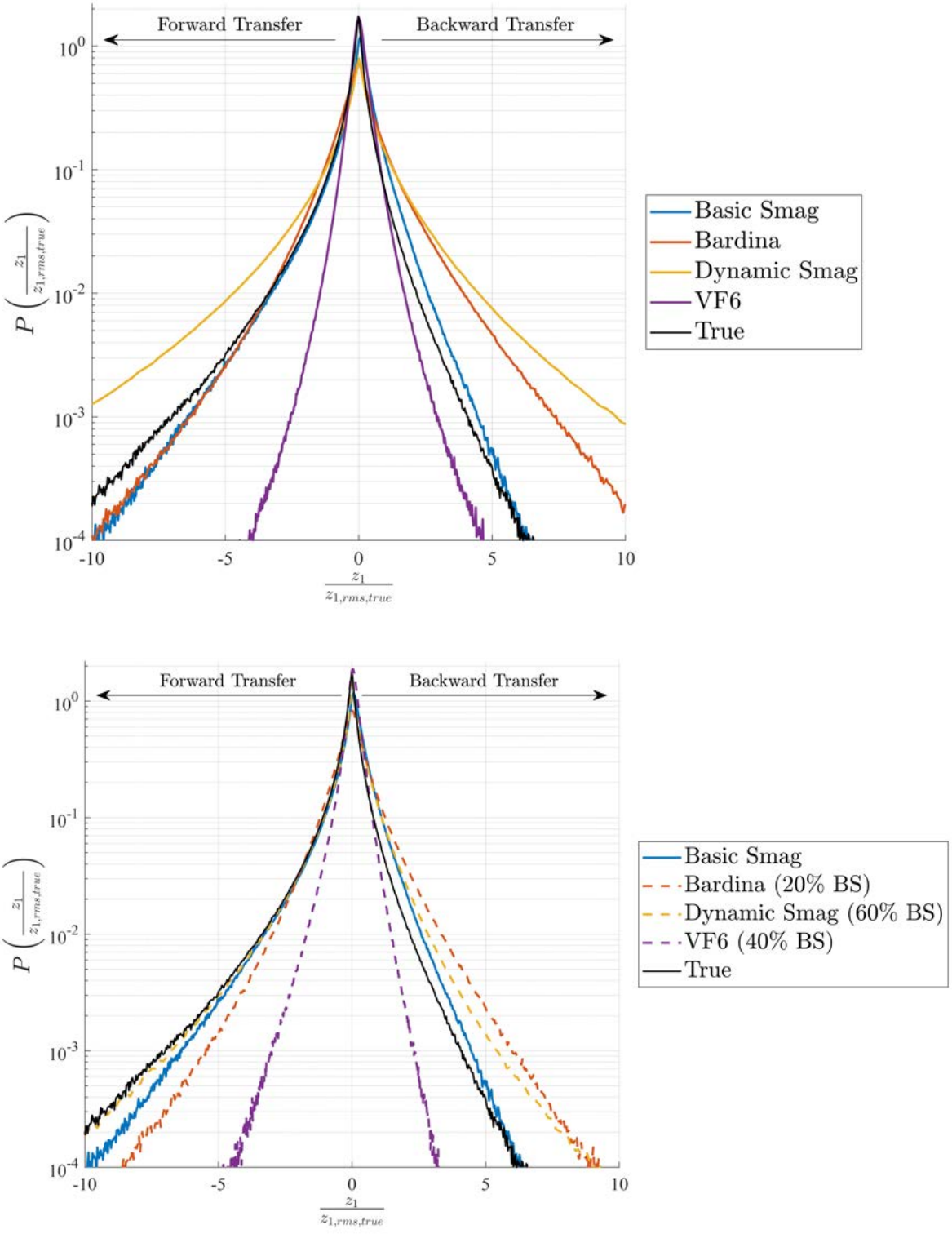

Figure 40. PDFs for $z_1(\mathbf{x}, t)$ from *a priori* tests with high-Re data using box filters having $(k_{\widehat{\Delta}},\, k_{\widetilde{\Delta}}) = (30,\, 60)$, for $c_{BS,z} = 0$ in (8.11) *(top)* and with minimum required $c_{BS,z}$ value from Chapter 8 for stable forward simulations *(bottom)*.

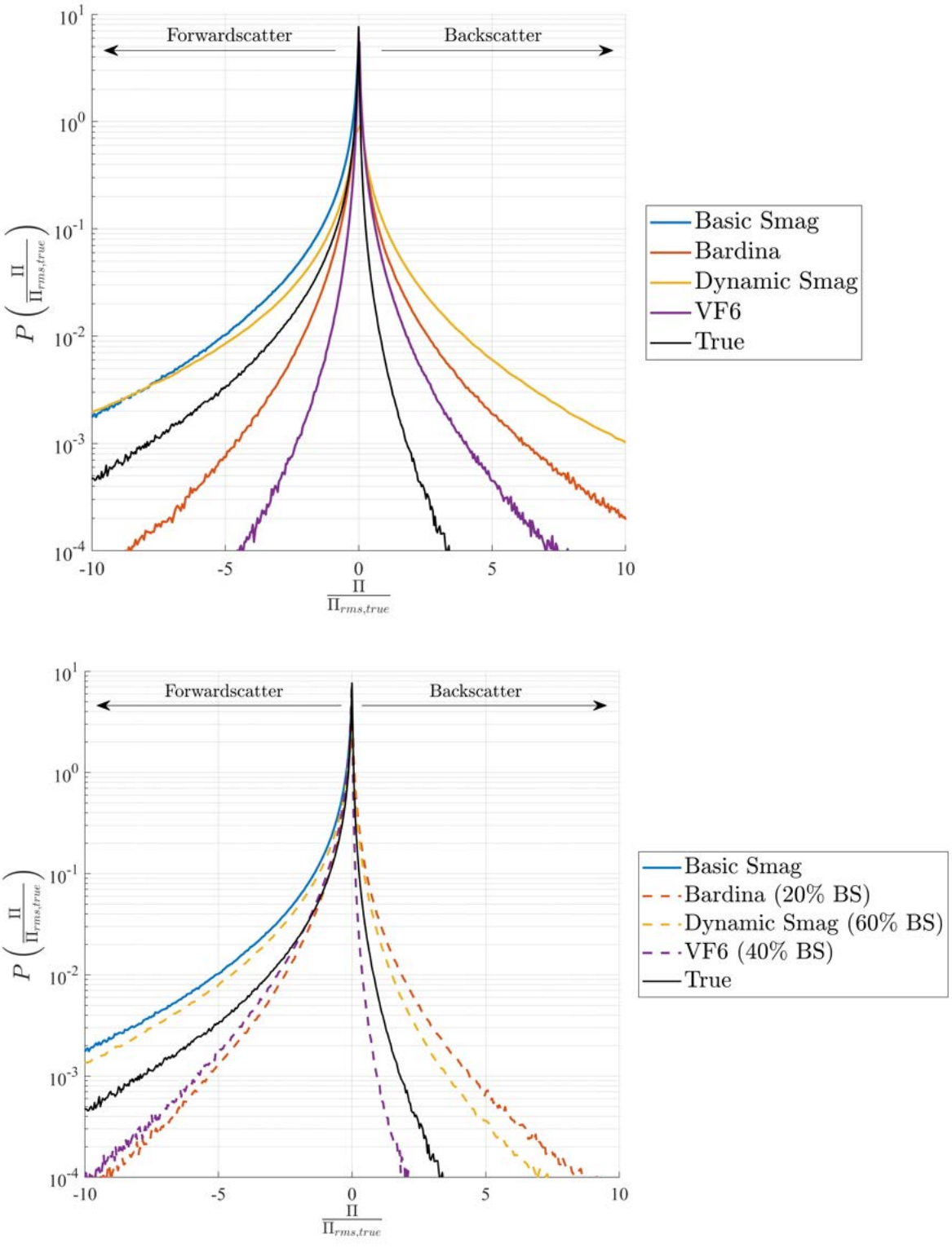

Figure 41. PDFs for $\Pi(\mathbf{x}, t)$ from *a priori* tests with high-Re data using box filters having $(k_{\widehat{\Delta}}, k_{\widetilde{\Delta}}) = (30, 60)$, for $c_{BS,z} = 0$ in (8.11) *(top)* and with minimum required $c_{BS,z}$ value from Chapter 8 for stable forward simulations *(bottom)*.

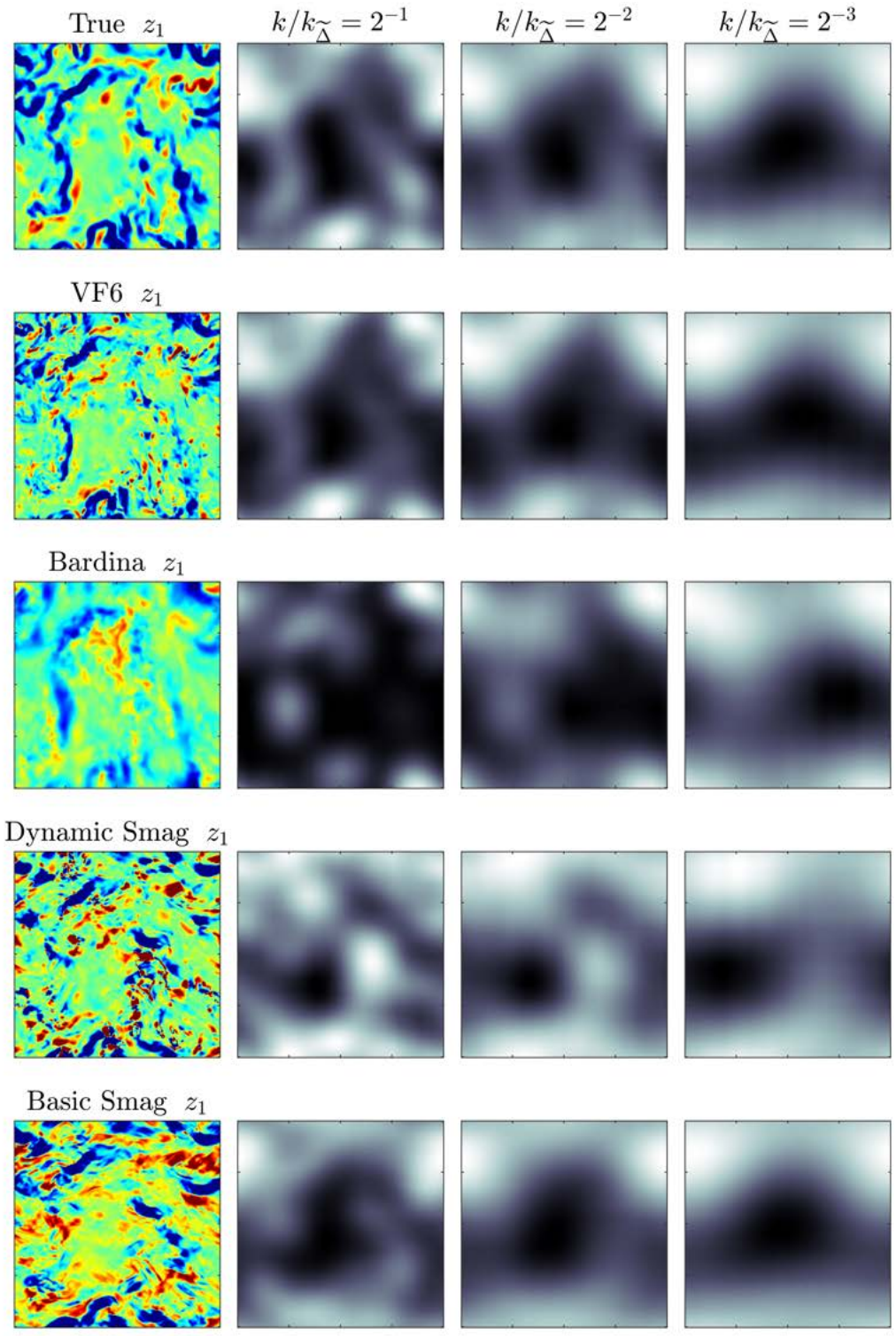

Figure 42. Typical results for support density fields $G_{\Delta_\Gamma}(\mathbf{x}, t)$ at various $k_{\Delta_\Gamma}/k_{\widetilde{\Delta}}$ for subgrid scalar flux fields $z_1(\mathbf{x}, t)$ from *a priori* tests with high-Re dataset using box filters having $(k_{\widehat{\Delta}},\, k_{\widetilde{\Delta}}) = (5,\, 10)$.

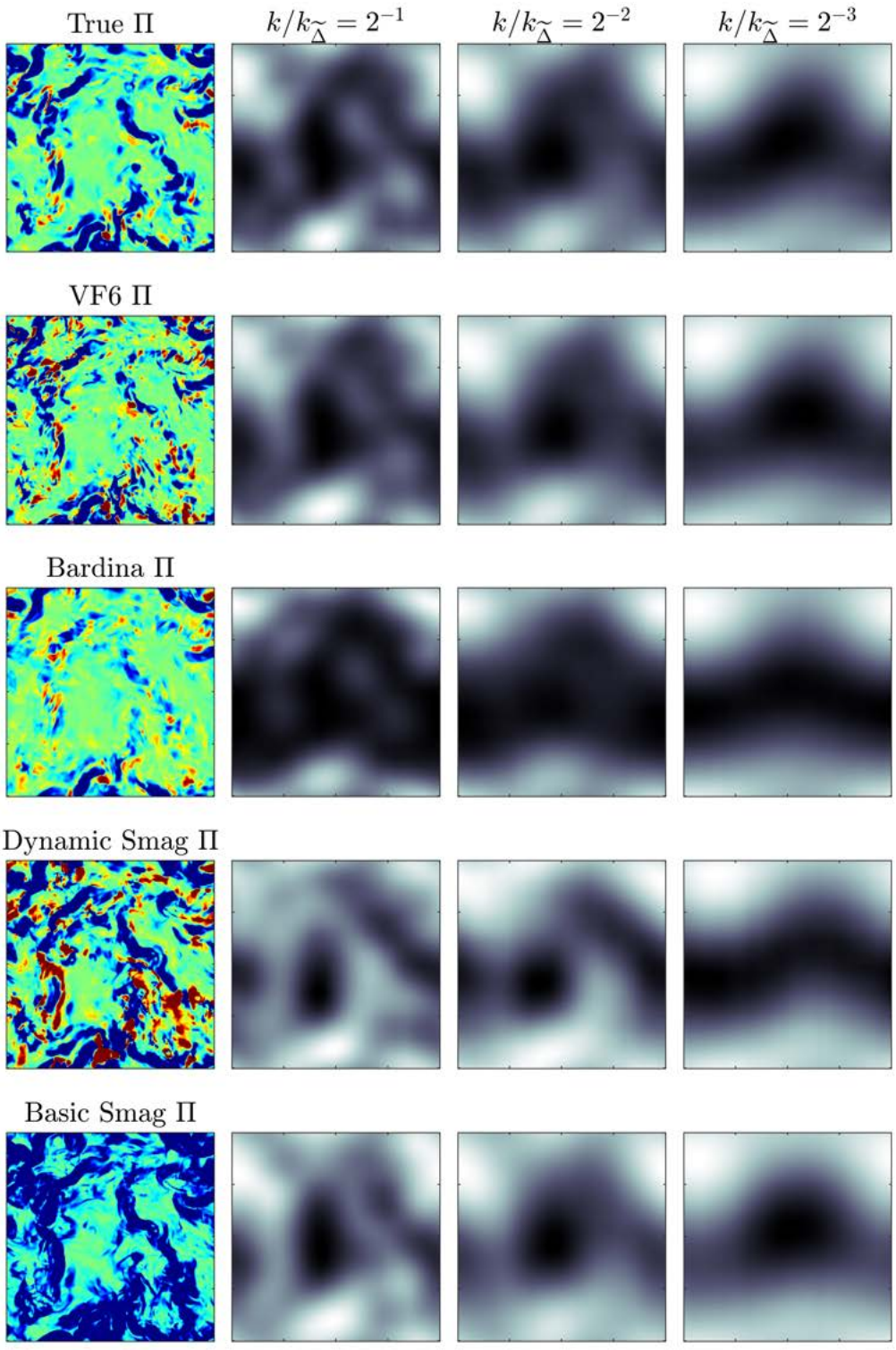

Figure 43. Typical results for support density fields $G_{\Delta_\Gamma}(\mathbf{x}, t)$ at various $k_{\Delta_\Gamma}/k_{\widetilde{\Delta}}$ for subgrid scalar energy production fields $\Pi(\mathbf{x}, t)$ from *a priori* tests with high-Re dataset using box filters having $(k_{\widehat{\Delta}}, k_{\widetilde{\Delta}}) = (5, 10)$.

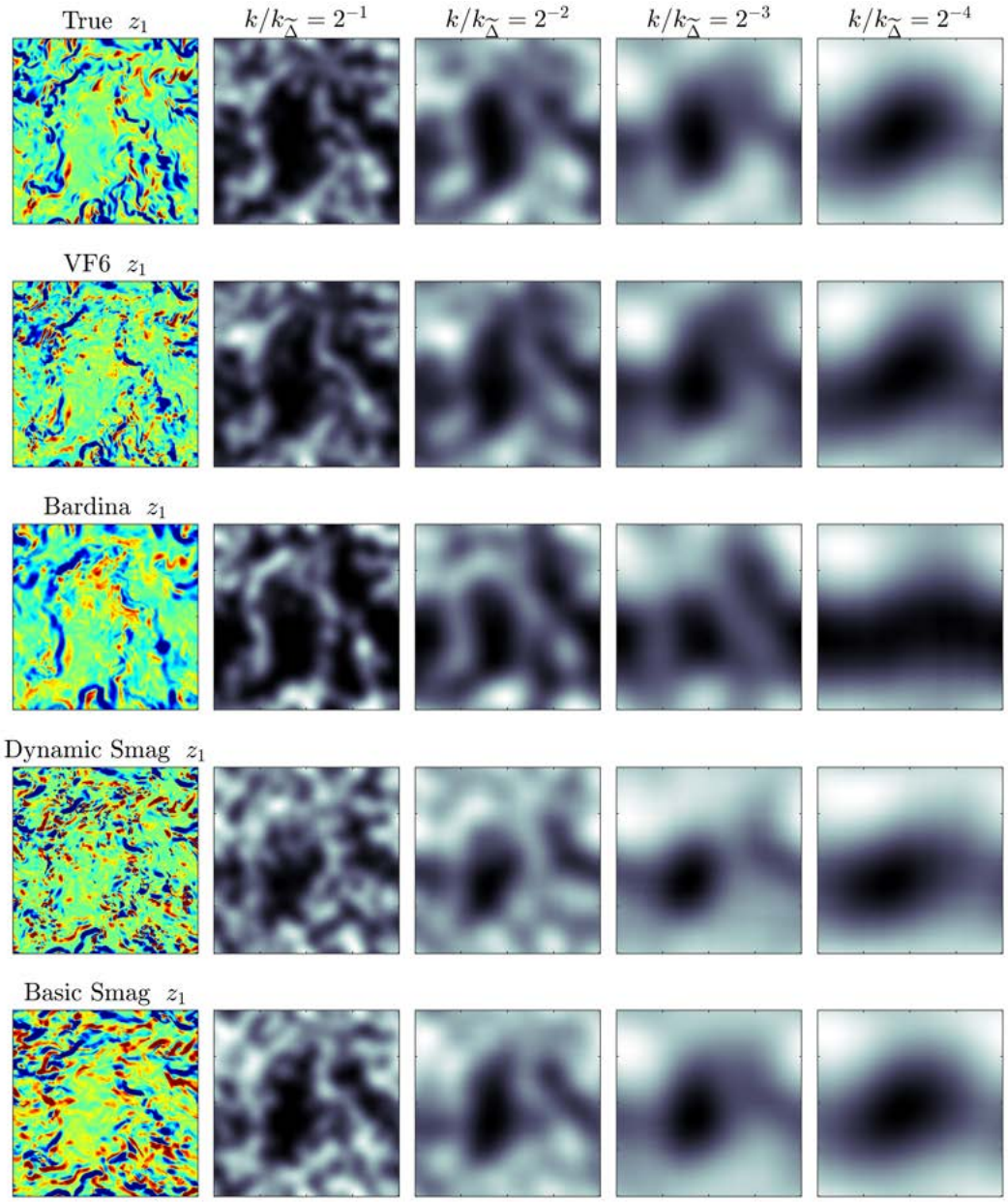

Figure 44. Typical results for support density fields $G_{\Delta_\Gamma}(\mathbf{x}, t)$ at various $k_{\Delta_\Gamma}/k_{\widetilde{\Delta}}$ for subgrid scalar flux fields $z_1(\mathbf{x}, t)$ from *a priori* tests with high-Re dataset using box filters having $(k_{\widehat{\Delta}},\, k_{\widetilde{\Delta}}) = (10,\, 20)$.

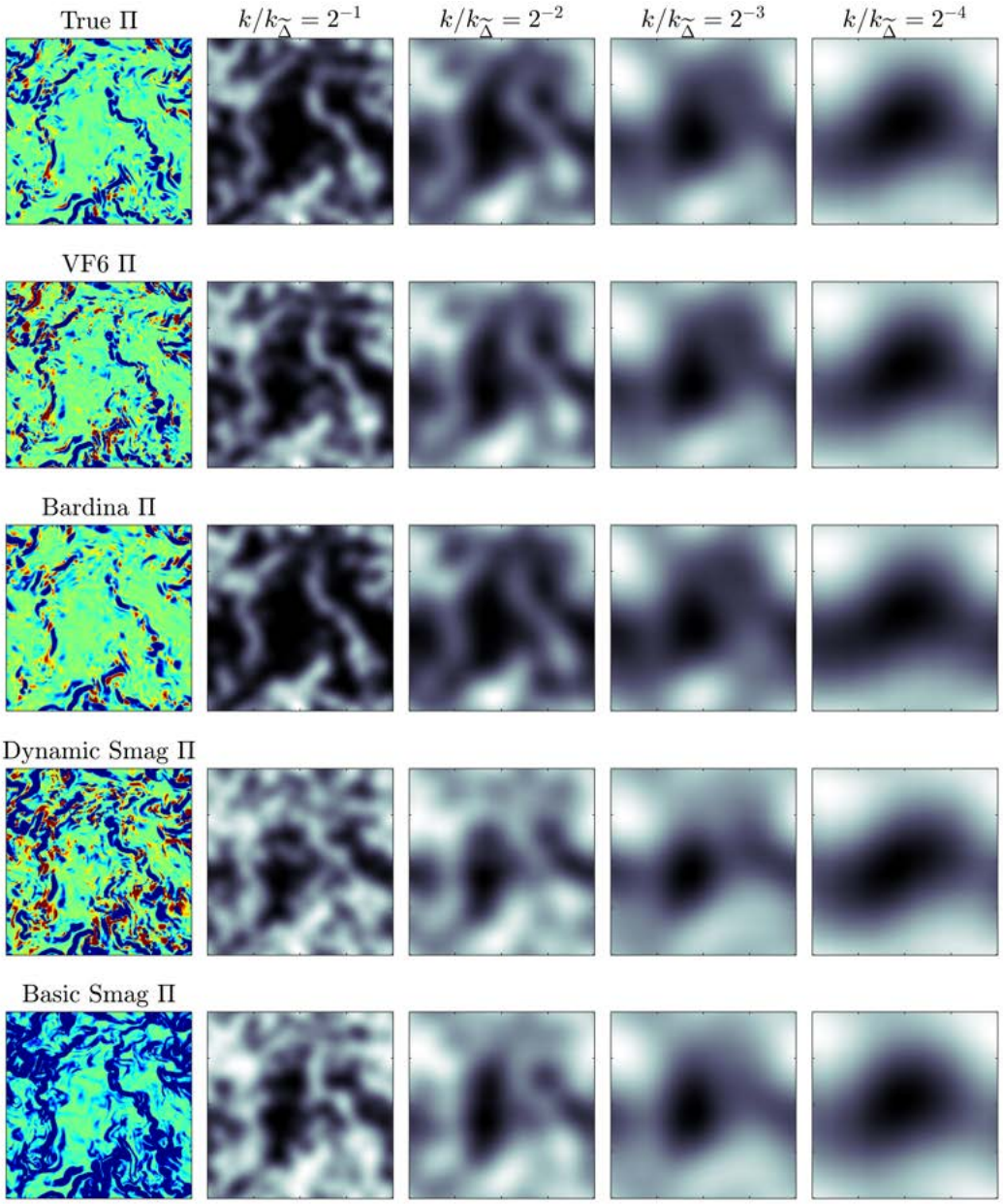

Figure 45. Typical results for support density fields $G_{\Delta_\Gamma}(\mathbf{x}, t)$ at various $k_{\Delta_\Gamma}/k_{\widetilde{\Delta}}$ for subgrid scalar energy production fields $\Pi(\mathbf{x}, t)$ from *a priori* tests with high-Re dataset using box filters having $(k_{\widehat{\Delta}}, k_{\widetilde{\Delta}}) = (10, 20)$.

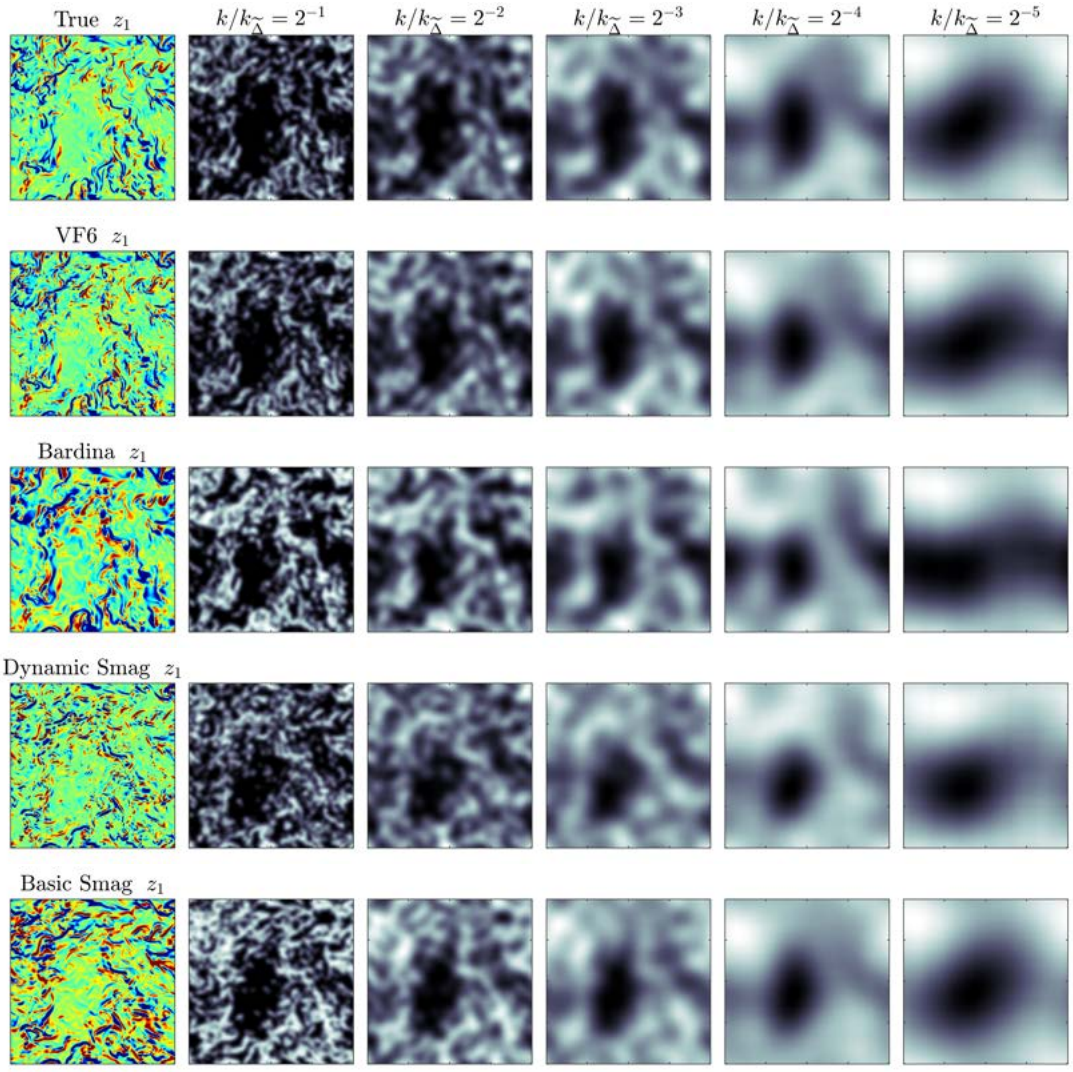

Figure 46. Typical results for support density fields $G_{\Delta_\Gamma}(\mathbf{x}, t)$ at various $k_{\Delta_\Gamma}/k_{\widetilde{\Delta}}$ for subgrid scalar flux fields $z_1(\mathbf{x}, t)$ from *a priori* tests with high-Re dataset using box filters having $(k_{\widehat{\Delta}},\, k_{\widetilde{\Delta}}) = (20,\, 40)$.

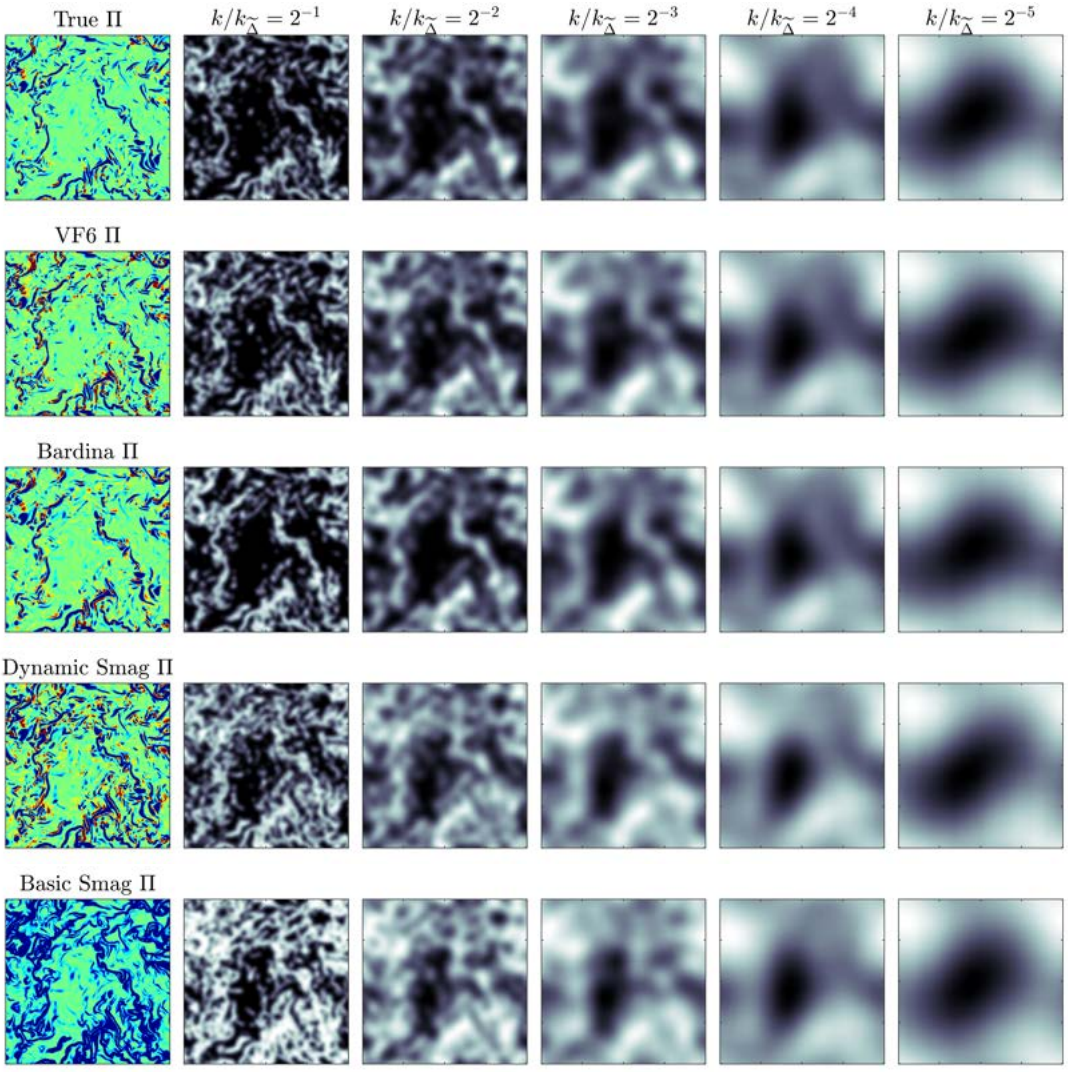

Figure 47. Typical results for support density fields $G_{\Delta_\Gamma}(\mathbf{x}, t)$ at various $k_{\Delta_\Gamma}/k_{\widetilde{\Delta}}$ for subgrid scalar energy production fields $\Pi(\mathbf{x}, t)$ from *a priori* tests with high-Re dataset using box filters having $(k_{\widehat{\Delta}}, k_{\widetilde{\Delta}}) = (20, 40)$.

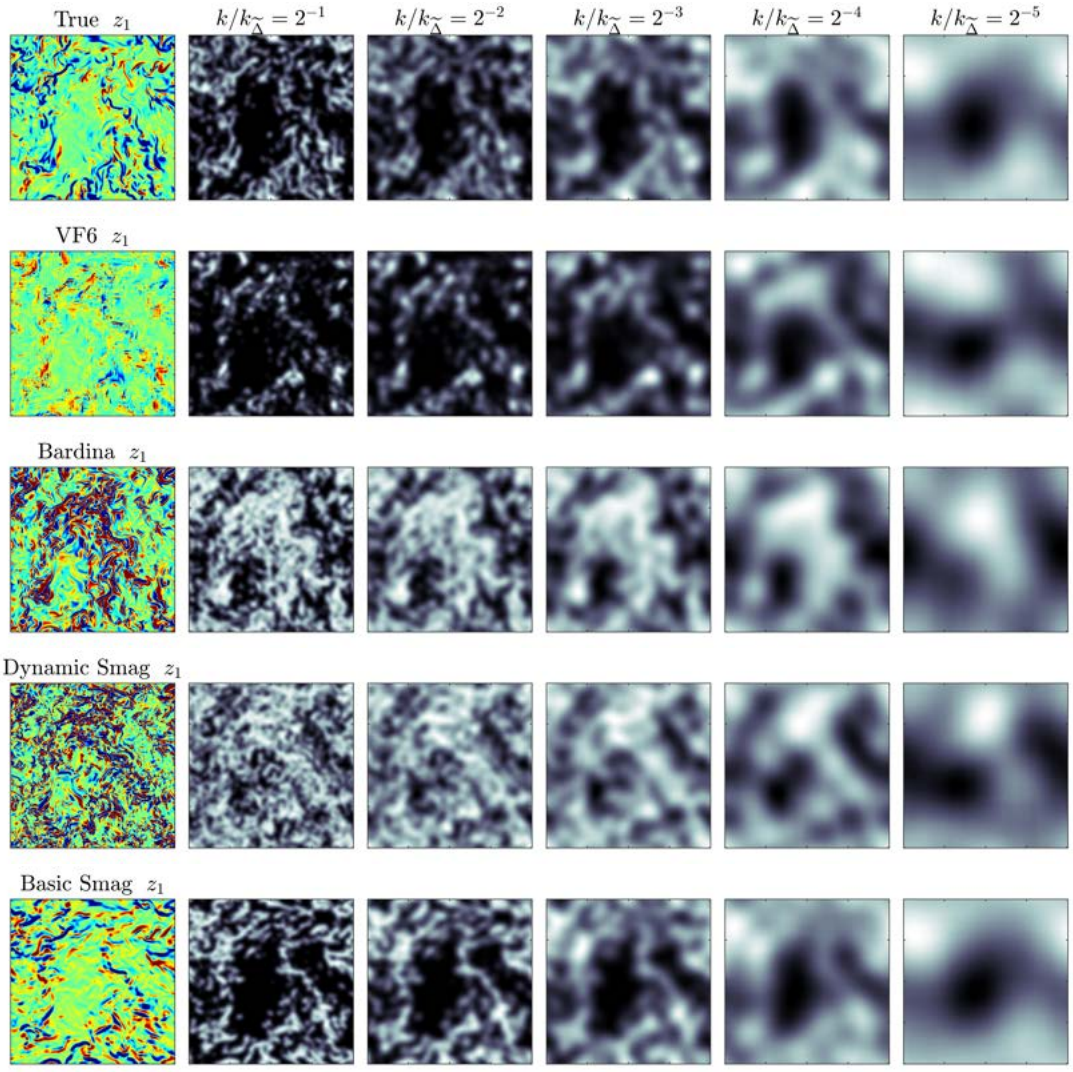

Figure 48. Typical results for support density fields $G_{\Delta_\Gamma}(\mathbf{x}, t)$ at various $k_{\Delta_\Gamma}/k_{\widetilde{\Delta}}$ for subgrid scalar flux fields $z_1(\mathbf{x}, t)$ from *a priori* tests with high-Re dataset using box filters having $(k_{\widehat{\Delta}},\, k_{\widetilde{\Delta}}) = (30,\, 60)$.

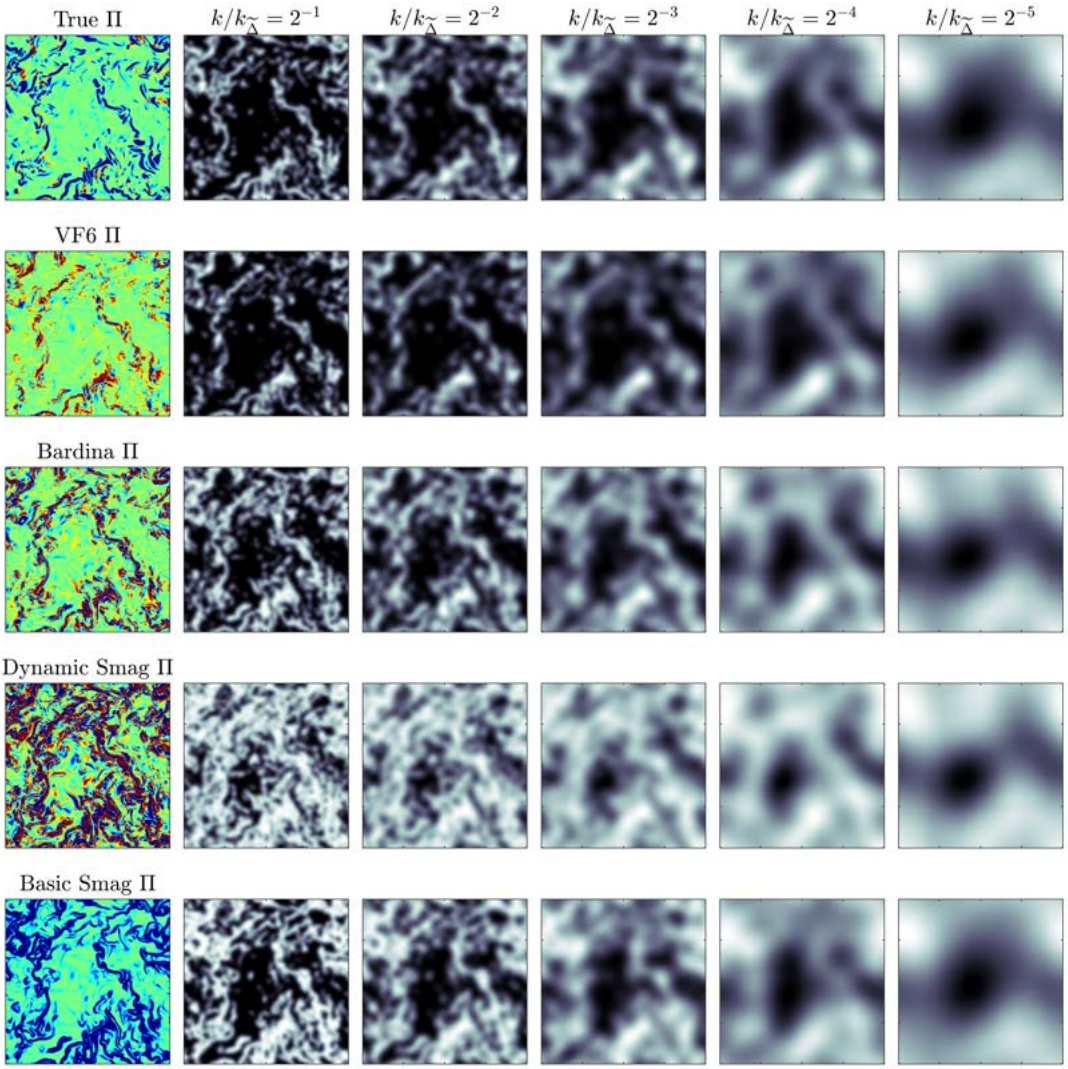

Figure 49. Typical results for support density fields $G_{\Delta_\Gamma}(\mathbf{x}, t)$ at various $k_{\Delta_\Gamma}/k_{\widetilde{\Delta}}$ for subgrid scalar energy production fields $\Pi(\mathbf{x}, t)$ from *a priori* tests with high-Re dataset using box filters having $(k_{\widehat{\Delta}}, k_{\widetilde{\Delta}}) = (30, 60)$.

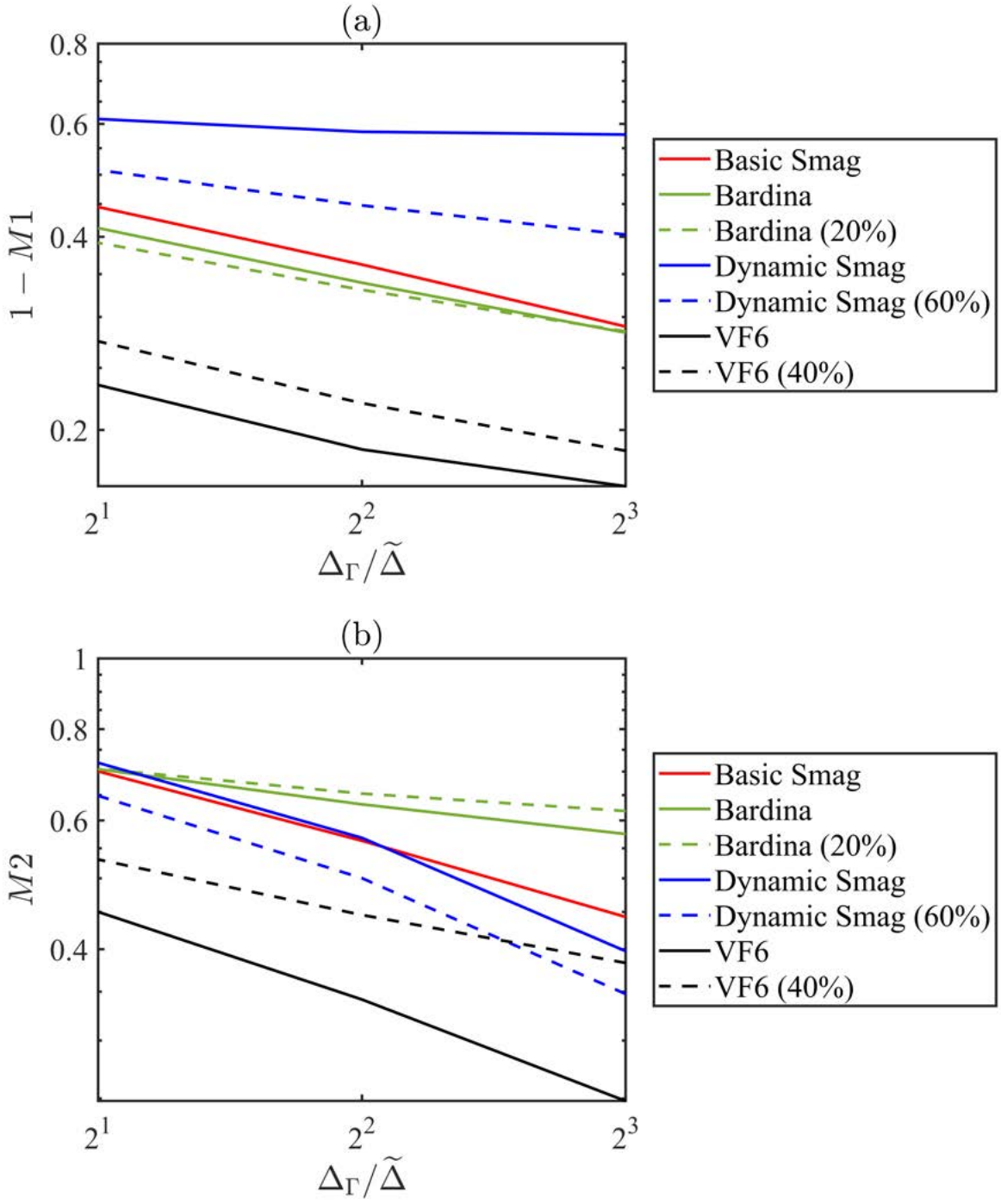

Figure 50. Metrics for scale-by-scale accuracy in support density $G_{\Delta_\Gamma}(\mathbf{x}, t)$ for $z_i(\mathbf{x}, t)$ with $c_{BS,z} = 0$ in (8.11) and $(c_{BS,z})_{min}$ from Chapter 8 for stable forward simulations, from *a priori* tests with high-Re data using box filters $(k_{\widehat{\Delta}}, k_{\widetilde{\Delta}}) = (5, 10)$. Smaller values correspond to greater accuracy.

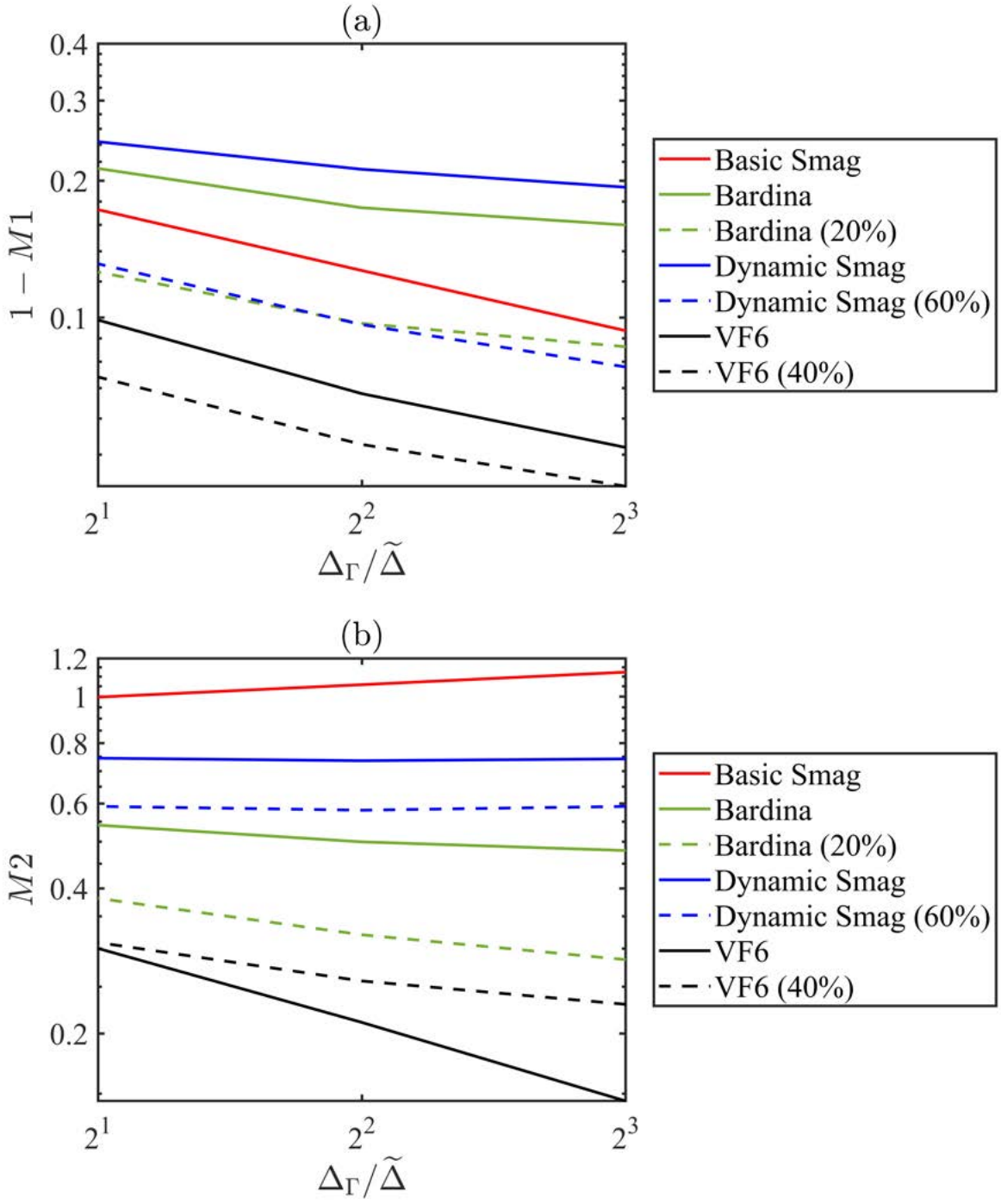

Figure 51. Metrics for scale-by-scale accuracy in support density $G_{\Delta_\Gamma}(\mathbf{x}, t)$ for $\Pi(\mathbf{x}, t)$ with $c_{BS,z} = 0$ in (8.11) and $(c_{BS,z})_{min}$ from Chapter 8 for stable forward simulations, from *a priori* tests with high-Re data using box filters $(k_{\widehat{\Delta}}, k_{\widetilde{\Delta}}) = (5, 10)$. Smaller values correspond to greater accuracy.

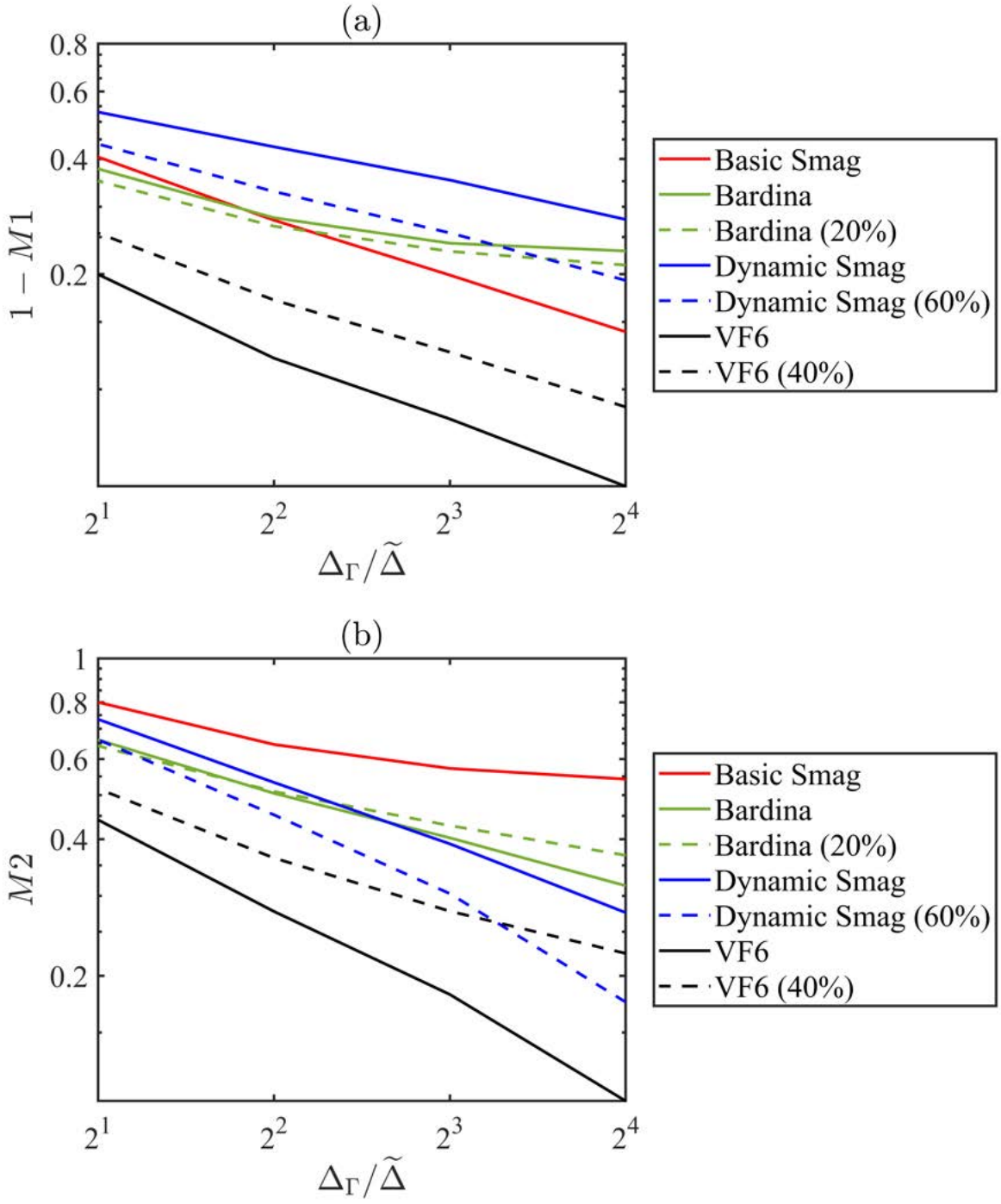

Figure 52. Metrics for scale-by-scale accuracy in support density $G_{\Delta_\Gamma}(\mathbf{x}, t)$ for $z_i(\mathbf{x}, t)$ with $c_{BS,z} = 0$ in (8.11) and $(c_{BS,z})_{min}$ from Chapter 8 for stable forward simulations, from *a priori* tests with high-Re data using box filters $(k_{\widehat{\Delta}}, k_{\widetilde{\Delta}}) = (10, 20)$. Smaller values correspond to greater accuracy.

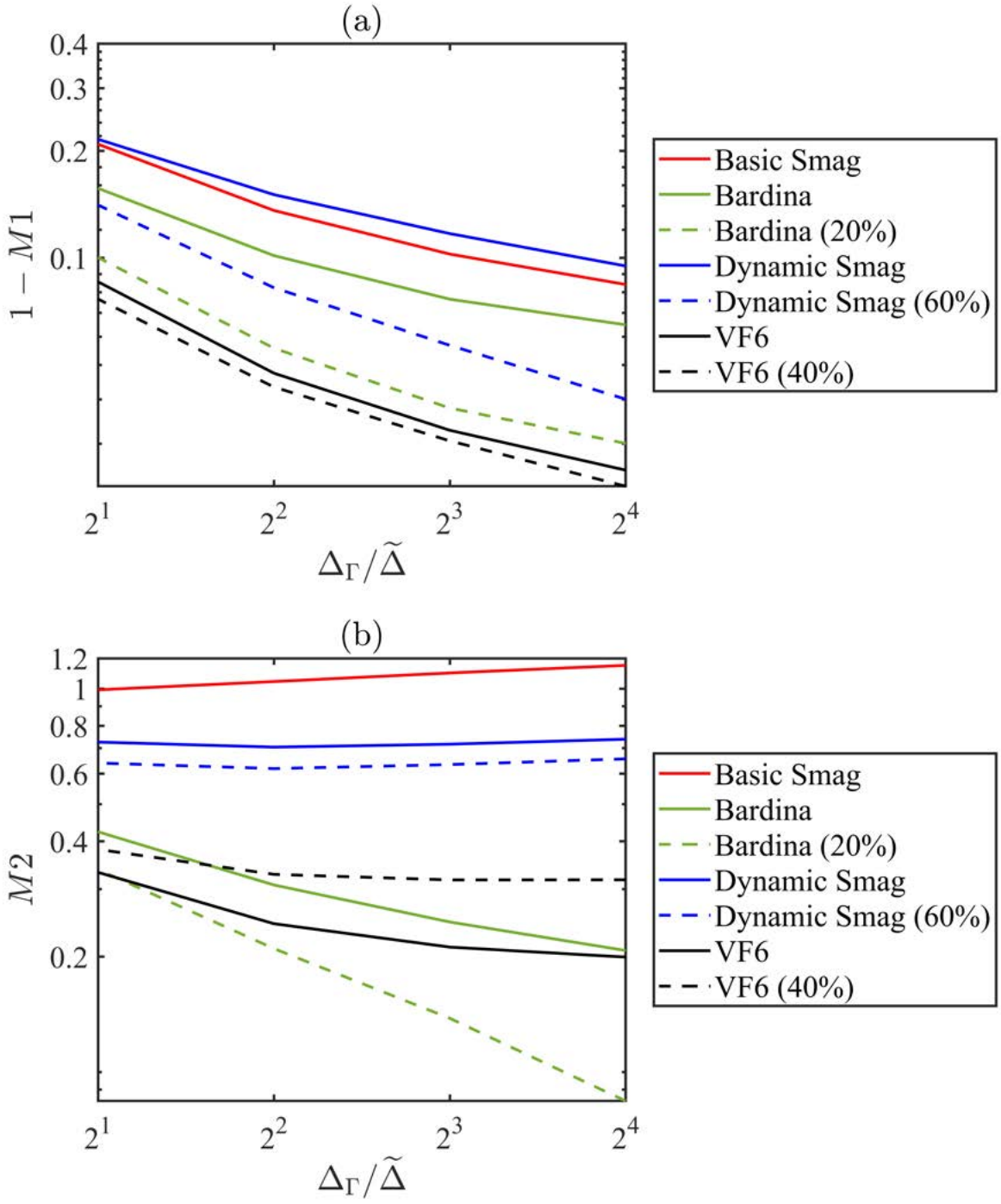

Figure 53. Metrics for scale-by-scale accuracy in support density $G_{\Delta_\Gamma}(\mathbf{x}, t)$ for $\Pi(\mathbf{x}, t)$ with $c_{BS,z} = 0$ in (8.11) and $(c_{BS,z})_{min}$ from Chapter 8 for stable forward simulations, from *a priori* tests with high-Re data using box filters $(k_{\widehat{\Delta}}, k_{\widetilde{\Delta}}) = (10, 20)$. Smaller values correspond to greater accuracy.

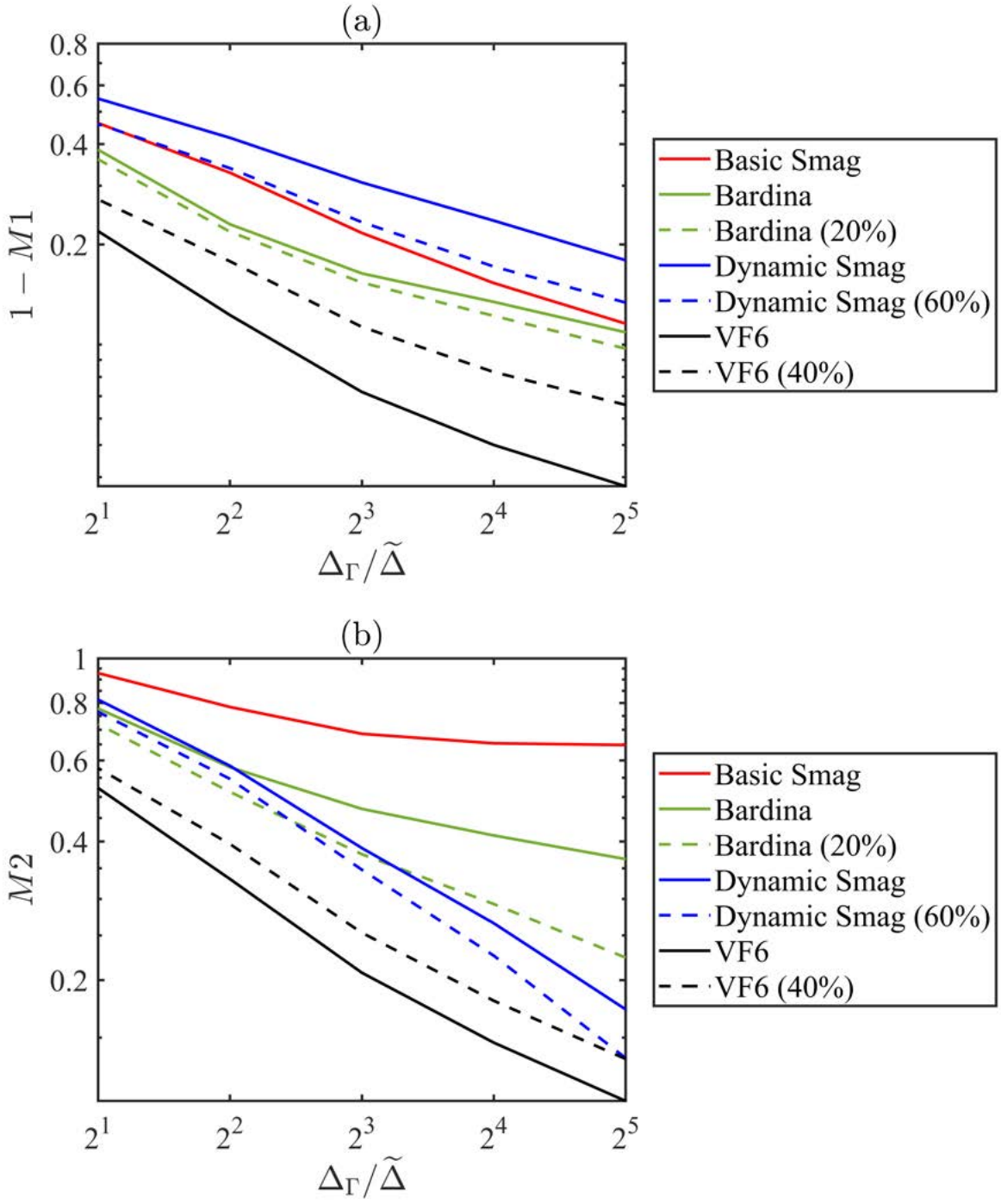

Figure 54. Metrics for scale-by-scale accuracy in support density $G_{\Delta_\Gamma}(\mathbf{x}, t)$ for $z_i(\mathbf{x}, t)$ with $c_{BS,z} = 0$ in (8.11) and $(c_{BS,z})_{min}$ from Chapter 8 for stable forward simulations, from *a priori* tests with high-Re data using box filters $(k_{\widehat{\Delta}}, k_{\widetilde{\Delta}}) = (20, 40)$. Smaller values correspond to greater accuracy.

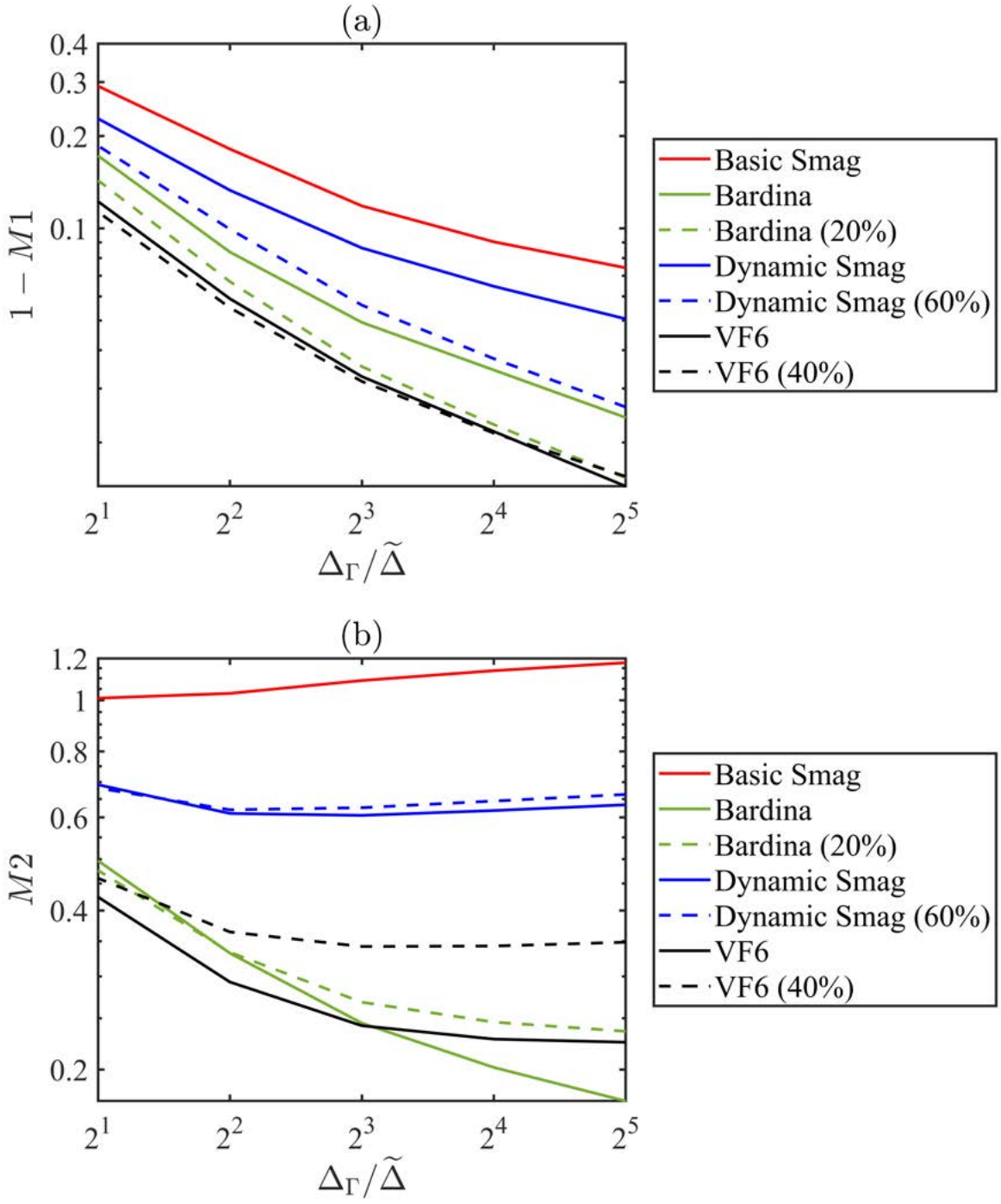

Figure 55. Metrics for scale-by-scale accuracy in support density $G_{\Delta_\Gamma}(\mathbf{x}, t)$ for $\Pi(\mathbf{x}, t)$ with $c_{BS,z} = 0$ in (8.11) and $(c_{BS,z})_{min}$ from Chapter 8 for stable forward simulations, from *a priori* tests with high-Re data using box filters $(k_{\widehat{\Delta}}, k_{\widetilde{\Delta}}) = (20, 40)$. Smaller values correspond to greater accuracy.

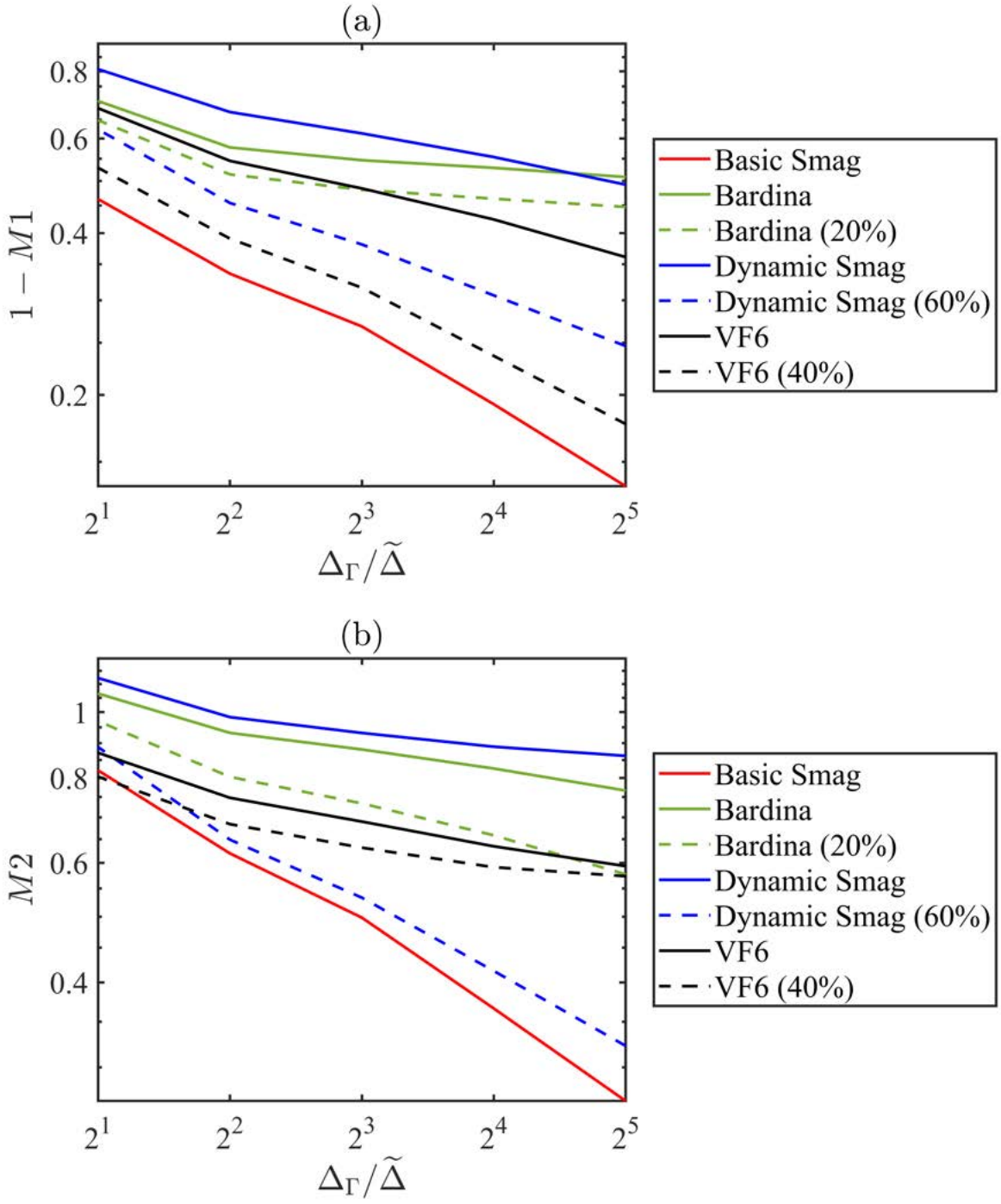

Figure 56. Metrics for scale-by-scale accuracy in support density $G_{\Delta_\Gamma}(\mathbf{x}, t)$ for $z_i(\mathbf{x}, t)$ with $c_{BS,z} = 0$ in (8.11) and $(c_{BS,z})_{min}$ from Chapter 8 for stable forward simulations, from *a priori* tests with high-Re data using box filters $(k_{\widehat{\Delta}}, k_{\widetilde{\Delta}}) = (30, 60)$. Smaller values correspond to greater accuracy.

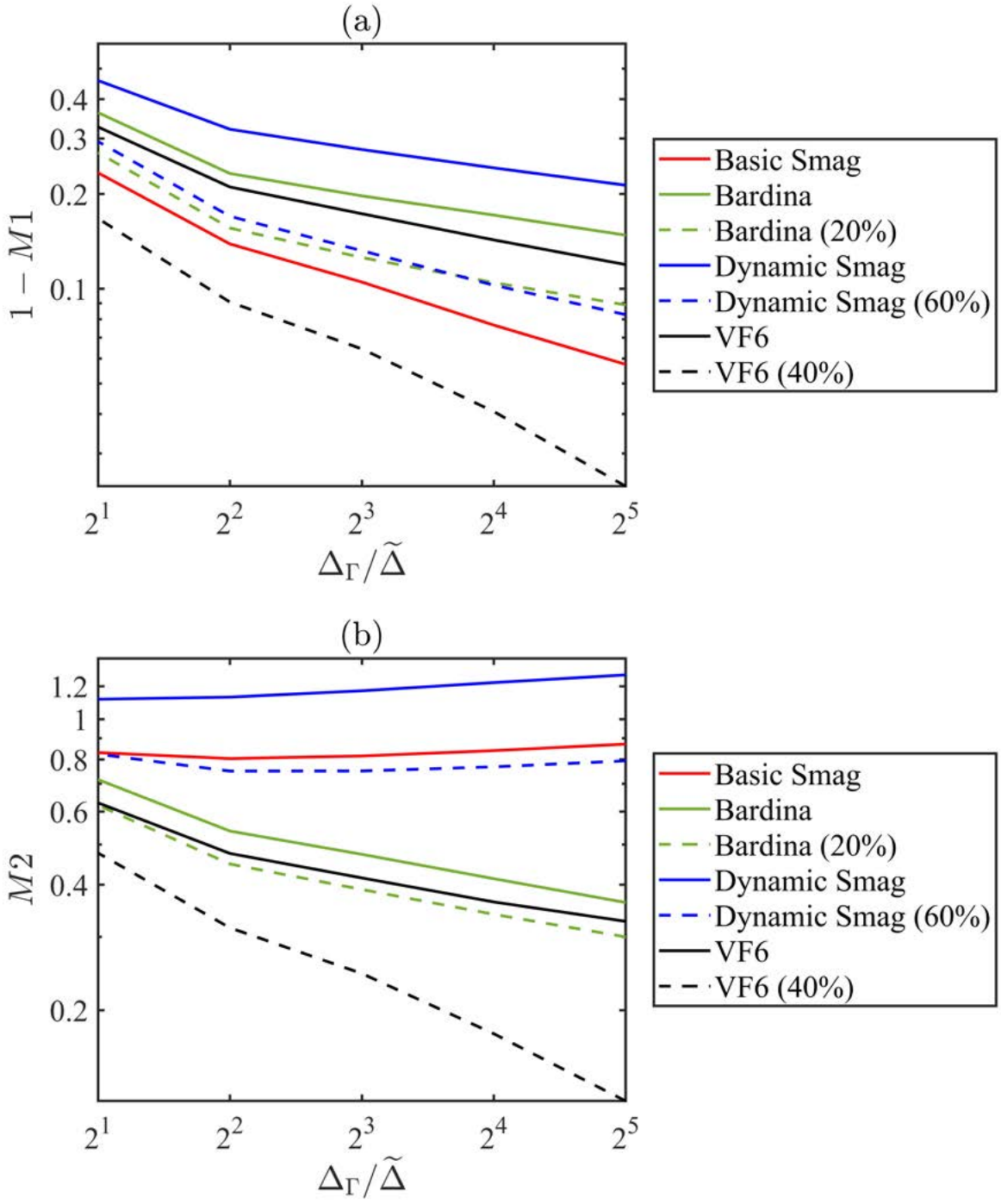

Figure 57. Metrics for scale-by-scale accuracy in support density $G_{\Delta_\Gamma}(\mathbf{x}, t)$ for $\Pi(\mathbf{x}, t)$ with $c_{BS,z} = 0$ in (8.11) and $(c_{BS,z})_{min}$ from Chapter 8 for stable forward simulations, from *a priori* tests with high-Re data using box filters $(k_{\widehat{\Delta}}, k_{\widetilde{\Delta}}) = (30, 60)$. Smaller values correspond to greater accuracy.

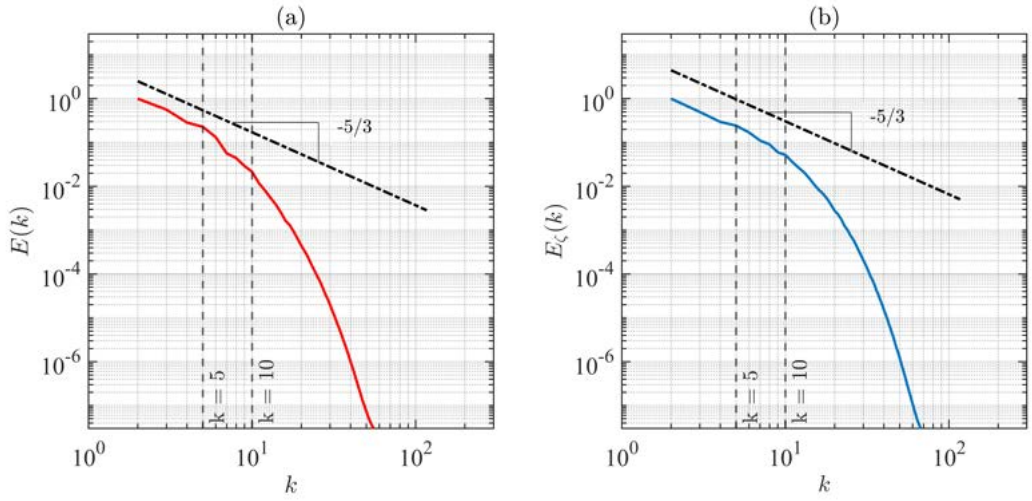

Figure 58. Locations of test-scale and LES-scale filters for $(k_{\widehat{\Delta}}, k_{\widetilde{\Delta}}) = (5, 10)$ in kinetic energy spectrum $E(k)$ (left) and scalar energy spectrum $E_\varphi(k)$ (right) from the low-Re DNS dataset.

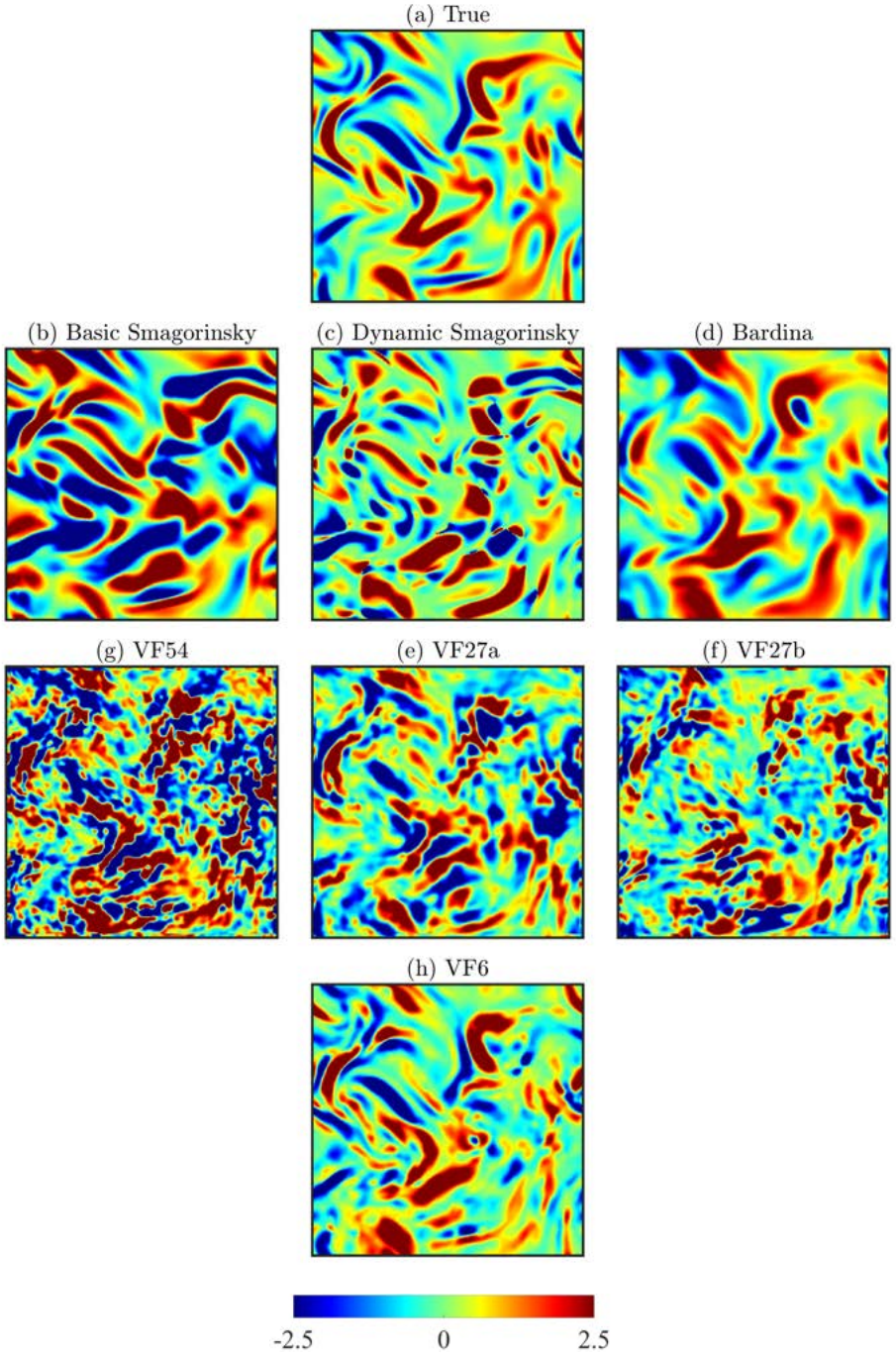

Figure 59. Typical results for subgrid scalar flux component $z_1(\mathbf{x}, t)$ from *a priori* tests with the low-Re dataset using box filters with $(k_{\widehat{\Delta}}, k_{\widetilde{\Delta}}) = (5, 10)$.

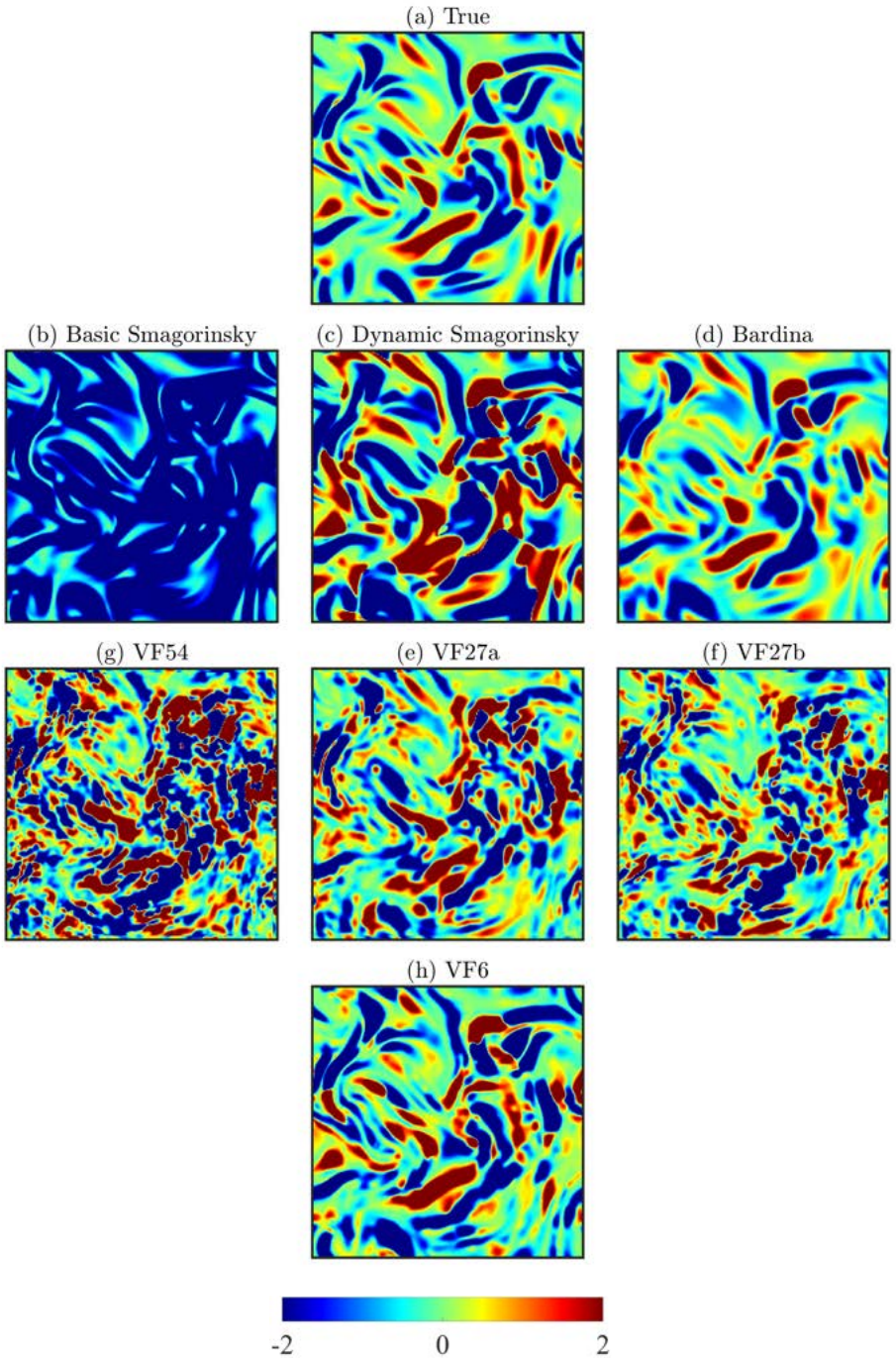

Figure 60. Typical results for subgrid scalar energy production $\Pi(\mathbf{x}, t)$ from *a priori* tests with the low-Re dataset using box filters with $(k_{\widehat{\Delta}}, k_{\widetilde{\Delta}}) = (5, 10)$.

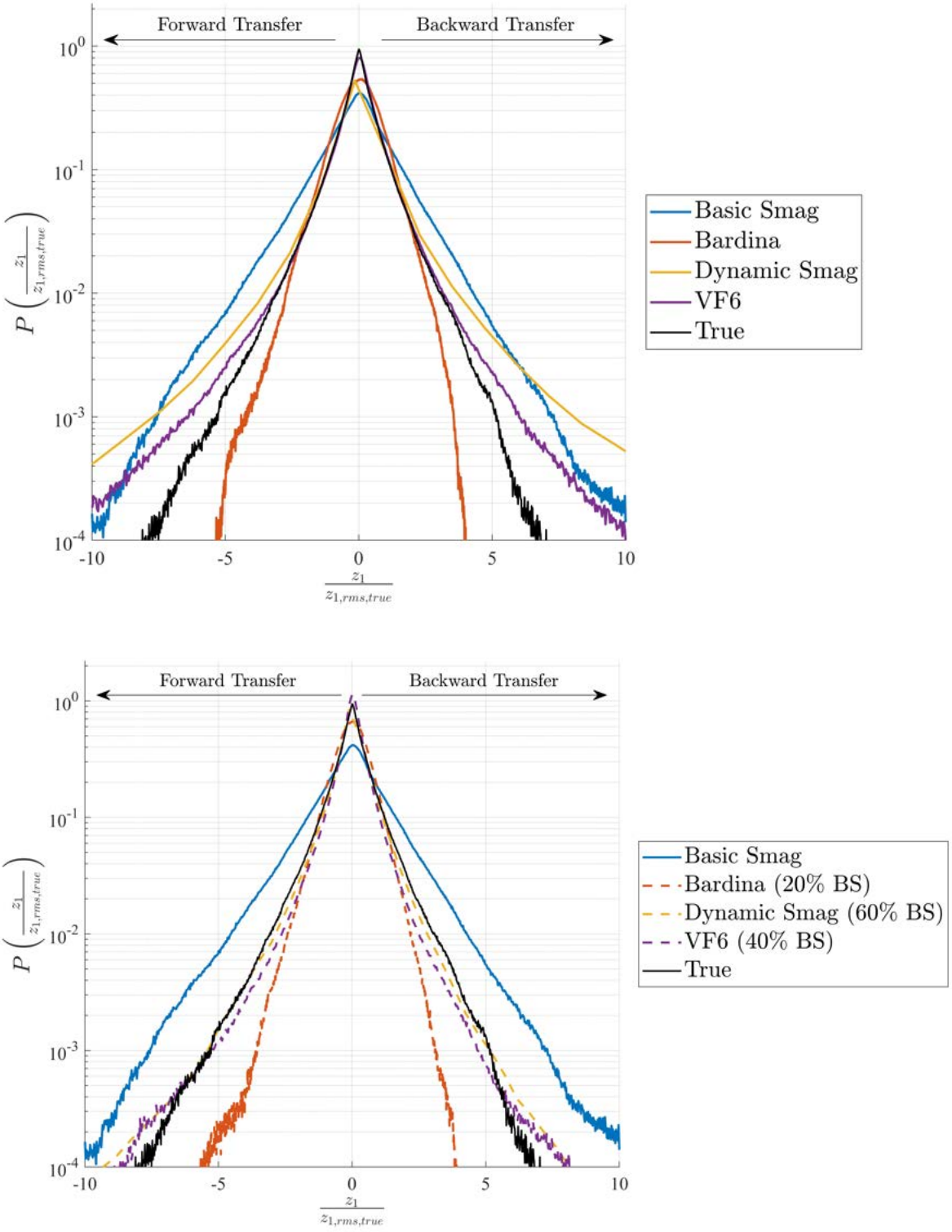

Figure 61. PDFs for $z_1(\mathbf{x}, t)$ from *a priori* tests with low-Re data using box filters having $(k_{\widehat{\Delta}}, k_{\widetilde{\Delta}}) = (5, 10)$, for $c_{BS,z} = 0$ in (8.11) *(top)* and with minimum required $c_{BS,z}$ value from Chapter 8 for stable forward simulations *(bottom)*.

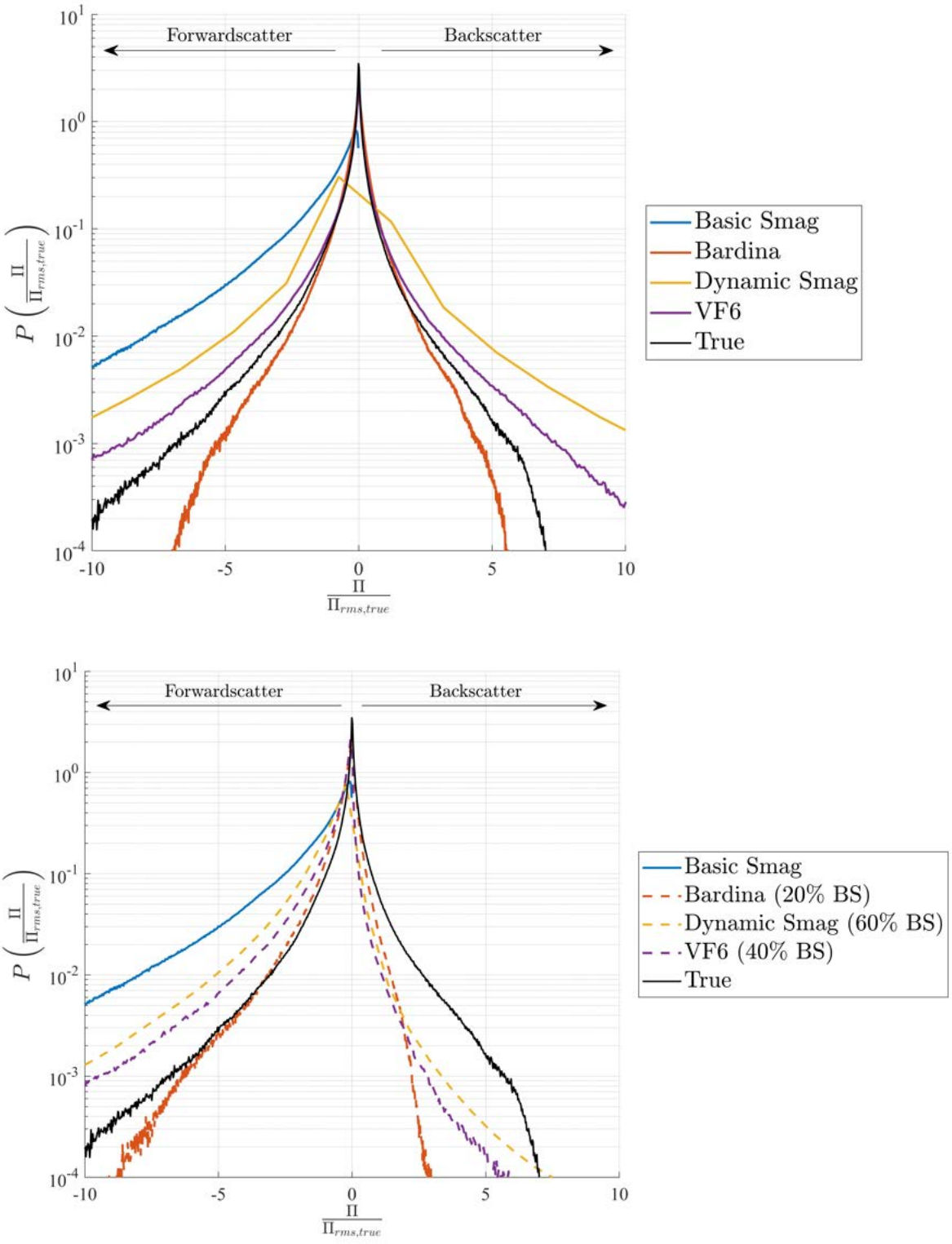

Figure 62. PDFs for $\Pi(\mathbf{x}, t)$ from *a priori* tests with low-Re data using box filters having $(k_{\widehat{\Delta}}, k_{\widetilde{\Delta}}) = (5, 10)$, for $c_{BS,z} = 0$ in (8.11) *(top)* and with minimum required $c_{BS,z}$ value from Chapter 8 for stable forward simulations *(bottom)*.

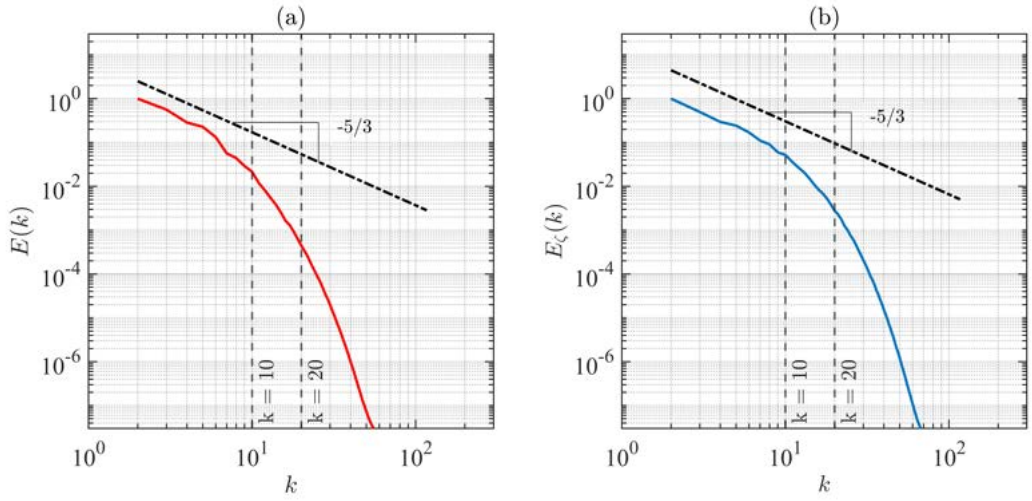

Figure 63. Locations of test-scale and LES-scale filters for $(k_{\widehat{\Delta}}, k_{\widetilde{\Delta}}) = (10, 20)$ in kinetic energy spectrum $E(k)$ (left) and scalar energy spectrum $E_\varphi(k)$ (right) from the high-Re DNS dataset.

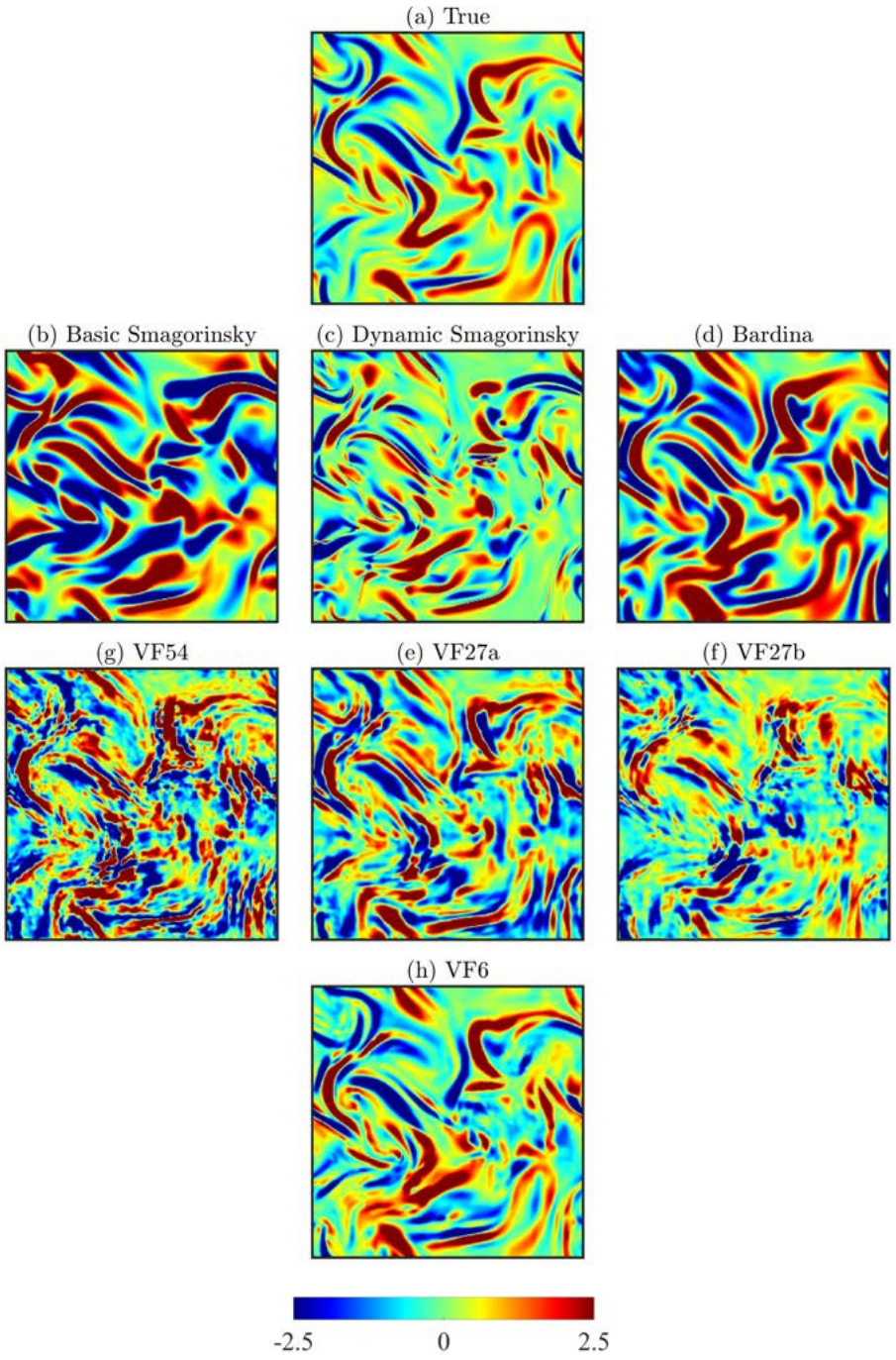

Figure 64. Typical results for subgrid scalar flux component $z_1(\mathbf{x}, t)$ from *a priori* tests with the low-Re dataset using box filters with $(k_{\widehat{\Delta}}, k_{\widetilde{\Delta}}) = (10, 20)$.

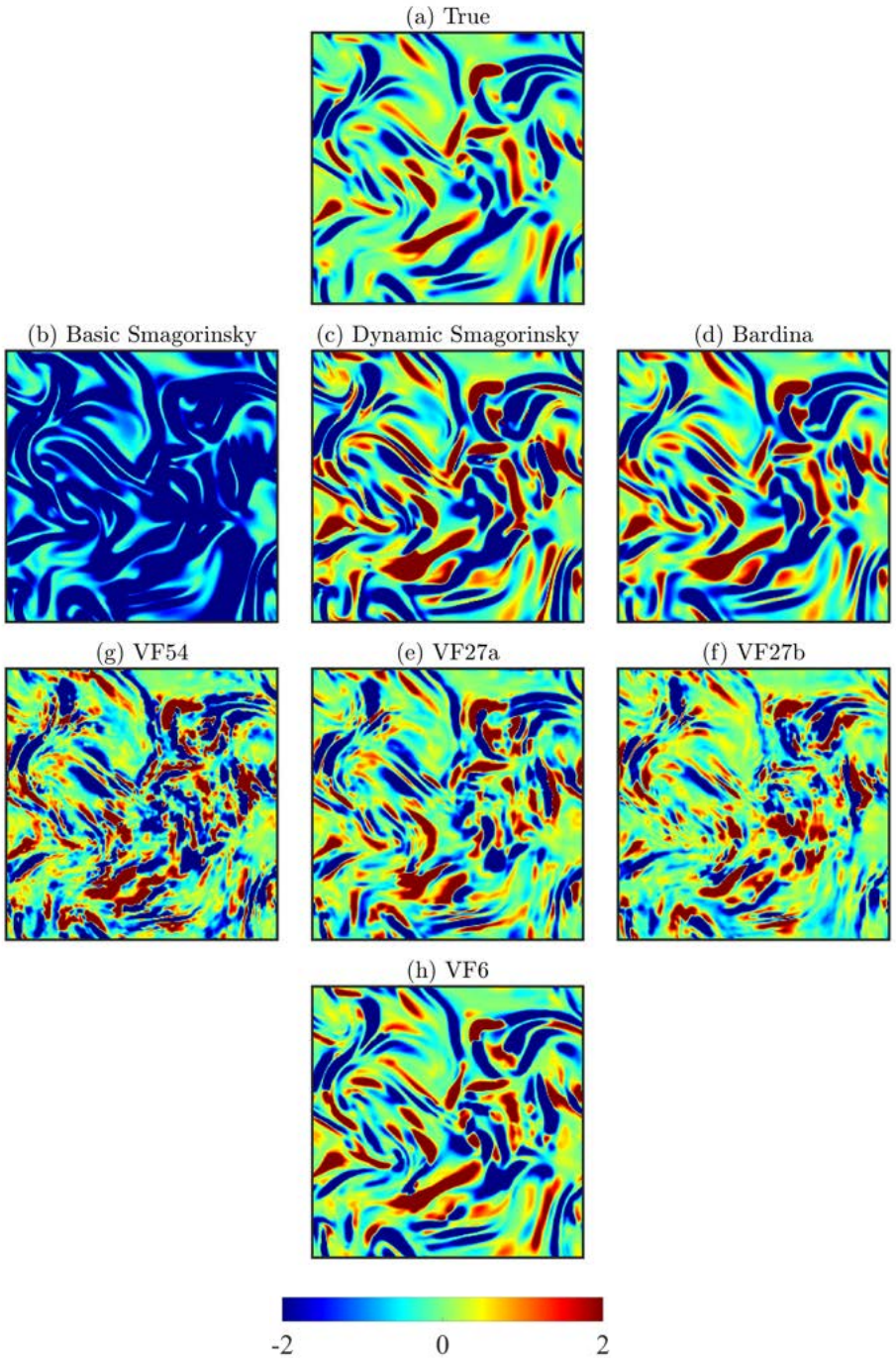

Figure 65. Typical results for subgrid scalar energy production $\Pi(\mathbf{x}, t)$ from *a priori* tests with the low-Re dataset using box filters with $(k_{\widehat{\Delta}}, k_{\widetilde{\Delta}}) = (10, 20)$.

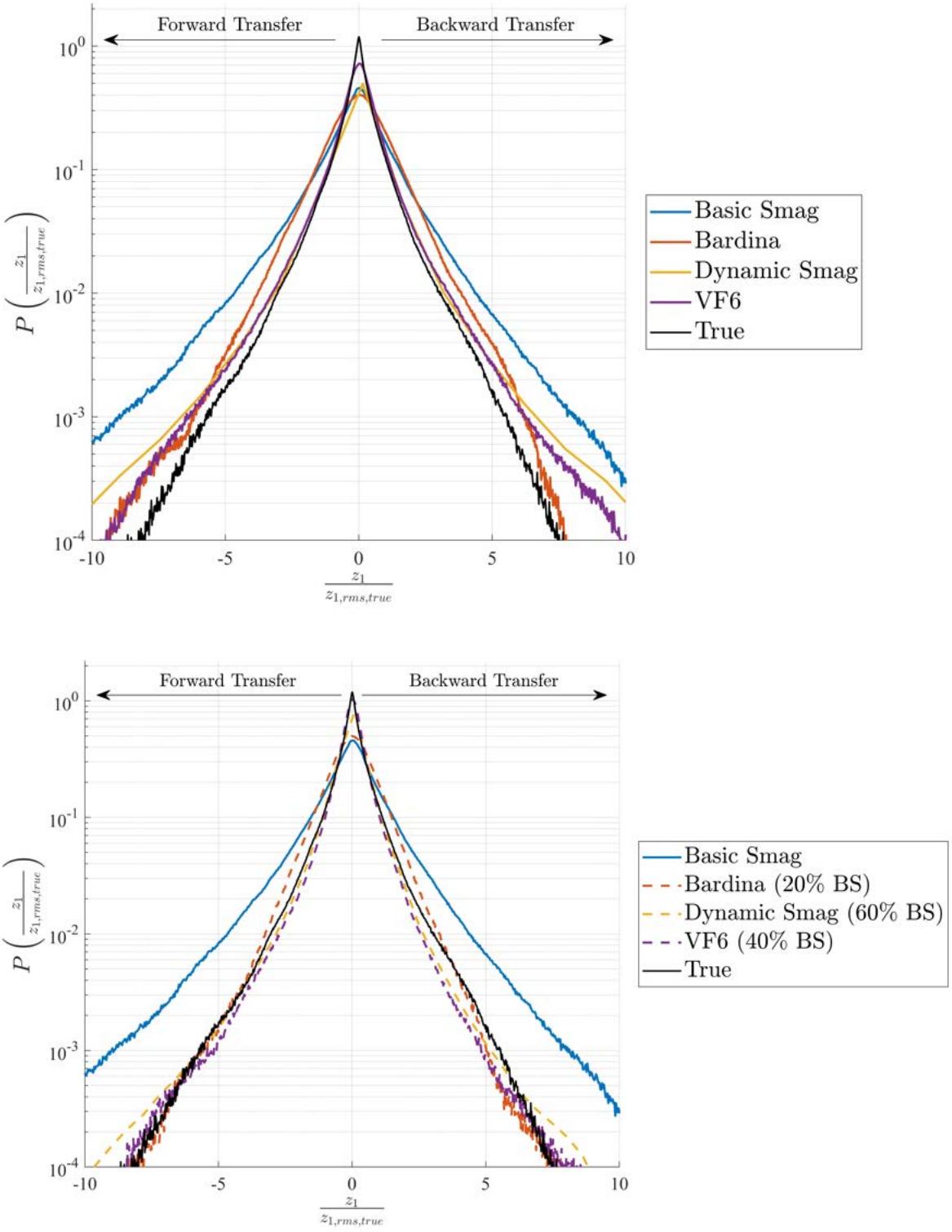

Figure 66. PDFs for $z_1(\mathbf{x}, t)$ from *a priori* tests with low-Re data using box filters having $(k_{\widehat{\Delta}}, k_{\widetilde{\Delta}}) = (10, 20)$, for $c_{BS,z} = 0$ in (8.11) *(top)* and with minimum required $c_{BS,z}$ value from Chapter 8 for stable forward simulations *(bottom)*.

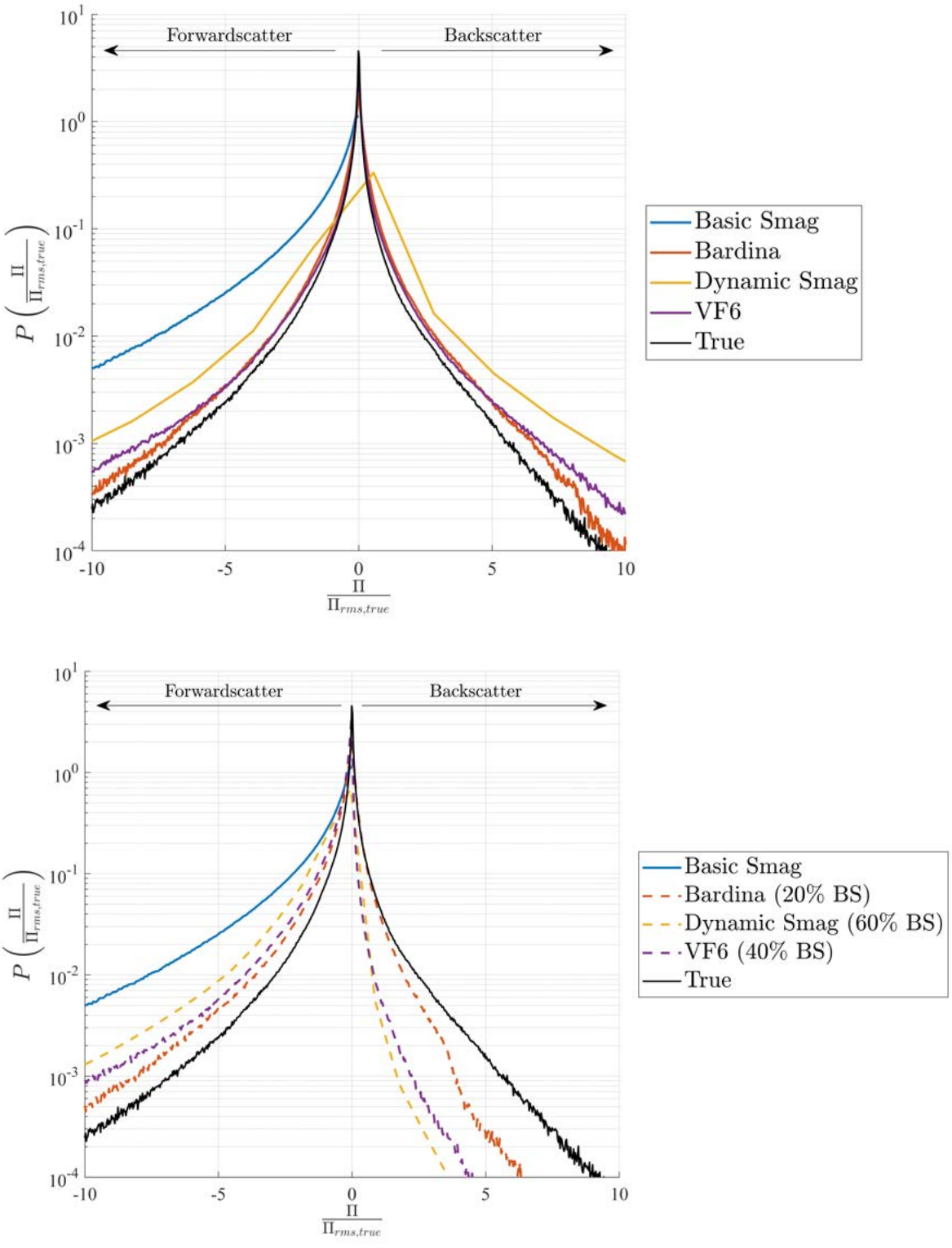

Figure 67. PDFs for $\Pi(\mathbf{x}, t)$ from *a priori* tests with low-Re data using box filters having $(k_{\widehat{\Delta}}, k_{\widetilde{\Delta}}) = (10, 20)$, for $c_{BS,z} = 0$ in (8.11) *(top)* and with minimum required $c_{BS,z}$ value from Chapter 8 for stable forward simulations *(bottom)*.

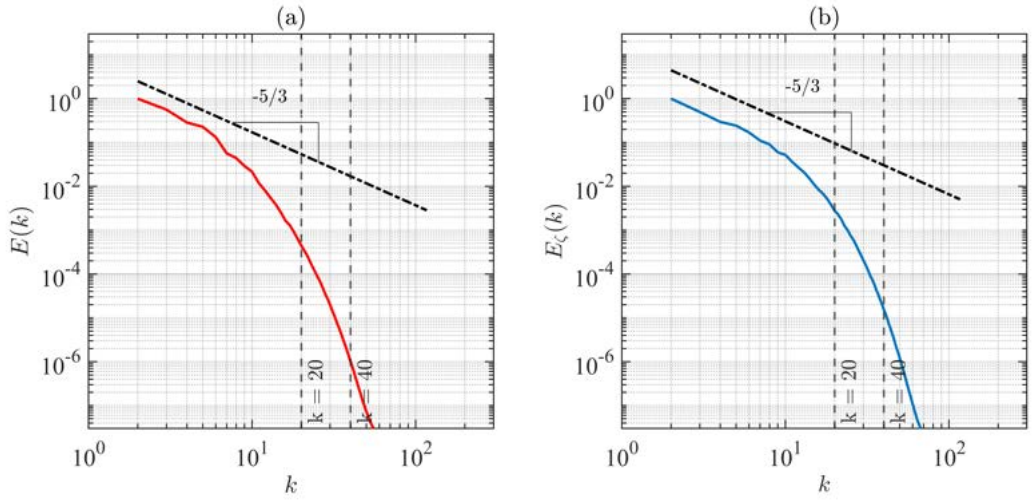

Figure 68. Locations of test-scale and LES-scale filters for $(k_{\widehat{\Delta}}, k_{\widetilde{\Delta}}) = (20, 40)$ in kinetic energy spectrum $E(k)$ (left) and scalar energy spectrum $E_\varphi(k)$ (right) from the high-Re DNS dataset.

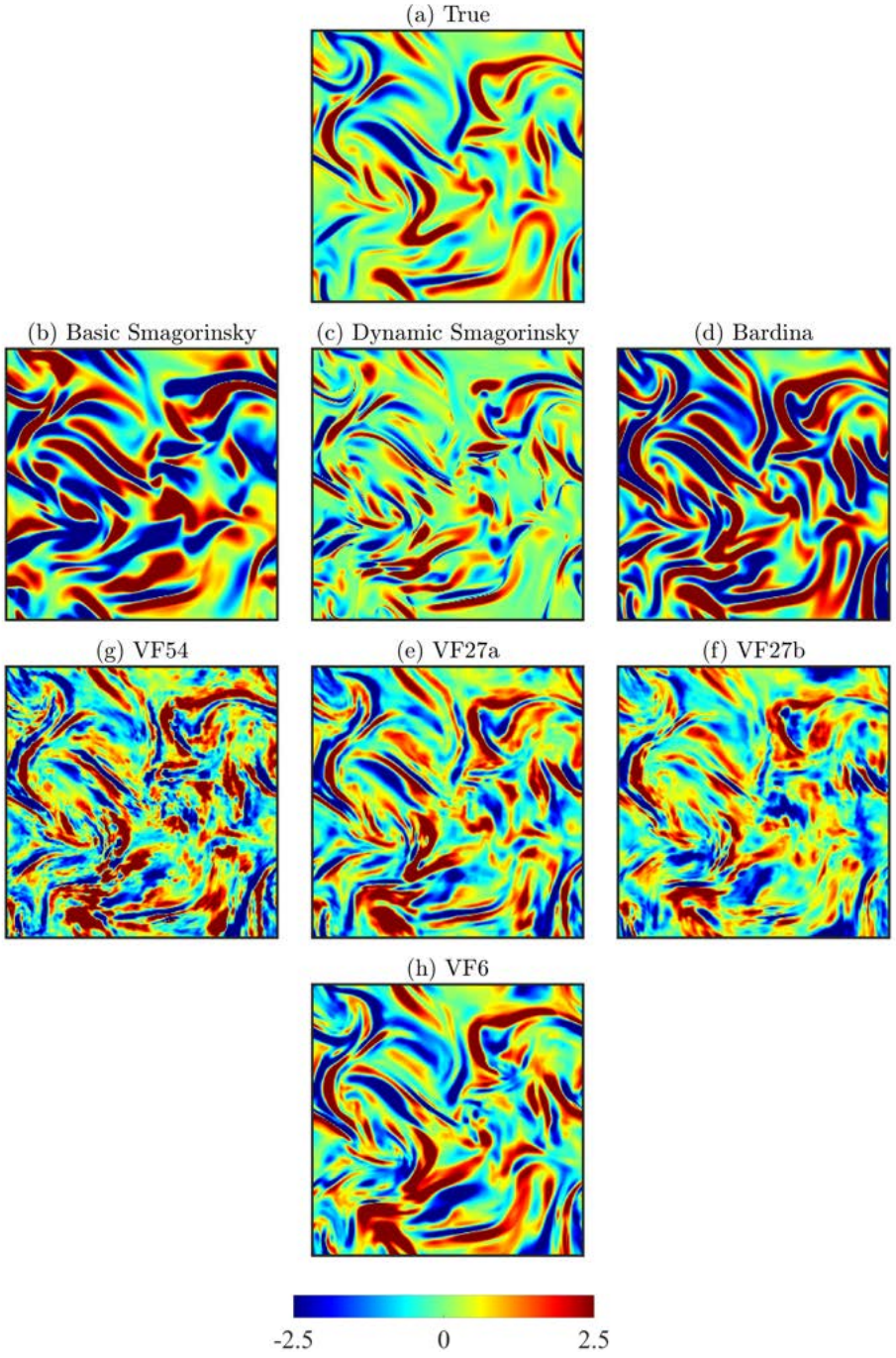

Figure 69. Typical results for subgrid scalar flux component $z_1(\mathbf{x}, t)$ from *a priori* tests with the low-Re dataset using box filters with $(k_{\widehat{\Delta}}, k_{\widetilde{\Delta}}) = (20, 40)$.

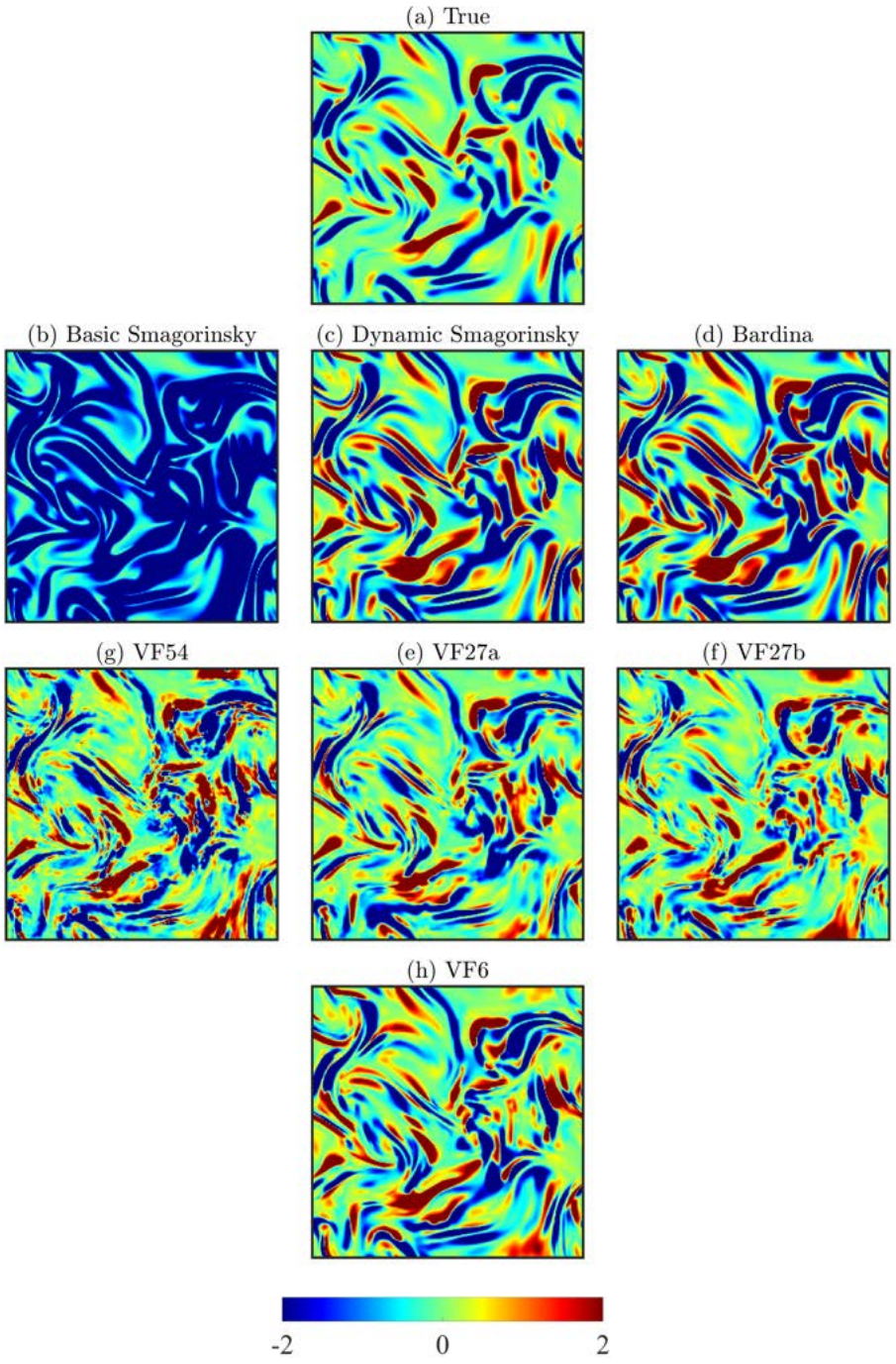

Figure 70. Typical results for subgrid scalar energy production $\Pi(\mathbf{x}, t)$ from *a priori* tests with the low-Re dataset using box filters with $(k_{\widehat{\Delta}}, k_{\widetilde{\Delta}}) = (20, 40)$.

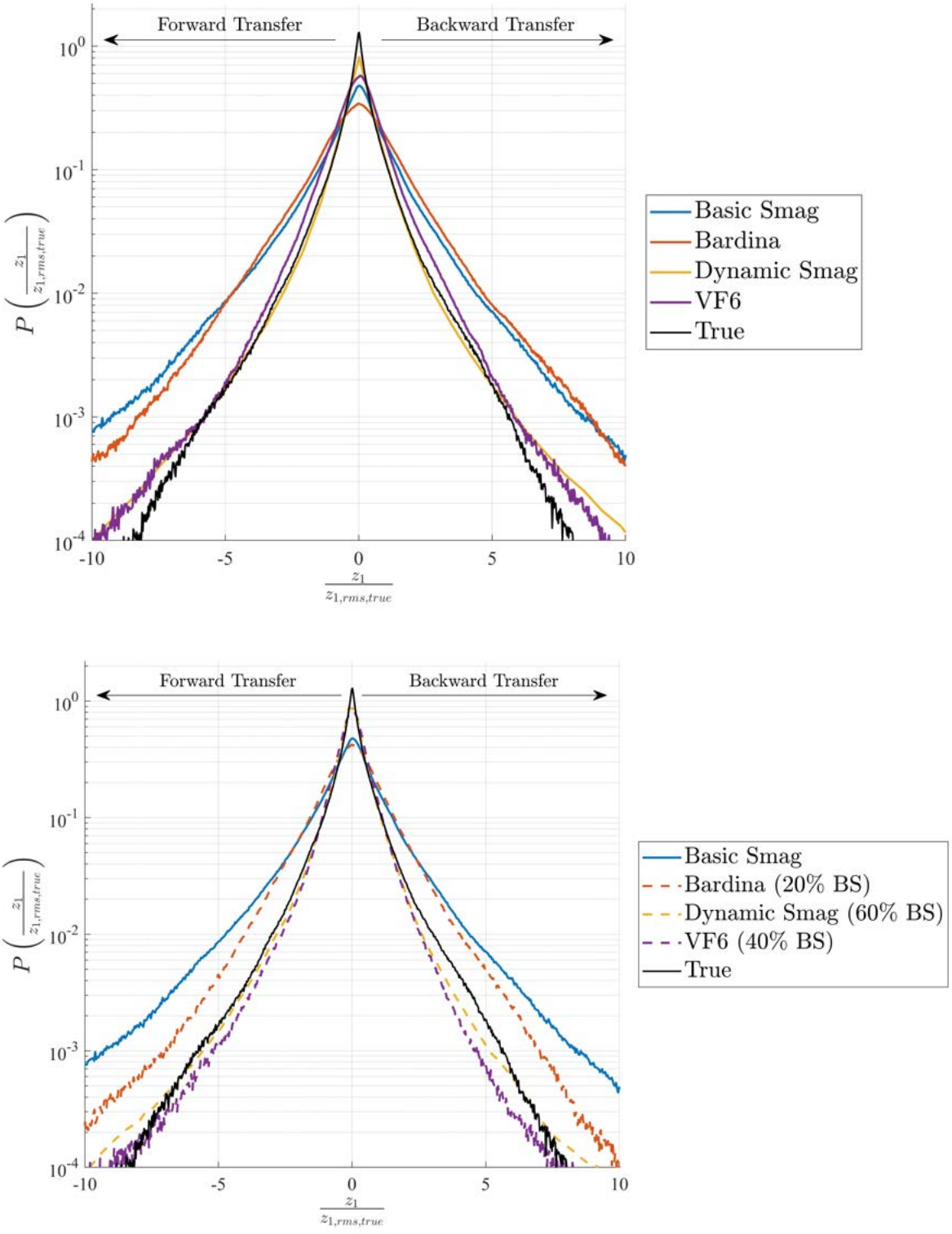

Figure 71. PDFs for $z_1(\mathbf{x}, t)$ from *a priori* tests with low-Re data using box filters having $(k_{\widehat{\Delta}}, k_{\widetilde{\Delta}}) = (20, 40)$, for $c_{BS,z} = 0$ in (8.11) *(top)* and with minimum required $c_{BS,z}$ value from Chapter 8 for stable forward simulations *(bottom)*.

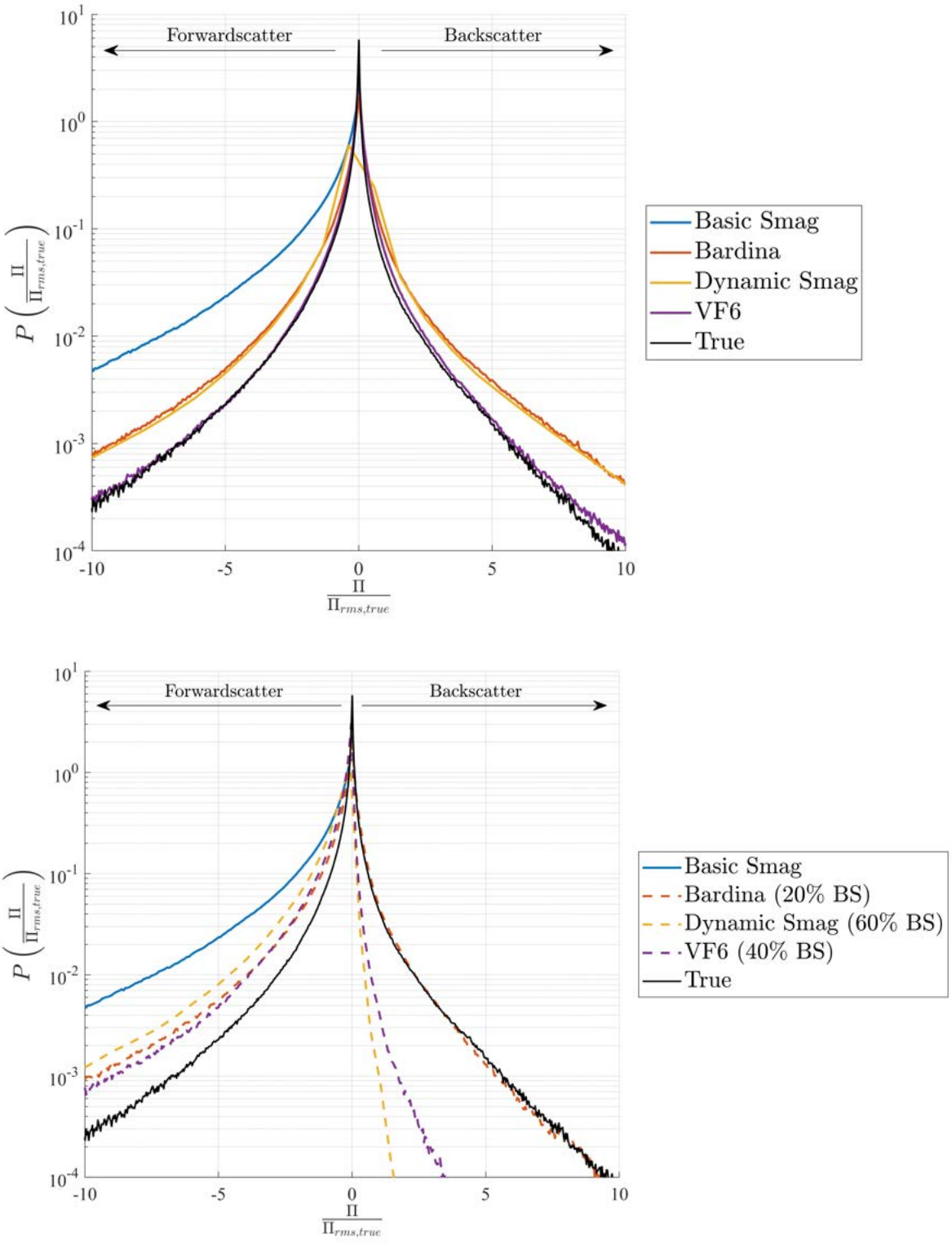

Figure 72. PDFs for $\Pi(\mathbf{x}, t)$ from *a priori* tests with low-Re data using box filters having $(k_{\widehat{\Delta}}, k_{\widetilde{\Delta}}) = (20, 40)$, for $c_{BS,z} = 0$ in (8.11) *(top)* and with minimum required $c_{BS,z}$ value from Chapter 8 for stable forward simulations *(bottom)*.

Chapter 8

STABILITY OF SUBGRID SCALAR FLUX REPRESENTATIONS

Results from the *a priori* tests in Chapter 7 showed that the subgrid scalar flux representation VF6 in (3.33) – which in Section 3.2 is shown to be the complete and minimal tensorally-correct representation for the subgrid scalar flux $\mathbf{z}$ in the strain rate and rotation rate tensors, $\mathbf{S}$ and $\mathbf{R}$, and the scalar gradient vector $\nabla\varphi$ – is the most accurate of the subgrid scalar flux representations considered there. This chapter now uses forward simulations to assess the computational stability of autonomic closure with the VF6 representation for the subgrid scalar flux, and compares with the stability of traditional LES closure based on the dynamic Smagorinsky model in Section 7.1.2 and the Bardina scale similarity model in Section 7.1.3.

8.1 Scalar Mixing Simulations with the Pseudo-Spectral LES Code

The filtered scalar transport equation in (1.10) was added in the pseudo-spectral code to enable forward simulations of turbulent conserved scalar mixing with high-order accuracy. All cases simulated an initial scalar field being mixed by statistically-stationary homogeneous isotropic turbulence in a 64^3 domain with periodic boundary conditions. The underlying turbulent flow was sustained by forcing at wavenumbers $2 \leq k \leq 4$, as described in Section 6.1. The scalar field was initialized only after the turbulence had reached its statistically-stationary state, with the initial scalar field consisting of a one period of a sinusoidal variation with $0 \leq \varphi \leq 1$ along one direction of the domain, as shown in the upper row of Figure 73. Thereafter the scalar field was mixed by the underlying turbulent flow and reached a statistically homogeneous isotropic state, as shown in the bottom row of Figure 73. The Schmidt number in all cases was $Sc = 1$. Since no scalar energy is added during the simulation, the scalar

field $\varphi(\mathbf{x},t)$ gradually homogenizes and the associated scalar energy $E_\varphi(\mathbf{x},t)$ thus decreases during the course of the simulation.

For the given sinusoidal initial condition, the domain-averaged scalar energy

$$E_\varphi(t) \equiv \frac{1}{V}\int_V \frac{1}{2}\widetilde{\varphi}^2 \; dV \tag{8.1}$$

has initial value $E_\varphi(0) \equiv E_{\varphi,\,0} = 0.1875$, and when the scalar field fully homogenizes as $t \to \infty$ it reaches $E_\varphi(\infty) \equiv E_{\varphi,\,\infty} = 0.125$. Defining the relative scalar energy as

$$\Sigma_\varphi(t) \equiv \frac{E_\varphi(t) - E_{\varphi,\,\infty}}{E_{\varphi,\,0} - E_{\varphi,\,\infty}}\,, \tag{8.2}$$

then this satisfies

$$\Sigma_\varphi(0) = 1 \quad \text{and} \quad \Sigma_\varphi(\infty) = 0\,. \tag{8.3}$$

8.1.1 Asymptotic Scalar Energy Decay Scaling

For the statistically homogeneous scalar field in these simulations, from (1.12) the domain-averaged scalar energy E_φ satisfies

$$\frac{dE_\varphi}{dt} \;=\; -D_\varphi \left\langle \frac{\partial\widetilde{\varphi}}{\partial x_i}\frac{\partial\widetilde{\varphi}}{\partial x_i} \right\rangle_V \;\equiv\; -\chi\,, \tag{8.4}$$

where χ is the domain-averaged scalar energy dissipation rate. With $k(t)$ denoting the turbulence kinetic energy and $\epsilon(t)$ its dissipation rate, it can be anticipated that

$$\chi = f\Big(E_\varphi\,,(k/\epsilon)\Big)\,, \tag{8.5}$$

for which dimensional consistency then requires

$$\chi \sim E_\varphi\,(\epsilon/k)\,. \tag{8.6}$$

Using C_χ to denote the proportionality constant, which must be dimensionless and universal, then gives

$$\frac{dE_\varphi}{dt} \;=\; -C_\chi\,E_\varphi\,(\epsilon/k)\,. \tag{8.7}$$

Defining the scaled time $\tau = t/(k/\epsilon)$ this becomes

$$\frac{dE_\varphi}{d\tau} \;=\; -C_\chi\,E_\varphi\,. \tag{8.8}$$

and thus

$$E_\varphi(t) = E_{\varphi,0} \cdot \exp - C_\chi(\tau - \tau_0)\,. \tag{8.9}$$

For $\tau \gg \tau_0$, (8.9) and (8.2) with (8.3) then show that the asymptotic scalar energy decay scaling in these simulations must be

$$\Sigma_\varphi(t) = \exp - C_\chi \left(\frac{t}{(k/\epsilon)} \right) \tag{8.10}$$

8.1.2 Comparison with Simulation Results

To test the scaling in (8.10), Figure 74 shows the scalar energy from a simulation with the basic Smagorinsky model for the subgrid stress and also the basic Smagorinsky model for the subgrid scalar flux. Since both models are purely dissipative, this simulation is guaranteed to remain stable. The top panel shows the time evolution of E_φ, which as noted above has the initial value $E_{\varphi,0} = 0.1875$ and the asymptotic final value $E_{\varphi,\infty} = 0.125$, where the latter is shown by the dashed line in Figure 74. The bottom panel in Figure 74 shows the corresponding relative scalar energy in (8.2) in semi-logarithmic form, for which the exponential asymptotic decay in (8.10) would appear as a straight line with its slope equal to C_χ. It is apparent in the lower panel that, after a time $\tau_0 \approx 2$, during which all memory of the initial conditions in the scalar field is lost, the relative scalar energy $\Sigma_\varphi(t)$ clearly follows the asymptotic decay in (8.10), as the underlying homogeneous isotropic turbulence acts to homogenize the scalar field and thereby drive $\Sigma_\varphi \to 0$. By $\tau \approx 35$ the relative scalar energy has decreased to near the machine limit of the simulation.

Figure 75 shows results from several such simulations, graphed the same way as in the bottom panel of Figure 74, that have different values for E_f in the kinetic energy forcing and different values for the initial scalar energy $E_{\varphi,0}$. The changes in E_f cause $k(t)$ and $\epsilon(t)$ to differ among these cases, and as a result in the top panel of Figure 75 where the relative scalar energy Σ_φ is graphed in the dimensional time t, the slopes are different, corresponding to different decay rates. However in the bottom panel, where

the same results are graphed in the scaled time $\tau = t/(k/\epsilon)$ as in (8.10), the curves essentially collapse to within the statistical convergence limits of the volume average due to the finite domain size. This is supported by Figure 76, showing the derivative of each curve, where the variations between cases are seen to be no larger than the variations with time for any given case. Table 10 gives the resulting average slope, which corresponds to the universal constant C_χ in (8.10), and the 95% statistical uncertainty interval for each case, where the differences between cases are indeed seen to be smaller than the statistical uncertainty.

In rest of this chapter, results from forward simulations based on traditional and autonomic closure with various combinations of subgrid stress representations and subgrid scalar flux representations, and with various levels of added dissipation, are presented in the same form as the upper and lower panels in Figure 74 to assess the computational stability of these representations.

8.2 Computational Stability of Turbulent Conserved Scalar Mixing

As in Figure 74, which corresponds to Case 1 in Table 11, Figures 77-85 show the domain-averaged scalar energy $E_\varphi(t)$ in (8.1) and the relative scalar energy $\Sigma_\varphi(t)$ in (8.2) from forward simulations of turbulent conserved scalar mixing for all other cases in Table 11. Each case corresponds to a particular combination of the subgrid stress representation for $\boldsymbol{\tau}$ and the subgrid scalar flux representation for $\mathbf{z}$. As in Section 8.1, in all cases the scalar field was initialized as shown in the top row of Figure 73 only after the underlying turbulent flow had reached its statistically-stationary homogeneous isotropic state. Since the scalar is passive, from each of the subgrid stress representations for $\boldsymbol{\tau}$ the resulting turbulent kinetic energy $k(t)$, the domain-average $\langle k \rangle(t)$, and the kinetic energy spectrum $E(k)$ are similar to those shown in Figures 11-20 in Chapter 6.

Importantly, for each case in Table 11, Figures 77-85 show the resulting $\Sigma_\varphi(t)$ for varying levels of added dissipation in both the subgrid stress representation for $\boldsymbol{\tau}$ and

the subgrid scalar flux representation for $\mathbf{z}$. Since the basic Smagorinsky models for $\boldsymbol{\tau}$ in Section 5.1.1.1 and $\mathbf{z}$ in Section 7.1.1 are both purely dissipative, added dissipation was introduced in each representation $(\ )^R$ as

$$\tau_{ij} = (1 - c_{BS,\tau})\,\tau_{ij}^R + c_{BS,\tau}\,\tau_{ij}^{BS} \tag{8.11a}$$

$$z_i = (1 - c_{BS,z})\,z_i^R + c_{BS,z}\,z_i^{BS} \tag{8.11b}$$

where $(\ )^{BS}$ denotes the basic Smagorinsky model, and $c_{BS,\tau}$ and $c_{BS,z}$ are constants that set the desired amount of added dissipation in each representation.

The following sections identify insights obtained from these forward simulations as they relate to the computational stability of traditional closure with prescribed models for $\boldsymbol{\tau}$ and $\mathbf{z}$, and the stability of autonomic closure with various generalized representations for $\boldsymbol{\tau}$ and $\mathbf{z}$.

8.2.1 Traditional Closure with Prescribed Models

Cases 1, 2, and 3 in Table 11 correspond to traditional closures for $\boldsymbol{\tau}$ and $\mathbf{z}$ via prescribed models. In each case, the basic Smagorinsky model in Section 5.1.1.1 was used to represent $\boldsymbol{\tau}$, while $\mathbf{z}$ was represented with either the basic Smagorinsky model in Section 7.1.1, the dynamic Smagorinsky model in Section 7.1.2, or the Bardina scale similarity model in Section 7.1.3. Corresponding results for $E_\varphi(t)$ and $\Sigma_\varphi(t)$ for each combination are shown in Figures 74, 77, and 78.

In Figure 74, the basic Smagorinsky models for both $\boldsymbol{\tau}$ and $\mathbf{z}$ are manifestly stable, though they are seen in Figures 2-4 and Figures 23-74 to give highly inaccurate representations of the relevant the $\tau_{ij}(\mathbf{x},t)$ and $z_i(\mathbf{x},t)$ fields and their associated subgrid production fields $P(\mathbf{x},t)$ and $\Pi(\mathbf{x},t)$.

In Figure 77, when instead the Bardina scale similarity model is used for $\mathbf{z}$ as in Case 2, it is technically stable even with no added dissipation, in the sense that blowup does not occur, but at least 30% added dissipation must be included to avoid the clearly nonphysical initial increase in domain-averaged scalar energy $E_\varphi(t)$, which

instead must solely decrease with time throughout these simulations. This initial increase can be best seen in the top panel, and indicates near-instability of the Bardina scale similarity model. With 10% and 20% added dissipation, this nonphysical initial increase in $E_\varphi(t)$ is reduced but still present. Only when the added dissipation is increased to 30% does this increase in scalar energy disappear.

In Figure 78, when instead the dynamic Smagorinsky model is used for $\mathbf{z}$ in Case 3, it can be seen that at least 50% added dissipation is needed to avoid computational blowup, though the lower panel shows incipient blowup being encountered repeatedly during such a simulation. Only when the added dissipation is increased to 60% does the forward simulation with the dynamic Smagorinsky model remain manifestly stable.

8.2.2 Autonomic Closure with Parametric Representations

Cases 4-10 in Table 11 correspond to autonomic closure for $\boldsymbol{\tau}$ and/or $\mathbf{z}$ based on various combinations of the parametric representations TF5 and/or VF6, as well as with traditional prescribed models for $\mathbf{z}$. Corresponding results for $E_\varphi(t)$ and $\Sigma_\varphi(t)$ for each combination are shown in Figures 79-85.

In Figure 79, when the tensorally-correct, complete and minimal VF6 representation is used for $\mathbf{z}$ in Case 4, it can be seen that at least 30% added dissipation must be included in it to achieve a technically stable forward simulation, in the sense that blowup does not occur. However, both panels indicate near-blowup via the spikes in the scalar energy. Only when the added dissipation in $\mathbf{z}$ is increased to 40% does the simulation become manifestly stable. This is not only substantially lower than the corresponding 90% value for the dynamic Smagorinsky model in Figure 82, but the *a priori* tests in Chapter 7 showed the VF6 representation to be far more accurate in representing $z_i(\mathbf{x}, t)$ fields and their associated subgrid scalar energy production fields $\Pi(\mathbf{x}, t)$.

Figure 80 shows results for Case 5, in which the basic Smagorinsky model for the subgrid stress $\boldsymbol{\tau}$ is replaced by the TF5 representation without any added dissipation,

while the basic Smagorinsky model for the subgrid scalar flux $\mathbf{z}$ is used. The resulting simulation is manifestly stable even with any added dissipation in the TF5 representation. This is to be expected from Figure 20 and Section 6.2.3.4, where the TF5 representation for $\boldsymbol{\tau}$ is shown to be stable even without any added dissipation. Since the scalar is passive, it does not affect the stability of the underlying turbulent flow from the $\boldsymbol{\tau}$ representation.

In Figure 81, when the TF5 representation for $\boldsymbol{\tau}$ without any added dissipation is retained, but now the Bardina scale similarity model without any added dissipation is used for $\mathbf{z}$, corresponding to Case 6 in Table 11, the forward simulation is unstable. This instability cannot be due to the TF5 representation for $\boldsymbol{\tau}$, since TF5 is shown in Figure 20 and Section 6.2.3.4 to be stable without any added dissipation. Thus the instability results from the Bardina model for $\mathbf{z}$. It can be seen in Figure 81 that 10% added dissipation in the Bardina model produces a technically stable forward simulation, in the sense that blowup in the scalar energy does not occur. However, the same clearly nonphysical initial increase in domain-averaged scalar energy $E_\varphi(t)$ occurs as was seen from the Bardina model in Figure 77. Only when the added dissipation in the Bardina model is increased to 20% does the simulation remain stable while avoiding the nonphysical increase in domain-averaged scalar energy.

In Figure 82, the TF5 representation for $\boldsymbol{\tau}$ without any added dissipation is retained, but now the dynamic Smagorinsky model is used for $\mathbf{z}$, corresponding to Case 7. It can be seen that at least 80% added dissipation must be included in the dynamic Smagorinsky model for $\mathbf{z}$ to achieve a stable simulation. This instability cannot be due to the TF5 representation for $\boldsymbol{\tau}$, since this is shown in Figure 20 and Section 6.2.3.4 to be stable without any added dissipation, and thus the instability results from the dynamic Smagorinsky model for $\mathbf{z}$. Even with 80% added dissipation, the lower panel in Figure 82 shows large spikes that indicate near-blowup of the model.

Only when the added dissipation in the dynamic Smagorinsky model for $\mathbf{z}$ is increased to 90% does the forward simulation become manifestly stable.

In Figure 83, the TF5 representation for $\boldsymbol{\tau}$ without any added dissipation is retained, but now the tensorally-correct, complete and minimal VF6 representation is used for $\mathbf{z}$, corresponding to Case 8. It can be seen that at least 80% added dissipation must be included in the VF6 representation to achieve a stable simulation. As noted for Cases 5 and 6, the instability at lower levels of added dissipation in VF6 cannot be due to the TF5 representation for $\boldsymbol{\tau}$, since it is manifestly stable without any added dissipation, and is instead due to the VF6 representation for $\mathbf{z}$. It is evident in Figure 83 that adding 80% dissipation to VF6 produces manifestly a stable simulation.

Figure 84 examines the potential benefit of adding a relatively small amount of dissipation (15%) to the TF5 representation for $\boldsymbol{\tau}$, even though it is stable without any added dissipation, to understand how this affects the amount of dissipation that must be added to the VF6 representation for $\mathbf{z}$ to achieve a stable simulation. This corresponds to Case 9 in Table 11, and in Figure 85 it can be seen that 60% added dissipation in VF6 then suffices for stability, rather than the 80% added dissipation that was needed in Case 8.

Figure 85 similarly examines the benefit of adding 15% dissipation in the TF5 representation for $\boldsymbol{\tau}$, even though it is stable without any added dissipation, to understand how this affects the amount of dissipation that must be added to the dynamic Smagorinsky model for $\mathbf{z}$ to achieve a stable simulation. It can be seen that 70% added dissipation then produces a technically stable forward simulation, in the sense that blowup in the scalar energy does not occur, though this still produces continual large spikes in the domain-averaged scalar energy. Only when the added dissipation in the dynamic Smagorinsky model for $\mathbf{z}$ is increased to 80% does the forward simulation become manifestly stable. This is only slightly lower than the 90%

minimum added dissipation that is needed in Figure 82 for Case 7 that has no added dissipation in the TF5 representation for $\boldsymbol{\tau}$.

Case	$C_\chi \pm 2\sigma$
1	0.9182 ± 0.1928
2	0.9537 ± 0.1716
3	0.9326 ± 0.3738
4	0.8631 ± 0.1806
5	0.8136 ± 0.2706

Table 10. Average and 95% uncertainty interval for decay rate C_χ in asymptotic scalar energy decay scaling from the five cases shown in Figure 76.

Case	SGS Model	$(c_{BS,\tau})_{min}$	SGF Model	$(c_{BS,z})_{min}$	Figure
1	Basic Smag	N/A	Basic Smag	N/A	Fig. 74
2	Basic Smag	N/A	Bardina	0-30%	Fig. 77
3	Basic Smag	N/A	Dyn Smag	50-60%	Fig. 78
4	Basic Smag	N/A	VF6	20-40%	Fig. 79
5	TF5	0%	Basic Smag	N/A	Fig. 80
6	TF5	0%	Bardina	10-20%	Fig. 81
7	TF5	0%	Dyn Smag	80-90%	Fig. 82
8	TF5	0%	VF6	80%	Fig. 83
9	TF5	15%	VF6	60%	Fig. 84
10	TF5	15%	Dyn Smag	80%	Fig. 85

Table 11. Combinations of subgrid stress representation for $\boldsymbol{\tau}$ and subgrid scalar flux representation for $\mathbf{z}$, with corresponding minimum $c_{BS,\tau}$ and $c_{BS,z}$ values needed in (8.11) for stable forward simulations, for each case in Figures 74-85.

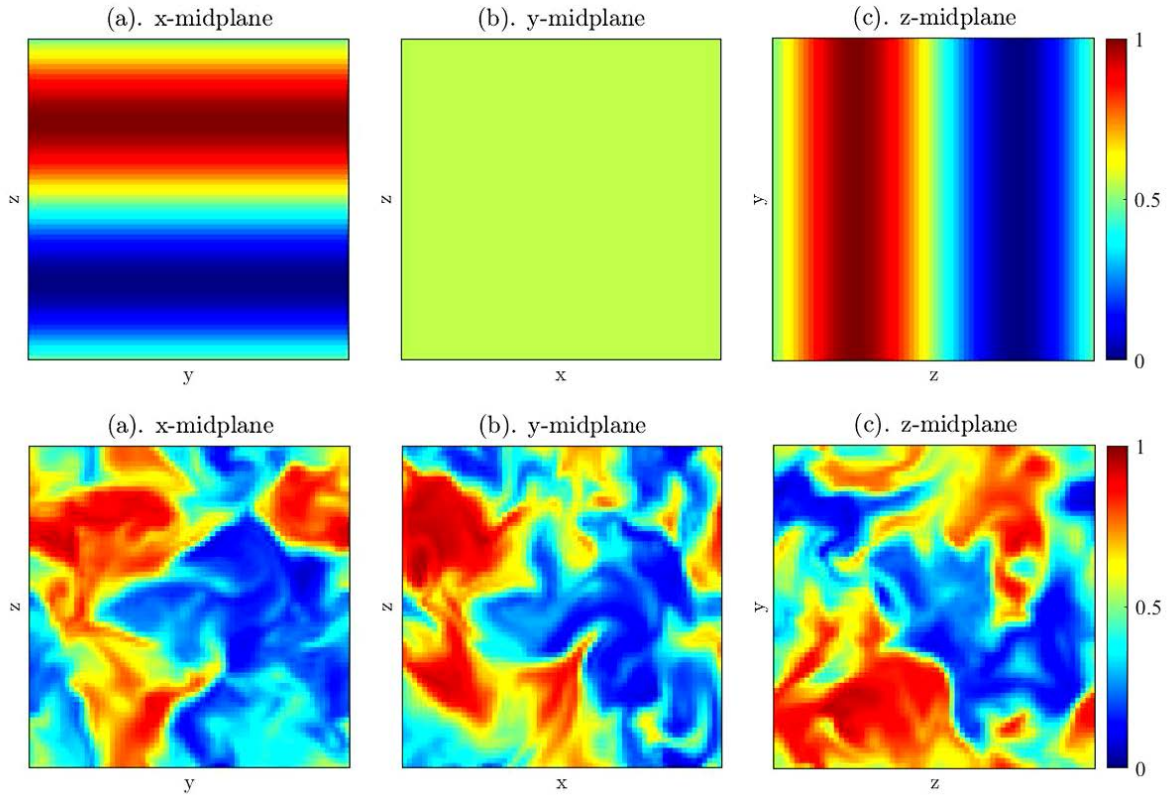

Figure 73. Scalar field initial condition in x, y, and z mid-planes of the domain *(upper row)* and typical resulting scalar field $\varphi(\mathbf{x}, t)$ at later time *(lower row)*.

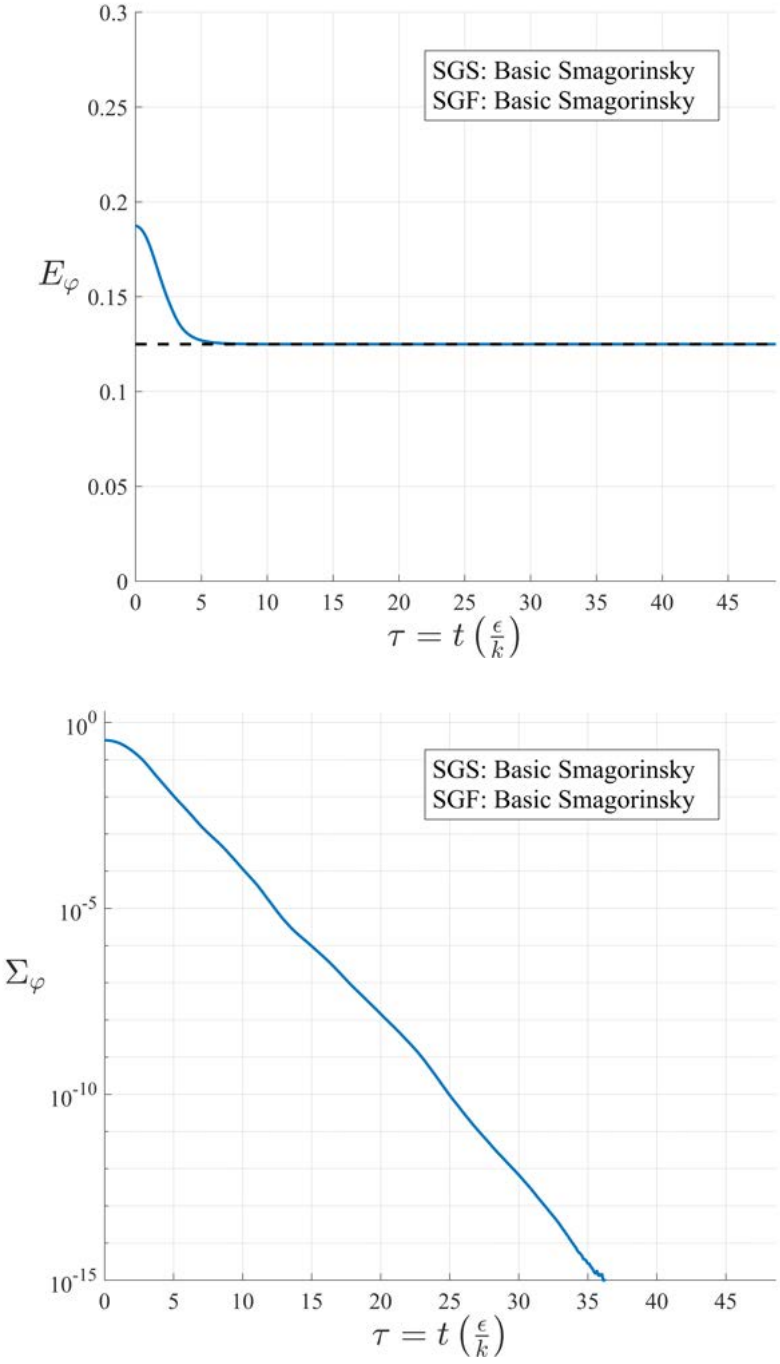

Figure 74. Domain-averaged scalar energy $E_\varphi(t)$ (upper panel) and corresponding relative scalar energy $\Sigma_\varphi(t)$ (lower panel) from basic Smagorinsky model for $\boldsymbol{\tau}$ and basic Smagorinsky model for $\mathbf{z}$ (Case 1 in Table 11).

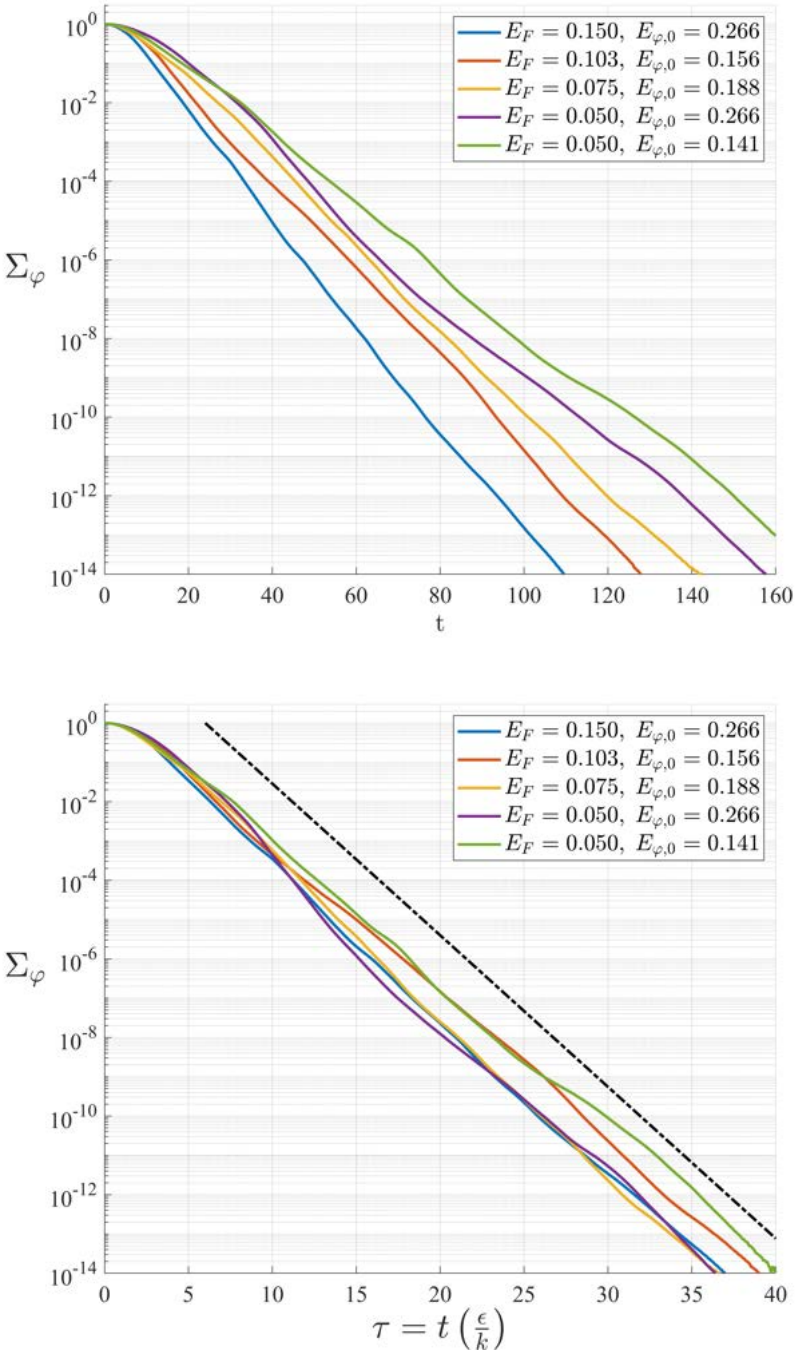

Figure 75. Similar to lower panel in Figure 74 but for differing levels of energy forcing and initial scalar energy, showing scalar energy decay in dimensional time (upper panel) and resulting collapse in properly scaled time (lower panel).

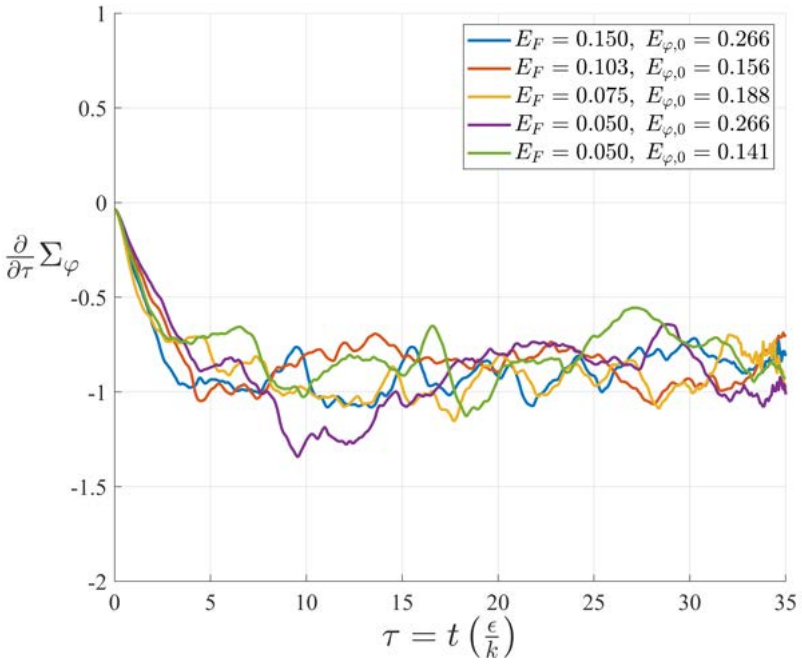

Figure 76. Scaled-time derivative of the relative scalar energy $\Sigma_\varphi(\tau)$ in the lower panel of Figure 75. Corresponding average value over $5 \leq \tau \leq 35$ and associated 95% uncertainty level are shown for each case in Table 10.

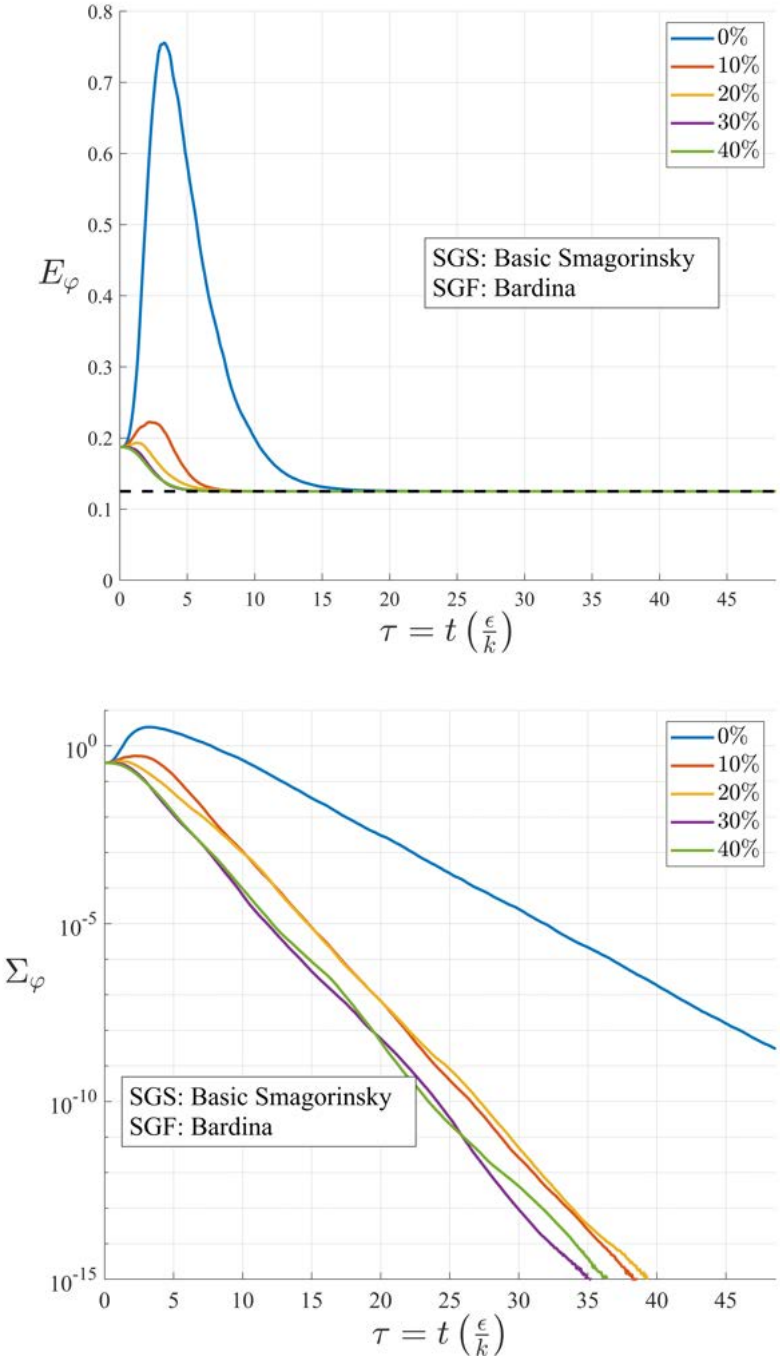

Figure 77. Domain-averaged scalar energy $E_\varphi(\tau)$ (top) and corresponding relative scalar energy $\Sigma_\varphi(\tau)$ (bottom) from basic Smagorinsky model for $\boldsymbol{\tau}$ and Bardina scale similarity model for $\mathbf{z}$ (Case 2 in Table 11) with $c_{BS,\tau} = 0$ and various levels of added dissipation via $c_{BS,z}$ in (8.11).

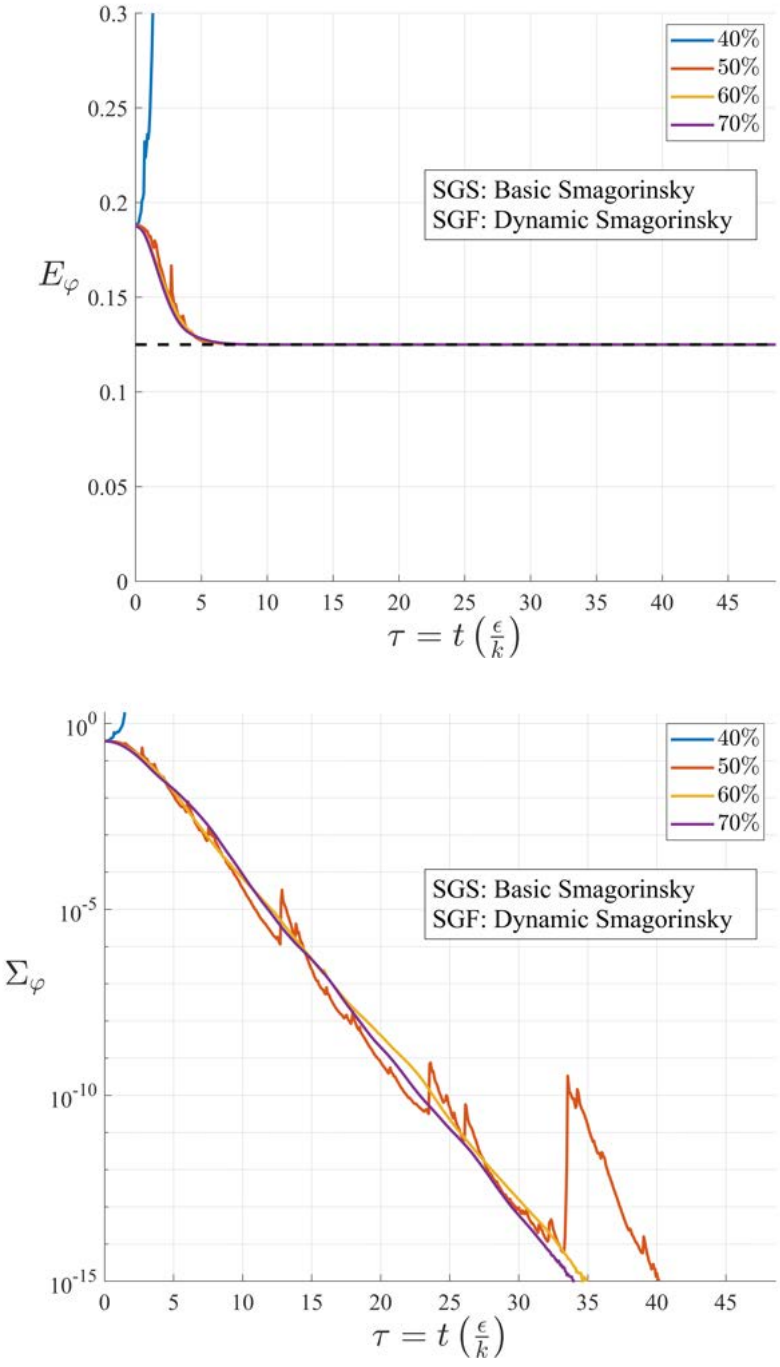

Figure 78. Domain-averaged scalar energy $E_\varphi(\tau)$ (top) and corresponding relative scalar energy $\Sigma_\varphi(\tau)$ (bottom) from basic Smagorinsky model for $\boldsymbol{\tau}$ and dynamic Smagorinsky model for $\mathbf{z}$ (Case 3 in Table 11) with $c_{BS,\tau} = 0$ and various levels of added dissipation via $c_{BS,z}$ in (8.11). Simulations with $c_{BS,z} < 0.50$ produced blowup in the scalar energy.

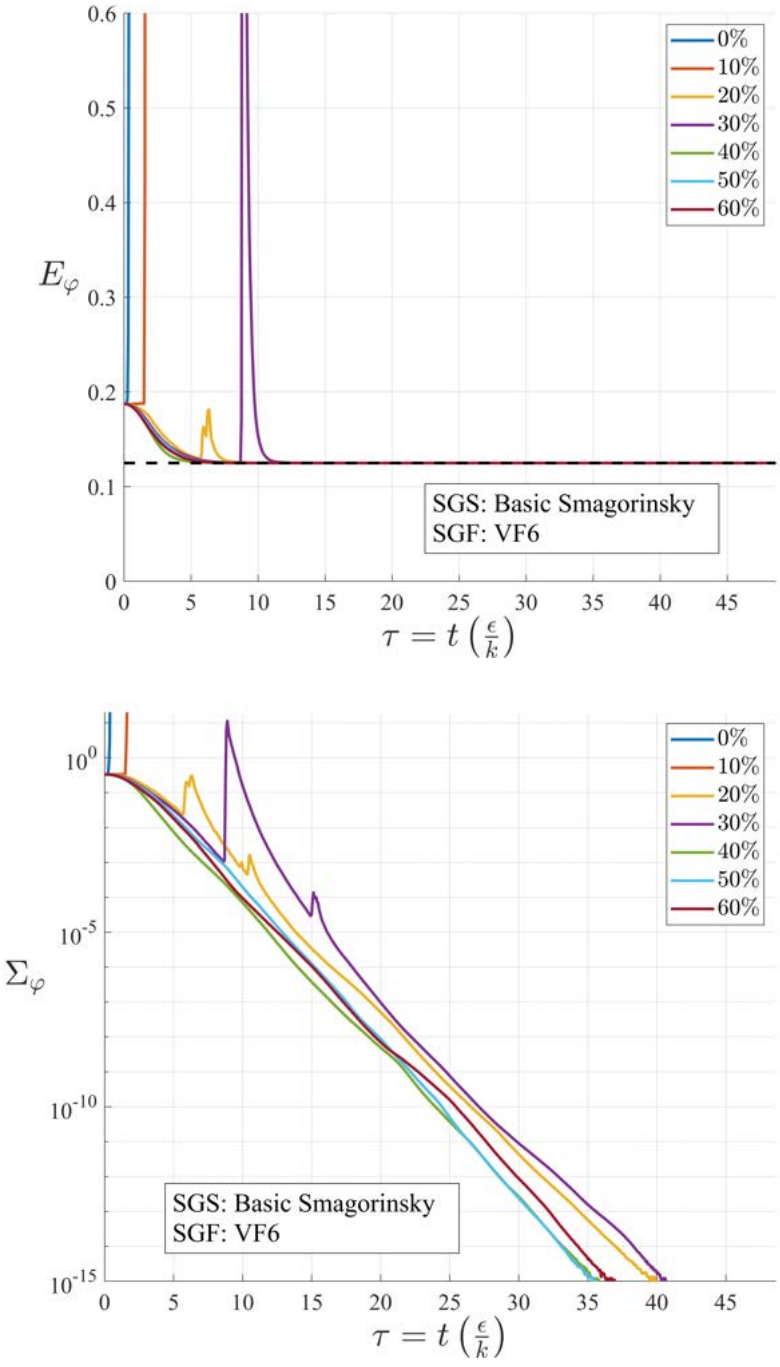

Figure 79. Domain-averaged scalar energy $E_\varphi(\tau)$ (top) and corresponding relative scalar energy $\Sigma_\varphi(\tau)$ (bottom) from basic Smagorinsky model for $\boldsymbol{\tau}$ and VF6 representation for $\mathbf{z}$ (Case 4 in Table 11) with $c_{BS,\tau} = 0$ and various levels of added dissipation via $c_{BS,z}$ in (8.11). Simulations with $c_{BS,z} < 0.20$ produced blowup in the scalar energy.

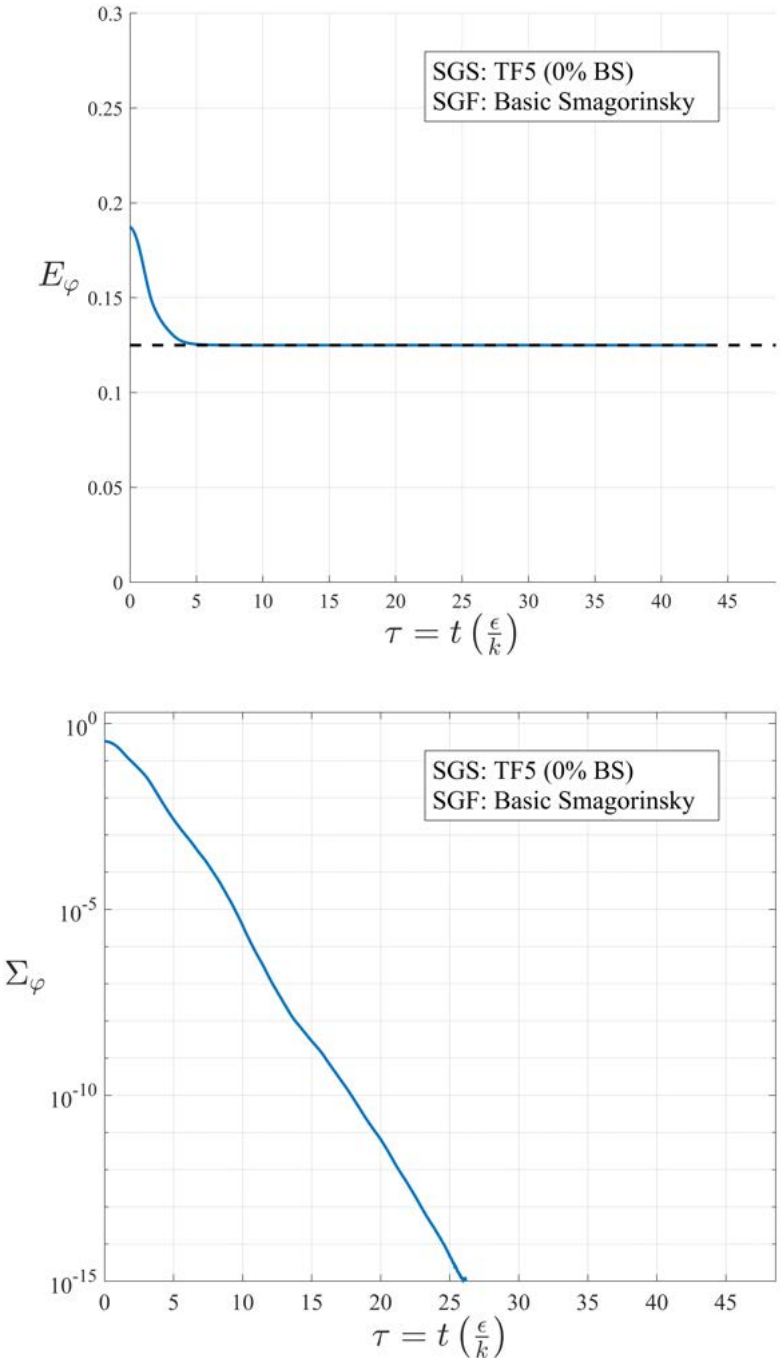

Figure 80. Domain-averaged scalar energy $E_\varphi(\tau)$ (top) and corresponding relative scalar energy $\Sigma_\varphi(\tau)$ (bottom) from TF5 representation for $\boldsymbol{\tau}$ and basic Smagorinsky model for $\mathbf{z}$ (Case 5 in Table 11) with $c_{BS,\tau} = 0$ and $c_{BS,z} = 1$ in (8.11).

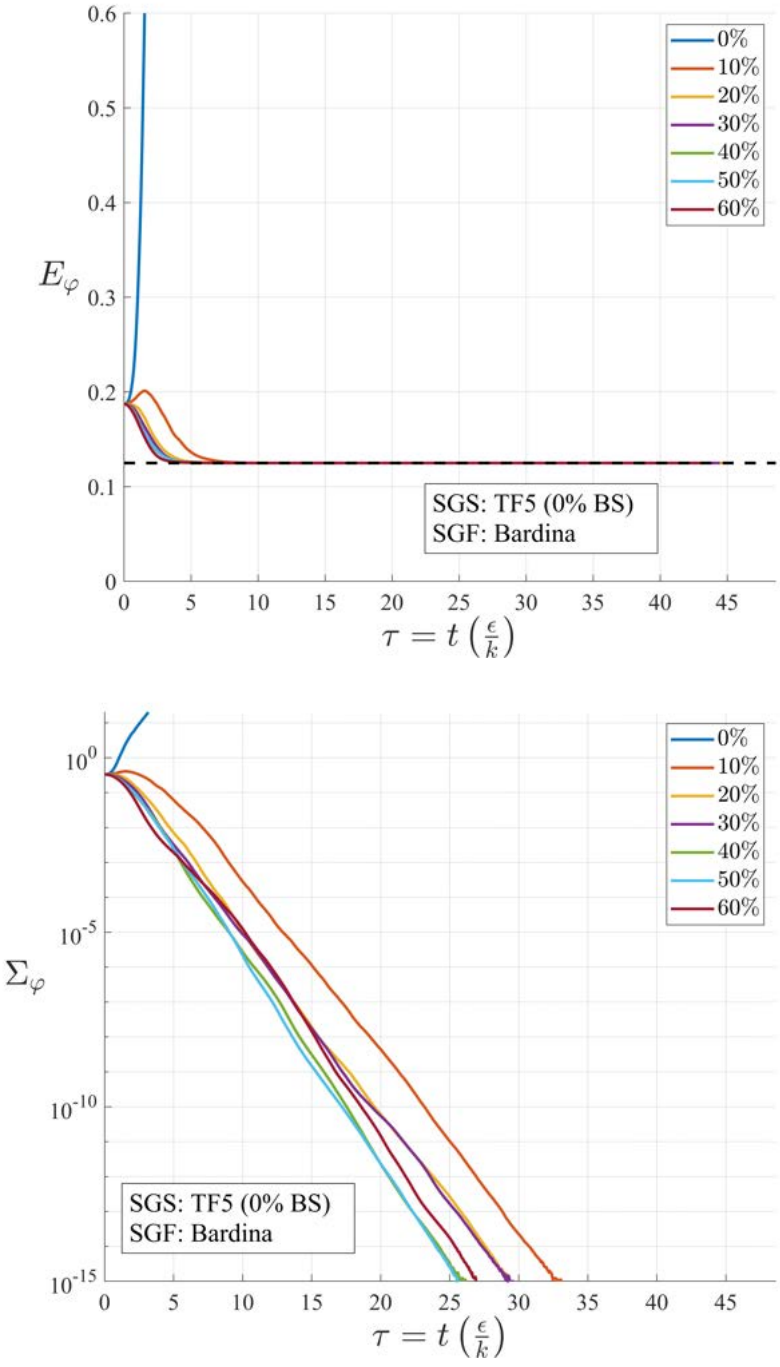

Figure 81. Domain-averaged scalar energy $E_\varphi(\tau)$ (top) and corresponding relative scalar energy $\Sigma_\varphi(\tau)$ (bottom) from TF5 representation for $\boldsymbol{\tau}$ and Bardina scale similarity model for $\mathbf{z}$ (Case 6 in Table 11) with $c_{BS,\tau} = 0$ and various levels of added dissipation via $c_{BS,z}$ in (8.11). Simulations with $c_{BS,z} < 0.20$ produced blowup or nonphysical increase in the scalar energy.

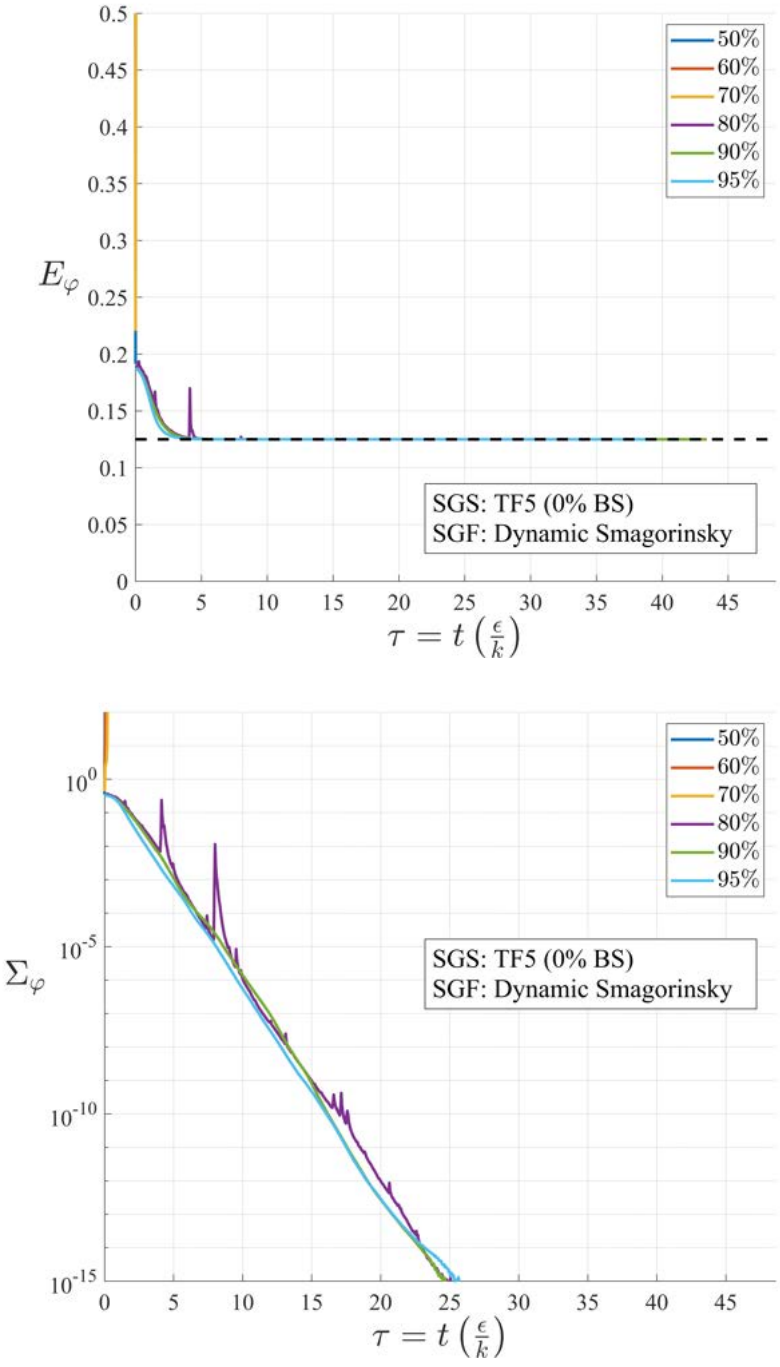

Figure 82. Domain-averaged scalar energy $E_\varphi(\tau)$ (top) and corresponding relative scalar energy $\Sigma_\varphi(\tau)$ (bottom) from TF5 representation for $\boldsymbol{\tau}$ and dynamic Smagorinsky model for $\mathbf{z}$ (Case 7 in Table 11) with $c_{BS,\tau} = 0$ and various levels of added dissipation via $c_{BS,z}$ in (8.11). Simulations with $c_{BS,z} < 0.90$ produced blowup or nonphysical increase in the scalar energy.

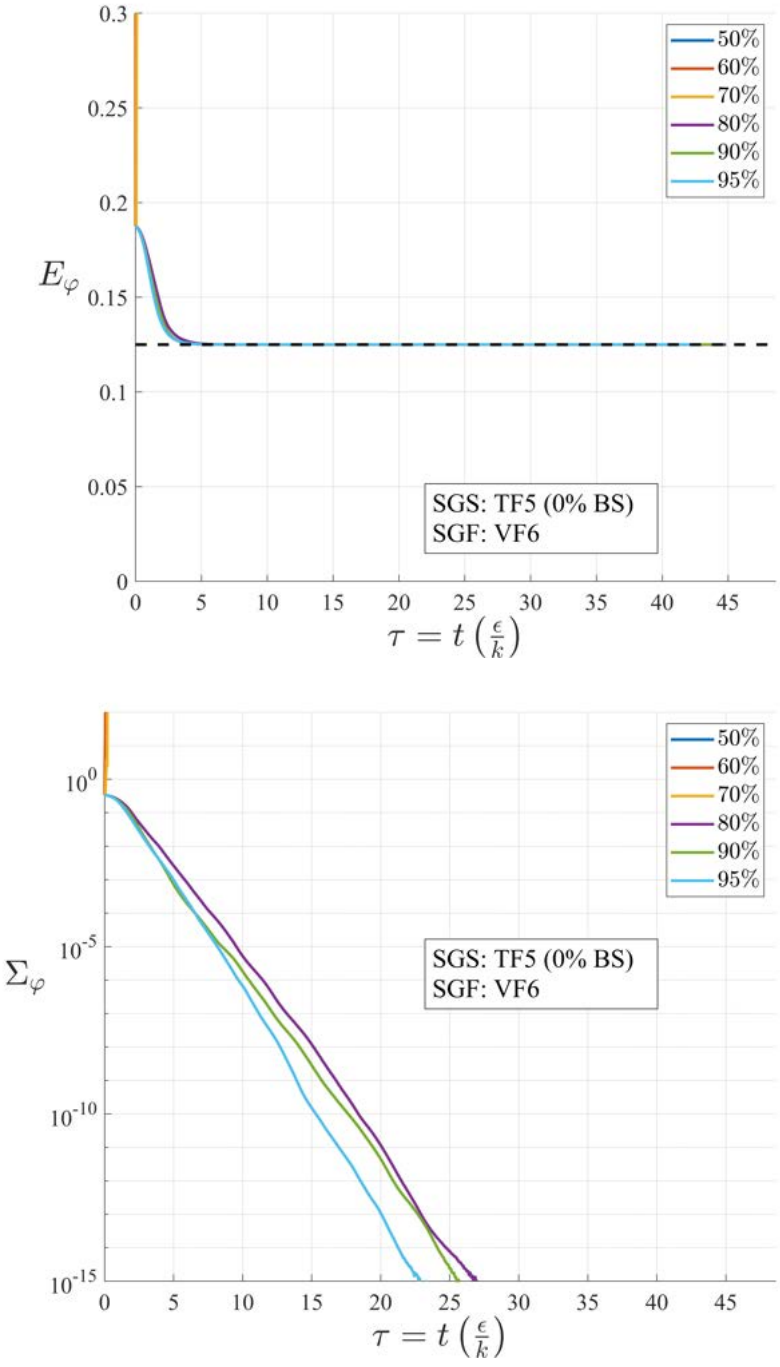

Figure 83. Domain-averaged scalar energy $E_\varphi(\tau)$ (top) and corresponding relative scalar energy $\Sigma_\varphi(\tau)$ (bottom) from TF5 representation for $\boldsymbol{\tau}$ and VF6 representation for $\mathbf{z}$ (Case 8 in Table 11) with $c_{BS,\tau} = 0$ and various levels of added dissipation via $c_{BS,z}$ in (8.11). Simulations with $c_{BS,z} < 0.80$ produced blowup in the scalar energy.

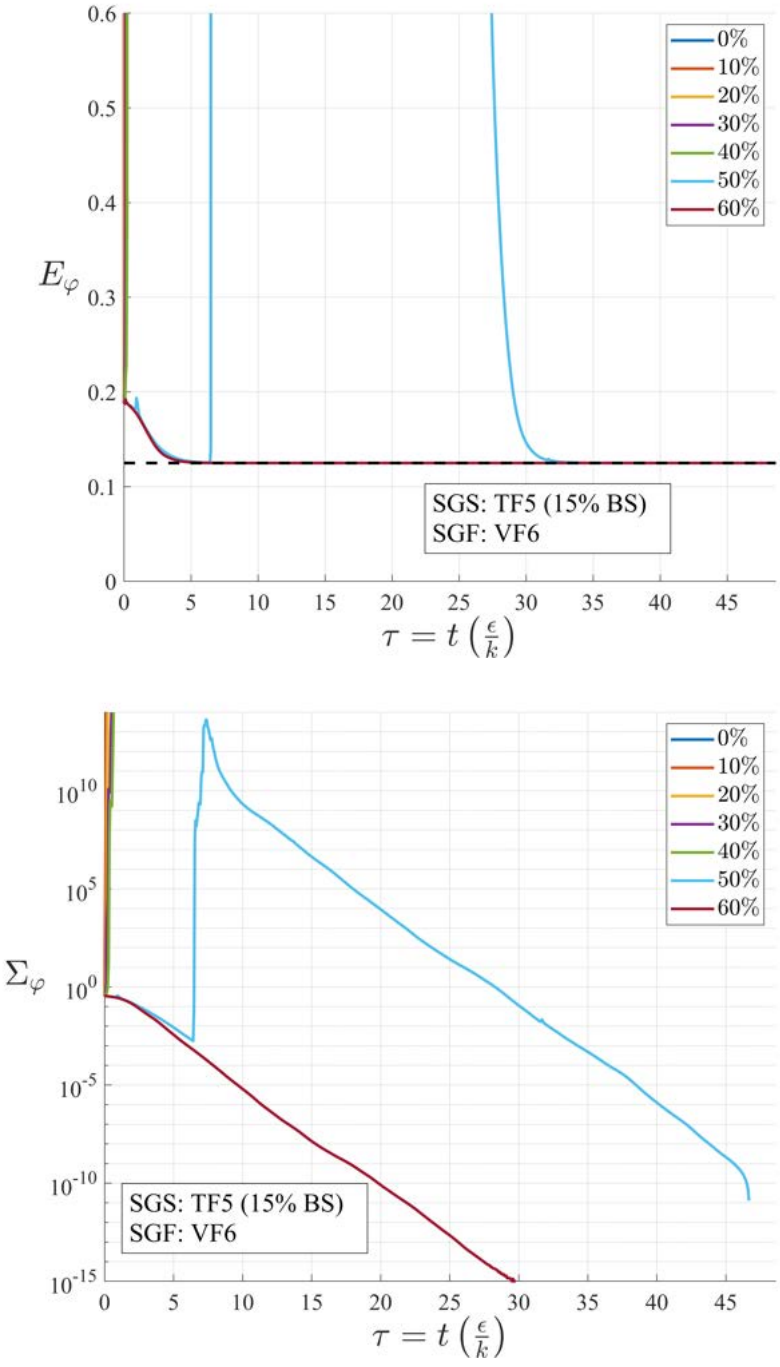

Figure 84. Domain-averaged scalar energy $E_\varphi(\tau)$ (top) and corresponding relative scalar energy $\Sigma_\varphi(\tau)$ (bottom) from TF5 representation for $\boldsymbol{\tau}$ and VF6 representation for $\mathbf{z}$ (Case 9 in Table 11) with $c_{BS,\tau} = 0.15$ and various levels of added dissipation via $c_{BS,z}$ in (8.11). Simulations with $c_{BS,z} < 0.60$ produced blowup or nonphysical increase in the scalar energy.

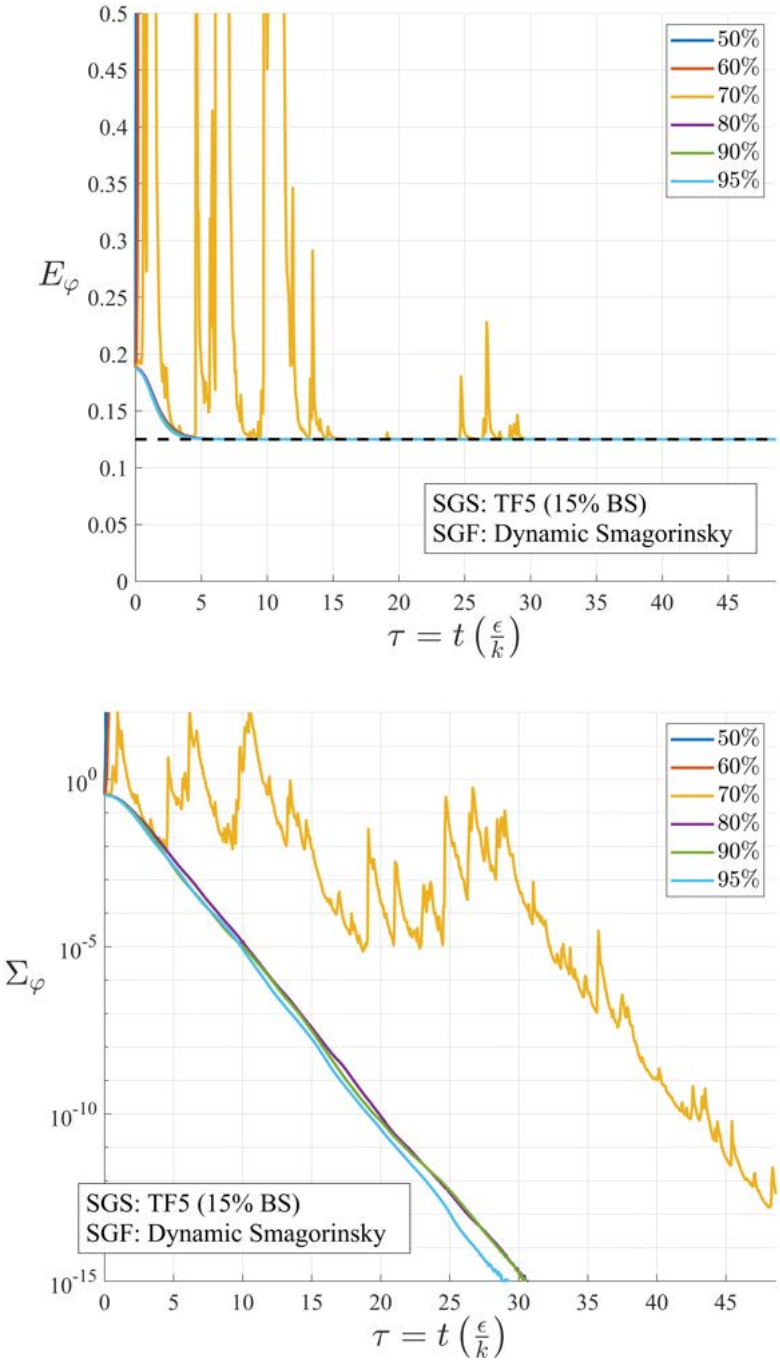

Figure 85. Domain-averaged scalar energy $E_\varphi(\tau)$ (top) and corresponding relative scalar energy $\Sigma_\varphi(\tau)$ (bottom) from TF5 representation for $\boldsymbol{\tau}$ and dynamic Smagorinsky model for $\mathbf{z}$ (Case 10 in Table 11) with $c_{BS,\tau} = 0.15$ and various levels of added dissipation via $c_{BS,z}$ in (8.11). Simulations with $c_{BS,z} < 0.80$ produced blowup or nonphysical increase in the scalar energy.

Chapter 9

A POSTERIORI TEST: SCALAR MIXING IN TURBULENT FLOW

Whereas Chapters 5 and 7 assess the accuracy of tensorally-correct representations for the subgrid stress tensor and subgrid scalar flux vector via *a priori* tests, and Chapters 6 and 8 assess the computational stability of these representations via forward simulations with a high-order pseudo-spectral code, this chapter assesses the accuracy in the resulting resolved velocity and scalar fields when these representations with their required minimum added stabilization are used in a forward simulation.

This is done by comparing statistics for the resolved velocity and scalar fields from a forward simulation based on autonomic closure, using the generalized representation TF5 for the subgrid stress $\boldsymbol{\tau}$ and the generalized representation VF6 for the subgrid scalar flux $\mathbf{z}$, against corresponding statistics obtained from filtering the velocity and scalar fields from a direct numerical simulation (DNS) of the same test problem. Similar comparisons are also made from forward simulations based on traditional closure using prescribed models for the subgrid stress and subgrid scalar flux. Together these comparisons against filtered DNS statistics assess the accuracy in the velocity and scalar fields obtained from autonomic closure versus traditional closure.

By choosing the test problem as conserved scalar mixing in homogeneous isotropic turbulence in a periodic domain, the required DNS fields are well within computational reach. The resulting filtered DNS statistics then provide the "truth data" against which corresponding LES results from any chosen closure approach can be compared.

It will be seen in this chapter that autonomic closure with these tensorally-correct representations TF5 for $\boldsymbol{\tau}$ in (3.13) and VF6 for $\mathbf{z}$ in (3.33), with the added dissipation in (8.11), provide *substantially* more accurate results for turbulent conserved scalar mixing than do widely used conventional prescribed closure models.

9.1 Description of the *A Posteriori* Tests

The large eddy simulations (LES) were conducted with the same high-order pseudo-spectral LES code described in Sections 1.6, 6.1, and 8.1 using 32^3 grids with side lengths $L = 2\pi$ and periodic boundary conditions for a dimensionless viscosity $\nu = 3.3(10^{-3})$. The spectrally-sharp LES-scale filter was applied at $k_{\widetilde{\Delta}} = 28$, and the corresponding spectrally-sharp test-scale filter was applied at $k_{\widehat{\Delta}} = 14$. The energy forcing in the velocity field was the same as described in Section 6.1, and the scalar field initialization was the same as described in Section 8.1.

Based on the results in Chapter 8, LES based on autonomic closure used the TF5 representation for the subgrid stress with 15% added dissipation, and the VF6 representation for the subgrid scalar flux with 60% added dissipation. For comparison, a second LES based on traditional prescribed subgrid models was conducted at the same conditions, but using the basic Smagorinsky model for the subgrid stress and the basic Smagorinsky model for the subgrid scalar flux.

A direct numerical simulation (DNS) was also conducted with the same high-order pseudo-spectral code and at the same conditions, but on a 128^3 grid. The viscosity noted above was chosen to produce well-resolved DNS data having a sufficiently wide inertial range so that the LES-scale filter at $k_{\widetilde{\Delta}} = 28$ was within the inertial range. This allowed the DNS velocity and scalar fields to be filtered at the same LES-filter scale, thereby producing filtered velocity and scalar fields from which statistics could be obtained for direct comparison with the corresponding statistics from the LES based on autonomic closure with the TF5/VF6 representations and from LES based on traditional closure with prescribed subgrid models.

9.2 Statistical Quantities in the Governing Equations

Regarding statistical quantities associated with only the resolved-scale velocity fields, these *a posteriori* tests consider the resolved-scale momentum and kinetic

energy

$$\widetilde{u}_i \quad \text{and} \quad \frac{1}{2}\,\widetilde{u}_i\widetilde{u}_i \tag{9.1}$$

and terms on the right side of the kinetic energy transport equation in (1.6), including

$$\frac{\partial}{\partial x_j}\left(\widetilde{u}_i\widetilde{S}_{ij}\right) \ , \quad \frac{\partial}{\partial x_j}\left(\widetilde{u}_i\widetilde{\tau}_{ij}\right) \ , \quad \widetilde{S}_{ij}\widetilde{S}_{ij} \ , \quad \text{and} \quad \tau_{ij}\widetilde{S}_{ij} \ , \tag{9.2}$$

that account, respectively, for conservative redistribution of kinetic energy by the viscous stresses and by the subgrid stresses, for viscous dissipation of kinetic energy, and for subgrid production of kinetic energy.

Similarly, regarding statistical quantities associated with the resolved-scale scalar fields, these *a posteriori* tests consider the resolved-scale scalar and scalar energy

$$\widetilde{\varphi} \quad \text{and} \quad \frac{1}{2}\,\widetilde{\varphi}^2 \tag{9.3}$$

and terms on the right side of the scalar energy transport equation in (1.12), including

$$\frac{\partial^2 E_\varphi}{\partial x_j \partial x_j} \ , \quad \frac{\partial}{\partial x_j}\left(\widetilde{\varphi} z_j\right) \ , \quad \frac{\partial\widetilde{\varphi}}{\partial x_j}\frac{\partial\widetilde{\varphi}}{\partial x_j} \ , \quad \text{and} \quad z_j\frac{\partial\widetilde{\varphi}}{\partial x_j} \ , \tag{9.4}$$

that account, respectively, for conservative redistribution of scalar energy by the viscous stresses and by the subgrid stresses, for viscous dissipation of scalar energy, and for subgrid production of scalar energy.

9.3 Inner-Scale and Outer-Scale Statistical Quantities

Each of the quantities q in Section 9.2 is either an inner-scale quantity or an outer-scale quantity, depending on whether the spectrum associated with its energy $\frac{1}{2}q^2$ has, respectively, a positive ($p > 0$) or a negative ($p < 0$) inertial-range scaling k^p.

Since any general velocity-based quantity q having dimensions $[L^n/T^m]$ has an associated energy spectrum $Q(k)$ for which

$$\langle q^2 \rangle = \int_0^\infty Q(k)\,dk \ , \tag{9.5}$$

the dimensions of the spectrum Q must be $[L^{2n+1}/T^{2m}]$. Following classical inertial-range scaling arguments, in the inertial range $Q(k)$ will depend on the average

kinetic energy dissipation rate $\epsilon \sim [L^2/T^3]$ and wavenumber $k \sim [1/T]$, and thus on dimensional grounds Q must scale as

$$Q(k) \sim \epsilon^{\frac{2}{3}m} \, k^{\frac{4}{3}m-(2n+1)} \, . \tag{9.6}$$

Based on the dimensions of each of velocity-based statistical quantity in Section 9.2, from (9.6) it can be determined whether it is an inner-scale or outer-scale quantity. The effects of an improved subgrid stress closure methodology can be expected to be most prominent for inner-scale quantities.

Similarly, using A for the units of the scalar, since any general scalar-based quantity q having dimensions $[A^a \, L^n/T^m]$ has an associated energy spectrum $Q(k)$ for which

$$\langle q^2 \rangle = \int_0^\infty Q(k) \, dk \, , \tag{9.7}$$

the dimensions of the spectrum Q must be $[A^{2a} \, L^{2n+1}/T^{\,2m}]$. From classical inertial-range scaling arguments, in the inertial range $Q(k)$ will depend on the average scalar energy dissipation rate $\chi \sim [A^2/T]$, the average kinetic energy dissipation rate $\epsilon \sim [L^2/T^3]$ and wavenumber $k \sim [1/T]$, and so on dimensional grounds must scale as

$$Q(k) \sim \chi^a \, \epsilon^{\frac{2}{3}m-\frac{1}{3}a} \, k^{\frac{4}{3}m-(2n+1)-\frac{2}{3}a} \tag{9.8}$$

Based on the dimensions of each of scalar-based statistical quantity in Section 9.2, from (9.8) it can be determined whether it is an inner-scale or outer-scale quantity. The effects of an improved subgrid scalar flux closure methodology can be expected to be most prominent for inner-scale quantities.

9.4 Results from *A Posteriori* Tests

9.4.1 Velocity-Based Statistics

Velocity-based statistics are affected only by the representation for the subgrid stress, and not by the subgrid scalar flux representation. For each of the velocity-based quantities in (9.1) and (9.2), its dimensions determine whether its inertial-range

scaling exponent k^p, as described in Section 9.3, will be positive or negative. Positive scaling exponents ($p > 0$) mean that most of the energy associated with fluctuations in the quantity come from large wavenumbers, corresponding to small length scales, as thus these are termed "inner-scale quantities". Negative scaling exponents ($p < 0$) mean that most of the energy associated with fluctuations in the quantity come from small wavenumbers, corresponding to large length scales, as thus these are termed "outer-scale quantities".

9.4.1.1 Inner-scale quantities

Only two of the quantities in (9.1) and (9.2) are inner-scale quantities, namely

$$\frac{\partial}{\partial x_j}\left(\widetilde{u}_i \widetilde{S}_{ij}\right) \quad \text{and} \quad \widetilde{S}_{ij}\widetilde{S}_{ij} \ , \tag{9.9}$$

and thus for these it is expected that the effects of an improved subgrid closure will be more pronounced than for outer-scale velocity-based statistics. Probability density functions for these two inner-scale quantities are shown in Figures 86 and 87 from the filtered DNS fields *(black)*, from LES based on traditional closure with prescribed subgrid models *(red)*, and from LES based on autonomic closure with the TF5/VF6 representations *(blue)*. In both figures, and especially in Figure 86, substantially better agreement with the DNS results is seen from LES based on autonomic closure with the TF5/VF6 representations.

9.4.1.2 Outer-scale quantities

The other quantities in (9.1) and (9.2) are all outer-scale quantities, namely

$$\widetilde{u}_i \ , \quad \frac{1}{2}\,\widetilde{u}_i\widetilde{u}_i \ , \quad \frac{\partial}{\partial x_j}\left(\widetilde{u}_i\widetilde{\tau}_{ij}\right) \quad \text{and} \quad \tau_{ij}\widetilde{S}_{ij} \ , \tag{9.10}$$

and thus for these it is expected that the effects of an improved subgrid closure will be less pronounced than for inner-scale velocity-based statistics. Figures 88-91 show probability density functions for these outer-scale quantities from the filtered DNS fields *(black)*, from LES based on traditional closure with prescribed subgrid models

(red), and from LES based on autonomic closure with the TF5/VF6 representations *(blue)*. As expected, differences in the results from the two LES closure approaches are less pronounced in these outer-scale quantities.

9.4.2 Scalar-Based Statistics

Unlike velocity-based statistics, scalar-based statistics are affected by both the subgrid stress representation and the subgrid scalar flux representation. For each of the scalar-based quantities in (9.3) and (9.4), its dimensions determine whether its inertial-range scaling exponent k^p, as described in Section 9.3, will be positive or negative. Positive scaling exponents ($p > 0$) again mean that most of the energy associated with fluctuations in the quantity come from large wavenumbers, corresponding to small length scales, as thus these are termed "inner-scale quantities". Negative scaling exponents ($p < 0$) mean that most of the energy associated with fluctuations in the quantity come from small wavenumbers, corresponding to large length scales, as thus these are termed "outer-scale quantities".

9.4.2.1 Inner-scale quantities

Only two of the quantities in (9.3) and (9.4) are inner-scale quantities, namely

$$\frac{\partial^2 E_\varphi}{\partial x_j \partial x_j} \quad \text{and} \quad \frac{\partial \widetilde{\varphi}}{\partial x_j}\frac{\partial \widetilde{\varphi}}{\partial x_j} \tag{9.11}$$

and thus for these it is expected that the effects of improved closures for both the subgrid stress and the subgrid scalar flux will be more pronounced than for outer-scale velocity-based statistics. Probability density functions for these two inner-scale quantities are shown in Figures 92 and 93 from the filtered DNS fields *(black)*, from LES based on traditional closure with prescribed subgrid models *(red)*, and from LES based on autonomic closure with the TF5/VF6 representations *(blue)*. In both figures, substantially better agreement with the DNS results is seen from LES based on autonomic closure with the TF5/VF6 representations than from traditional closure with prescribed models.

9.4.2.2 Outer-scale quantities

The other quantities in (9.3) and (9.4) are all outer-scale quantities, namely

$$\widetilde{\varphi} \ , \quad \frac{1}{2}\widetilde{\varphi}^2 \ , \quad \frac{\partial}{\partial x_j}\left(\widetilde{\varphi} z_j\right) \ , \quad \text{and} \quad z_j \frac{\partial \widetilde{\varphi}}{\partial x_j} \ . \tag{9.12}$$

Figures 94-97 show probability density functions for these outer-scale quantities from the filtered DNS fields *(black)*, from LES based on traditional closure with prescribed subgrid models *(red)*, and from LES based on autonomic closure with the TF5/VF6 representations *(blue)*. In all cases, substantially better agreement with the DNS results is seen from LES based on autonomic closure with the TF5/VF6 representations than from traditional closure with prescribed models.

For such outer-scale quantities it might be expected that the effects of improved closures for both the subgrid stress and the subgrid scalar flux might be less pronounced than for inner-scale velocity-based statistics. However, it is possible that the combined effects of the substantially improved subgrid stress representation TF5 compared to the basic Smagorinski model for the subgrid stress, and the substantially improved subgrid scalar flux representation VF6 compared to the basic Smagorinski model for the subgrid scalar flux, together with the inherent ability of the autonomic closure methodology to adapt far more freely than is possible in traditional closure with prescribed subgrid models, collectively give the improved agreement seen in Figures 92-97 over traditional closure with Smagorinski models.

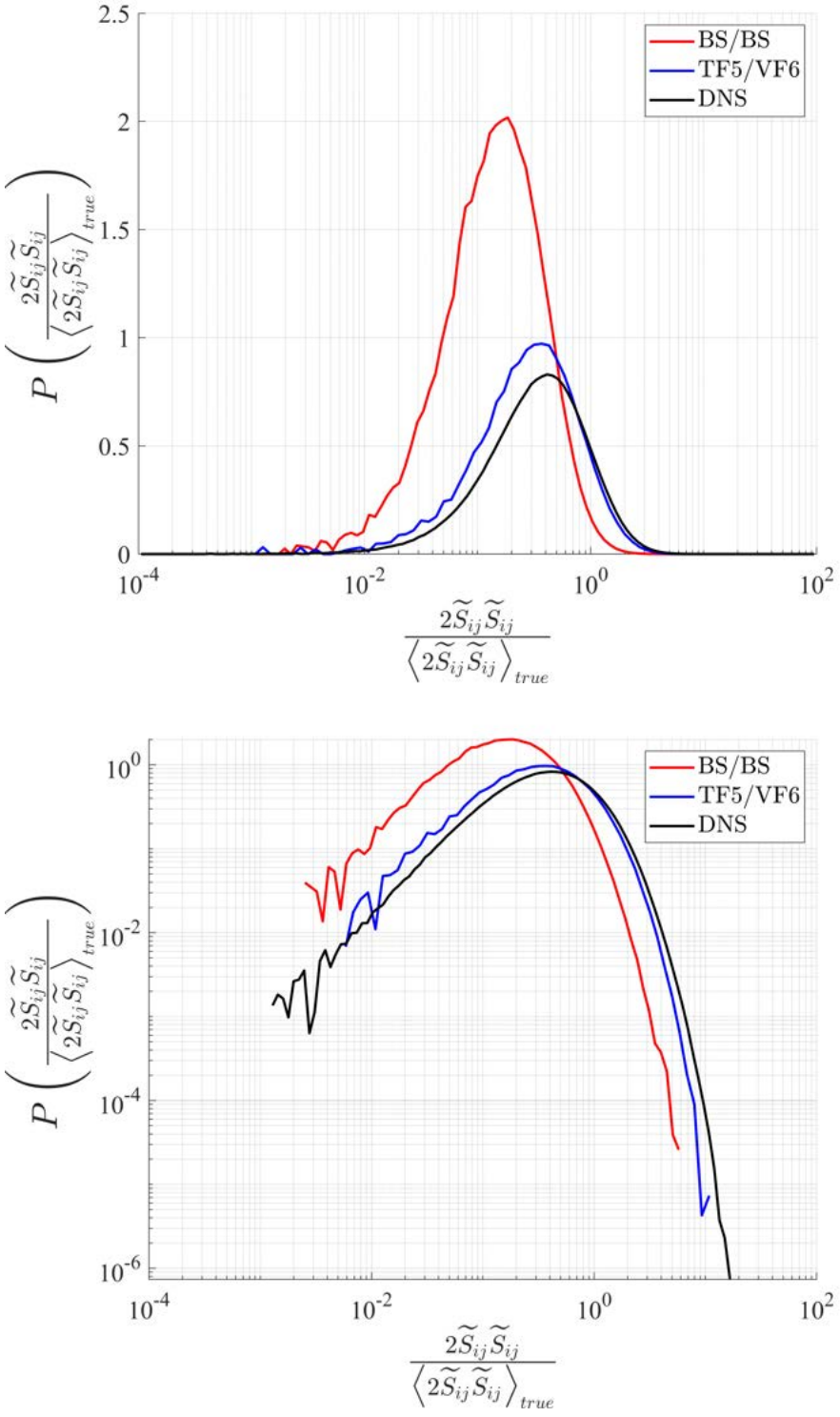

Figure 86. PDFs of the kinetic energy dissipation rate from forward simulations based on traditional closure with basic Smagorinsky models for both $\boldsymbol{\tau}$ and $\mathbf{z}$ *(red)*, autonomic closure with TF5 and VF6 representations for $\boldsymbol{\tau}$ and $\mathbf{z}$ *(blue)*, and corresponding filtered DNS *(black)*.

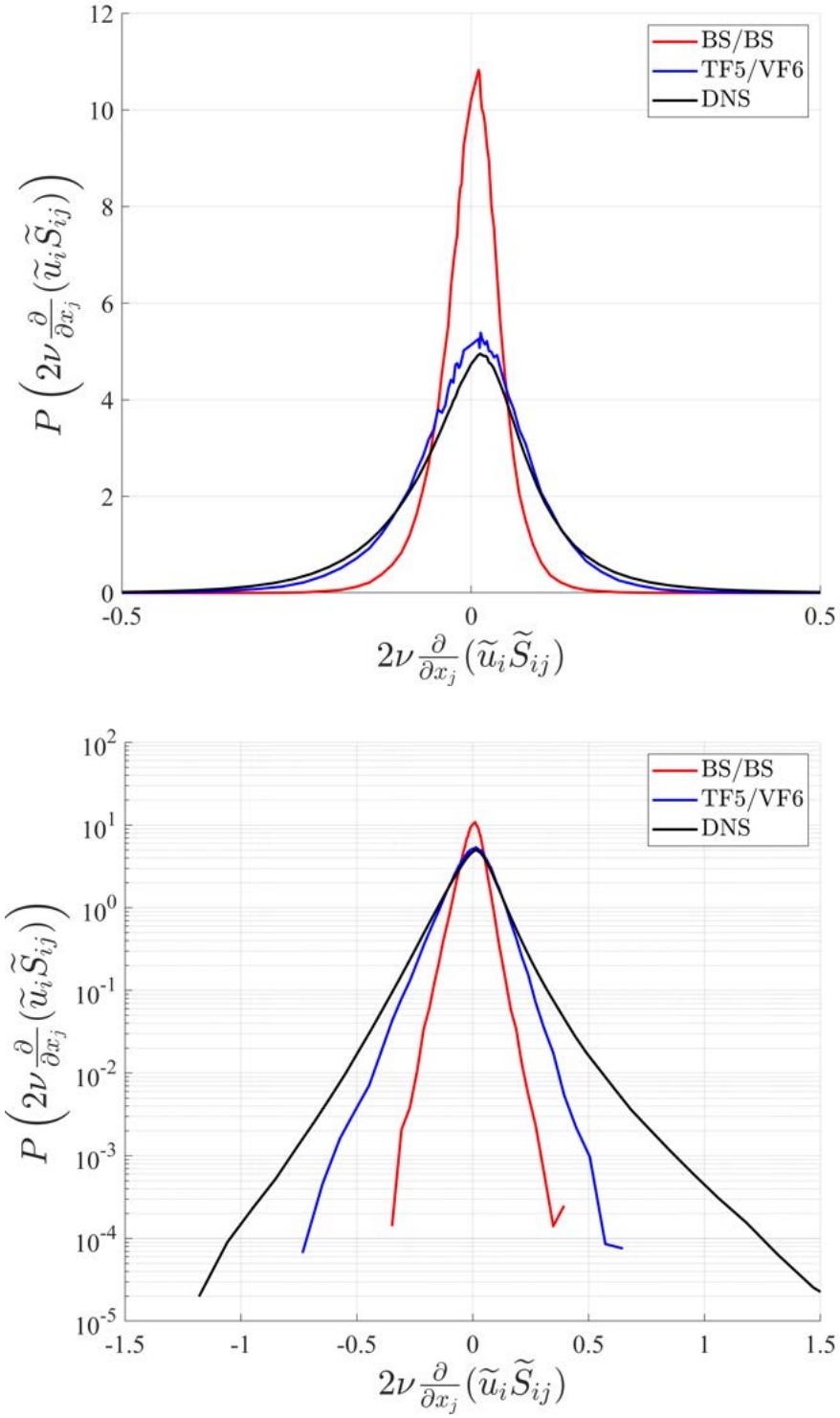

Figure 87. PDFs of the viscous diffusion of resolved kinetic energy in forward simulations based on traditional closure with basic Smagorinsky models for both $\boldsymbol{\tau}$ and $\mathbf{z}$ *(red)*, autonomic closure with TF5 and VF6 representations for $\boldsymbol{\tau}$ and $\mathbf{z}$ *(blue)*, and corresponding filtered DNS *(black)*.

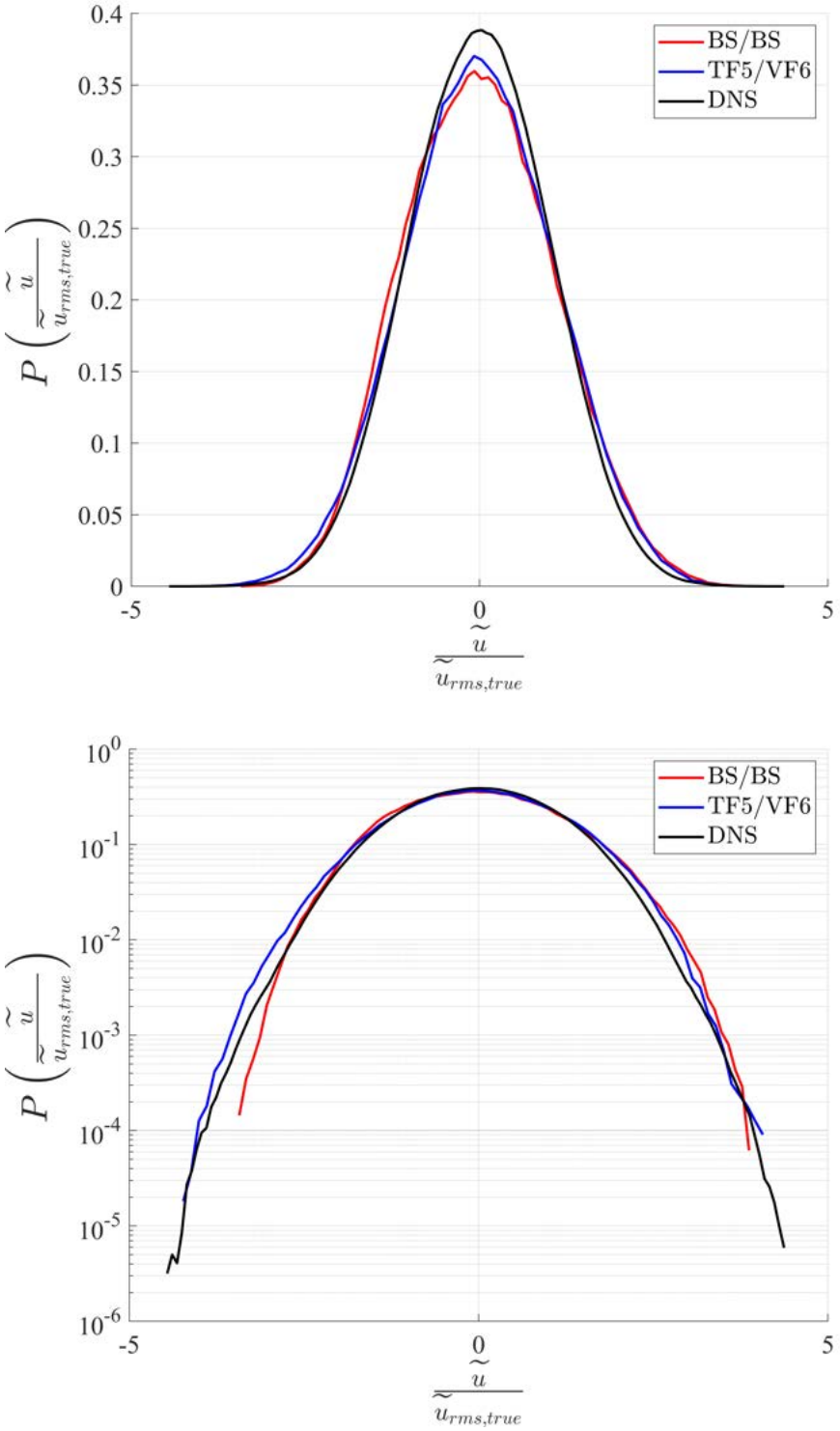

Figure 88. PDFs of the resolved velocity in forward simulations based on traditional closure with basic Smagorinsky models for both $\boldsymbol{\tau}$ and $\mathbf{z}$ *(red)*, autonomic closure with TF5 and VF6 representations for $\boldsymbol{\tau}$ and $\mathbf{z}$ *(blue)*, and corresponding filtered DNS *(black)*.

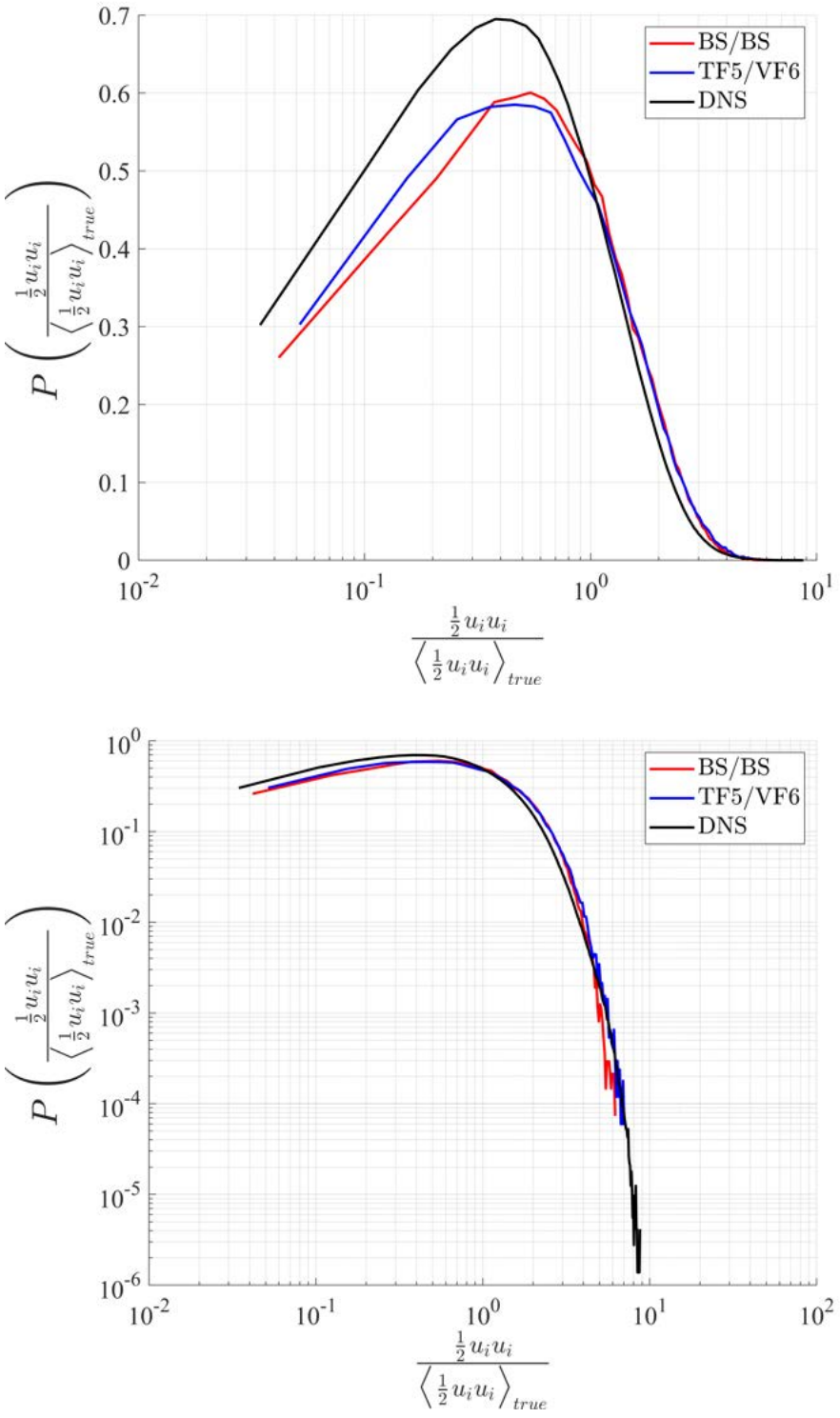

Figure 89. PDFs of the resolved kinetic energy in forward simulations based on traditional closure with basic Smagorinsky models for both $\boldsymbol{\tau}$ and $\mathbf{z}$ *(red)*, autonomic closure with TF5 and VF6 representations for $\boldsymbol{\tau}$ and $\mathbf{z}$ *(blue)*, and corresponding filtered DNS *(black)*.

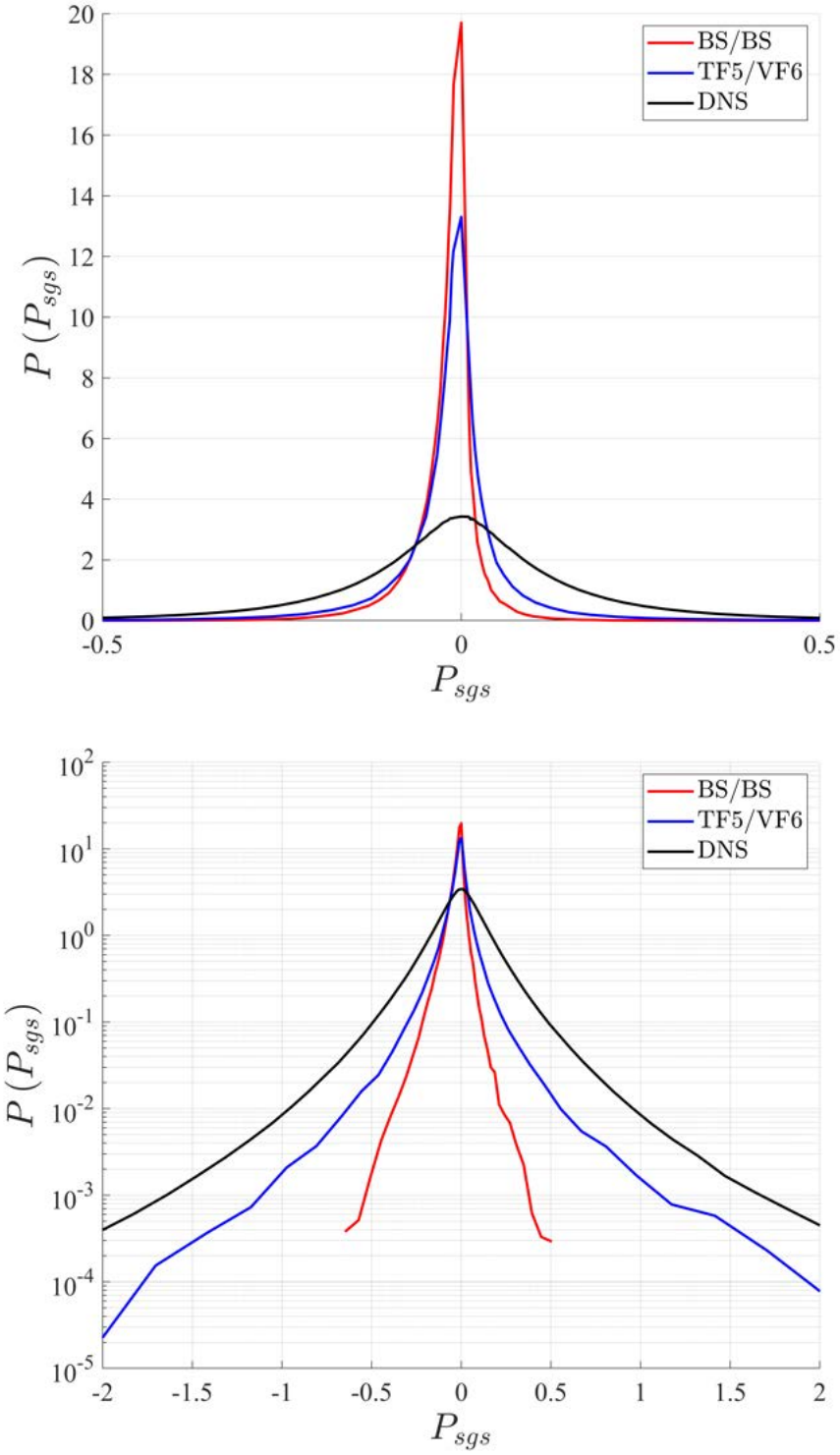

Figure 90. PDFs of the subgrid production $P = \tau_{ij}\widetilde{S}_{ij}$ in forward simulations based on traditional closure with basic Smagorinsky models for both $\boldsymbol{\tau}$ and $\mathbf{z}$ *(red)*, autonomic closure with TF5 and VF6 representations for $\boldsymbol{\tau}$ and $\mathbf{z}$ *(blue)*, and corresponding filtered DNS *(black)*.

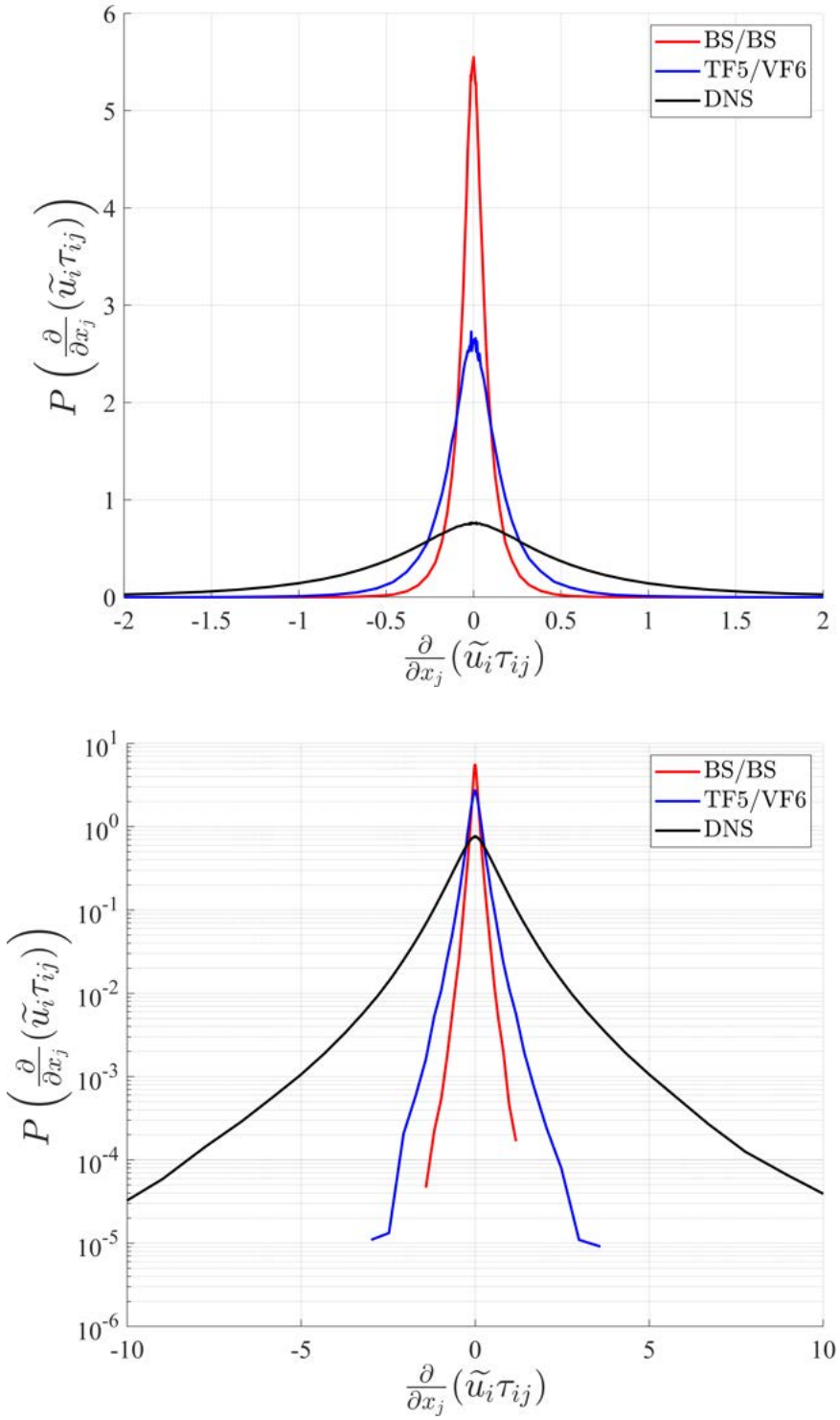

Figure 91. PDFs of the kinetic energy transport by the subgrid stress in forward simulations based on traditional closure with basic Smagorinsky models for both $\boldsymbol{\tau}$ and $\mathbf{z}$ *(red)*, autonomic closure with TF5 and VF6 representations for $\boldsymbol{\tau}$ and $\mathbf{z}$ *(blue)*, and corresponding filtered DNS *(black)*.

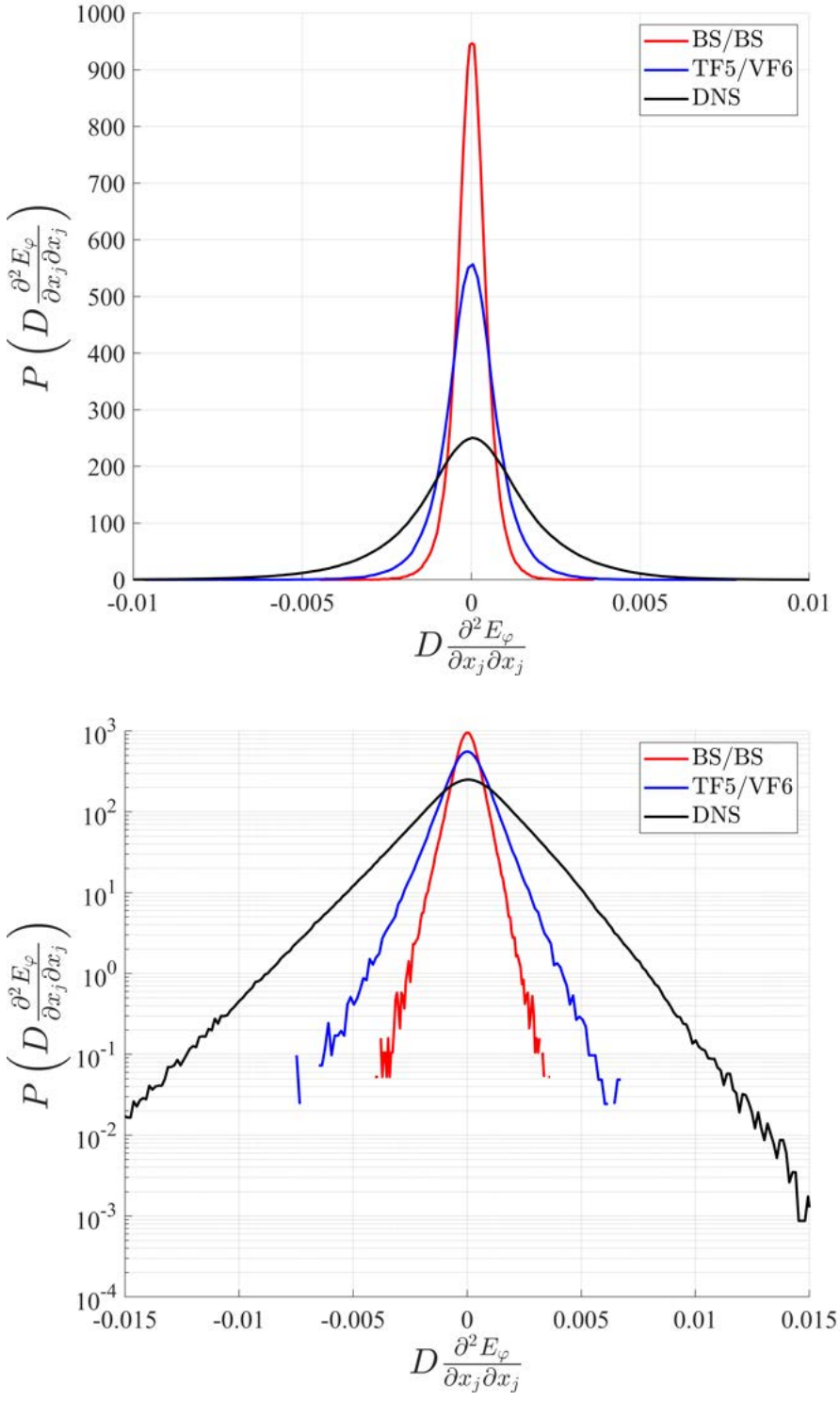

Figure 92. PDFs of the scalar energy transport via diffusion in forward simulations based on traditional closure with basic Smagorinsky models for both $\boldsymbol{\tau}$ and $\mathbf{z}$ *(red)*, autonomic closure with TF5 and VF6 representations for $\boldsymbol{\tau}$ and $\mathbf{z}$ *(blue)*, and corresponding filtered DNS *(black)*.

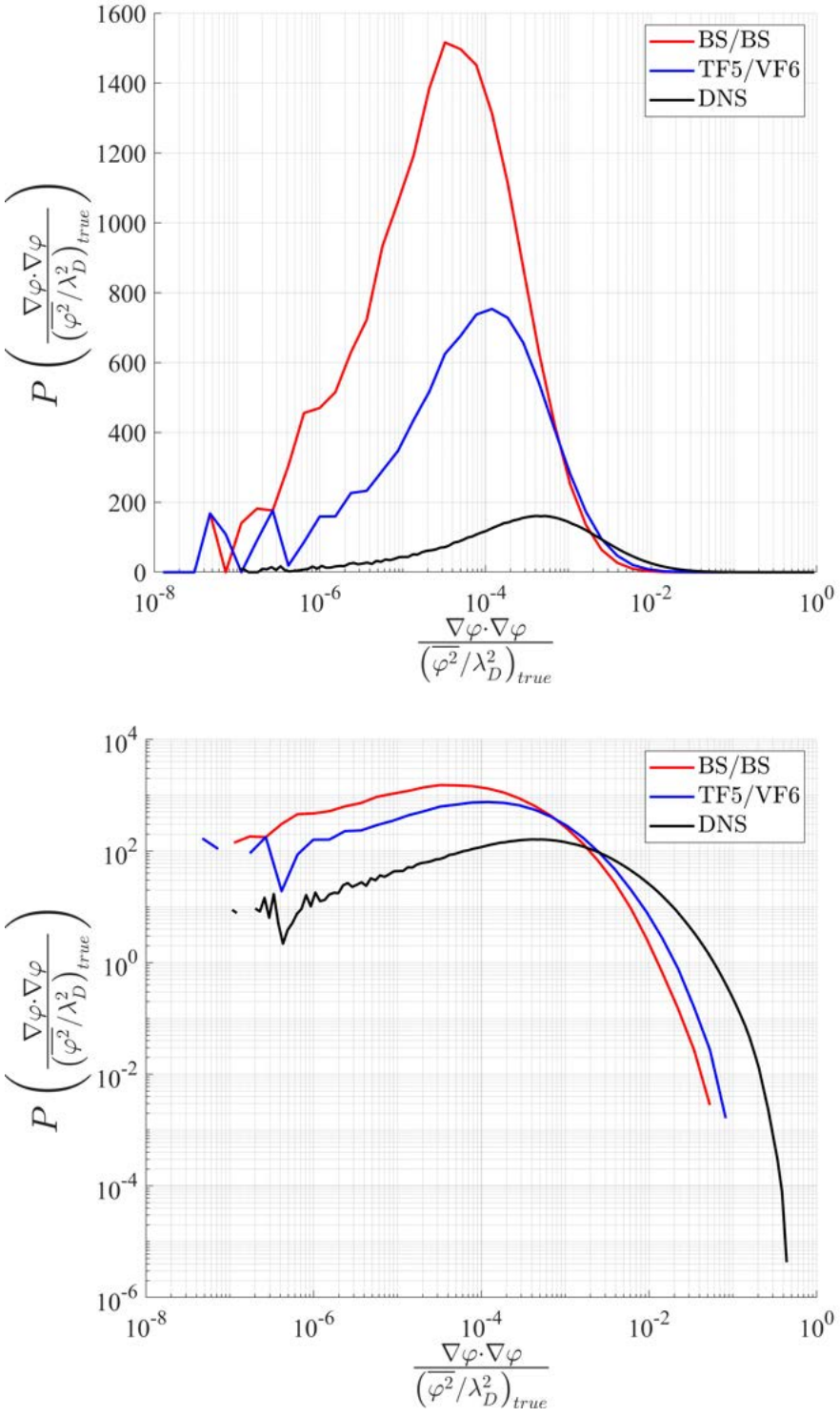

Figure 93. PDFs of the scalar energy dissipation in forward simulations based on traditional closure with basic Smagorinsky models for both $\boldsymbol{\tau}$ and $\mathbf{z}$ *(red)*, autonomic closure with TF5 and VF6 representations for $\boldsymbol{\tau}$ and $\mathbf{z}$ *(blue)*, and corresponding filtered DNS *(black)*.

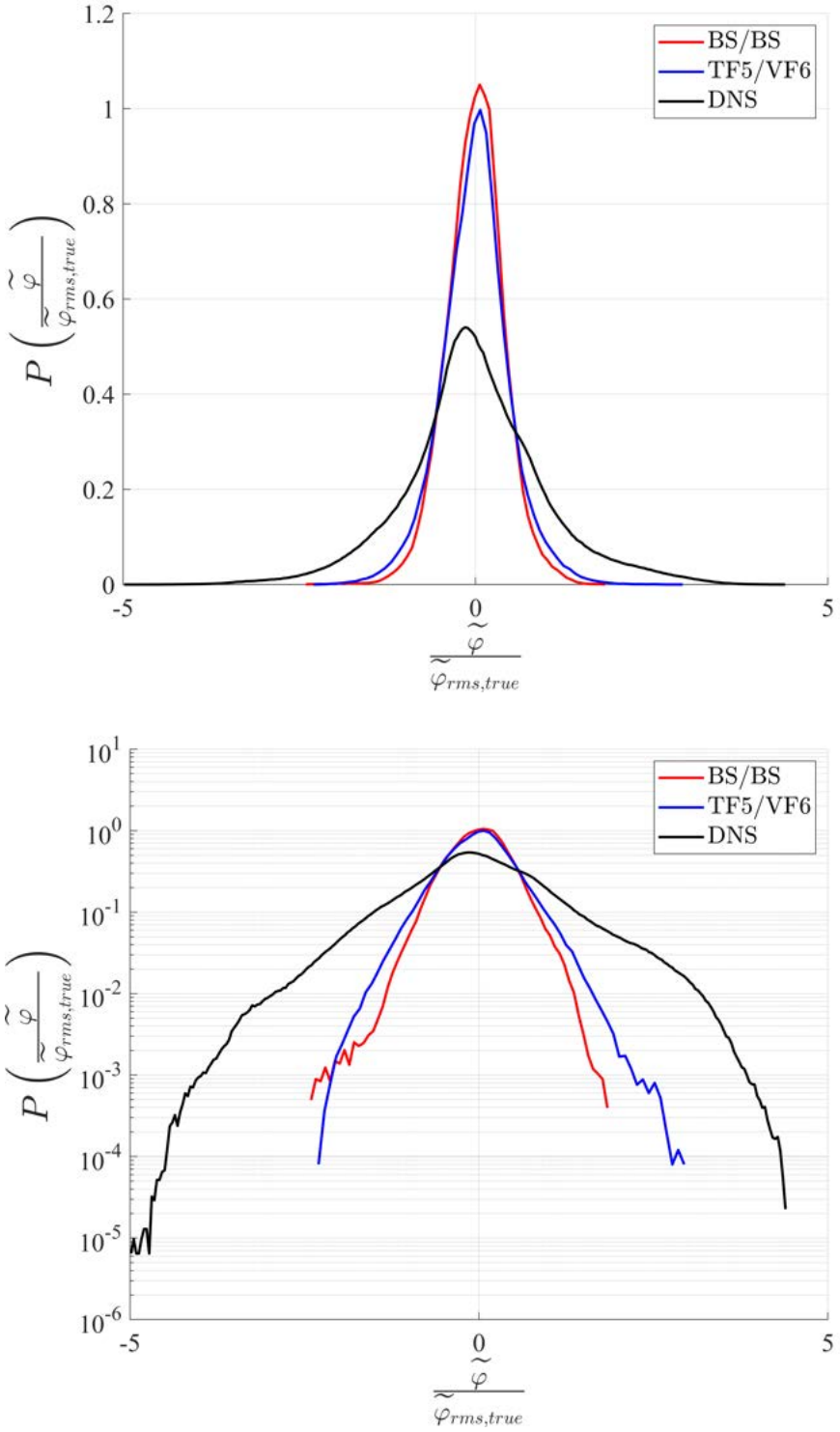

Figure 94. PDFs of resolved scalar values in forward simulations based on traditional closure with basic Smagorinsky models for both $\boldsymbol{\tau}$ and $\mathbf{z}$ *(red)*, autonomic closure with TF5 and VF6 representations for $\boldsymbol{\tau}$ and $\mathbf{z}$ *(blue)*, and corresponding filtered DNS *(black)*.

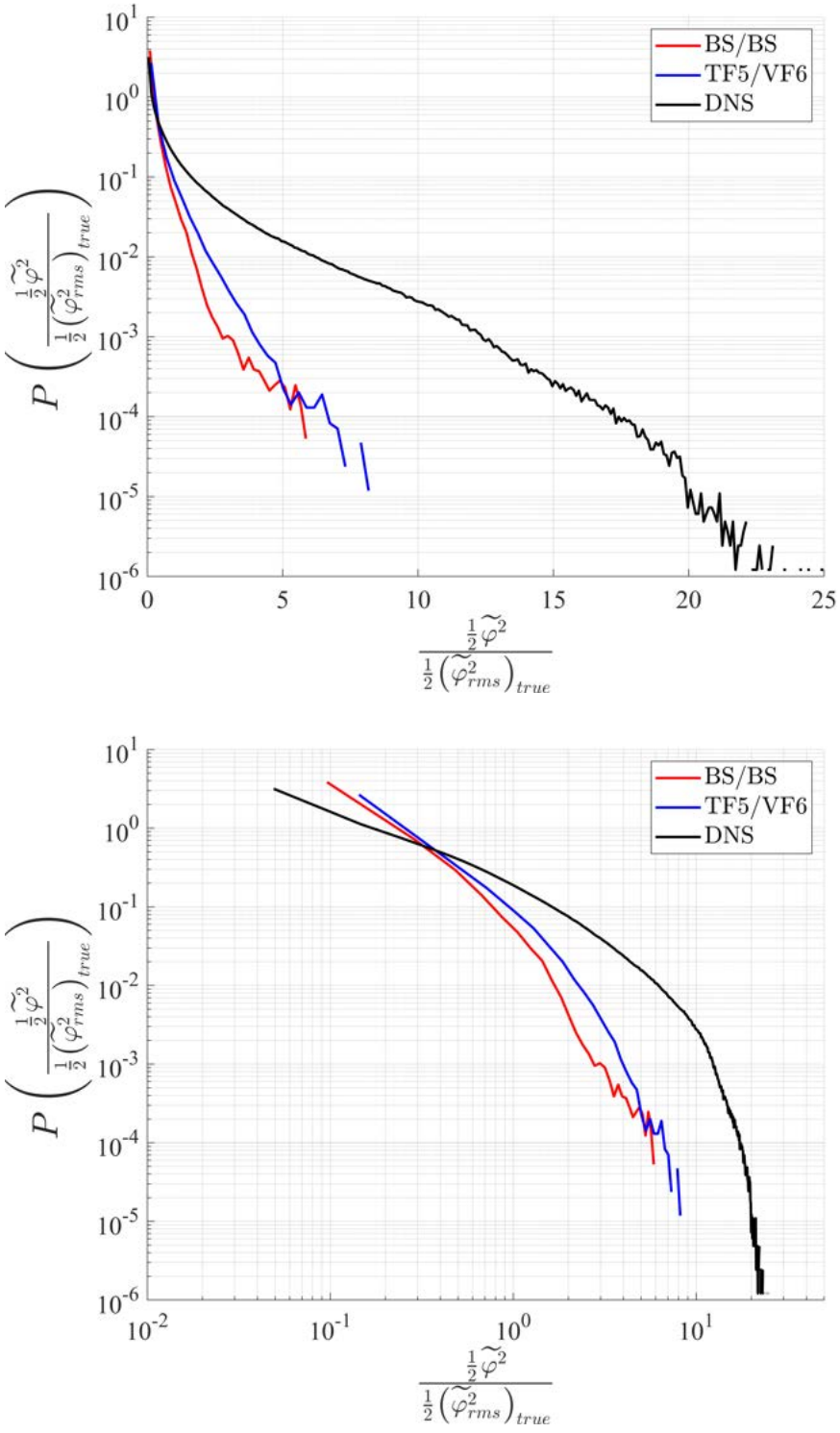

Figure 95. PDFs of resolved scalar energy in forward simulations based on traditional closure with basic Smagorinsky models for both $\boldsymbol{\tau}$ and $\mathbf{z}$ *(red)*, autonomic closure with TF5 and VF6 representations for $\boldsymbol{\tau}$ and $\mathbf{z}$ *(blue)*, and corresponding filtered DNS *(black)*.

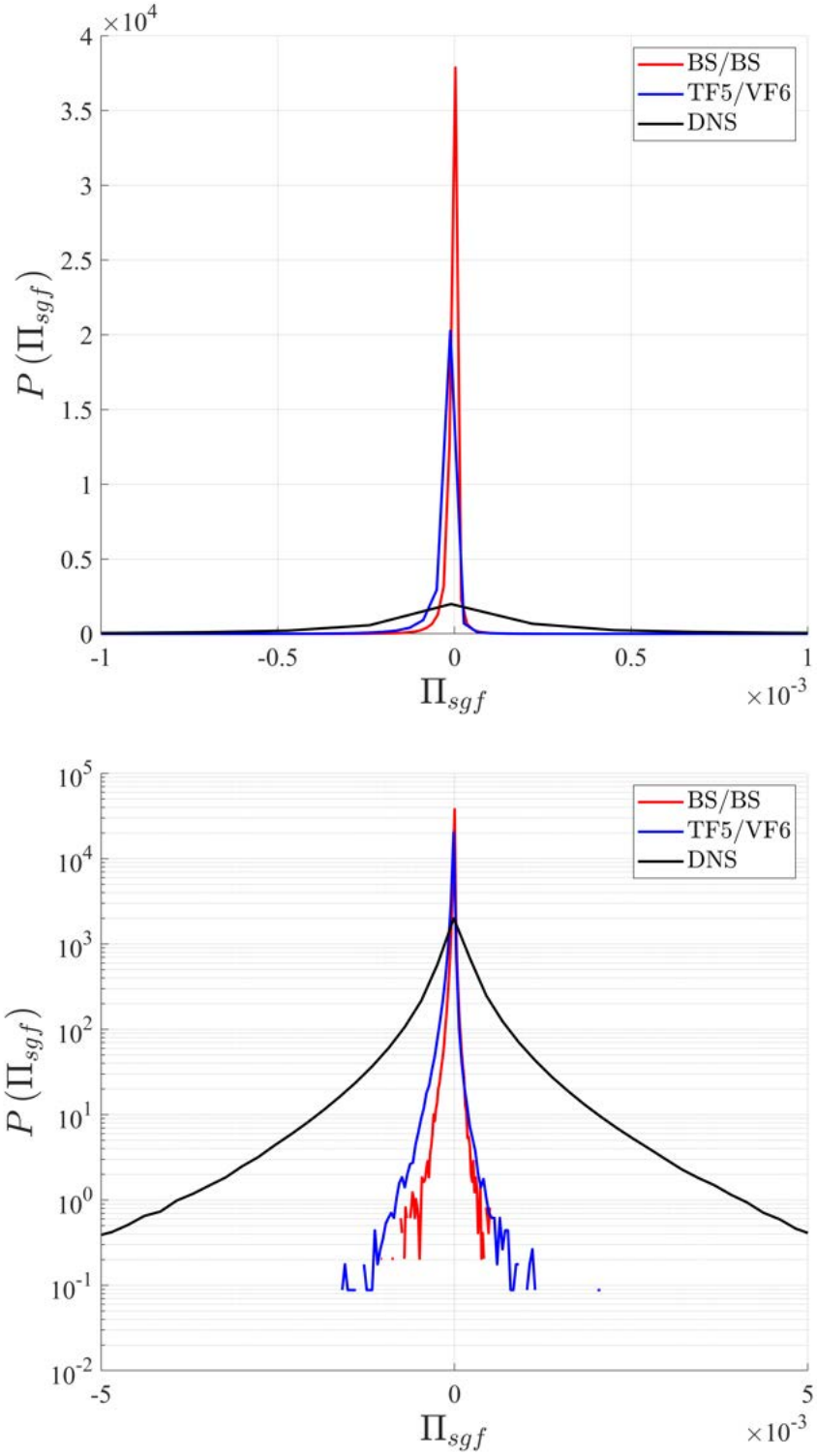

Figure 96. PDFs of scalar energy production $\Pi = z_i \frac{\partial \widetilde{\varphi}}{\partial x_i}$ in forward simulations based on traditional closure with basic Smagorinsky models for both $\boldsymbol{\tau}$ and $\mathbf{z}$ *(red)*, autonomic closure with TF5 and VF6 representations for $\boldsymbol{\tau}$ and $\mathbf{z}$ *(blue)*, and corresponding filtered DNS *(black)*.

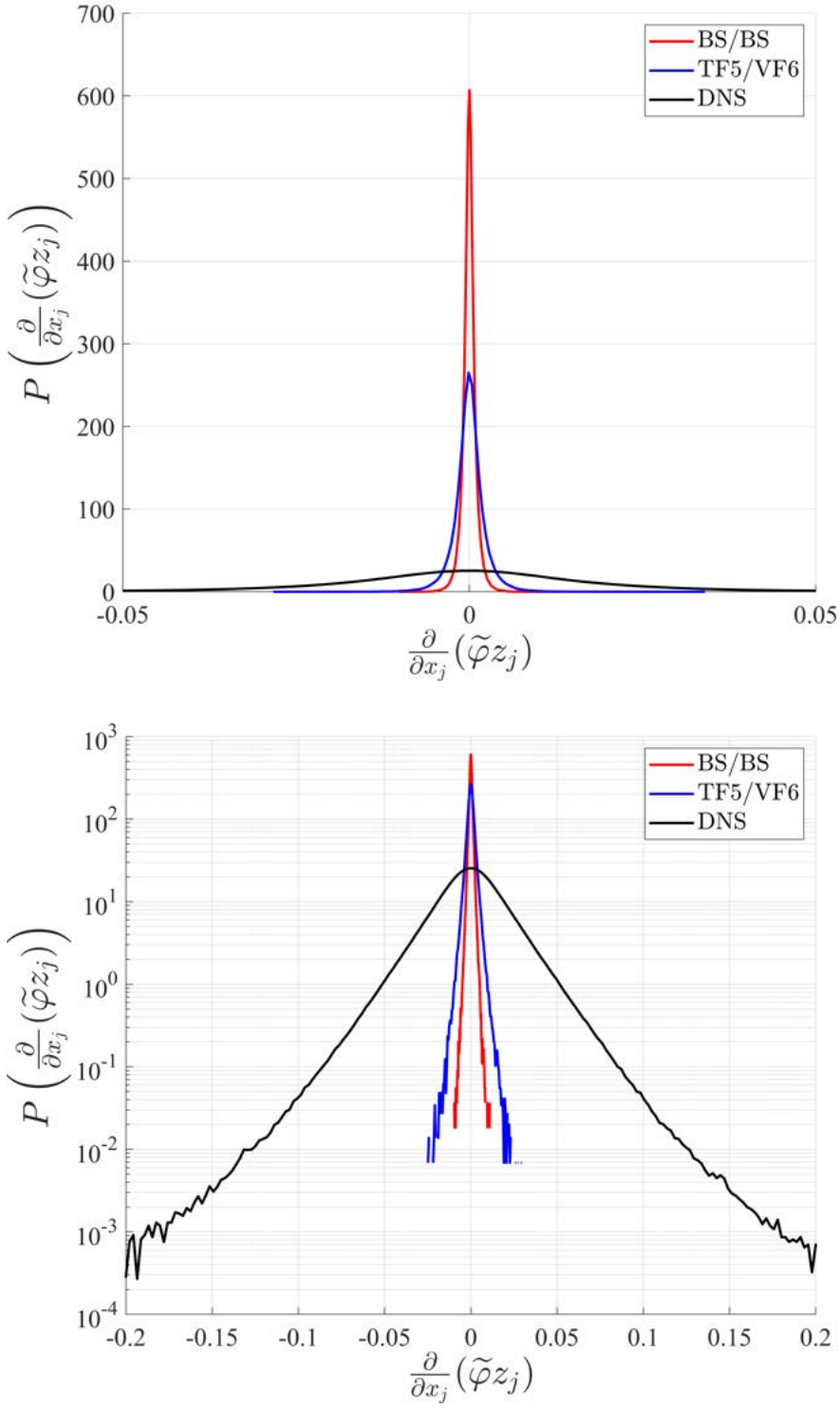

Figure 97. PDFs of scalar energy transport by the subgrid scalar flux in forward simulations based on traditional closure with basic Smagorinsky models for both $\boldsymbol{\tau}$ and $\mathbf{z}$ *(red)*, autonomic closure with TF5 and VF6 representations for $\boldsymbol{\tau}$ and $\mathbf{z}$ *(blue)*, and corresponding filtered DNS *(black)*.

Chapter 10

CONCLUSIONS

Autonomic closure is a recently-proposed subgrid closure methodology for large eddy simulation (LES) that replaces the prescribed subgrid models used in traditional LES closure with highly generalized representations of subgrid terms, and solution of a local system identification problem, that allows the simulation itself to determine the local relation between each subgrid term and the resolved variables at every point and time. This study has sought to *(i)* develop computationally efficient tensorally-correct generalized representations for the subgrid stress tensor $\boldsymbol{\tau}$ and the subgrid scalar flux vector $\mathbf{z}$, *(ii)* assess the accuracy of these representation via *a priori* tests, *(iii)* assess the computational stability of these representations in forward simulations with a high-order pseudo-spectral code, and *(iv)* conduct *a posteriori* tests of autonomic closure with these representations to quantify the improvement in accuracy that this new closure methodology provides for multiphysics LES requiring accuracy extending across the entire range of resolved scales. Major conclusions from the present study can be summarized as follows:

1. This study has, for the first time, demonstrated fully dynamic implementations of autonomic closure for $\boldsymbol{\tau}$ and $\mathbf{z}$, and has thereby enabled the first LES based on fully dynamic autonomic closure for simulating problems involving turbulent conserved scalar mixing.

2. The fundamentally complete and minimal tensor representation theory of Smith (1971) enables tensorally-correct generalized representations for subgrid terms such as $\boldsymbol{\tau}$ and $\mathbf{z}$ to be expressed in parametric quantities that can be formed from the resolved variables in the simulation; such tensorally-correct representations

offer inherent computational efficiencies over nonparametric and non-tensorally-correct representations.

3. A complete and minimal representation for the subgrid stress tensor in products of the strain rate and rotation rate tensors, $\mathbf{S}$ and $\mathbf{R}$, has been derived in this study based on the Smith (1971) tensor representation theory. This representation, termed "TF8" is more compact than a previous 11-term representation originally proposed by Lumley (1970) and Pope (1975).

4. Based on prior work showing that the subgrid stress tensor $\boldsymbol{\tau}$ can be accurately represented in forms that extend only up to second-order products of velocity components, the TF8 representation can be truncated to retain tensor products only up to second-order, producing a tensorally correct representation termed "TF5".

5. Using the complete and minimal representation theory of Smith (1971), the subgrid scalar flux $\mathbf{z}$ can be represented in the strain rate and rotation rate tensors, $\mathbf{S}$ and $\mathbf{R}$, and the scalar gradient vector $\nabla\varphi$, in a complete and minimal 6-term form termed "VF6".

6. *A priori* tests have shown that the TF5 representation for the subgrid stress tensor $\boldsymbol{\tau}$, and the VF6 representation for the subgrid scalar flux vector $\mathbf{z}$, produce substantially more accurate fields for $\boldsymbol{\tau}(\mathbf{x}, t)$ and $\boldsymbol{z}(\mathbf{x}, t)$ than do traditional prescribed subgrid models, including the basic Smagorinsky model, the dynamic Smagorinsky model, and the Bardina scale similarity model.

7. A compact and fully general result has been developed for rescaling the coefficient associated with any term in any generalized representation for the subgrid stress $\boldsymbol{\tau}$ from the test-filter scale to the LES-filter scale. A corresponding compact

and fully general result has been obtained for rescaling the coefficient associated with any term in any generalized representation for the subgrid scalar flux $\mathbf{z}$.

8. In forward simulations with a high-order pseudo-spectral code, the TF5 representation for $\boldsymbol{\tau}$ is inherently stable without the need for any added dissipation or other stabilization. With just 10-15% added dissipation it produces a kinetic energy spectrum $E(k)$ that shows $k^{-5/3}$ inertial-range scaling over the entire range of scales in the simulation; this is precisely what the energy spectrum should look like from a large eddy simulation that properly transfers momentum and energy within resolved scales and between resolved and subgrid scales.

9. *A posteriori* tests based on forward simulations of turbulent conserved scalar mixing with the same high-order pseudo-spectral code show that velocity and scalar statistics from autonomic closure with the TF5 representation for $\boldsymbol{\tau}$ and VF6 representation for $\mathbf{z}$ compare substantially better with corresponding statistics of filtered fields from direct numerical simulation (DNS) than do the statistics from traditional closure using prescribed models.

10. Collectively, the results from this study have demonstrated that fully dynamic autonomic closure is a practical approach for LES of multiphysics problems that require accuracy across all resolved scales, extending even to the smallest resolved scales in the simulation.

REFERENCES

[1] S. Bose and P. Moin. "A dynamic slip boundary condition for wall-modeled large-eddy simulation". In: *Phys. Fluids* 26.1 (2014), p. 015104.

[2] U. Piomelli. "Wall-layer models for large-eddy simulations". In: *Prog. Aerosp. Sci.* 44.6 (2008), pp. 437–446.

[3] U. Piomelli. "Wall-modeled large-eddy simulations: Present status and prospects". In: *Direct and Large-Eddy Simulation VII*. Springer, 2010, pp. 1–10.

[4] S. Kawai and J. Larsson. "Wall-modeling in large eddy simulation: Length scales, grid resolution, and accuracy". In: *Phys. Fluids* 24.1 (2012), p. 015105.

[5] J. C. Tyacke, M. Mahak, and P. G. Tucker. "Large-scale multifidelity, multi-physics, hybrid Reynolds-averaged Navier–Stokes/large-eddy simulation of an installed aeroengine". In: *J. Prop. Power* 32.4 (2016), pp. 997–1008.

[6] P. Schmitt, T. Poinsot, B. Schuermans, and K. Geigle. "Large-eddy simulation and experimental study of heat transfer, nitric oxide emissions and combustion instability in a swirled turbulent high-pressure burner". In: *J. Fluid Mech.* 570 (2007), pp. 17–46.

[7] A. Neophytou, B. Cuenot, and P. Duchaine. "Large-eddy simulation of ignition and flame propagation in a trisector combustor". In: *J. Prop. Power* 32.2 (2015), pp. 345–359.

[8] R. Baurle. "Hybrid Reynolds-averaged/large-eddy simulation of a scramjet cavity flameholder". In: *AIAA J.* 55.2 (2016), pp. 544–560.

[9] A. Poubeau, R. Paoli, A. Dauptain, F. Duchaine, et al. "Large-eddy simulations of a single-species solid rocket booster jet". In: *AIAA J.* 53.6 (2014), pp. 1477–1491.

[10] F. Xiao, M. Dianat, and J. J. McGuirk. "Large eddy simulation of liquid-jet primary breakup in air crossflow". In: *AIAA J.* 51.12 (2013), pp. 2878–2893.

[11] M. Bini and W. Jones. "Large-eddy simulation of particle-laden turbulent flows". In: *J. Fluid Mech.* 614 (2008), pp. 207–252.

[12] G. Aubard, X. Gloerfelt, and J.-C. Robinet. "Large-eddy simulation of broadband unsteadiness in a shock/boundary-layer interaction". In: *AIAA J.* 51.10 (2013), pp. 2395–2409.

[13] M. S. Loginov, N. A. Adams, and A. A. Zheltovodov. "Large-eddy simulation of shock-wave/turbulent-boundary-layer interaction". In: *J. Fluid Mech.* 565 (2006), pp. 135–169.

[14] U. Piomelli. "Large-eddy simulation: achievements and challenges". In: *Prog. Aerosp. Sci.* 35.4 (1999), pp. 335–362.

[15] K. Mahesh, G. Constantinescu, S. Apte, G. Iaccarino, et al. "Large-eddy simulation of reacting turbulent flows in complex geometries". In: *J. Appl. Mech.* 73.3 (2006), pp. 374–381.

[16] M. Dianat, Z. Yang, D. Jiang, and J. McGuirk. "Large eddy simulation of scalar mixing in a coaxial confined jet". In: *Flow Turbul. Combust.* 77.1-4 (2006), p. 205.

[17] G. C. Burton. "The nonlinear large-eddy simulation method applied to Sc 1 and Sc » passive-scalar mixing". In: *Phys. Fluids* 20.3 (2008), p. 035103.

[18] G. C. Burton. "Study of ultrahigh Atwood-number Rayleigh–Taylor mixing dynamics using the nonlinear large-eddy simulation method". In: *Phys. Fluids* 23.4 (2011), p. 045106.

[19] J. M. Mejıa, A. Sadiki, A. Molina, F. Chejne, et al. "Large eddy simulation of the mixing of a passive scalar in a high-Schmidt turbulent jet". In: *J. Fluids Eng.* 137.3 (2015), p. 031301.

[20] H. Pitsch. "Large-eddy simulation of turbulent combustion". In: *Annu. Rev. Fluid Mech.* 38 (2006), pp. 453–482.

[21] B. Franchetti, F. C. Marincola, S. Navarro-Martinez, and A. Kempf. "Large eddy simulation of a pulverised coal jet flame". In: *Proc. Comb. Inst.* 34.2 (2013), pp. 2419–2426.

[22] D. K. Tafti, L. He, and K. Nagendra. "Large eddy simulation for predicting turbulent heat transfer in gas turbines". In: *Phil. Trans. R. Soc. A* 372.2022 (2014), p. 20130322.

[23] A. Irannejad and F. Jaberi. "Large eddy simulation of turbulent spray breakup and evaporation". In: *Int. J. Multiphase Flow* 61 (2014), pp. 108–128.

[24] S. De and S. H. Kim. "Large eddy simulation of dilute reacting sprays: Droplet evaporation and scalar mixing". In: *Comb. Flame* 160.10 (2013), pp. 2048–2066.

[25] S. Elghobashi. "On predicting particle-laden turbulent flows". In: *Appl. Sci. Res.* 52.4 (1994), pp. 309–329.

[26] F. Xiao, Z. Wang, M. Sun, J. Liang, et al. "Large eddy simulation of liquid jet primary breakup in supersonic air crossflow". In: *Int. J. Multiphase Flow* 87 (2016), pp. 229–240.

[27] P. Sagaut. *Large eddy simulation for incompressible flows: An Introduction*. Springer Berlin, 2006.

[28] M. Germano. "Turbulence: the filtering approach". In: *J. Fluid Mech.* 238 (1992), pp. 325–336.

[29] S. Pope. *Turbulent Flows*. Cambridge University Press, Cambridge, UK, 2000, pp. 1361–1362.

[30] T. Lund and H. Kaltenbach. *Experiments with explicit filtering for LES using a finite-difference method*. Annual Research Briefs, 1995, pp. 91–105. Center for Turbulence Research, Stanford University.

[31] C. Meneveau and J. Katz. "Scale-invariance and turbulence models for large-eddy simulation". In: *Annu. Rev. Fluid Mech.* 32.1 (2000), pp. 1–32.

[32] S. Liu, C. Meneveau, and J. Katz. "On the properties of similarity subgrid-scale models as deduced from measurements in a turbulent jet". In: *J. Fluid Mech.* 275 (1994), pp. 83–119.

[33] S. Menon, P.-K. Yeung, and W.-W. Kim. "Effect of subgrid models on the computed interscale energy transfer in isotropic turbulence". In: *Comput. Fluids* 25.2 (1996), pp. 165–180.

[34] Y. Shi, Z. Xiao, and S. Chen. "Constrained subgrid-scale stress model for large eddy simulation". In: *Phys. Fluids* 20.1 (2008), p. 011701.

[35] A. E. Tejada-Martınez and K. E. Jansen. "A dynamic Smagorinsky model with dynamic determination of the filter width ratio". In: *Phys. Fluids* 16.7 (2004), pp. 2514–2528.

[36] C. Yu, Z. Xiao, and X. Li. "Scale-adaptive subgrid-scale modelling for large-eddy simulation of turbulent flows". In: *Phys. Fluids* 29.3 (2017), p. 035101.

[37] C. B. da Silva and J. C. Pereira. "The effect of subgrid-scale models on the vortices computed from large-eddy simulations". In: *Phys. Fluids* 16.12 (2004), pp. 4506–4534.

[38] S. Ghosal. "An analysis of numerical errors in large-eddy simulations of turbulence". In: *J. Comput. Phys.* 125.1 (1996), pp. 187–206.

[39] J. Meyers, B. J. Geurts, and M. Baelmans. "Database analysis of errors in large-eddy simulation". In: *Phys. Fluids* 15.9 (2003), pp. 2740–2755.

[40] A. Kravchenko and P. Moin. "On the effect of numerical errors in large eddy simulations of turbulent flows". In: *J. Comput. Phys.* 131.2 (1997), pp. 310–322.

[41] F. K. Chow and P. Moin. "A further study of numerical errors in large-eddy simulations". In: *J. Comput. Phys.* 184.2 (2003), pp. 366–380.

[42] S. Liu, C. Meneveau, and J. Katz. "Experimental study of similarity subgrid-scale models of turbulence in the far-field of a jet". In: *Appl. Sci. Res.* 54.3 (1995), pp. 177–190.

[43] S. Liu, J. Katz, and C. Meneveau. "Evolution and modelling of subgrid scales during rapid straining of turbulence". In: *J. Fluid Mech.* 387 (1999), pp. 281–320.

[44] F. Sarghini, U. Piomelli, and E. Balaras. "Scale-similar models for large-eddy simulations". In: *Phys. Fluids* 11.6 (1999), pp. 1596–1607.

[45] J. Smagorinsky. "General circulation experiments with the primitive equations". In: *Mon. Weather Rev.* 91 (1963), p. 99.

[46] M. Germano, U. Piomelli, P. Moin, and W. H. Cabot. "A dynamic subgrid-scale eddy viscosity model". In: *Phys. Fluids A* 3.7 (1991), pp. 1760–1765.

[47] D. K. Lilly. "A proposed modification of the Germano subgrid-scale closure method". In: *Phys. Fluids A* 4.3 (1992), pp. 633–635.

[48] P. Moin, K. Squires, W. Cabot, and S. Lee. "A dynamic subgrid-scale model for compressible turbulence and scalar transport". In: *Phys. Fluids A* 3.11 (1991), pp. 2746–2757.

[49] U. Piomelli. "High Reynolds number calculations using the dynamic subgrid-scale stress model". In: *Phys. Fluids A* 5.6 (1993), pp. 1484–1490.

[50] J. Bardina, J. Ferziger, and W. Reynolds. "Improved subgrid-scale models for large-eddy simulation". In: *AIAA* 80-1357 (1980).

[51] J. Bardina, J. H. Ferziger, and W. C. Reynolds. *Improved turbulence models based on large eddy simulation of homogeneous, incompressible turbulent flows*. Tech. rep. TF-19. Stanford University, 1983.

[52] K. Horiuti. "The role of the Bardina model in large eddy simulation of turbulent channel flow". In: *Phys. Fluids A* 1.2 (1989), pp. 426–428.

[53] Y. Zang, R. L. Street, and J. R. Koseff. "A dynamic mixed subgrid-scale model and its application to turbulent recirculating flows". In: *Phys. Fluids A* 5.12 (1993), pp. 3186–3196.

[54] R. Akhavan, A. Ansari, S. Kang, and N. Mangiavacchi. "Subgrid-scale interactions in a numerically simulated planar turbulent jet and implications for modelling". In: *J. Fluid Mech.* 408 (2000), pp. 83–120.

[55] T. S. Lund, S. Ghosal, and P. Moin. "Numerical experiments with highly-variable eddy viscosity models". In: *Engineering Applications to Large Eddy Simulation*. Ed. by R. S. Piomelli U. Vol. 162. New York: ASME, 1993, pp. 7–11.

[56] S. Ghosal, T. S. Lund, P. Moin, and K. Akselvoll. "A dynamic localization model for large-eddy simulation of turbulent flows". In: *J. Fluid Mech.* 286 (1995), pp. 229–255.

[57] V. Gravemeier. "A consistent dynamic localization model for large eddy simulation of turbulent flows based on a variational formulation". In: *J. Comput. Phys.* 218.2 (2006), pp. 677–701.

[58] R. N. King, P. E. Hamlington, and W. Dahm. "Autonomic subgrid-scale closure for large eddy simulations". In: *53rd AIAA Aerospace Sciences Meeting*. 2015-1285. 2015.

[59] R. N. King, P. E. Hamlington, and W. J. A. Dahm. "Autonomic subgrid-scale closure for large eddy simulations". In: *15th European Turbulence Conference*. 2015, pp. 15–16.

[60] R. N. King, P. E. Hamlington, and W. J. Dahm. "Autonomic closure for turbulence simulations". In: *Phys. Rev. E* 93.3 (2016), p. 031301.

[61] A. Kshitij. "Accurate and Efficient Autonomic Closure for Turbulent Flows". In: *ProQuest Dissertations and Theses* May (2019), p. 149.

[62] A. Kshitij, E. W. Stallcup, P. E. Hamlington, and W. J. Dahm. "Balancing Accuracy and Efficiency in the Autonomic Closure Methodology for Large Eddy Simulations". In: *AIAA Science and Technology Forum*. 2021.

[63] G. Smith. "On isotropic functions of symmetric tensors, skew-symmetric tensors and vectors". In: *Int. J. Engg. Sci.* 9.10 (1971), pp. 899–916.

[64] S. Pennisi and M. Trovato. "On the irreducibility of Professor GF Smith's representations for isotropic functions". In: *Int. J. Engg. Sci.* 25.8 (1987), pp. 1059–1065.

[65] Q.-S. Zheng. "Theory of representations for tensor functions–A unified invariant approach to constitutive equations". In: *Appl. Mech. Rev.* 47.11 (1994), pp. 545–587.

[66] M. Itskov. *Tensor algebra and tensor analysis for engineers*. Springer, 2007.

[67] J. Lumley. "Toward a turbulent constitutive relation". In: *J. Fluid Mech.* 41.2 (1970), pp. 413–434.

[68] S. B. Pope. "A more general effective-viscosity hypothesis". In: *J. Fluid Mech.* 72.2 (1975), pp. 331–340.

[69] T. S. Lund and E. Novikov. *Parameterization of subgrid-scale stress by the velocity gradient tensor*. Annual Research Briefs, 1992, pp. 27-43. Center for Turbulence Research, Stanford University.

[70] T. B. Gatski and C. G. Speziale. "On explicit algebraic stress models for complex turbulent flows". In: *J. Fluid Mech.* 254 (1993), pp. 59–78.

[71] M. Oberlack. *Invariant modeling in large-eddy simulation of turbulence*. Annual Research Briefs, 1997, pp.91-105. Center for Turbulence Research, Stanford University.

[72] "General explicit algebraic stress relations and best approximation for three-dimensional flows". In: *Int. J. Engg. Sci.* 36.7-8 (1998), pp. 739–763. DOI: 10.1016/s0020-7225(97)00122-5.

[73] D. Razafindralandy, A. Hamdouni, and M. Oberlack. "Analysis and development of subgrid turbulence models preserving the symmetry properties of the Navier–Stokes equations". In: *Eur. J. Mech. B/Fluids* 26.4 (2007), pp. 531–550.

[74] S. Fu, C. Wang, and Y. Guo. "On the minimal representation of non-linear eddy-viscosity models". In: *J. Turb.* 12.47 (2011), N47. DOI: 10.1080/14685248.2011.633085.

[75] G. E. Smith and G. Bao. "Isotropic Invariants of Traceless Symmetric Tensors of Orders Three and Four". In: *Int. J. Engg. Sci.* 35.15 (1997), pp. 1457–1462.

[76] *Johns Hopkins University Turbulence Database*. URL: http://turbulence.pha.jhu.edu/.

[77] Y. Li, E. Perlman, M. Wan, Y. Yang, et al. "A public turbulence database cluster and applications to study Lagrangian evolution of velocity increments in turbulence". In: *J. Turb.* 9 (2008), N31.

[78] D. A. Donzis and P. K. Yeung. "Resolution effects and scaling in numerical simulations of passive scalar mixing in turbulence". In: *Physica D: Nonlinear Phenomena* 239.14 (2010), pp. 1278–1287. DOI: 10.1016/j.physd.2009.09.024.

[79] P. E. Hamlington, R. Darragh, C. A. Briner, C. A. Z. Towery, et al. "Lagrangian analysis of high-speed turbulent premixed reacting flows : Thermochemical trajectories in hydrogen – air flames". In: 186 (2017), pp. 193–207. DOI: 10.1016/j.combustflame.2017.08.001.

[80] J. M. Stone, T. A. Gardiner, P. Teuben, J. F. Hawley, et al. “ATHENA : A NEW CODE FOR ASTROPHYSICAL MHD”. In: (2008).